UNIVERSITY
OF LATVIA

FACULTY OF PHYSICS, MATHEMATICS AND OPTOMETRY

Edgars Butanovs

SYNTHESIS AND PROPERTIES OF TRANSITION METAL DICHALCOGENIDE BASED CORE-SHELL NANOWIRES

Doctoral Thesis

Submitted for the Doctoral degree in Physics
Subfield of Materials Physics

Scientific advisor:
Dr. phys. Boris Polyakov

RIGA, 2020

The doctoral thesis work was carried out in Institute of Solid State Physics, University of Latvia from 2016 to 2020.

The thesis contains an introduction, 5 chapters and a reference list.

Form of the thesis: dissertation in materials physics

Supervisor: *Dr. phys.* **Boris Polyakov**, senior researcher

Reviewers:

1. *Dr. habil. phys.* **Linards Skuja**, senior researcher, Institute of Solid State Physics, University of Latvia
2. *Dr. sc. ing.* **Andris Šutka**, senior researcher, Riga Technical University
3. *Dr. sci.* **Alexey Romanov**, professor, ITMO University (Saint Petersburg, Russia)

The thesis will be defended at the public session of the Doctoral Committee of Physics, Astronomy and Mechanics of University of Latvia on September 11, 2020 in the conference hall of Institute of Solid State Physics, 8 Kengaraga street.

The thesis is available at the Library of the University of Latvia, Raiņa bulv. 19.

Chairman of the Doctoral Committee — *Dr. habil. phys.* **Uldis Rogulis**

Secretary of the Doctoral Committee — **Karlīna Engere**

ABSTRACT

This Dissertation is dedicated to the development and characterization of various material nanowire (NW) and transition metal dichalcogenide *core-shell* heterostructures.

Novel synthesis methods of highly-crystalline *core-shell* NWs have been demonstrated, the nanomaterials structure, composition, morphology and photoelectrical properties have been characterized. The following results can be highlighted:

- Synthesis of novel ZnO-WS_2 *core-shell* NW heterostructures. Fabrication of as-grown nanostructure single-nanowire photodetector and demonstration of enhanced photoelectric properties in comparison to pure ZnO NWs.
- Synthesis of novel GaN-ReS_2, ZnS-ReS_2 and ZnO-ReS_2 *core-shell* NW heterostructures. Development of new few-layer ReS_2 synthesis method - sulfurization of a pre-deposited ReO_x coating.
- Synthesis of novel ZnO-MoS_2 *core-shell* NW heterostructures by decomposition and sulfurization of a pre-deposited $(NH_4)_6Mo_7O_{24}\cdot 4H_2O$ coating, and comparison with sputter-deposited MoO_3 coating conversion.
- Synthesis of novel PbI_2-decorated ZnO NW heterostructures. Development of new few-layer PbI_2 synthesis method - iodination of a pre-deposited PbO_x coating. Fabrication of as-grown nanostructure single-nanowire photodetectors and demonstration of their photoelectric properties.

The synthesis methods developed in this work are not limited to the demonstrated heterostructures and can be applied for other materials. Furthermore, this work provides an insight into how a few-atomic-layer thin coating can change the photoelectric properties of a ZnO nanowire.

Keywords: nanowire, transition metal dichalcogenide, 2D materials, zinc oxide, photodetector, nanofabrication

CONTENTS

LIST OF ABBREVIATIONS 7

1. INTRODUCTION 9

1.1 Problems and motivation 9

1.2 Objective and tasks 10

1.3 Scientific novelty 11

1.4 Contribution of the Author 11

1.5 Outline of the Dissertation 11

2. LAYERED 2D TRANSITION METAL DICHALCOGENIDES 13

2.1 Introduction 13

2.2 Physical properties of TMDs 14

2.3 Synthesis methods and device fabrication 17

2.4 Perspective applications 23

3. NANOWIRES 27

3.1 Introduction 27

3.2 Materials, properties and applications 28

3.3 Nanowire synthesis via *vapour-liquid-solid* mechanism 30

3.4 *Core-shell* heterostructures 32

4. EXPERIMENTAL METHODS 34

4.1 Physical vapour deposition 34

4.2 Chemical vapour deposition 35

4.3 Electron microscopy 36

4.4 X-ray diffraction and spectroscopy methods 37

4.5 Optical lithography 38

4.6 Single-nanowire device fabrication and photoelectric measurements 39

5. RESULTS AND DISCUSSION 43

5.1 Tungsten disulfide WS_2 43

5.1.1 ZnO-WS_2 *core-shell* nanowires 43
5.1.2 GaN-WS_2 *core-shell* nanowires 47
5.1.3 WS_2 reference sample 49
5.2 Rhenium disulfide ReS_2 49
5.2.1 GaN-ReS_2, ZnS-ReS_2 and ZnO-ReS_2 *core-shell* nanowires 50
5.2.2 ReS_2 reference sample 53
5.3 Molybdenum disulfide MoS_2 54
5.3.1 ZnO-MoS_2 *core-shell* nanowires 55
5.3.2 MoS_2 reference sample 59
5.4 Lead iodide PbI_2 59
5.4.1 PbI_2-decorated ZnO nanowires 60
5.4.2 PbI_2 reference sample 64
5.5 Single nanowire photodetectors 64
5.5.1 PbS, In_2S_3, CdS and ZnSe nanowire photodetectors 65
5.5.2 ZnO-WS_2 *core-shell* nanowire photodetectors 67
5.5.3 PbI_2-decorated ZnO nanowire photodetectors 70
6. CONCLUSIONS AND THESIS 72
Thesis 73
LIST OF PUBLICATIONS 74
PARTICIPATION IN SUMMER SCHOOLS AND CONFERENCES 75
REFERENCES 76
ACKNOWLEDGEMENTS 85
APPENDIX A 86
APPENDIX B 89
PUBLICATIONS 91

LIST OF ABBREVIATIONS

1D	One-dimensional
2D	Two-dimensional
3D	Three-dimensional
CVD	Chemical vapour deposition
DC	Direct current
DI	Deionized
DOS	Density of states
EBL	Electron-beam lithography
EQE	External quantum efficiency
FET	Field-effect transistor
FIB	Focused ion beam
GIS	Gas injection system
LED	Light-emitting diode
MEMS	Microelectromechanical systems
MOCVD	Metal-organic chemical vapour deposition
NW	Nanowire
PL	Photoluminescence
PVD	Physical vapour deposition
R_λ	Spectral responsivity
SAED	Selected area electron diffraction
SCLC	Space-charge limited current
SEM	Scanning electron microscope
TEM	Transmission electron microscope
TFT	Thin-film transistor
TMD	Transition metal dichalcogenide
vdW	van der Waals
VLS	Vapour-liquid-solid
XRD	X-ray diffraction

1. INTRODUCTION

Nanomaterials are defined as materials with at least one spatial dimension in the scale of 10^{-9} m, or usually below 100 nm [1]. They are classified by the number of dimensions in the nanoscale, for instance, 2D materials have one dimension below 100 nm, 1D and 0D materials have two and all three dimensions in nanoscale, respectively. Some common examples of nanomaterials are nanoparticles and quantum dots (0D), nanowires and nanotubes (1D), layered van der Waals materials (2D).

The field of nanomaterials and nanotechnology emerged in the second half of the 20th century and has grown immensely in the last 30 years, mainly due to the advancement of complicated characterization techniques, such as electron and probe microscopies, which was prompted by the rapid progress of computing technologies. The available characterization tools allowed investigation and manipulation of materials in nanoscale, leading to several discoveries, like carbon fullerenes and nanotubes, that promoted the research even further. Nanomaterials exhibit physical and chemical properties different from their bulk counterparts due to the large surface/volume ratio and, thus, the important contribution of surface atoms, as well as quantum confinement and other quantum phenomena [1]. Besides the miniaturization of current device designs, unique properties and extraordinary phenomena of nanoscale materials leads to entirely new applications in fields of physics, chemistry, biology and medicine.

Currently nanotechnology is a substantial part of materials science and physics research, which is focused on synthesis and characterization of nanomaterials, and development of nanoscale device fabrication techniques. There is always an active search for new materials that exhibit promising and novel properties for different applications.

1.1 Problems and motivation

Nanowires (NWs) – 1D nanostructures – are being explored as promising materials for applications in electronics, optoelectronics, photonics and microelectromechanical systems (MEMS), and their potential has been demonstrated in many proof-of-concept devices [2]. Depending on the application, two different approaches of NW integration in devices can be distinguished – single-NW devices consist of individual separate NWs as the active components, whereas “bulk” devices contain periodic NW arrays or randomly dispersed NWs. Some NW applications, mainly the single-NW devices, struggle in assembly and scalability of the device fabrication to create a cost-effective production process that could compete with current technologies, such as silicon microfabrication. Several concepts have been proposed, for instance, controlled printing of NWs with roll-to-roll technology that uses microfluidics to align the NWs [3]. However, many other NW applications are entirely novel or complementary to current technologies and might be implemented in a much more scalable fashion, which is presently an active research field. Otherwise, entirely new applications or device concepts need to be proposed and developed. The necessary scientific research is not only related to developing competitive upscaling methods but also to producing new NW-based materials and studying their fundamental properties for novel applications [4]. One way to enhance and engineer NW characteristics, such as spectral absorption range and electrical properties, is to

create *core-shell* heterostructures – to modify the surface of a NW by a relatively thin coating (compared to the diameter of the NW) of a different material [5]. Surface of NWs has a significantly reduced lattice mismatch restriction compared to conventional semiconductor thin film growth thus enabling greater flexibility in choosing the materials to produce heterostructures and in engineering their properties [6,7].

Layered 2D van der Waals (vdW) materials have attracted great interest since the isolation of monolayer graphene in 2004 due to their unique structure and the promising physical properties that appear when the thickness of the material is reduced to one atomic layer [8]. Transition metal dichalcogenides (TMDs) are layered materials with a general chemical formula MX_2, where M is a periodic table Group 4 – 7 transition metal and X is a chalcogen, and are being actively researched for applications in electronics and optoelectronics due to their thickness-dependent bandgap [9]. TMDs layers have terminated surfaces without dangling bonds and are bound together by weak vdW forces, therefore, can be sequentially stacked unstrained without any covalent interlayer bonding even if materials are slightly lattice-mismatched [10]. There is an on-going search for large-scale synthesis methods of TMDs on different substrates before any practical applications could be realized [11].

Combining NWs and TMDs in *core-shell* heterostructures could lead to new knowledge about the interface formation between different materials and solid-state reactions in such systems, to novel nanostructures with enhanced properties, and development of new TMDs synthesis methods as NWs are a convenient template to study materials growth.

1.2 Objective and tasks

The main objective of this work is to synthesise novel *core-shell* nanowire heterostructures based on semiconductor nanowires and transition metal dichalcogenides, and to characterize the synthesised materials.

The following tasks have been defined:

1. To synthesise different material semiconductor NWs by *vapour-liquid-solid* (VLS) method and explore the potential of using such together with different TMDs in *core-shell* heterostructures.

2. To develop or adapt different methods of growing highly crystalline few-layer TMDs around NWs by chemical conversion of a pre-deposited coating.

3. To characterize as-grown nanostructures to obtain information about their structure, composition, morphology and optical properties, and use it to tune the growth process.

4. To test some selected synthesized materials for fabrication of single-nanowire photodetector devices, and to determine their photoelectric properties.

5. To assess the role of the shell on the NW photoelectric properties, and evaluate the potential of using such heterostructures in different practical applications.

All the research described in this Dissertation was carried out in Institute of Solid State Physics of University of Latvia.

1.3 Scientific novelty

The work summarized in this Dissertation encompasses new knowledge on synthesis of several different few-layer TMDs and on preparation of novel *core-shell* NW heterostructures, and includes elaboration on their physical properties. The following results can be highlighted:

1. Development of a versatile two-step method for growth of various layered vdW materials on semiconductor NWs. The procedure consists of deposition of a sacrificial coating on NWs via sputtering or immersion which is afterwards chemically converted in a reactive vapour at elevated temperature. In this work, highly-crystalline WS_2, ReS_2, MoS_2 and PbI_2 shells were successfully grown on monocrystalline NWs. The synthesis method is not limited to the demonstrated *core-shell* heterostructures but can also be applied for other materials.

2. Investigation of photoelectric properties of the selected novel as-grown heterostructures. ZnO-WS_2 *core-shell* NW two-terminal devices exhibit enhanced spectral responsivity up to 7 A/W at 405 nm illumination in comparison to pure ZnO NWs, and light absorption in the WS_2 shell extends the active spectral range to the red part of the spectrum. Up to 0.6 A/W high spectral responsivity was measured for the PbI_2-decorated ZnO NW photodetector devices at 405 nm illumination, and significantly decreased dark current was observed in comparison to pure ZnO NWs. Notably, ZnO NW surface passivation with layered vdW materials shell also improves their photoresponse time for almost two orders of magnitude due to thus limited photo-induced processes related to adsorption/desorption of atmospheric oxygen species which typically slows down photoresponse in ZnO NWs.

1.4 Contribution of the Author

The direct contribution of the Author is as follows: growth of NWs via VLS method; development of the sulfurization/iodination processes and tuning of the process parameters for *core-shell* heterostructure synthesis; characterization with scanning electron microscope and X-ray diffraction; single-nanowire photodetector device fabrication including optical lithography, *lift-off* and *in situ* NW manipulations inside SEM-FIB; photoelectric measurements of the as-fabricated devices; analysis and interpretation of the obtained data.

Body of the article was written by the Author for Publications I, III and VI, parts of the article were written by the Author for Publications II and IV.

1.5 Outline of the Dissertation

This Dissertation is organized in six chapters.

Chapter 1 is the introduction where the scope of the Dissertation is defined and motivated, as well as the objective, tasks, scientific novelty and contribution of the Author is stated.

Chapter 2 is a general overview of layered 2D transition metal dichalcogenides based on the most recent literature, and focuses on topics related to the Thesis. Information about the materials, their properties, synthesis, device fabrication methods and perspective applications is given and discussed.

Similarly, Chapter 3 is a general overview of semiconductor nanowires with a focus on the materials properties and applications, *vapour-liquid-solid* synthesis, and *core-shell* nanowire heterostructures.

Experimental methods used in this work are described in Chapter 4. Details about physical and chemical deposition methods, characterization techniques and device fabrication are given.

Chapter 5 consists of the obtained results and discussion. Novel *core-shell* nanowires with WS_2, ReS_2, MoS_2 and PbI_2 shells and different material cores (ZnO, GaN etc.) were synthesised and characterized, as well as as-grown single-nanowire photodetectors were fabricated and their photoelectric properties investigated.

Main conclusions and Thesis of the Dissertation are given in Chapter 6, which is followed by Author's list of publications, attended conferences and summer schools, list of references, and acknowledgements.

Technical details on synthesis procedures of nanowires, nanowire heterostructures and on photodetector device fabrication are given in Appendix A.

Appendix B contains characterization data (SEM images and XRD patterns) of the synthesised pure nanowires which were used in this study.

Copies of the articles, in which the obtained results have been published, are appended in the end of this Dissertation.

2. LAYERED 2D TRANSITION METAL DICHALCOGENIDES

2.1 Introduction

A specific type of materials - layered van der Waals (vdW) materials - have attracted great interest since the isolation of monolayer graphene in 2004, due to their unique structure and the promising physical properties that appear when the thickness of the material is reduced to one atomic layer. These materials have an atomic structure similar to well-known graphite – strong in-plane bonds and weak interlayer bonding [8]. Bulk materials of this group have been widely studied in the last century, as most of these materials are quite abundant and have been used in different technological fields, however until 2004 it was believed that it is not possible to obtain an only one separate stable layer [12]. There was some research done in 1960s that showed that electrical conductivity in a few-layer graphite is higher when measured laterally in-plane rather than between the planes, but it was still assumed and assumptions justified by experimental and theoretical research that stable two-dimensional (2D) atomic crystals cannot exist separately in nature, as all attempts to obtain such were unsuccessful – with the used methods the layers tended to curl, roll or deform in other ways [13–15]. The ground-breaking discovery by K. Novoselov and A. Geim in 2004 proved otherwise – by mechanically exfoliating highly crystalline graphite with a Scotch tape they were able to obtain one atomic layer of graphite (graphene) on an oxidized silicon substrate and measure its electrical properties [12]. In the following few years it was demonstrated that such graphene crystals exhibit extraordinary electrical and mechanical properties, therefore opening a new field in materials science and nanotechnology [16]. For their contribution, Geim and Novoselov were awarded The Nobel Prize in Physics in 2010.

Afterwards, 2D materials became one of the "hottest" topics in modern physics – in 2011 an intensive research started on layered transition metal dichalcogenide (TMD) semiconductors, mainly MoS_2 and WS_2 [17–19], and around 2015 more exotic compounds were started to be studied, such as NbS_2 and ReS_2 [11,20]. Since 2004 the number of published scientific papers with keywords "2D materials" has increased nearly exponentially as shown in *Fig. 2.1*, taken from Web of Science (WoS) publication data. Nowadays it is an ongoing wide research field that focuses on many different materials, specific synthesis and characterization approaches, device fabrication and applications [11]. *Fig. 2.2* depicts the large family of 2D materials. It includes several subgroups, classified by materials chemical formula and atomic structure: (1) transition metal dichalcogenides (i.e. MoS_2, WSe_2) and their related compounds (2) group IIIA chalcogenides (i.e. GaS, InSe) and (3) Group IVA dichalcogenides (i.e. SnS_2), most of these compounds are semiconductors, semi-metals or metals; (4) insulator hexagonal boron nitride (*h*-BN); (5) black phosphorus; (6) X-enes (i.e. graphene, germanene); (7) MX-enes (transition metal carbides and nitrides); and other compounds, such as few oxides, halides etc. [21–23] Some of these materials are naturally occurring, however some are only synthesised chemically, *h*-BN for example. The focus of the dissertation is on TMDs, however, lead iodide PbI_2 is also investigated, thus, despite PbI_2 being a metal halide, all of the investigated layered materials henceforth are called TMDs due to their structural similarity and for the sake of convenience.

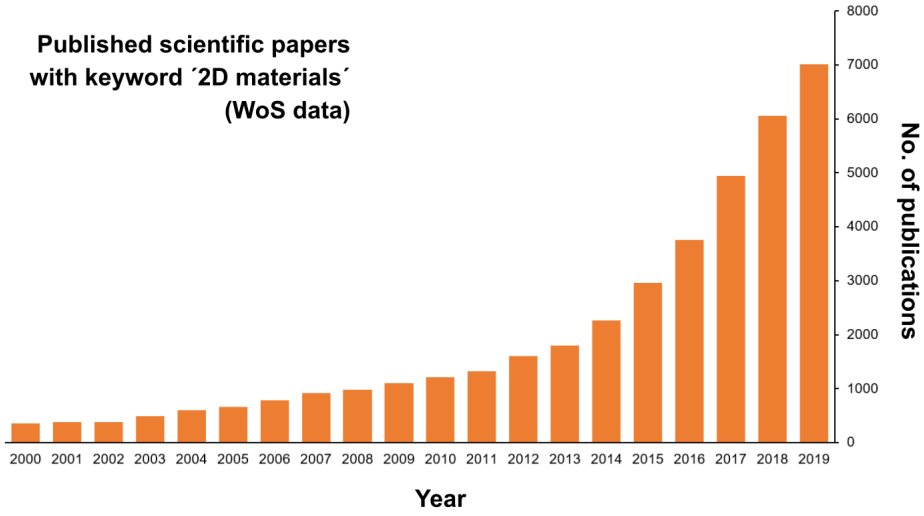

Figure 2.1. Number of published scientific papers since 2000 with keyword "2D materials". Adapted from Web of Science (WoS) publication data.

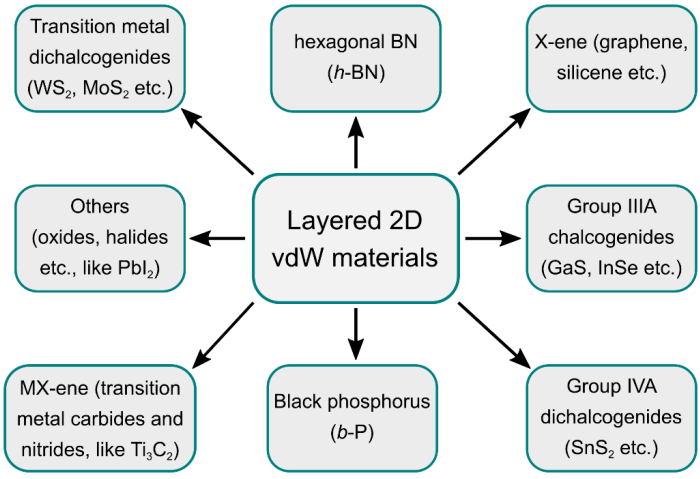

Figure 2.2. Classification of layered 2D vdW materials.

2.2 Physical properties of TMDs

TMDs can be described by a general chemical formula MX_2, where M is a periodic table Group 4 – 7 transition metal and X is a chalcogen (Group 16 elements S, Se and Te) [8]. Depending on the group the transition metal belongs to, the TMDs properties can vary significantly. Typically, a TMD monolayer is made of hexagonally-positioned metal atom layer, "sandwiched" between two layers of chalcogen atoms (see *Fig. 2.3*). In the layer metal

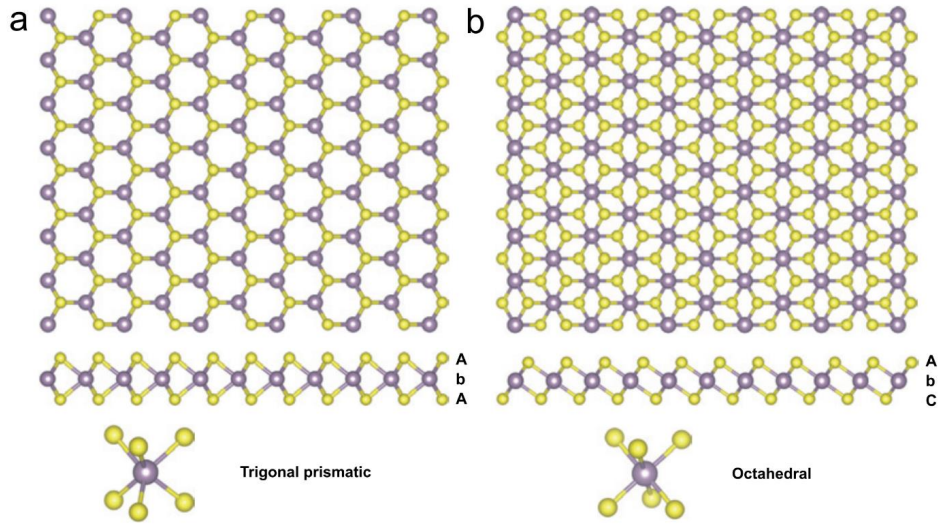

Figure 2.3. A schematic representation of the atomic structure of transition metal dichalcogenides – (a) trigonal prismatic and (b) octahedral. Adapted from [8].

and chalcogen atoms are connected by strong covalent bonds, while the layers are bound together by weak van der Waals forces. The interlayer distance in TMDs is usually around 6 - 7 Å, and the length of the covalent bond varies between 3.15 – 4.03 Å, depending on the size of the metal and the chalcogen atoms [8]. TMDs are chemically quite inert as they have no dangling bonds on the surface due to the fact, that all the electrons in the compound atoms are paired.

Metal atom coordination in TMDs is usually trigonal prismatic or octahedral [8], as shown in *Fig. 2.3*. Bulk TMDs exhibit many different crystalline modifications and polytypes, because individual MX_2 monolayers, which each already consists of three atomic layers (X-M-X) that can be in one of the two coordination, can stack on top of each other in different ways. Common phases are 1T, 2H and 3R, where the letter depicts trigonal, hexagonal or rhombohedral phase respectively, while the number shows how many X-M-X elements are in the primitive cell. Furthermore, 2H phase can have three different polytypes (ways how the layers can stack on top of each other). For example, naturally occurring WS_2 and MoS_2 commonly are in 2H phase, where the stacking sequence is AbA BaB (the letter shows the position of the atom in the layer, the capital letters depict chalcogen atoms, the small – metal atoms), however synthesised materials usually are in 3R phase with the stacking sequence AbA CaC BcB [8]. Another example - TiS_2, a Group 4 transition metal chalcogenide, is usually in 1T phase with a stacking sequence AbC AbC. Monolayers can only be in trigonal prismatic or octahedral phase, which is usually depicted as 1H- or 1T-MX_2. The thermodynamically most stable phase is mostly determined by the number of d-electrons in the transition metal atom. All Group 4 metal chalcogenides are in an octahedral phase, in Group 5 compounds one can find both octahedral and trigonal prismatic phases, Group 6 compounds typically have trigonal prismatic geometry, and Group 7 usually exhibit degenerate octahedral phase [8].

When discussing materials applications in electronics and photonics, knowing their electronic band structure is of great importance as it explains many electrical and optical

properties. The electronic structure of TMDs is dependent on the metal atom coordination and the number of its d-electrons, therefore, they have a broad spectrum of electrical properties [24]. Due to the progressive filling of d bands from Group 4 to Group 7, compounds can exhibit metallic conductivity (orbitals partially filled) or can be semiconductors (orbitals fully occupied). The chalcogen atom affects the electronic structure much less than the metal atom, however a trend can still be observed due to the broadening of the d bands – with an increasing atomic number of the chalcogen the bandgap decreases. For example, the bandgap values of MoS_2, $MoSe_2$ and $MoTe_2$ decreases gradually from 1.3 to 1.0 eV [25]. Interesting differences in the electronic structure of semiconducting TMDs is observed between bulk and monolayer material due to the changes in interlayer coupling, symmetry elements and degree of quantum confinement. For instance, bulk MoS_2 is an indirect-bandgap semiconductor with a bandgap around 1 eV with the valence band maximum at Γ point and the conduction band minimum between Γ-K symmetry lines of the Brillouin zone, however a MoS_2 monolayer has a 1.8 eV wide direct bandgap at the K point (see *Fig. 2.4*) [17,18]. Experimentally, this indirect-to-direct bandgap transition can be observed as an increase of the photoluminescence intensity for monolayer compared to the one of a bulk material, as the direct recombination is a much more effective process. The direct bandgap of many monolayer TMDs is one of the main reasons for the intensive research done on these materials, because the use of direct bandgap semiconductors is a necessity for an effective operation of optoelectronic devices. On the other hand, there are theoretical and experimental studies that shows band structure shift from direct bandgap to indirect bandgap when the PbI_2 thickness is reduced from bulk to monolayer, therefore monolayer PbI_2 is not expected to be an efficient material for optoelectronics applications [26,27]. Another exception – ReS_2 exhibits much weaker interlayer coupling, therefore it remains a direct bandgap semiconductor in both bulk, few-layer and monolayer forms [28].

Obviously, for electronic and photonic applications, good electrical and optical properties of the used materials are needed. Electronic and optoelectronic devices usually require an insulating substrate or an insulating interlayer between specific parts of the device,

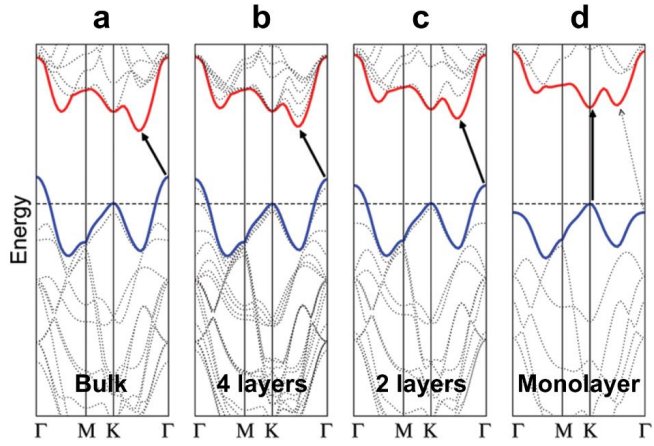

Figure 2.4. Calculated band structures of (a) bulk, (b) 4-layer, (c) bilayer and (d) monolayer MoS_2. The arrows show the lowest energy transitions. Adapted from [18].

good electrical contacts and a semiconductor between them. The variety of available 2D vdW materials allows to fabricate all-2D-material devices, where usually *h*-BN is used as an insulator, graphene as a metal, and TMDs as semiconductors [11]. Most 2D materials have good mechanical properties – their electrical and optical characteristics deteriorate only slightly when bending or applying tensile stress [29]. That allows them to be incorporated in devices on flexible substrates, such as polymers, thus enabling development of wearable, transparent flexible and stretchable electronics in future [30,31].

TMDs are being widely researched for potential applications in electronic and optoelectronic devices as a large portion of the materials are semiconductors with a wide range of bandgaps, starting from visible to infrared. Current limitations of their use in high-performance switching devices is their relatively low carrier mobility of few hundred cm^2/Vs, whereas they have a big advantage over graphene due to the high on/off switching ratio of $\sim 10^5$. TMDs monolayer strong photoluminescence and large optical absorption makes them promising candidates for different optoelectronics applications, like light-emitting diodes, phototransistors etc. on transparent flexible substrates [9].

2.3 Synthesis methods and device fabrication

It is intuitive, that an isolated TMD monolayer cannot be stable in air just by itself – since a single layer is less than 1 nm thick, vdW forces make it bend, roll and wrinkle, making other types of nanostructures [32]. Therefore, TMDs are either synthesised on top of a supporting substrate or dispersed in a stabilizing liquid. The substrates can be different wafers, such as silicon and sapphire, or flexible polymer film, depending on the material and the perspective application.

When the appropriate substrate has been chosen, one must choose the desired approach of synthesis – *top-down* or *bottom-up*. Top-down methods usually involve bulk material crystal that is being reduced in size, for example cleaved, micropatterned, etched etc., to lower its dimension to 2D. Alternatively, bottom-up methods involve combining and stacking material atoms together, and usually these include thermodynamically or kinetically driven processes, such as condensation of vapour. Each approach has its pros and cons, as will be discussed further.

2.3.1 Top-down methods

As mentioned previously, top-down approach usually involves a larger crystal which is being exfoliated. TMDs crystallites have recently become a commercially available material, or they can be grown by so called vapour-transport method [33]. In short, a quartz ampule is loaded with elemental precursor powders, Mo and S in case of MoS_2 growth, for instance, in stoichiometrical proportions, and a small amount of transport agent powder is added, commonly iodine due to its volatility and tendency to make compounds with transition metals. Afterwards, the quartz ampoule is evacuated to obtain vacuum, and sealed. By maintaining a small temperature gradient (typically, the temperatures are above 1000°C), one can achieve the following chemical reactions (process is schematically depicted in *Fig. 2.5*):

$$Me + 2X \rightarrow MeX_2$$

$$MeX_2 + 2I_2 \rightarrow MeI_4 + 2X \text{ (at } T_{high})$$

$$MeI_4 + 2X \rightarrow MeX_2 + 2I_2 \text{ (at } T_{low})$$

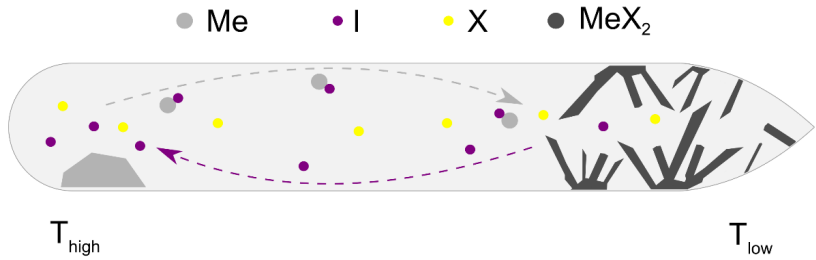

Figure 2.5. A schematic representation of vapour-transport method, used for growing single-crystalline transition metal dichalcogenides. Iodine acts as a transport agent by carrying the precursor atoms from the high-temperature end of the quartz ampule to the cold end where the growth of the crystallites takes place.

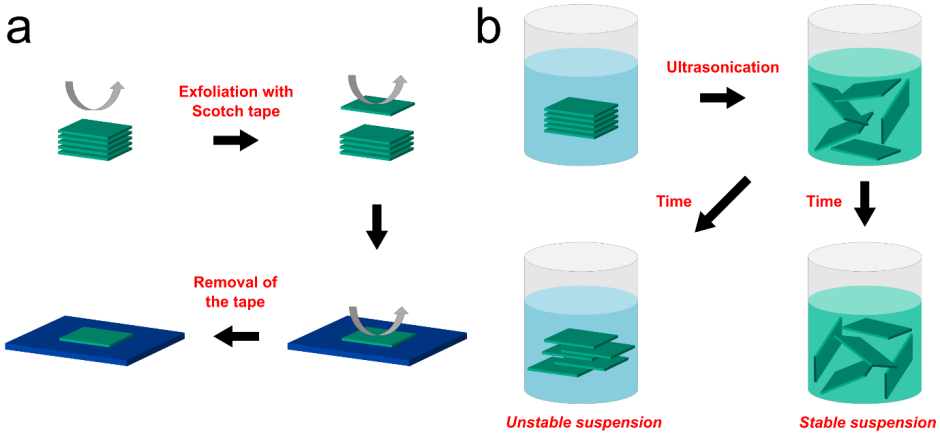

Figure 2.6. A schematic representation of the main top-down methods used to obtain 2D materials flakes: (a) mechanical exfoliation using an adhesive tape, and (b) liquid exfoliation using ultrasound.

The crystallite growth occurs at the cold end of the ampoule. To obtain reasonably large crystallites that can be used for exfoliation of 2D crystals, the process can take up to several days due to the very slow growth rate and the small temperature difference.

When one has obtained the bulk crystalline material, either mechanical or liquid exfoliation can be performed. The simplest version of micromechanical exfoliation, that was used in the early research of 2D crystals, is using a Scotch tape [34]. Basically, it involves three steps (see *Fig. 2.6 (a)*): (1) an adhesive tape is applied on the surface of the available bulk crystal; (2) the tape is peeled of the crystal to obtain thin layers of the material attached to the glue of the tape due to the weak vdW forces between the layers (some more peeling with another tape can be performed on these thin layers to obtain higher quantity of monolayers); (3) the tape with the 2D crystals is pressed against the substrate and removed, followed by washing in acetone or similar solvent. This cleavage method is relatively simple, fast and cost-effective; however, the monolayer yield of this process is very low, therefore can only be utilized for laboratory scale studies and not for large-scale production [24]. As the process does not use any chemicals and is only based on the shear force applied on the crystal during the peeling process,

high crystallinity is maintained, hence, it is suitable for fundamental studies of the material properties. Further characterisation of 2D crystals, obtained by this method, is time consuming, as one needs to locate the monolayers by a manual visual inspection via optical or electron microscopy. There are several approaches proposed to broaden the scale of the production of this method, for example, using large-area customized stamps [35], however significant increase of the monolayer yield has not yet been demonstrated.

On the other hand, for low-cost mass production of 2D atomic crystals, solution processing can be utilized [36–38]. Liquid-phase exfoliation involves dispersion of the bulk material in a suitable solvent and a use of ultrasound or ion intercalation to separate individual layers (note that no chemical reactions occur between the solvent and the bulk materials, the process is only physical). Ultrasonication is the most common type of liquid exfoliation when the bulk material is dispersed in a liquid medium and ultrasonicated for several hours. High energy ultrasonic waves create localised bubbles in the liquid (called "cavitation"), and, when these bubbles collapse, the release of pressure generates high shear forces that overcome the interlayer vdW forces and separate the layers. Another commonly used method is ion intercalation - small molecules of ionic species (like Li+, Na+ and K+) are added to the solvent so they can intercalate between the bulk material layers and effectively increase the interlayer distance, weakening the vdW forces. Afterwards, the layers can be easily separated by mild sonication or stirring. Compared to ultrasonic exfoliation, which uses high energy ultrasonic waves, ion intercalation approach allows to obtain relatively larger flakes of monolayers; however, it usually introduces structural changes, defects and impurities. After the exfoliation process, the resultant suspension can be centrifuged to select crystals of desired thickness and lateral size, as, for instance, monolayers require much higher centrifugation rates to sediment than thicker crystals [39]. This is a great benefit of this method, because the physical properties of 2D materials, such as bandgap width, are strongly layer-dependent; yet, lateral size selection is quite limited as currently the biggest disadvantage of this approach is that only 2D crystals with a maximum size of around micrometre can be obtained. Another very important liquid-phase exfoliation parameter which govern the quality of the resultant suspension, besides exfoliation time and centrifugation rate, is the choice of the solvent [38,40]. One must use a solvent with appropriately chosen surface tension that is similar to the surface energy of the vdW material to reduce the energetic cost of the exfoliation and also prevent re-aggregation of the layers with time - to obtain a stable suspension (see *Fig. 2.6 (b)*). It is of benefit to use a solvent which is easily removable, for example, after a drop of suspension is dispersed on a substrate. Ethanol, water, isopropanol (IPA), and pyrrolidone compounds are some common solvents used. Liquid-processed 2D materials is an important research field nowadays, as the exfoliated materials can be ordered by the size and thickness in uniform suspensions, depending on the applications. A range of printing techniques, inkjet or flexographic for instance, are available to be used in high-volume low-cost production to fabricate devices on either rigid or flexible substrates [41].

2.3.2 Bottom-up methods

In general, many bottom-up methods exist, yet only few are used to obtain TMDs. To name few, one can use pulsed laser deposition, molecular beam epitaxy or chemical synthesis, however these methods are usually either slow, costly, non-scalable or creates low quality material. The most common bottom-up approach for growing TMDs is chemical vapour deposition (CVD), as it can potentially be scaled up for mass production [42,43]. The technique

in the broadest sense is defined as a method of growing solid thin films or coatings by a dissociation and/or chemical reactions of vapour-phase precursors in an activated (usually heat) environment. There is still an ongoing research on growing a high-quality wafer-scale 2D TMDs with CVD technique as the process is complicated and involves many parameters. Mechanically exfoliated TMDs are still used for fundamental research as the quality is much higher than CVD-grown crystals, however CVD is one of the most promising approaches for production and future applications [9].

Several different CVD approaches for growth of TMDs mono- and few-layer 2D crystals can be distinguished. Most commonly used method is a vapour phase reaction between transition metal oxide and chalcogen precursors. Typically, the corresponding metal oxide powder is being evaporated simultaneously with a chalcogen powder in a high-temperature reactor (simple quartz tube reactor is often used), followed by a vapour-phase reaction to form the corresponding TMDs, which diffuse to the substrate to produce layered 2D crystals. An example of such setup is schematically represented in *Fig. 2.7* for growth of transition metal sulphides on SiO_2/Si substrate. This way, one can obtain 2D TMDs with relatively large grain size (up to several tens of micrometres) and high crystalline quality [44,45]. However, some transition metal oxides have high melting points (titanium and niobium oxides, for instance), therefore it is difficult to effectively evaporate them. For such materials, transition metal chlorides or oxychlorides can be used instead, as they usually have much lower melting temperatures. Another approach is to directly evaporate TMD powder in a hot zone of the furnace, transport the vapour with a carrier gas to the substrate in the cold zone, where nucleation and crystal growth takes place. The thickness and grain size of the 2D crystals can be controlled by adjusting the growth temperature and time. With the both mentioned approaches it is possible to grow single-crystalline domains of various TMD materials, however, the use of solid precursors makes it difficult to precisely adjust the vapour pressure and supersaturation, thus limiting uniform growth over a large area [42,43]. Growth of 2D TMDs over the entire wafer area with a good spatial homogeneity has been demonstrated using metal-organic precursors via the MOCVD technique [46], therefore making it a prospective method for future large-scale production.

Another methodology how to obtain 2D TMD crystals is to convert previously deposited precursor thin films. One commonly used approach involves transformation of a transition metal or transition metal oxide film in chalcogenide vapour at elevated temperatures, where the starting material film has been deposited on the substrate by physical vapour

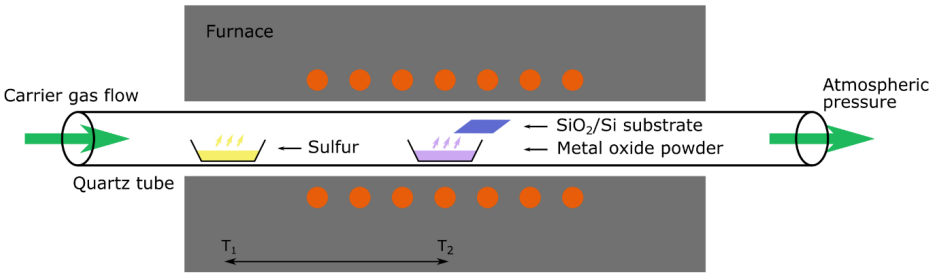

Figure 2.7. A schematic representation of a typical quartz tube reactor used for growth of 2D transition metal sulfides from vapour phase.

deposition (magnetron sputtering etc.) [19,47–49]. The benefit of this method is that the wafer-scale TMD thin films can be readily obtained, however, it usually produces polycrystalline films with small grain size due to the amorphous nature of the precursor films. Moreover, thermal decomposition of thiosalts can be used to obtain 2D crystals. For example, to obtain 2D MoS_2 on a substrate, the substrate is first dip-coated in a $(NH_4)_2MoS_4$ solution, followed by a decomposition at a high temperature, which involves N and H atom disassociation from the substrate and MoS_2 layer growth [50].

2.3.3 Preparation of heterostructures and vdW epitaxy

Fabrication of scalable high quality 2D material heterostructures is required for most potential future applications. Currently, there are two general approaches used for layered vdW material heterostructure preparation: transfer via viscoelastic polymer stamps and direct sequential growth [51]. The latter method is rather recently developed and is still very limited, thus the former is the main technique of stacking different 2D material flakes for fundamental studies and proof-of-concept demonstrations. The flake transfer with stamps is based on the mechanical exfoliation method described previously, however, some extra steps are added and different materials are used to make heterostructures [52]. Firstly, a flake of the first material is obtained on the desired substrate by a typical mechanical exfoliation from a larger single crystal and identified with an optical microscope. A transparent polymer stamp (usually PDMS or PMMA) with the flake of the second material is aligned in the XY plane on top of the first flake in an optical microscope and XYZ micrometre sample stage setup, and then mechanically pressed (Z direction) against the substrate. Dry stamping is usually used as the stamp is just slowly peeled off from the substrate afterwards, instead of using organic solvents to dissolve or loosen the stamp which typically leaves some organic residues. After this procedure, a mono- or few-layer flake of the second material should have been left on top of the first one due to the cleavage and bonding of vdW layers. One can repeat the process to obtain several different flakes on top of each other to fabricate the desired heterostructure depending on the application, for example graphene/MoS_2/graphene or graphene/MoS_2/WSe_2/graphene heterostructures [53]. It is common to encapsulate the heterostructures in *h*-BN by placing a large *h*-BN flake on top of the whole heterostructure since it has been proved to protect it from degradation. This deterministic flake transfer via viscoelastic polymer stamps is a very slow method with a very limited reproducibility and control of as-deposited flake thickness, however, it is still widely used because it makes the highest quality interfaces between high quality 2D materials flakes.

Direct bottom-up sequential growth of 2D materials on top of each other is currently being investigated as the main heterostructure fabrication method in future due to its scalability [43]. In conventional semiconductor industry epitaxial growth enables fabrication of most of nanoelectronic and optoelectronic devices, however, a lattice mismatch which results in strain and defects strictly limits the possible material combinations in the heterostructures (lattice mismatch can only be up to few percent). The term “epitaxial growth” means a commensurate growth – the top crystalline layer arranges itself to the underlaying one directionally and without strain. As schematically depicted in *Fig. 2.8*, vdW materials, which have terminated surfaces without dangling bonds, therefore, grow without covalent interlayer bonding, may be sequentially grown on top of each other unstrained by “van der Waals epitaxy” due to this weak interlayer vdW interaction, even if materials are lattice-mismatched [10,54,55]. This vdW epitaxy has even been demonstrated for a lattice mismatch up to 23%. Moiré patterns can be observed on such epitaxial vdW heterostructures and their periodicity can be used to study

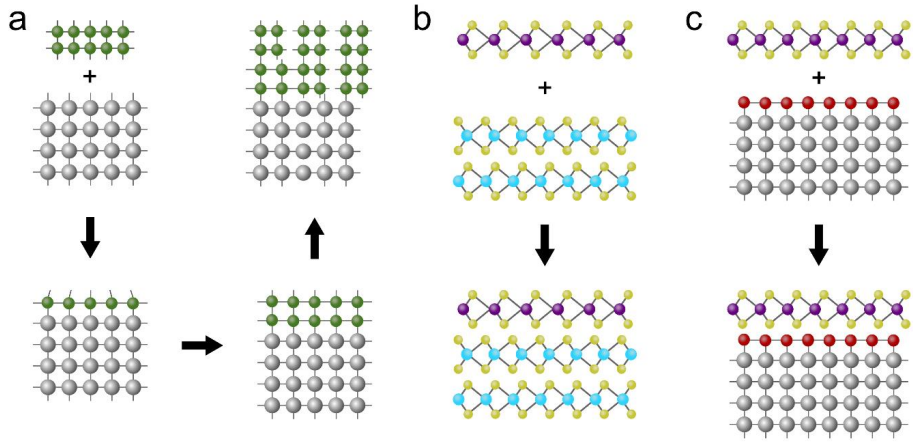

Figure 2.8. A schematic representation of epitaxial growth of different type of crystals: (a) conventional epitaxy of semiconductor crystals usually leads to strain and dislocations at the interface if the lattice mismatch is too large; (b, c) vdW epitaxy allows unstrained growth of layered materials on top of different substrates with relatively large lattice mismatch due to the weak interlayer bonding.

rotational alignment of the layers [56]. The most studied vdW epitaxial growth approach is CVD, which can be performed in two ways – either on top of mechanically exfoliated flake, or by sequential two-step growth. The former is easier to realize however the heterostructure size is limited by the size of the flake. The latter is performed by sequentially switching the chemical precursors during the synthesis, enabling the growth of the second material on top of the first one which acts as a seed layer [43,57]. Furthermore, some material precursors can be evaporated simultaneously to promote heterostructure growth if the materials have sufficiently different nucleation and growth rates [58]. Also, in principle, by repeating sequential growth one can realize a superlattice, however, it is very challenging, maybe even impossible, as the process would require switching temperatures that would lead to some less-temperature-tolerant material thermally-induced degradation [43]. This must also be considered when growing multicomponent heterostructures. The field of vdW epitaxial growth is still fresh, and a lot of research must be performed to overcome difficulties related to the small lateral size of heterostructure grains, reproducibility, limited yield, as well as more combinations of materials must be studied.

2.3.4 Electric contacts in 2D TMD-based devices

A critical and non-trivial step in the fabrication of semiconductor devices is preparing low-resistance electrical contacts to a semiconductor material. Low-resistance contacts are necessary to allow efficient charge flow in both directions, without any blocking due to a Schottky barrier. Such contacts are usually called ohmic contacts since they exhibit linear current-voltage curve following Ohm's law. Both ohmic and Schottky contacts depend on the Schottky barrier height, which sets the threshold for the excess energy that electrons need in order to pass from the semiconductor to the metal. The barrier height should be small in most of the junction surface to achieve low-resistance contact. The height of the barrier can be roughly estimated as the difference between the semiconductor-vacuum electron affinity and

the metal-vacuum work function, however, in practice this assumption works only loosely. Generally, metals with low work function tend to form good contacts to n-type semiconductors and metals with high work function to p-type semiconductors. Practically, there are metal-induced interface states in the bandgap of the semiconductor that are occupied by electrons, and that pin the Fermi level to the centre of the bandgap, called Fermi level pinning.

Currently there is a challenge to reduce high contact resistances in devices based on 2D semiconductor TMDs [11]. The interface states at the metal/TMD contacts pin the Fermi levels, and that leads to considerable Schottky barriers. The barriers are particularly high for the p-type semiconductors, although there are methods how to overcome this issue to obtain low-resistance contacts with 2D TMDs. One can eliminate the interface states by introducing 2D material layer between the metal and the TMD or choose a buffer layer that forms a contact with zero Schottky barrier height [59]. The simplest solution is to take a metallic 2D material monolayer with a high work function, such as NbS_2 or TaS_2, for p-type contact, or lower work function material like graphene for n-type contact, and use it as the contact layer, since it forms a barrierless contact irrespective to the metal work function. Otherwise, one can use a buffer, such as monolayer *h*-BN or a very thin oxide layer with high (for p-type contacts) electron affinity, which suppresses the interface states and is thin enough to allow efficient electron injection through the junction. A benefit of using these additional 2D material layers to form barrierless contacts with metals is that they do not need to be lattice matched due to the vdW bonding [60], although the extra fabrication steps slightly complicates the process. That, however, is a minor issue compared to the ability to obtain high quality low-resistance contacts.

The conventional method to fabricate metal contacts for the proof-of-concept devices based on 2D TMDs is electron-beam lithography (EBL). The contact deposition process consists of several steps. Firstly, the sample substrate is spin-coated with an e-beam sensitive resist. Secondly, the TMD flake or stack of layers (heterostructure) is located on the substrate, and the electrode patterns are drawn in the interface of the e-beam tool. The patterns are irradiated to locally change the resist properties. Thirdly, the sample is developed to remove the irradiated resist (in case of a positive resist), leaving the underlaying substrate exposed in the patterned regions. Finally, the desired thickness of the metal film is deposited on top of the sample via thermal evaporation, followed by the lift-off procedure to remove the resist with the metal coating, leaving the desired metal electrode pattern on the substrate. Typically, gold or platinum electrodes are used with TMDs, although other metals have been used [59,60].

2.4 Perspective applications

2D TMDs are regarded as very attractive for wide range of applications including electronics, optoelectronics and photonics, energy, sensing and piezoelectric devices [9]. The mentioned applications are motivated by the unique properties of 2D TMDs, such as tunable electronic structure, optical transparency, mechanical strength, and sensor sensitivity, some of which mainly arise due to the high surface contribution in monolayer. A particularly interesting and promising application is the use of 2D materials in flexible electronics, which is considered as potentially ubiquitous in future devices in every-day life. Flexible technology merges a variety of scalable devices, such as transistors, displays, solar cells, sensors and energy storage on flexible substrates for either large-area applications or compact wearable electronics [30,41].

Currently there still are numerous challenges and issues to be overcome before 2D materials can be used in any practical application, as 2D materials have only been studied for a decade or so. Firstly, it is controlled large-scale growth of 2D heterostructures. Large-scale growth of monolayer TMDs and graphene with satisfactory properties has been demonstrated [42,43], however, direct growth of heterostructures (several layers of different 2D materials on top of each other) has not mainly due to the initial choice of the substrate, materials relative thermal stability and complexity of precise control of temperature and gas partial pressures [11]. Currently, either very small scale heterostructures have been grown via CVD or made by dry-transfer technique [51,61]. Secondly, the control of the carrier type and concentration in 2D TMDs which is crucial for industrial semiconductor applications have not yet been fully studied [62]. Material doping or alloying have been investigated as potential methods of modifying electronic properties of the materials [63,64]. Thirdly, ensuring ohmic contacts in semiconductor devices is required for any real application [59,60]. In conventional semiconductors, ion implantation at the metal contact area allows to generate a gradual ion density distribution to reduce the contact resistance, however, the concept is ambiguous and not applicable in 2D materials, therefore, several other methods are being investigated, such as layer phase engineering and use of graphene as an electrode material. The challenges mentioned above are only the few main ones, as many other more specific ones exist in more specialized application fields.

There are some more exotic phenomena observed in 2D materials worth noting, that might be of practical use in future. Spintronics, in contrast to electronics where the signal is transported by a carrier charge, uses the carrier spin information to transport the signal. Materials which have a strong spin-splitting due to some kind of symmetry breaking or non-equilibrium state allow spin-polarized carrier population. Graphene shows very long spin lifetime at room temperature thus could be used as a spin transport layer [65,66]. Effective spin injection from TMDs to graphene has been demonstrated, therefore such graphene/TMD heterostructures could be used in future spintronics devices. On the other hand, TMDs exhibit different spin characteristics at K and K` points in the electronic band structure due to strong spin-orbit coupling which leads to a possibility to control electrons and their spins at different positions in momentum space [65]. The carriers in these valleys can be spin-selectively controlled by circularly polarized light. Use of these phenomena for a potential information storage and manipulation in future devices has been termed as “valleytronics”, and use of 2D materials in both of these new fields are currently being extensively investigated.

2.4.1 Electronic and optoelectronic devices

One of the main and most elementary components in electronics are field-effect transistors (FET). The conventional silicon-based semiconductor FETs are close to the miniaturization limit, therefore, there is an on-going research to find competitive alternatives. Sub-10 nm channel lengths lead to undesirable effects, such as current tunnelling, surface scattering, velocity saturation etc. Use of atomically thin layers of 2D semiconductors might resolve many of the issues seen in traditional devices, provided that fabrication and integration challenges can be overcome [67]. Moreover, 2D materials could potentially be used in flexible electronics as thin-film transistors (TFT) [31]. Due to graphene’s zero bandgap, its application as a semiconductor in switching devices is very limited, however, in recent studies it is mainly used as a transparent electrode because of its excellent electronic properties [68]. Other metallic TMDs, such as NbS_2, are also being investigated for transparent conductor material applications

[49]. As for 2D FETs, most of the current research is focused on semiconductor TMDs, such as MoS_2, WSe_2. TFTs based on TMDs feature high on/off current ratio, high current saturation and decent carrier mobility, robust electronic performance after mechanical bending, as well as several GHz cut-off frequencies have been observed on plastic substrates [9,24,62,67].

The most basic optoelectronic component is a light detector (photodetector), used in imaging, communications, positioning and guidance. Good photodetector characteristics are a small device size, fast response time and high sensitivity over a wide wavelength range [69,70]. The good physical properties of semiconductor 2D materials makes them perspective candidates for such optoelectronics applications. Basically, there are two main photon-matter interaction principles in devices: photoconduction and the photovoltaic effect. When photo-excited carriers contribute to the current (increase conductivity) it is called photoconductivity, however, when photo-excited carriers are transformed into current due to the built-in electric field, it is called the photovoltaic effect. Photoresistors and phototransistors made from monolayer TMDs, including MoS_2 and WSe_2, exhibit excellent properties such as high responsivity and high quantum efficiency [69,70]. Furthermore, the size-dependent bandgap and the large variety of different TMD materials allows one to control the response spectrum. Photodetection properties of the most common TMDs materials have been studied quite extensively, however, the applications require further in-depth research, and investigation of other less-known compounds.

An important potential optoelectronic application of TMDs is in thin-film solar cells. Monolayer TMDs direct bandgaps in the visible range and the relatively high abundance of their elements on Earth makes them appealing as the light-absorbing layers in photovoltaic devices, including flexible solar cells for using on buildings and curved structures [71]. Most of TMDs have work functions and valence and conduction band edges that are compatible with currently used electrode materials work functions [59]. By combining different TMDs with different work functions together in heterostructures, one can accumulate photoexcited charge carriers in separate layers. Atomically sharp p-n junctions can be made if p- and n-type TMDs are used in such heterostructures (n-type MoS_2 with p-type WSe_2, for instance), hence achieving very efficient charge separation and high quantum efficiency [53]. Furthermore, by sandwiching such TMDs heterostructure between graphene electrodes, one can form good ohmic contacts that is necessary for efficient extraction of photocarriers, however, a potential difference needs to be provided (either by different doping of the two graphene layers or applying external gate or bias voltage) to achieve carrier separation since these structures are usually symmetric [60]. The p-n junctions based on TMDs can also be operated in a regime of electrical injection of charge carriers, photons being emitted when electrons and hole recombine (electroluminescence) – the principle used in LEDs and diode lasers [72,73]. Electroluminescence in TMDs heterostructures has been demonstrated, however, there are still many challenges to be overcome to efficiently use these materials for light emission, such as difficulty to control the current distribution due to the comparable resistance of the junction and the p- and n-type electrodes, and the difficulty to control the dwell time of the injected carriers in the semiconductor layer as the photoemission process is much slower than the characteristic time of the carrier transport through the junction [74]. The latter can be controlled by adding additional tunnel barriers, such as few layers of h-BN, to increase the dwell time of electrons and holes in the TMD layer and to allow them radiatively recombine [74]. In principle, semiconductor diode lasers can be prepared similarly by additionally adding the resonator

layers, however, there must be more research done beforehand in the direction of achieving efficient electroluminescence in 2D heterostructures.

2.4.2 Sensors and other applications

Nowadays sensors can be perceived as devices that are used to interact between computers and the world around them, or just used to indicate or measure some physical or chemical parameters. Most commonly an information about chemical, mechanical or light changes in the surroundings is converted to an electrical signal, which can be analysed afterwards. There is a huge demand for cost-effective, low power consuming, reliable, portable and selective high sensitivity sensors, and it has stimulated the recent extensive research on 2D materials for sensing applications [9]. Graphene and 2D TMDs have been demonstrated to be potentially excellent gas [75,76], chemical and biomolecule [77,78] sensors that perform with high sensitivity and low noise, mainly due to their high surface-to-volume ratio. When exposed to gases, vapours or large molecules, there can be changes in the charge transfer (resistivity), doping, shifts in vibrational properties or in permittivity due to the adsorbed molecules. The high surface-to-volume ratio of 2D materials enables detection of a large amount of target analysts per unit area, a rapid response and recovery, and low power consumption. Graphene, MoS_2 and some other materials have been shown to exhibit good sensing properties of NO, NO_2, NH_3 and other gases [75], as well as several types of biomolecules, such as DNA, glucose, dopamine [77]. The biocompatibility of many 2D materials makes them very suitable for biosensing and other bio-applications, which is still growing and is becoming a very important field of materials science.

To convert mechanical stress into an electrical signal, or vice versa, piezoelectric materials are used. Piezoelectricity can be obtained by accumulating polarization charge in non-centrosymmetric non-metallic materials via mechanical stress, and it has been widely applied in sensors, actuators, microelectromechanical systems (MEMS) etc. Remarkably, several materials, which are not piezoelectric in a bulk form, obtain noncentrosymmetry when reduced to a monolayer, which is the case of many vdW materials, including graphene, h-BN and many TMDs [79]. The emergence of 2D piezoelectricity is usually attributed to the crystal structure, however, surface piezoelectricity can also be induced in 2D materials by introducing adatoms and defects, which is particularly interesting for engineering the piezoelectric properties [80]. For instance, graphene monolayer is intrinsically centrosymmetric, yet piezoelectricity can be induced by adatom adsorption or by incorporating non-centrosymmetric in-plane defects. Together with the superior mechanical (flexibility and strength), optical, chemical and other properties of 2D materials, their principal compatibility with the conventional integrated circuits and MEMS and the possible piezoelectricity engineering could lead to new advanced electromechanical devices in future [81].

Another important group of potential applications of 2D vdW materials is energy. Graphene and TMDs are being intensively investigated as electrode materials for energy storage, including Li-ion batteries and supercapacitors [9]. They exhibit good electrochemical properties and conductivity, there are more sites provided for ions to accommodate due to their layered structure and large surface area, as well as structure stability is maintained during charge and discharge cycles, making them excellent candidates for energy storage. Furthermore, 2D TMDs are being investigated as perspective materials for electro- and photocatalytic hydrogen evolution [82].

3. NANOWIRES

3.1 Introduction

One-dimensional (1D) nanostructures, such as nanowires, nanorods, nanobelts and nanotubes, have been extensively studied for more than two decades due to their unique physical properties. Nanowires (NWs) are usually defined as materials with thickness or diameter below 100 nm while their length exceeds 1 μm. During the early stage of NWs research, the work was mainly focused on the development of synthesis processes to confine the growth of the nanostructure in one direction, and on deeper understanding of NWs fundamental properties. Although the theoretical model for whiskers growth with vapour-liquid-solid (VLS) mechanism was already known since 1960s [83], growth of semiconductor nanowhiskers was experimentally demonstrated only in the early 1990s by several groups [84,85], and that facilitated NWs research to become one of the most active areas in the nanoscale field. That was mainly promoted by the interesting and novel physical properties that 1D semiconductors exhibit. Later, the ability to grow high quality and crystallinity NWs with controllable size, phase and composition enabled demonstration of proof-of-concept devices in electronics, photonics, optoelectronics, photovoltaics, sensors and other fields. Currently, the intensity of NWs research has peaked, as can be seen from Web of Science (WoS) publication data shown in *Fig. 3.1*. Some of the main directions nowadays are investigations of hybrid NWs and heterostructures [5], development and study of complex photonic and/or plasmonic NW-based integrated circuits [86], metallic NW-based flexible and transparent electrode fabrication [87], and, of course, large-scale assembly of NW devices that could enable mass production [88]. An important emerging phenomenon in NWs research is the need for full understanding not only of the behaviour of each individual component in hybrid materials systems but also

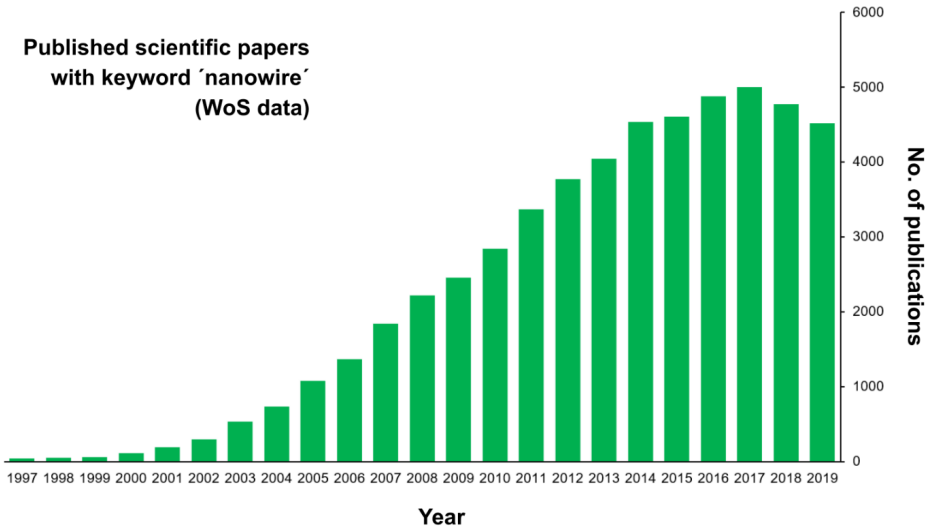

Figure 3.1. Number of published scientific papers since 1997 with keyword “nanowire”. Adapted from Web of Science (WoS) publication data.

the interfaces and interaction between them which determines the performance and properties of the device [2].

3.2 Materials, properties and applications

3.2.1 Nanowire materials and properties

Generally, functional NWs can be classified into two large groups – metallic and semiconducting, and that determines the perspective applications where such NWs can be applied. Most commonly studied metallic NWs are Ag, Cu and Au NWs, which are synthesised via polyol process or hydrothermally [87]. As for semiconductor NWs, many classes exist: the most well studied elemental semiconductors Si and Ge, III-V compounds (GaN, GaAs, InP etc.), II-VI compounds (CdS, In_2S_3, ZnSe etc.), oxides (ZnO, MgO, SnO_2, ITO etc.) and carbides (SiC) [89]. In this work, different compound semiconductor NWs were studied, therefore, the focus will be on these materials in this section.

It is important to discuss the unique properties of NWs besides the possible miniaturization, that make them so attractive to study and to compete with the well-developed silicon and thin film technologies. Firstly, their one-dimensionality allows to overcome some technical problems that optically active thin films face in regard to integration with silicon. To merge photonics and electronics on one platform, one must eliminate interfacial lattice mismatch that leads to defective and inefficient optical materials. Relaxed interfaces can be achieved by growing III-V semiconductors NWs on lattice mismatched substrates, thus enabling next generation computation devices [4]. Secondly, size reduction of well-known materials to nanoscale can alter and improve their physical characteristics and device performance, as well as introduce completely novel properties. Some of the size-dependent properties are photon absorption and emission, charge carrier transport and elastic modulus. There are diverse behaviours of mechanical properties reported in literature for NWs of various diameters due to different investigative measurement techniques, however, typical mechanical properties of NWs tend to be good enough for potential applications in flexible electronics and for printing of NWs [3,87]. Regarding the electronic transport in NWs, single-crystalline structure can be obtained over a length of several micrometres thus eliminating charge carrier scattering on grain boundaries and that promotes good electrical properties, however, if the diameter of a NW is reduced to a value close to electron mean free path, scattering on the surface can become significant. Furthermore, as NWs have large surface-to-volume ratio, both surface and bulk lattice may contribute to the macroscopic properties of a NW. Therefore, NWs might replace bulk materials in an application where surface-dominated property, for instance, surface charge carrier processes in chemical or biological sensing, determines the efficiency or sensitivity of the device. It has been reported in literature that physical characteristics and device performance are particularly sensitive to surface properties in ZnO NWs, as the surface states in ZnO NWs may be affected by atoms and ions from the surrounding atmosphere [90,91].

3.2.2 Perspective applications of nanowires

NWs have been extensively explored as potential building blocks for many different applications as their superior performance in devices has been demonstrated in comparison to conventional materials. However, most NW-based device demonstrations are limited to single-

NW devices, mainly due to the major bottleneck for NWs materials integration in large-scale electronic circuits. There has been a remarkable progress in controlled and uniform assembly of NWs via various contact and roll-to-roll printing, microfluidics and template-guided synthesis methods [88], although large scale and low cost process must still be developed.

NW-based field-effect transistors (FETs) are one of the key elements for many potential applications [92]. Their precisely controllable composition and electrical properties with bottom-up synthesis methods together with a small channel size leads to device performance that exceeds that of transistors prepared with top-down methods [93]. Consequently, there has been large amount of studies that report fabrication and characterization of NW-based FETs. Different semiconductor materials have been studied, including silicon [2], germanium [94], sulfides [95], oxides [96–98] and III-V semiconductors [2]; various FET geometries have been explored, such as back-gate, top-gate and wrap-around gate transistors, as well as different axial and radial heterostructures [2,93,99]. Tremendous efforts have been put into NW FET research – while some fields require more advanced assembly techniques to move from science to technology, other non-CMOS applications, for instance, flexible electronics, are much closer to real-world devices.

Optoelectronics is one of the most promising areas where semiconductor NWs might be potentially applied. Firstly, NWs could be used in inexpensive and efficient photovoltaics [100,101]. The potential of using NWs in solar cells is mainly due to geometrical effects rather than new physical properties, as they exhibit much larger surface-to-volume than thin film devices. That leads to improved light absorption and charge carrier separation, as well as NWs could be integrated on low cost flexible solar cells. Secondly, it has been widely reported that NWs photodetectors exhibit high photosensitivity and photoconductive gain [90,102,103]. Due to the large surface-to-volume ratio of NWs, they contain very high density of surface states that leads to Fermi pinning near the surface, thus forming a depletion space charge layer that separates electrons and holes and, consequently, enhances photocarrier lifetime. As high mobility can be easily achieved in single-crystalline defect-free NWs grown by VLS, that, in combination with long carrier lifetimes, leads to large photoconductive gain, therefore, making NW photodetectors very promising in different optical applications [104]. Thirdly, NW-based light-emitting diodes (LEDs) mimic the structure of commercially available LEDs in nanoscale by forming the necessary p-n junction either by a contact of two p- and n-type NWs or in a heterostructured (radial or axial) NW. Operation of NW-based LEDs have been demonstrated in different semiconductor materials, with electroluminescence emission peak wavelength ranging from UV to near infrared [105], thus making NWs attractive as versatile nanoscale light sources. Finally, semiconductor NWs due to their geometric features, high optical gain and potential low power consumption are very perspective as nanoscale lasers [106]. A single semiconductor NW with atomically smooth surface facets can be an optical cavity, a waveguide and an active medium necessary for laser operation. The small volume of NW materials leads to low lasing threshold compared to macroscopic lasers, thus such coherent light sources with a small footprint could be used in advanced integrated photonic circuits [105]. Laser operation has been shown in several different NW materials and heterostructures [2,105,107].

Demonstration of emerging NW-based optoelectronic devices promotes development of advanced integrated nanoscale photonics systems. To interconnect nanoscale optoelectronic devices, such as LEDs, lasers, photodetectors, frequency converters, filters and switches, flexible NW waveguides have been used [2,105,107]. The main requirements for low-loss NW waveguides are atomically smooth surfaces and large refractive index, and that can be satisfied

by many bottom-up grown NW materials, as well as by fabricating advanced *core-shell* NW heterostructures. It must be noted, that the miniaturization of integrated photonic devices is still limited by the light diffraction, and use of semiconductor NWs can only reduce the scale of the devices to half of the operation wavelength. By using plasmonic effects, the restriction can be reduced significantly. It has been shown that plasmonic and photonic waveguide modes can be coupled between metal and semiconductor NWs, thus paving way to hybrid deep-subwavelength circuits [86,108]. Generally, while there have been quite a few reports on different single-nanowire photonic device demonstrations, scalable assembly of NWs with high spatial and angular precision still remains the major challenge for chip-integrated nanophotonic circuit fabrication [105].

Due to their large surface-to-volume ratio, NWs can be very sensitive gas, chemical and biological molecule sensors [109]. Extremely low concentrations of adsorbed molecules can be measured by measuring changes in electrical signal of a single NW channel, which might occur because of different chemisorption mechanisms on the surface. There are many reports in literature about sensing of O_2, CO, NO_2, NH_3 and other gases with different materials NWs, as well as of biological molecules, such as DNA, viruses, cancer markers and antigens, by appropriate NW surface modifications [2,107]. NWs radii can be as small as electron exchange distance between surface and bulk, therefore, it allows high-sensitivity, high-selectivity and fast sensing compared to conventional sensors.

Other important area of NW applications is energy storage and conversion. NWs have been widely explored as potential electrode materials for batteries to increase their capacity [110]. Small diameter NWs, such as silicon, tend to be thermal insulators, contrary to the bulk material which is good thermal conductor, and together with their good electrical conductivity that makes them excellent thermoelectric generators [111]. Piezoelectric NWs, such as ZnO, have been demonstrated as efficient nanogenerators – to produce electric power from mechanical energy [112]. Furthermore, NWs are being extensively investigated as perspective materials in nanoelectromechanical systems (NEMS) applications due to their elastic properties and ability to achieve very high resonant frequencies, that could be used for very small mass sensors, as an example [2]. The mentioned applications of semiconductor NWs all are large research areas, and there are many others not mentioned here, which shows the great potential of such 1D nanostructured materials.

3.3 Nanowire synthesis via *vapour-liquid-solid* mechanism

In the beginning of NW research, many different NW synthesis methods were explored and developed, as precise control over materials properties, such as morphology, structure, stoichiometry, during the growth stage is necessary to fabricate devices with desired characteristics. Therefore, all the available methods have been extensively discussed in literature [2,107,113]. Generally, NW synthesis methods are grouped in “top-down” and “bottom-up” approaches. Top-down methods typically involve chemical or ion beam etching of a bulk material which has been patterned lithographically. Such process involves several complicated steps including material growth, photoresist deposition/removal, etching, and it becomes gradually more complex for high density NW arrays with small feature sizes, however, the method benefits from precise control over the placement of NWs on a substrate which is necessary for device fabrication at large scale. While bottom-up methods usually lack such

control over NW position on a substrate, the approach is much more widely used because it is more versatile, facile and potentially cheaper with great control over NW properties, even if *in-situ* or post-growth alignment methods need to be implemented. Bottom-up approach can be divided in solution-phase and gas-phase methods. Chemical solution-phase methods, such as solution-liquid-solid (SLS), supercritical fluid-liquid-solid (SFLS) and supercritical fluid-solid-solid (SFSS) variations, have been widely applied to grow colloidal NWs, and benefit from large-scale production, control of NW geometry and surface passivation. Gas-phase methods, such as vapour-liquid-solid (VLS), vapour-solid-solid (VSS) and vapour-solid (VS) variations, are the most adopted methods for growing semiconductor NWs due to their flexibility and high-quality of the as-grown NWs. Gas-phase methods can be further grouped in catalyst-free and metal-nanoparticle-mediated approaches. In this work, VLS method with a metal nanoparticle (NP) catalyst was used to grow NWs thus it will be discussed further in detail. Furthermore, bottom-up methods can be used together with templates to grow aligned NW arrays, for example, by filling pores of anodic aluminium oxide or polycarbonate membranes, by self-assembly, or by lithographically pre-defining the positions of the metal catalyst used in VLS growth. Otherwise, various post-synthesis microfluidic alignment or contact printing methods can be used to assemble NWs desirably [88].

VLS mechanism of micrometre-sized single-crystalline whiskers was first explained by Wagner et al. [83] in 1960s. The simplified general principle of the method is schematically depicted in *Fig. 3.2*, however, usually the growth involves more steps when several other complex processes may occur which usually depends on the materials used. Generally, the VLS growth of NWs typically consists of three steps: alloying, nucleation and growth. Firstly, the vapour-phase precursors are adsorbed and incorporated into the metal catalyst nanodroplet at elevated temperatures, and an alloy is formed. Depending on the materials used, the chemical reactions between the precursors to obtain NW material may occur either in gas-phase or on the surface of the metal droplet. Secondly, if the alloying process is complete and the precursor supply is maintained, nucleation takes places due to supersaturation, which leads to precipitation of the NW material seed at the liquid-solid interface. Finally, if continuous and uniform vapour flow is supplied, the NW grows in an atomic layer-by-layer fashion in one axial direction, limited by the droplet size, and the growth front is at the liquid-solid interface. Time and precursor vapour flow (partial pressure) typically determines the growth rate of the NWs, while temperature is set to be above eutectic temperature of the corresponding alloy. The growth temperature may determine the crystal phase of the material, and the phase of the NW can also be imposed by the substrate material if an epitaxial relationship exists.

Regarding the metal NP, it may not always be a catalyst which lowers the activation energy of the chemical reaction of precursors, although quite often it is called ‘catalyst’ in

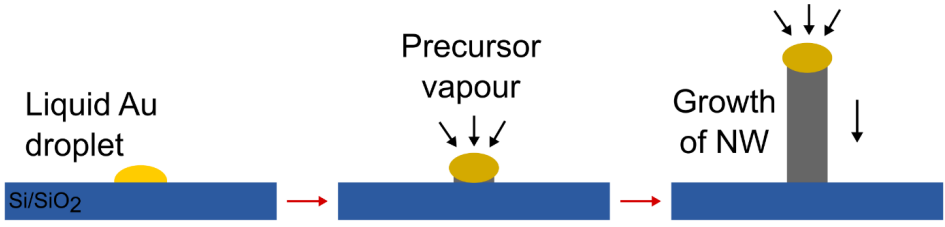

Figure 3.2. A schematic representation of *vapour-liquid-solid* growth mechanism.

literature. The choice of the metal material is quite limited due to several requirements that must be satisfied: catalyst cannot chemically react with the precursors; at the given temperature it must be in liquid phase and make an alloy with the desired material; it cannot be soluble in the substrate material; it must have small vapour pressure so it does not vaporize during the growth. Most commonly Au is used, while NW growth from Pt, Ni and other NPs can also be performed in several cases [2]. Au NPs are usually formed on the substrate via two different approaches: either by drop-casting pre-made NPs from a solution, or by depositing thin Au film on the substrate and annealing it above 300ºC to form Au islands. Furthermore, while general VLS model consider catalyst material to be stable, some studies show that there might be minor catalyst loss during VLS growth, as Au monolayer have been found on Si NWs and the substrate surface [114].

3.4 *Core-shell* heterostructures

To date, many fundamental properties of pure NWs are well understood. On the other hand, the combination of different materials in more complex hybrid NWs gives extra freedom to flexibly design their properties and add custom-made functionality [5]. Some possible 1D heterostructures are schematically depicted in *Fig. 3.3*, from which axial and radial heterostructures are being more commonly studied. Axial or segmented NW heterostructures with superlattices (see *Fig. 3.3(a)*) have been mostly synthesised by periodically switching gas-phase precursors during VLS growth, thus obtaining sharp interfaces between p- and n-type semiconductors in a single NW [115], that could be used in nanoscale electronic and optoelectronic devices. Radial or coaxial (commonly called *core-shell*) NWs (see *Fig. 3.3(b)*) are heterostructures where the core NW is coated by another material to enhance its characteristics. As the surface of a NW can greatly influence its properties, even a very thin coating might drastically change the performance of the NWs in different device applications.

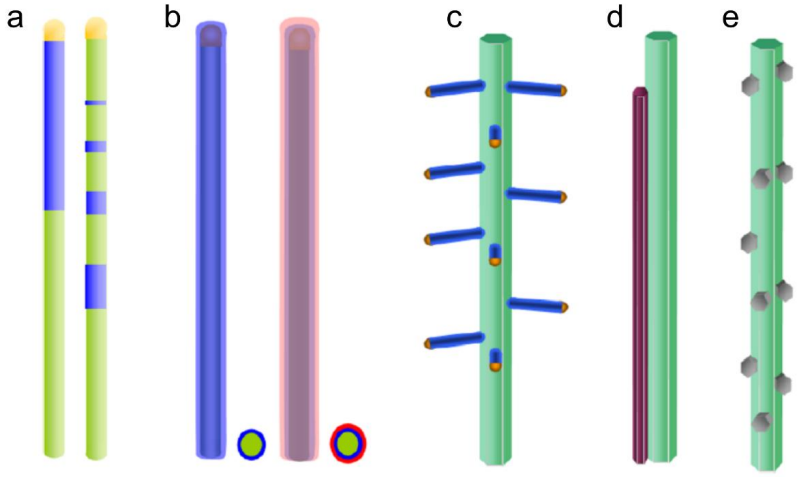

Figure 3.3. A schematic representation of different 1D heterostructure groups: (a) axial, (b) radial (*core-shell*), (c) hierarchical, (d) aligned and (e) 1D-0D (NP-decorated) nanowires. Adapted from [107].

Similarly, NP-decorated NWs (or 1D-0D heterostructures as shown in *Fig. 3.3(e)*) can exhibit novel behaviour due to the surface modification, while not completely covering the NW surface.

Core-shell NWs might be categorized in two groups, depending on the function of the *shell* material. The shell can be called active, if it is necessary for the operation of a device, for instance, if a p-n junction is formed between the core and the shell. There are quite a few reports in literature on semiconductor *core-shell* heterostructure devices, such as coaxial FETs [6], LEDs from simple p-n junctions [116] or multiple quantum well structures [117], and efficient solar cells due to improved charge carrier separation in the heterostructure [118–120]. Other examples of an active shell radial hybrid NW application is low loss waveguides with high gain optical amplification [121], and catalysis and hydrogen evolution [122]. Otherwise, the shell can be called passive, if it only improves some property of the core NW and it does not directly participate in the operation of the device. There are many reports on modification of NWs mechanical properties, such as increased elasticity, by a thin shell coating [5], for example, mechanical strength of Ag NWs was increased by coating with amorphous SiO_2 layer that might be important for flexible electronics applications [123], Young's modulus was tuned for Ge-Si core-shell NWs [124], and fracture strength was increased for ceramic SiC NWs with a SiO_2 coating [125]. Otherwise, a passive shell can be effectively used to passivate the surface states of a NW [126], to realize high electrical conductivity NW channels or to protect the NW from atmospheric conditions [5].

Core-shell NW fabrication methods mainly vary depending on the desired functionalities needed. Typically, the shell is formed in two step or multistep processes when either growth parameters or the synthesis method is changed. During CVD process, it is possible to switch from axial VLS growth mode to radial mode by changing the temperature and/or precursors, thus obtaining either a differently doped or a different material shell [107,122]. Otherwise, after the VLS growth of NWs, deposition method should be changed. Atomic layer deposition is an excellent method for precisely controllable deposition of amorphous oxides, such as SiO_2 and Al_2O_3, that are used for surface passivation, enhancement of mechanical properties and wrap-around gate dielectrics. Other thin film deposition methods, such as pulsed laser deposition and molecular beam epitaxy, have been used to deposit semiconductor materials directly on the NWs [127,128]. To grow uniform and highly crystalline shell with thin film deposition methods for semiconductor heterostructure applications, lattice parameters of both core and shell materials should be considered.

In this work, semiconductor materials *core-shell* NWs with layered TMDs shell were synthesised. Such novel heterostructures could be used for applications in optoelectronics and photo- or electrocatalytic hydrogen evolution reactions. There have been very few articles in literature on fabrication of similar *core-shell* nanostructures [129–133] and promising properties have been demonstrated, therefore, the scope of this Dissertation is to extend this field by exploring new materials combinations and complementary synthesis methods, and investigating the heterostructure applicability in optoelectronics and catalysis.

4. EXPERIMENTAL METHODS

4.1 Physical vapour deposition

Physical vapour deposition (PVD) of thin films encompasses various technologies that involve deposition of solid films on substrates by condensation of a vaporized solid material [134]. By physically ejecting atoms or molecules from a target material, thin film grows when they condense and nucleate on the surface of the substrate. There are several distinct PVD methods, simple thermal evaporation of a metal and reactive magnetron sputtering has been used in this work, utilizing *Sidrabe SAF25/50* multifunctional cluster tool.

Thermal evaporation has been used in this work for depositing thin 5 nm/45 nm Cr/Au electrodes on the SiO_2/Si substrate, where Cr layer is used to enhance Au adhesion to the surface. When a metal is placed in a crucible (a foil boat or a wire basket) and resistively heated to a high temperature, atoms are ejected from the material – evaporated (see *Fig 4.1(a)*). If the vacuum in the chamber is high enough and the mean free path of the ejected species is larger than the distance between the crucible and the substrate, the atoms reach the surface of the cold substrate and adsorb on it. The deposition rate depends on the material and its vapour pressure at the given temperature. The whole process of evaporation and film growth is more complicated as it involves complex sequence of events, however, for deposition of metallic electrodes there is no need to investigate the microstructure as there is only a need for good adhesion and conductivity. In the case of ZnO-PbI_2 NW heterostructure synthesis, PbI_2 powder was thermally evaporated on top of ZnO NWs sample to obtain uniform and crystalline coating due to the relatively low melting point (402°C) of the material.

Magnetron sputtering is based on a bombardment of a target material with energetic ions that leads to ejection of target atoms (see *Fig 4.1(b)*). A typical source of ions is plasma, which is obtained by applying a negative voltage to the target (cathode) and by ionization of an inert gas, usually argon. The positive argon ions accelerate in the electric field and bombard the target, therefore sputtering the material atoms and secondary electrons. These electrons are important for maintaining plasma, as magnets are typically placed under the target to create a magnetic field that attracts the electrons near the target surface so effective gas ionization is

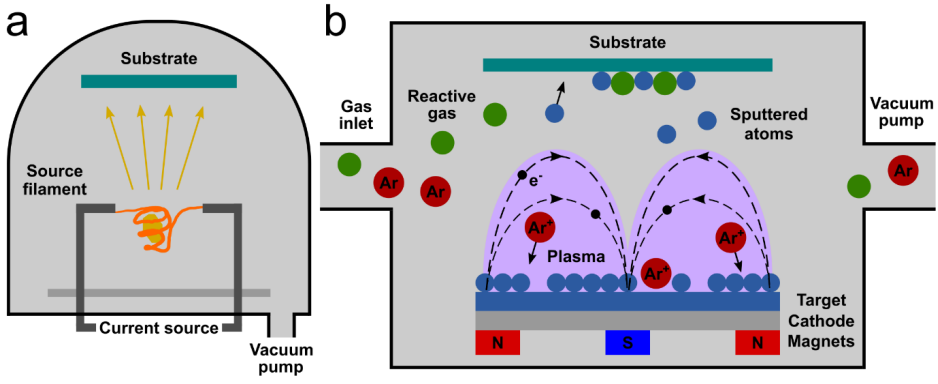

Figure 4.1. A schematic representation of PVD methods: (a) thermal evaporation of a metal inside a vacuum chamber, and (b) reactive DC magnetron sputtering of a metallic target.

sustained. As the process is carried out in high vacuum, the sputtered atoms reach the substrate, and a thin film is formed. Direct current (DC) voltage source is used for metallic targets, and a radiofrequency is used for insulating targets. Furthermore, a reactive process can be performed by introducing a reactive gas, such as oxygen, in the process chamber. The partial pressures of the reactive and inert gases control the stoichiometry of the film, therefore are used to tune its physical properties. In this work, different transition metal oxide coatings, such as WO_3, MoO_3, ReO_x, PbO_x, were obtained by reactive DC magnetron sputtering. Typically, 100 W DC power was used with different Ar/O_2 partial pressures and sputtering times, depending on the material.

4.2 Chemical vapour deposition

Chemical vapour deposition (CVD) technique in the broadest sense is defined as a method of growing a stable solid product (typically, thin films and coatings) by a dissociation and/or chemical reactions of vapour-phase precursors in an activated (typically by heating) environment [135]. Many different aspects are involved in the CVD process, therefore a diversity of specialized CVD techniques exist, categorized by a specific aspect of the technique, for example, precursor material, work pressure range, source of activation energy etc. CVD technique involves complex systems and multiparameter processes, however it has several advantages: 1) it can produce uniform films at reasonably high deposition rates with controllable crystal structure and film morphology; 2) it is not a line-of-sight process, therefore can be used to uniformly coat substrates with complex shapes; 3) the variety of available precursors enables the deposition of wide range material films and coatings.

In this work, thermally activated atmospheric pressure CVD system with a horizontal quartz tube reactor was utilized, similar to one schematically depicted in *Fig. 2.7*. While such CVD system does not allow precise control over process parameters other than temperature, it greatly benefits from the versatility needed for fundamental research, for instance, a wide range of available precursor materials. Solid precursor materials are typically used in such systems to achieve vapour-phase or solid-state chemical reactions. Here, CVD was mainly used in two cases: NW growth via VLS mechanism, and sulfurization/iodination of transition metal oxide coatings. Additionally, CVD was also used to prepare selected reference samples, such as 2D WS_2 and MoS_2 microcrystals, via method previously described in *Chapter 2.3.2*. The detailed growth recipes for all the synthesised materials are given in *Appendix A*.

All of the NWs mentioned in this work were synthesised via VLS method in the CVD reactor (see *Chapter 3.3*). Each material NWs have their own optimal growth temperature and time, however in all the cases the NWs were grown on oxidized silicon wafers SiO_2/Si(100) (*Semiconductor Wafer, Inc.*) coated with spherical Au NPs (*BBI Solutions*, water suspension, 100 nm diameter) used as a catalyst. The temperature of the precursors and the substrate is determined by the used materials and desired growth rate. The precursor temperature affects the sublimation rate of the material and, thus, the vapour partial pressure which governs the growth rate, and is selected depending on the solid precursor melting/sublimation temperature. Similarly, the optimal substrate temperature range depends on the properties of the final material, and is determined experimentally. The substrates are simultaneously placed in a relatively wide temperature range, and after the synthesis process the temperature with the desired NW structure and morphology is selected. The growth time typically determines the length of the NWs.

In this work, to synthesise a layered material shell around a NW, typically a pre-deposited metal oxide coating was converted by a sulfurization/iodination reaction. Sulfur/iodine vapour was obtained by evaporating the corresponding powder in the necessary temperature and delivered to the sample by the carrier gas. By placing the sample in the required temperature, solid-state reaction occurs when the vapour diffuses into the oxide shell and reacts with it. By adjusting the temperature, one controls the diffusion rate, thus the degree of the crystallinity of the as-grown shell. The optimal temperature and process time corresponds to a fully converted highly crystalline few-layer shell, which is determined by TEM and XRD measurements.

4.3 Electron microscopy

Optical microscopy does not provide the sufficient resolution when working with nanomaterials due to the diffraction limitation as the size of the nanostructures are usually less than the light wavelength, therefore, electron microscopy methods are typically used instead. Wave-like nature of electrons allows them to be used to image materials with sub-nanometre resolution as the de Broglie wavelength is typically in picometre range, depending on the accelerating voltage (the actual resolution is limited by other practical aspects, such as electron beam width and interaction volume). Electron microscopes are usually differentiated in two types – scanning electron microscopes (SEM) [136] and transmission electron microscopes (TEM) [137]. The difference in the working principles is schematically depicted in *Fig. 4.2*.

SEM uses relatively lower energy electrons (5-20 kV accelerating voltage) to obtain information about the surface morphology from secondary and/or backscattered electrons. The incident electron beam is scanned over the surface in raster pattern, so a reconstructed image of the surface can be formed from each data point. Therefore, one of the greatest benefits of SEM

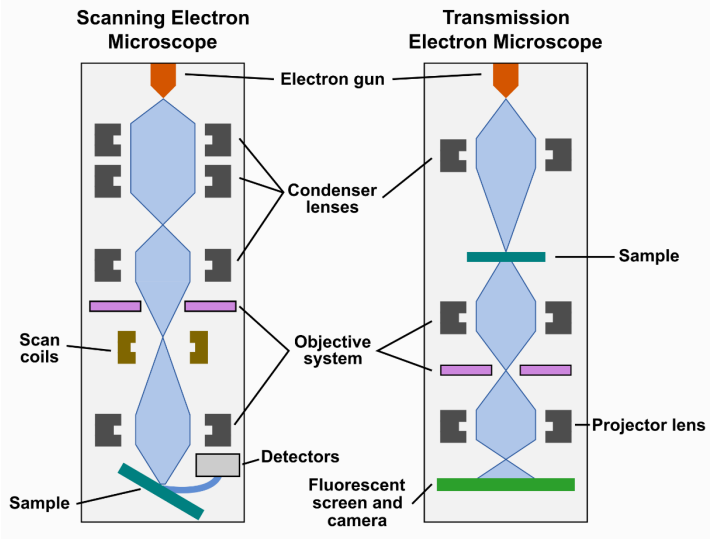

Figure 4.2. A schematic representation of working principles of scanning and transmission electron microscopes.

is a wide depth of field at large range of magnifications (from 10x to 500000x), in combination with high resolution. Although high vacuum and non-dielectric samples are necessary for operation, SEM is an essential tool in this work for imaging synthesised NWs and nanostructures (*Lyra, Tescan* SEM was used). Furthermore, built-in focused ion beam (FIB) with a gas injection system (GIS) was used for *in-situ* single-NW device fabrication.

In contrast to SEM, TEM reveals the inner atomic structure of the studied material, as the incident electron beam interacts with the sample when passing through it. The transmitted beam is projected onto a fluorescent screen or CCD camera, and an image of electron density distribution of the material in formed. As the electrons in the beam are usually accelerated by 50-200 kV or more, atomic resolution is often obtained, thus giving some information about the crystal structure - phase, lattice constant and plane orientation. Ultrathin (<100 nm) samples are needed for a detectable number of electrons to pass through, therefore, NWs are typically a convenient material to work with as no prior sample preparation is necessary. NWs are dispersed on a substrate holder – copper grid – and placed in TEM for the imaging, while for bulk materials and thin films a complicated thinning and lamellae manipulation procedure is required. In this work, TEM (*Tecnai GF20, FEI)* was used to visualize synthesised NW *core-shell* heterostructures and to determine the thickness of the shell layer, as the difference between core and shell can be clearly distinguishable due to the distinct crystal structures of the materials, especially the layered structure of TMDs shell can be easily recognized.

In a TEM, high-energy electrons due to their short wavelength can be used to study crystallographic properties of a material as its atoms may diffract them. A fraction of incident electrons will pass through the sample without deflecting, however, some will be scattered in specific angles which are determined by the crystal structure of the material. The resulting image on the TEM screen is a pattern of bright spots – selected area diffraction pattern, where each spot corresponds to a certain diffraction condition of the crystal structure. Diffraction spots will change if the sample is tilted in different angles, as distinct diffraction conditions will be satisfied. Furthermore, if the specimen is polycrystalline, the pattern will contain rings with various diameters, instead of spots. If the sample is made from several crystalline materials (for example, a NW heterostructure as in this work), the image will show several overlapping patterns which might be difficult or impossible to analyse. Here, diffraction patterns were analysed using CrysTBox software [138], which allows automatic spot identification, reciprocal lattice construction and crystal phase matching. This technique is called selected area electron diffraction (SAED) because a specific part of the sample can be selected from which to obtain the diffraction pattern. This is a great benefit compared to X-ray diffraction as it allows to examine areas with size in order of hundred nanometres instead of more than few millimetres.

4.4 X-ray diffraction and spectroscopy methods

X-ray diffraction (XRD) is a powerful method of analysing materials structure [139]. In a perfect crystal, atoms are arranged in a lattice with an interplanar distance d, and if d is in the same order as the wavelength λ of an incident X-ray beam, X-rays diffract in the crystal. Two X-ray beams interfere constructively, if their phase difference $2d\sin\theta$ is equal to integer n wavelengths, and that is described by Bragg's law: $n\lambda = 2d\sin\theta$. Measuring angles and intensities of the diffracted beams using a diffractometer gives a pattern with Bragg peaks. From the position, width and intensities of the peaks in the XRD pattern one can obtain information

about the materials structure – phase composition, lattice constant, degree of crystallinity, crystallite size and orientation. In this work, XRD was utilized to determine the phase composition of the synthesised samples using *Rigaku MiniFlex 600* X-ray powder diffractometer with Bragg-Brentano θ-2θ geometry and Cu anode X-ray tube (Cu $K\alpha$ radiation, λ = 1.5406 Å). *Crystallography Open Database* was used for phase identification.

Raman spectroscopy is based on Raman scattering – inelastic scattering of monochromatic light [140]. When a material absorbs the incident laser light, its molecules are excited to a higher virtual energy state, and photons are emitted after relaxation. Predominantly it relaxes back to the initial state (Rayleigh scattering), however, if there is an interaction with molecular vibrations, rotation or phonons in the system, inelastic scattering occurs and the photon energy may be shifted to a lower (Stokes shift) or a higher (anti-Stokes shift) frequency. This energy shift matches specific vibrational modes that are characteristic to specific molecules, therefore one can measure Raman spectrum (scattering intensity as a function of the shift in frequency units) to determine the chemical structure of a material. Not all molecular vibrations are Raman-active – there must be a change in electric dipole-electric dipole polarizability of the molecule, and the magnitude of the polarizability change determines the intensity of Raman scattering. In this work, micro-Raman measurements were performed using a confocal microscope with spectrometer *Nanofinder-S (SOLAR TII)*. Confocal microscopy allows to locate nanostructures on a substrate and focus the laser beam to around 1 μm diameter, thus it is possible to measure Raman spectra of single NWs and NW heterostructures. Many TMDs exhibit relatively strong Raman scattering, therefore, micro-Raman spectroscopy is a powerful technique to identify thin layers of TMDs on nanostructures, as have been demonstrated in this work.

Optical luminescence spectroscopy is used to investigate the optical properties of the material of interest. In this work, mostly semiconductor materials with a bandgap width in the visible spectrum are studied, therefore photoluminescence measurements give information about the width of the optical bandgap and defect bands, and this knowledge is valuable when designing and fabricating optoelectronic devices, such as photodetectors. When a material is illuminated with a light, whose wavelength corresponds to an energy slightly larger than the bandgap of the material, electrons absorb the photons and are excited to conduction band. When electrons reach the edge of the band by losing energy via nonradiative relaxation, they recombine with the holes in the valence band and emit a photon with an energy equal to the width of the bandgap [140]. Similarly, through recombination via a defect state, anion or cation vacancy, for instance, photons are emitted with the corresponding energy. Thus, by measuring the photoluminescence spectrum, one can obtain the information about these optical properties of the material.

4.5 Optical lithography

Optical lithography, or photolithography, is a microfabrication technique which is typically used to make desired patterns on thin films or in silicon wafers [141]. It uses light (usually UV) to pattern a photosensitive chemical photoresist, which is coated on the substrate, either by projecting a geometrical image from a mask or by a direct laser beam writing. The

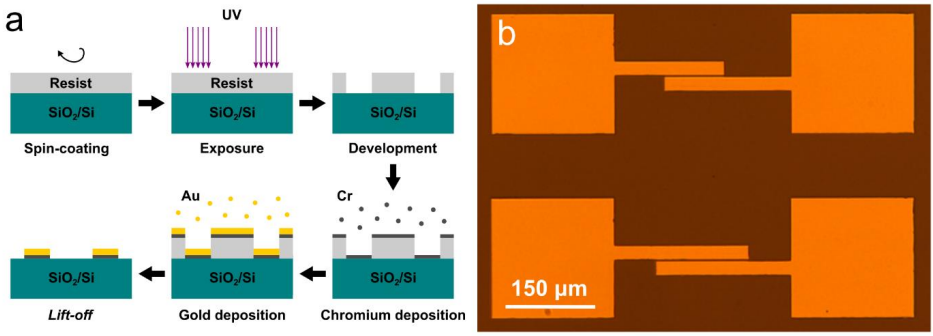

Figure 4.3. Fabrication of electrodes on SiO_2/Si wafer: (a) a schematic representation of optical lithography, metallization and *lift-off* steps, (b) as-prepared gold electrodes.

resist undergoes a chemical change, therefore, the exposed parts can be removed (or vice versa, depending on the resist tone – positive or negative) by developing to obtain the desired pattern. Here, a direct-write laser photolithography (*µPG101, Heidelberg Instruments*), followed by metallization and *lift-off*, was used to obtain gold microelectrodes on oxidized silicon wafers.

The process of fabricating the desired electrode pattern on a wafer consists of several steps, depicted in *Fig. 4.3(a)*. The technical details and parameters are given in *Appendix A*. Firstly, a positive photoresist layer is coated on a SiO_2/Si substrate by *spin-coating* technique, and it is important to achieve uniform thickness across the wafer to subsequently obtain high-quality electrodes. Secondly, the resist is exposed to light which follows a pattern design (prepared in *AutoCAD* or similar software), and a chemical developer is applied to remove the exposed resist. Thirdly, a 50 nm gold film is deposited on top of the patterned substrate by a thermal evaporation, which is a line-of-sight deposition method. A 5 nm nanometre chromium layer is usually deposited below the gold film to enhance its adhesion to the SiO_2/Si substrate. Worth noting, that the resist thickness must be significantly larger than the thickness of the metal film, otherwise the pattern side-walls will be coated and a successful *lift-off* will not be possible. Finally, to remove the unwanted metal film, *lift-off* is performed by immersing the substrate in a specific organic solvent, that dissolves the underlying resist and thus the unnecessary metal film detaches from the substrate. As-prepared metal electrodes are shown in *Fig. 4.3(b)*, where the large square electrodes are needed to attach macroscopic contacts, and a NW is subsequently placed on top of the both long "arms" with a gap width of 2 µm.

4.6 Single-nanowire device fabrication and photoelectric measurements

Compared to traditional silicon and thin film microfabrication techniques, most of the nanomaterials do not have conventional methods of fabricating devices. Commonly, electron-beam lithography (EBL) is used to selectively define electric contacts on top of nanostructures with sub-micrometre precision for *proof-of-concept* devices. Alternatively, one can mechanically *in-situ* place a nanostructure on top of pre-defined electrodes with a nanomanipulator inside a SEM-FIB, as have been demonstrated in this work. *Fig. 4.4* shows SEM images of the crucial steps of this procedure. Firstly, a single NW from the substrate is welded to the tungsten (W) nanomanipulator probe using electron-beam-assisted platinum (Pt)

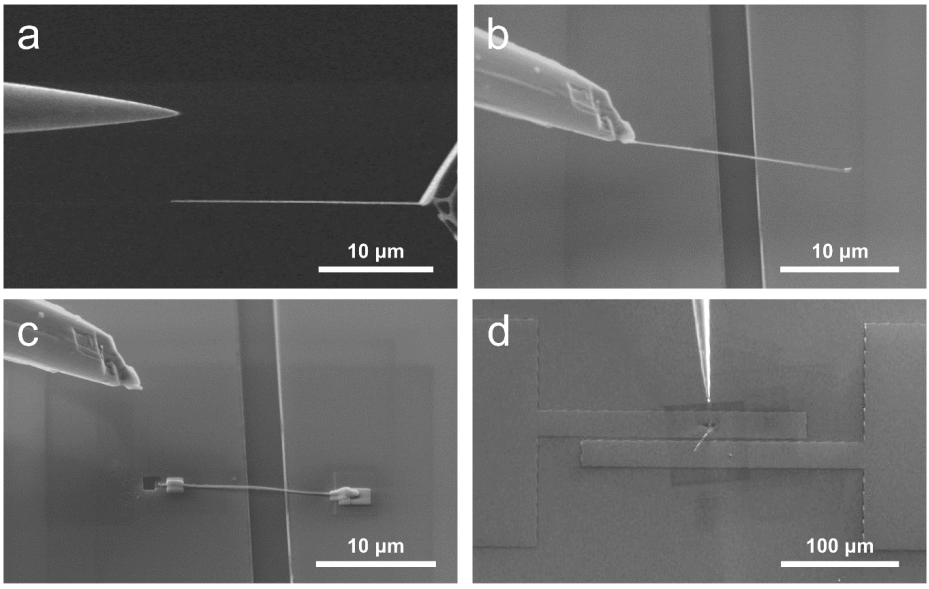

Figure 4.4. Fabrication of single-nanowire two-terminal device *in-situ* SEM-FIB. (a) A nanowire is selected from the sample and welded to the tungsten nanomanipulator probe via electron-beam-assisted Pt deposition, (b) then aligned and placed on top of the gold contacts, (c) welded to the electrodes and cut off from the nanomanipulator probe with gallium ion beam. (d) As-prepared device at smaller magnification.

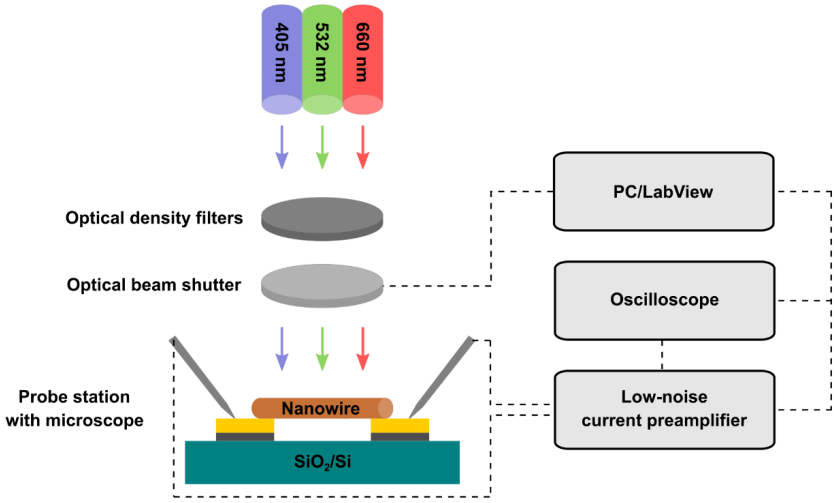

Figure 4.5. A schematic representation of the photoelectric measurements setup.

deposition, where Pt metalorganic is delivered by GIS. Afterwards, the NW is aligned and placed on top of the electrodes, welded with Pt deposition to ensure an electric contact and fixed position, and cut off from the nanomanipulator probe with gallium ion beam. The gap width

between the electrodes typically was 2-3 μm, therefore, the minimum NW length for a successful device fabrication was at least 10 μm.

As-prepared single-NW devices were characterized as two-terminal photodetectors. Current−voltage (*I*−*V*) characteristics and photoresponses to light of different wavelengths were measured with an experimental setup, schematically depicted in *Fig. 4.5*. Two-contact microprobe station was connected to a low-noise current preamplifier (*SR570, Stanford Research Systems*) and oscilloscope (*TDS2004B, Tektronix*). 405 nm, 532 nm and 660 nm wavelength semiconductor diode lasers with the power of 0.5 W/cm^2 were the illumination sources. Optical beam shutter (*Thorlabs SH05*) was used for time-resolved measurements; all the measurements were performed at room temperature and in air. *LabView*-based software was developed to control the experimental setup.

5. RESULTS AND DISCUSSION

5.1 Tungsten disulfide WS_2

Tungsten disulfide WS_2 is an indirect bandgap semiconductor material with a 1.3 eV gap, however, when reduced to monolayer, the gap becomes direct and shifts to around 1.9 eV [19]. 2D monolayer WS_2 crystals have been previously grown via several methods, such as CVD [44,142] and pre-deposited WO_3 film sulfurization [19,143]. WS_2 monolayers exhibit high PL quantum yield and decent carrier mobility (up to 200 $cm^2V^{-1}s^{-1}$), therefore have potential applications in future optoelectronics [19,44,73]. In this work, few-layer WS_2 was grown around ZnO and GaN NWs by a simple three-step route: as-grown ZnO and GaN NWs were coated with amorphous WO_3 layer using reactive DC magnetron sputtering, then ZnO- and GaN-WO_3 NWs were annealed in a quartz tube reactor in a sulfur atmosphere at 800°C to convert the oxide coating to WS_2, followed by annealing in N_2 atmosphere to sublimate the remaining WO_3 [144]. More technical details are given in *Appendix A*.

5.1.1 ZnO-WS_2 *core-shell* nanowires

As-grown ZnO-WS_2 NWs were first imaged and studied with SEM (see *Fig. 5.1*). The length and diameter of the pure and *core-shell* NWs is in the same range, thus the morphology of NWs is maintained after the heat treatment during the heterostructure preparation. The length of the NWs varies from 10 to 50 µm, the diameter is around 100 nm.

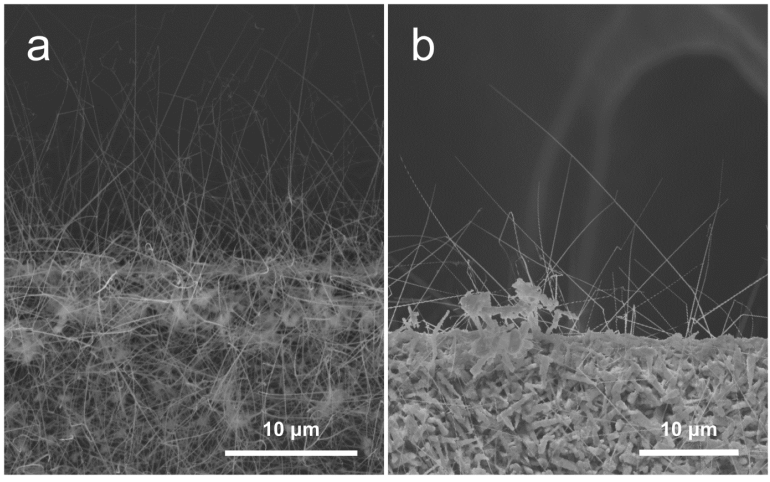

Figure 5.1. SEM images of (a) pure ZnO NWs, and (b) ZnO-WS_2 *core-shell* NWs.

To reveal the NW inner structure, TEM was used (see *Fig. 5.2*). Firstly, Au NPs were located at the end of NWs, which were used as catalysts for VLS growth. Secondly, few-layer WS_2 shell was observed on the ZnO NW surface, and is clearly visible as parallel black lines. The thickness of the shell was 1-5 monolayers (each consisting of S-W-S atomic planes), and the measured interlayer distance was around 6.3 Å, which corresponds to previously reported

distance 6.2-6.4 Å in WS_2 nanostructures [145]. Furthermore, the single-crystalline structure of ZnO NW core can be well seen.

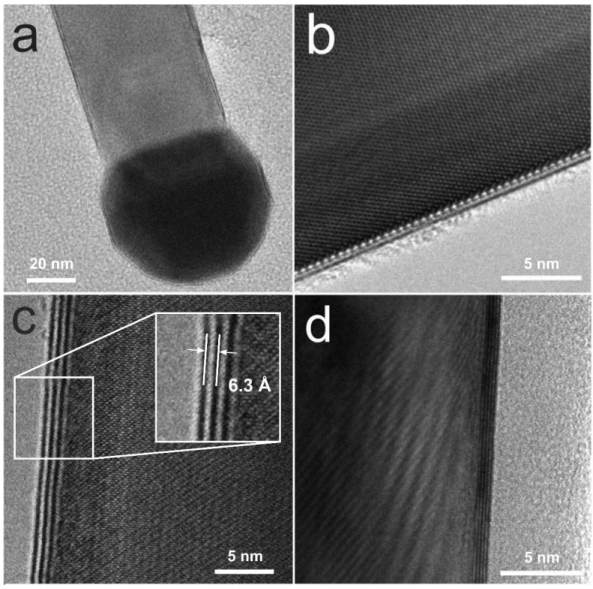

Figure 5.2. TEM images of ZnO-WS_2 *core-shell* NWs. WS_2 can be distinguished as parallel black lines on the NW surface. The inset shows the measured atomic interlayer distance in the WS_2 shell.

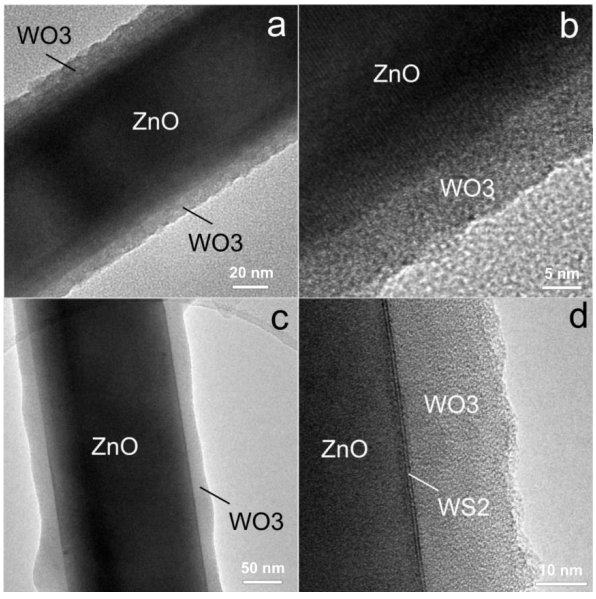

Figure 5.3. TEM images of (a, b) ZnO-WO_3 *core-shell* NWs, and (c,d) ZnO-WS_2-WO_3 NWs after sulfurization step at 800°C but before annealing at 700°C in inert atmosphere.

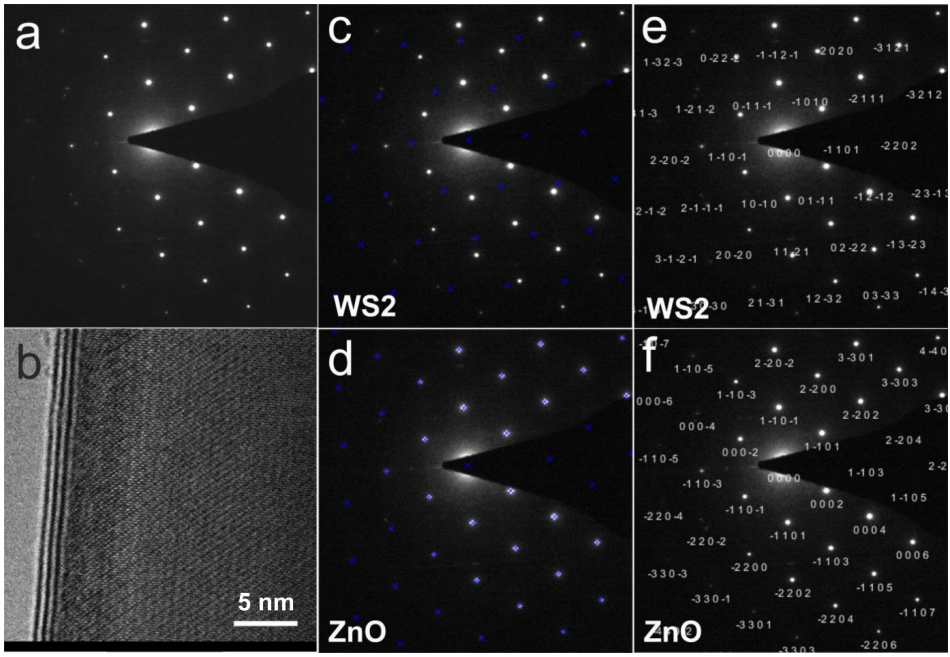

Figure 5.4. SAED analysis of ZnO-WS_2 *core-shell* NWs. (a) SAED pattern, (b) TEM image of the NW, (c-f) phase analysis.

To better understand the formation mechanisms of WS_2 layers, ZnO-WO_3 *core-shell* NW samples before and after sulfurization were imaged in TEM (see *Fig. 5.3*). Amorphous structure of the sputter-deposited WO_3 shell can be distinguished. After the sulfurization process, formation of WS_2 layers can be observed on the interface between ZnO core and WO_3 shell, indicating favourable growth of WS_2 on ZnO. The remaining WO_3 coating was removed from the heterostructures by annealing the NWs in inert atmosphere.

The measured SAED pattern of a ZnO-WS_2 NW is shown in *Fig. 5.4*. Analysis revealed only two distinct phases, WS_2 and ZnO, with high crystallinity. To complement the SAED measurement, XRD pattern of the NW array on Si(100)/SiO_2 substrate was also measured (see *Fig. 5.5*). Bragg peaks corresponding to WS_2 (ICDD-PDF #08-0237), ZnO (ICDD-PDF #36-1451), ZnS (ICDD-PDF #36-1450) phases and Si substrate were identified. Although the amount of ZnS in the sample was high enough to be detected by XRD, only a sub-monolayer was present in the ZnO-WS_2 NWs [144].

Micro-Raman spectroscopy was used to support the formation of WS_2 on ZnO NWs. Individual NWs were transferred on top of a clean Si(100)/SiO_2 substrate. *Fig. 5.6(a)* shows room-temperature micro-Raman spectra of a typical ZnO-WS_2 NW (see SEM image in the inset). The two main optical phonon modes $^1E_{2g}$ at 354 cm^{-1} and A_{1g} at 419 cm^{-1} were detected, as well as several other weak Raman bands of WS_2 phase were observed and are indicated with arrows. The positions of the measured bands correspond to the values of bulk WS_2 (355.5 and 420.5 cm^{-1}, respectively) [19], however, the intensity ratio between those bands implies that the thickness of the WS_2 shell is close to a monolayer [146]. The large peaks at 521 and 959 cm^{-1} correspond to optical modes of the silicon substrate. No Raman signal was obtained from the ZnO NW core due to its weak intensity when excited at 532 nm.

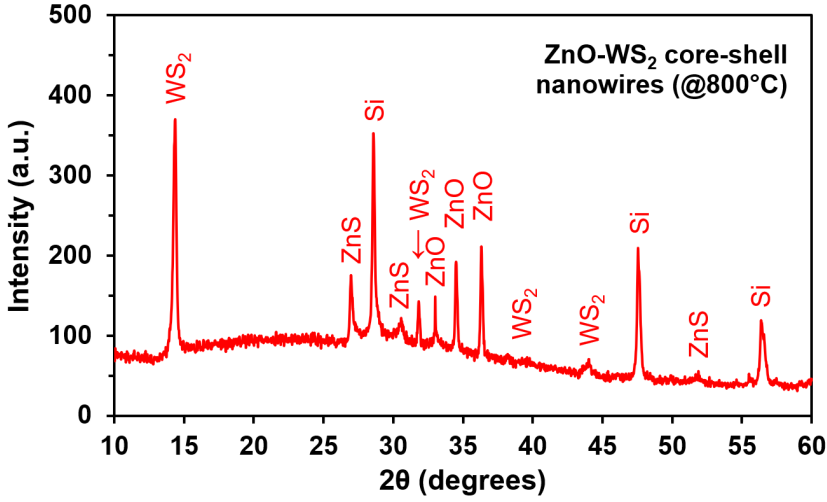

Figure 5.5. XRD pattern of ZnO-WS_2 *core-shell* NW array on Si(100)/SiO_2 substrate.

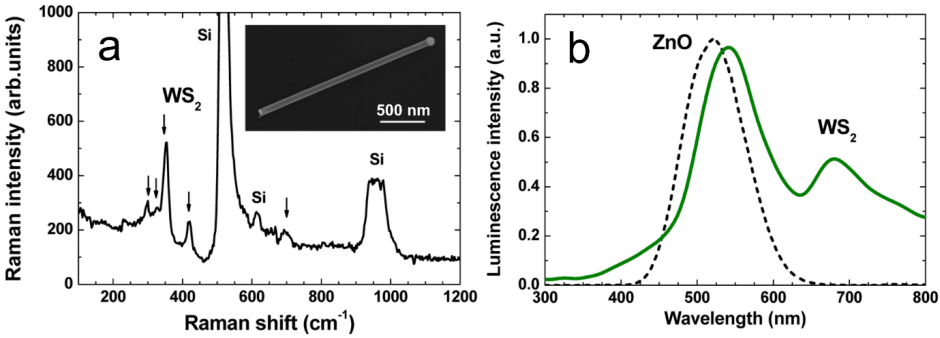

Figure 5.6. (a) Micro-Raman spectrum of a single ZnO-WS_2 *core-shell* NW on Si(100)/SiO_2 substrate (The inset shows a SEM image of the studied NW), (b) room-temperature photoluminescence spectra of pure ZnO NWs (dashed curve) and ZnO-WS_2 *core-shell* NWs (solid curve).

Room-temperature photoluminescence (PL) spectra of pure ZnO NWs and ZnO-WS_2 NWs are shown in *Fig. 5.6(b)*. Pure ZnO NWs typically exhibit a defect-related PL band at around 520 nm [147], which was observed in our measured spectrum. The PL spectrum of ZnO-WS_2 NWs is more complicated as it contains emission bands from both ZnO and WS_2 phases at around 540 nm and 680 nm, respectively. Here, ZnO-related band red-shifted in comparison to pure ZnO NWs, that may be caused by electron density redistribution, formation of ZnS submonolayer or influence of additional defects. Similarly, red-shift was observed for the WS_2-related band, as PL band of 2D WS_2 microcrystal reference sample is located at 640 nm that corresponds to direct bandgap of 1.9 eV. The shift of the WS_2 PL peak might originate from the influence of the underlaying ZnO NW substrate.

In collaboration with *Laboratory of Computer Modelling of Electronic Structure of Solids* in ISSP UL, large-scale *ab initio* calculations were performed to develop an atomistic

model of the ZnO and WS_2 interface. It was experimentally observed that $WS_2(0001)$ shell grew on $ZnO(1\bar{1}00)$ NW substrate. Through the theoretical calculations it was found that $WS_2(1\bar{1}00)$ submonolayer bridging structures act as pads between the core and the shell for such orientation to be stable (see *Fig. 5.7*). The stability of these submonolayers is higher if their quasimolecular groups are separated by at least a next-neighbour distance, and that reduces the strain of $WS_2(0001)$ shell. This model explains the strong adhesion of the WS_2 layer to ZnO NW and is in agreement with the experimentally estimated interplanar interface distance [144].

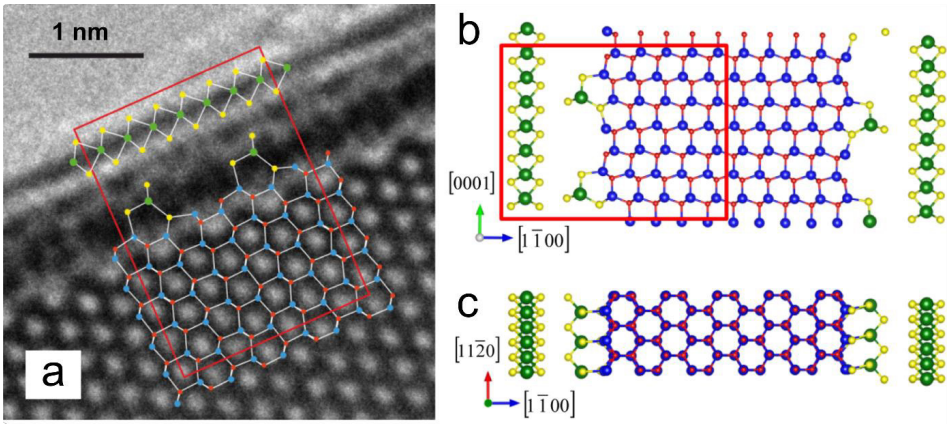

Figure 5.7. (a) Imposition of optimized atomistic model of $ZnO(1\bar{1}00)$/striped 0.5 ML $WS_2(1\bar{1}00)/WS_2(0001)$ interface on top of the TEM image of ZnO-WS_2 *core-shell* NW and sections of the same interface across (b) $(11\bar{2}0)$ and (c) (0001) planes.

5.1.2 GaN-WS_2 *core-shell* nanowires

Analogous to ZnO NWs, growth of WS_2 layers was also demonstrated on GaN NWs. SEM images of pure GaN and GaN-WS_2 *core-shell* NWs are shown in *Fig. 5.8*. It can be seen

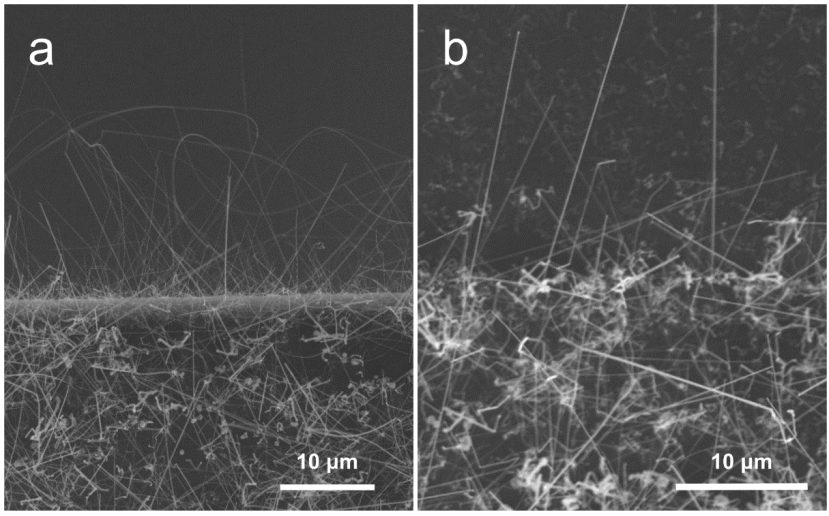

Figure 5.8. SEM images of (a) pure GaN NWs, and (b) GaN-WS_2 *core-shell* NWs.

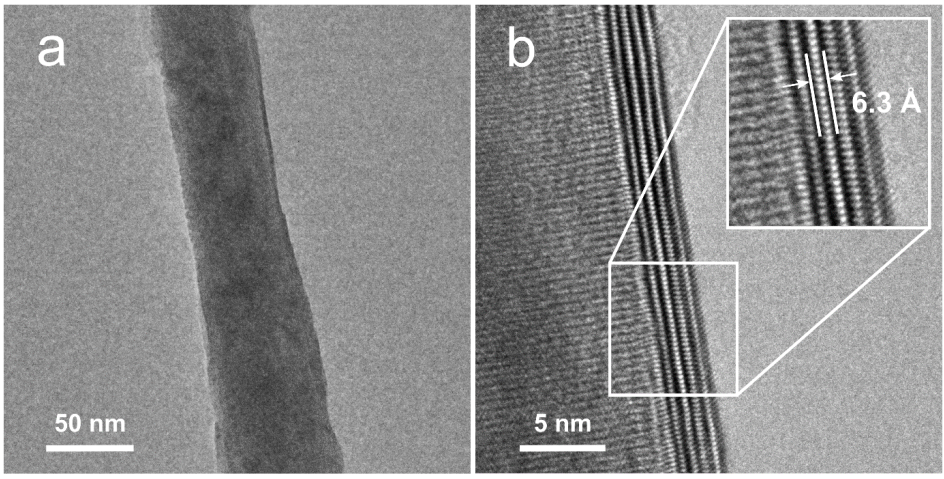

Figure 5.9. TEM images of GaN-WS_2 *core-shell* NWs. The inset shows the measured atomic interlayer distance in WS_2 shell.

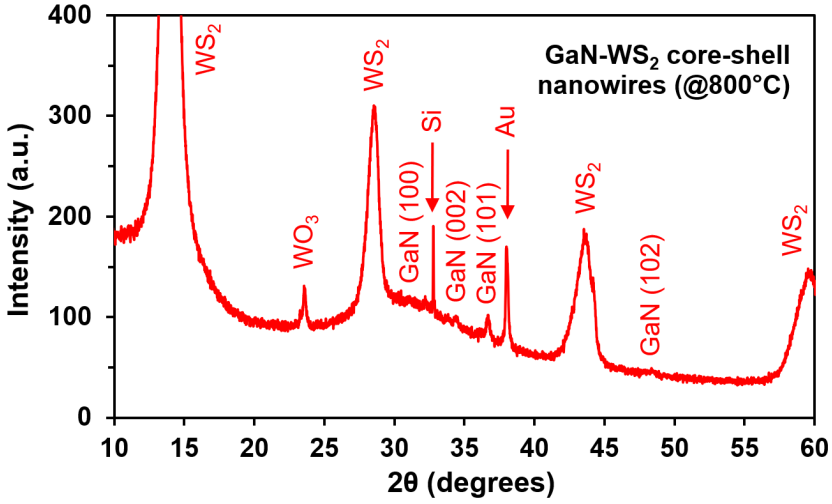

Figure 5.10. XRD pattern of GaN-WS_2 *core-shell* NW array on Si(100)/SiO_2 substrate.

that the NWs maintain their morphology and length after the heat treatment. The length of NWs varies from 10 to 30 μm, and diameter from 50 to 100 nm.

TEM images (see *Fig. 5.9*) show the *core-shell* NWs at a higher magnification. It can be seen that the surface of GaN NW is uniformly covered by few-layer WS_2. The measured WS_2 interlayer distance 6.3 Å corresponds to the previously observed value. To confirm the present phases, XRD measurement of the NW array on Si(100)/SiO_2 substrate was performed. The spectrum depicted in *Fig. 5.10* indicates that WS_2 and GaN phases are present as was expected, as well as Au from the NP catalyst and some remaining unconverted WO_3.

5.1.3 WS_2 reference sample

2D WS_2 flake reference sample was synthesised via the CVD method (experimental details of the process are given in *Appendix A*) to compare Raman and PL spectra (see *Fig. 5.11*) with the ones of *core-shell* NWs. In the Raman spectrum the main optical phonon modes $^1E_{2g}$ at 354 cm^{-1} and A_{1g} at 419 cm^{-1} were detected, as well as several other weak bands of WS_2 phase were observed and are indicated with arrows; the Raman spectrum of the 2D WS_2 microcrystal closely matches the one obtained from the ZnO-WS_2 *core-shell* NW. As for PL measurement, a broad band at 640 nm was recorded from the reference sample that corresponds to direct band gap of 1.9 eV. It was discussed previously, that the shift from 640 to 680 nm in ZnO-WS_2 *core-shell* NWs might originate from the influence of the underlaying ZnO NW substrate.

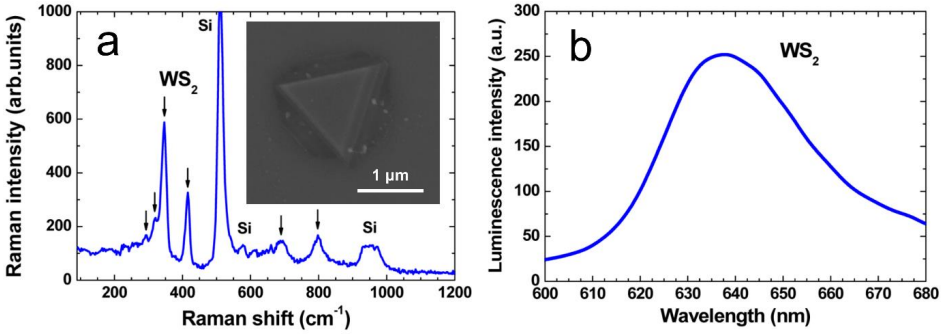

Figure 5.11. (a) Micro-Raman spectrum of a 2D WS_2 microcrystal on Si(100)/SiO_2 substrate (The inset shows a SEM image of the studied microcrystal), (b) room-temperature photoluminescence spectra of the 2D WS_2 microcrystal.

5.2 Rhenium disulfide ReS_2

ReS_2 exhibits much weaker interlayer coupling in comparison to other 2D materials with the indirect-to-direct bandgap transition in monolayers, therefore, it remains a direct bandgap (E_g ~ 1.5–1.6 eV) semiconductor in bulk, few-layer and monolayer forms [28]. It possesses a unique distorted octahedral (1T) structure resulting in distinct anisotropic optical and electrical properties along in-plane directions [20], that may be useful for emerging applications in electronics (carrier mobility around 30-40 $cm^2V^{-1}s^{-1}$) and optoelectronics [81,148]. 2D ReS_2 has been previously obtained by mechanical exfoliation [148] or variations of CVD: by evaporation different rhenium precursors (Re, ReO_3, Re_2O_7, NH_4ReO_4) [149,150] or by converting pre-deposited metallic Re film [151]. As ReS_2 exhibits strong interlayer decoupling, out-of-plane growth is predominant on many substrates, leading to growth of wrinkled low-quality polycrystalline films or thick flower-like ReS_2 via typical CVD process [150]. In this work, first time growth of few-layer ReS_2 on different semiconductor material NWs (GaN, ZnS, ZnO) was demonstrated. Amorphous non-stoichiometric ReO_x coating was deposited on pure NWs by reactive DC magnetron sputtering, followed by sulfurization of the coating in a quartz tube reactor at high temperature. More technical details are given in *Appendix A*.

5.2.1 GaN-ReS_2, ZnS-ReS_2 and ZnO-ReS_2 *core-shell* nanowires

SEM images of the as-grown *core-shell* nanostructures (see *Fig. 5.12*) show that the length of NWs is preserved after the procedure and matches their respective pure NWs length before the high-temperature treatment, as well as the density of the NW arrays is maintained. However, a morphology changes of ZnO-ReS_2 NWs upon heating at 800°C can be observed, that indicate an occurrence of a recrystallization process.

TEM was used to study the inner crystalline structure of the NW heterostructures. *Fig. 5.13* shows TEM images of as-grown GaN-ReS_2 (a,b), ZnS-ReS_2 (c,d) and ZnO-ReS_2 (e,f) *core-shell* NWs prepared at 800°C. The lower magnification images show that GaN and ZnS NWs maintain their straight shape, however, ZnO NWs undergo a transition to an irregular shape as

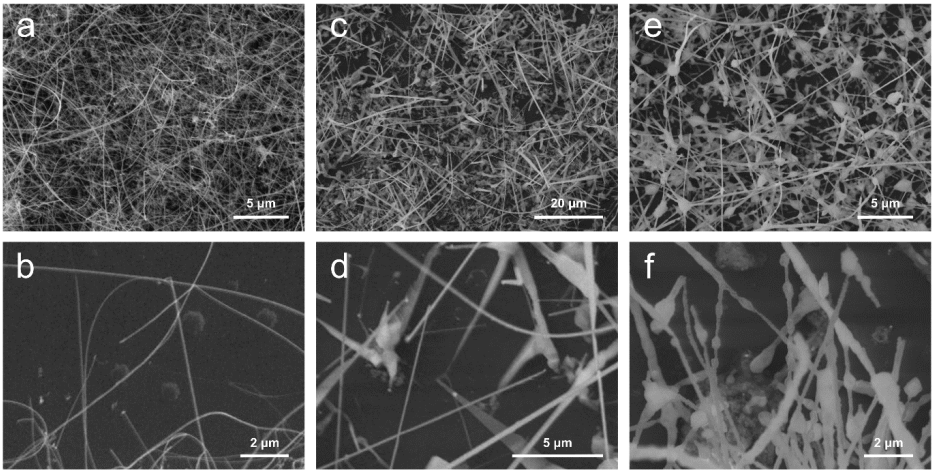

Figure 5.12. SEM images of (a,b) GaN-ReS_2, (c,d) ZnS-ReS_2 and (e,f) ZnO-ReS_2 *core-shell* NWs, prepared at 800°C, at different magnifications.

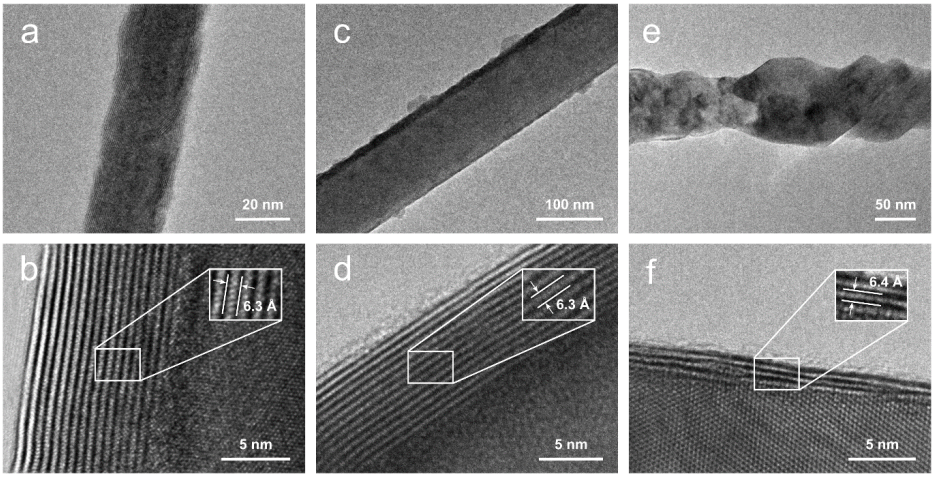

Figure 5.13. TEM images at different magnifications of as-grown (a,b) GaN-ReS_2, (c,d) ZnS-ReS_2, and (e,f) ZnO-ReS_2 *core-shell* NWs, prepared at 800°C. The insets show the measured atomic interlayer distances between ReS_2 layers.

was also observed in SEM. The higher magnification TEM images reveal the layered structure of ReS_2 shell (it can be seen as parallel black and white lines along the nanowire surface) with a measured interlayer distance of around 6.3-6.4 Å for all samples, that closely matches the lattice constant a = 6.45 Å of triclinic ReS_2 [152]. The typical thickness of the ReS_2 shell varies from 2-10 monolayers (each consisting of S-Re-S atomic planes), and the shell is uniformly distributed over the length of the NWs with only slight variations of thickness. Furthermore, the single-crystalline nature of the core NWs is visible (in NWs with diameter less than 80 nm) indicating high crystalline quality of the as-prepared *core-shell* heterostructures.

According to TEM measurements, the optimal sulfurization temperature was found to be 750-800°C in order to obtain high-quality single-crystalline ReS_2 layers from the magnetron-sputtered rhenium oxide coating. *Fig. 5.14* shows ReS_2 shell converted at 750°C which still

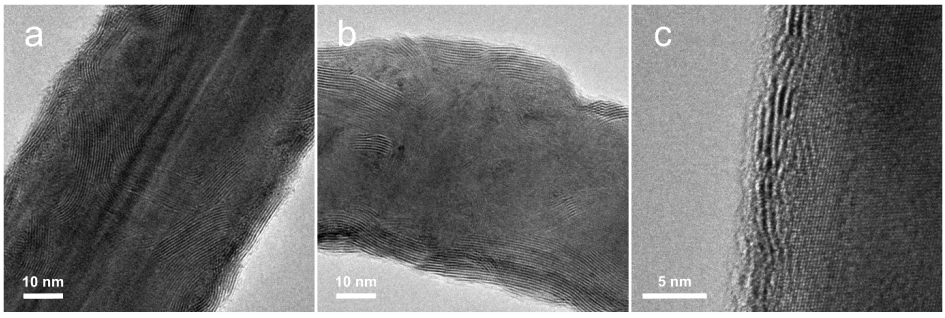

Figure 5.14. TEM images of GaN-ReS_2 *core-shell* NWs annealed at 750°C that shows the polycrystalline nature of ReS_2 shell.

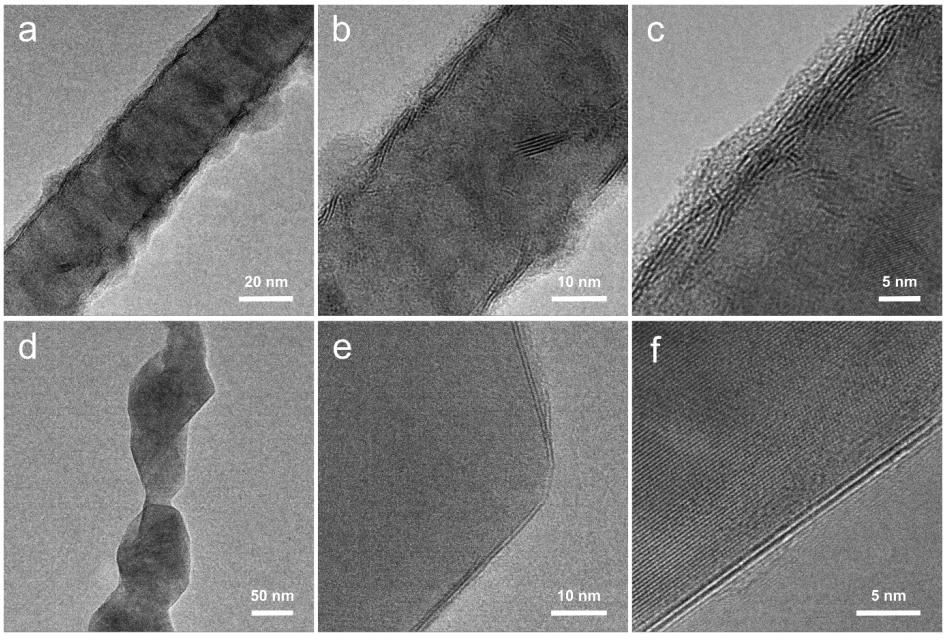

Figure 5.15. TEM images of ZnO-ReS_2 *core-shell* NWs annealed at (a-c) 700°C and (d-f) 750°C. A highly crystalline ReS_2 shell is obtained starting from 750°C, however, at this temperature also the conversion and recrystallization of ZnO NW core to ZnS phase occurs.

exhibits polycrystalline nature indicated by non-parallel placement of the layers while the TEM images in *Fig. 5.13* shows high crystallinity at 800°C. On the other hand, in the case of ZnO NWs, a structural change of the NW can be observed around 750°C, therefore a further study was performed. *Fig. 5.15* shows TEM images of ZnO-ReS_2 NWs converted at 700°C and 750°C. It is clearly seen that at 700°C the ReS_2 is still polycrystalline, whereas it becomes single-crystalline at higher temperatures, while the ZnO core re-crystallizes at 750°C. Evidently, ZnO NWs undergo a sulfurization process at this temperature and are converted to ZnS phase [153,154]. Worth noting, that no detectable formation of ZnS phase at 800°C was observed in previously discussed ZnO-WS_2 *core-shell* NWs due to the unique growth mechanism of the WS_2 shell [144].

To confirm the presence of phases in the as-grown *core-shell* NW samples, XRD measurements were performed on the nanowire arrays (converted at 800°C) on Si(100)/SiO_2 substrates (see *Fig. 5.16*). All XRD patterns contain a strong ReS_2 (002) peak of the triclinic phase (ICDD-PDF #52-0818) as well as Bragg peaks attributed to the Si(100) substrate at 33 degress and gold nanoparticles used for VLS growth (ICDD-PDF #04-0784). For GaN-ReS_2 and ZnS-ReS_2 NW samples, GaN (ICDD-PDF #50-0792) and ZnS (ICDD-PDF #36-1450) Bragg peaks are clearly apparent. For ZnO-ReS_2 NWs samples, both ZnO (ICDD-PDF #36-1451) and ZnS phases are present, confirming that ZnO NWs are partly or fully converted to ZnS above 750°C as was observed in TEM measurements. Worth noting, that the ratio between ReS_2 and nanowire XRD peak intensity is related not only to the amount of ReS_2 on the NWs, but also on the Si(100)/SiO_2 substrate, thus it cannot be properly used to quantitatively describe the phase composition ratio of the *core-shell* heterostructures. As the ZnO NWs undergo sulfurization process before single-crystalline ReS_2 shell is formed, such material might not be

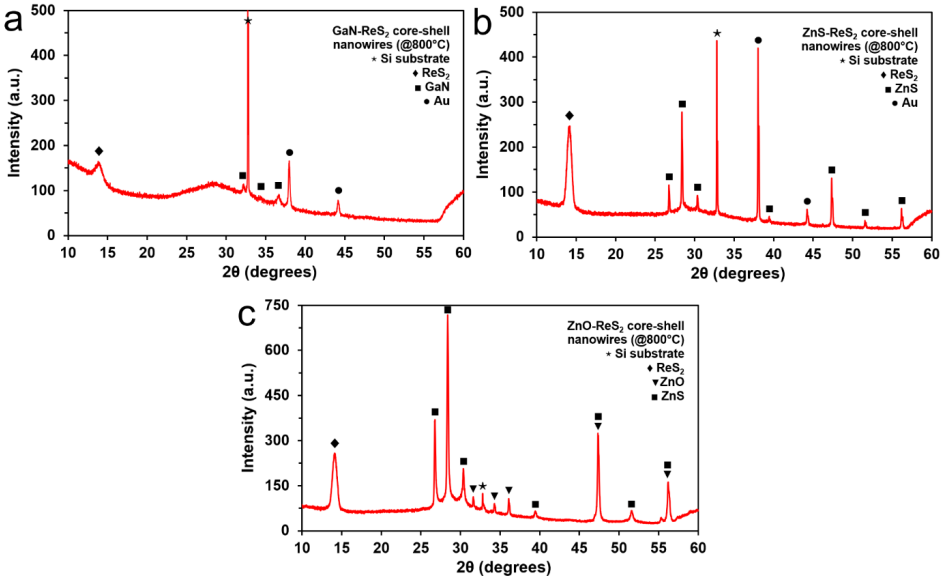

Figure 5.16. XRD patterns of as-grown (a) GaN-ReS_2, (b) ZnS-ReS_2, and (c) ZnO-ReS_2 *core-shell* NW arrays on Si(100)/SiO_2 substrates, prepared at 800°C. Note the ZnS phase peaks in ZnO-ReS_2 pattern that emerges due to a partial or full conversion of ZnO to ZnS which starts at around 750°C.

suitable template for ReS_2 growth, whilst it was possible to grow high-quality single-crystalline layers of ReS_2 on GaN and ZnS NWs.

To confirm the presence of ReS_2, micro-Raman scattering spectra of as-grown ZnO-ReS_2, ZnS-ReS_2 and GaN-ReS_2 *core-shell* NWs (measured in each case from a single NW) are compared to that of bulk ReS_2 in *Fig. 5.17*. ReS_2 Raman active modes are indicated by the vertical lines. All the Raman active phonon modes were observed in bulk ReS_2 and *core-shell* NWs. The Raman bands are narrower for bulk ReS_2 and GaN-ReS_2 NW, whereas they are slightly broadened for ZnO-ReS_2 and ZnS-ReS_2 NWs. The broadening leads to an overlap of nearest bands located around 280 cm^{-1}, 307 cm^{-1} and 322 cm^{-1}. The most intense bands (E_g-like modes) are located at about 152 cm^{-1}, 163 cm^{-1} and 213 cm^{-1} and mainly involve in-plane vibrations of Re atoms [155].

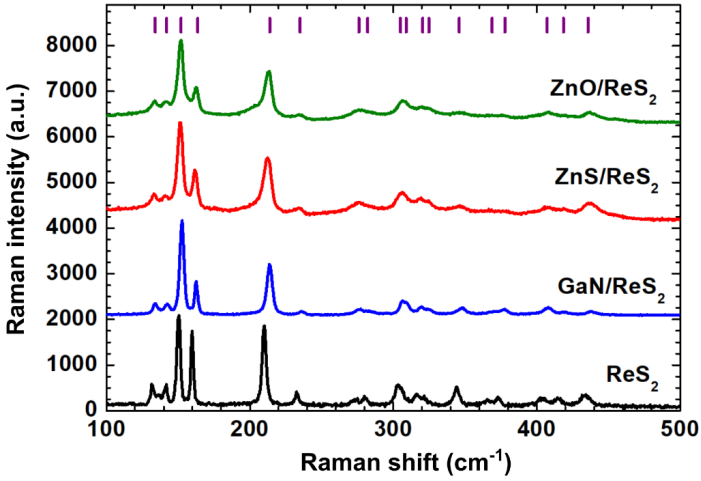

Figure 5.17. Micro-Raman spectra of ZnO-ReS_2, ZnS-ReS_2 and GaN-ReS_2 *core-shell* NWs, prepared at 800°C, and bulk ReS_2. Vertical lines indicate the positions of the Raman active A_g phonon modes.

5.2.2 ReS_2 reference sample

ReS_2 thin film on Si(100)/SiO_2 substrate, prepared the same way as on NWs, was taken as a reference sample. XRD measurements were performed on as-prepared ReS_2 thin films samples to investigate the degree of crystallinity at a wider range of sulfurization temperatures. *Fig. 5.18* shows XRD patterns of ReS_2 thin films, converted at 450°C, 700°C and 1000°C. Evolution of the ReS_2 (002) peak at 14.6 degrees with increasing temperature can be clearly seen from the patterns, as well as (004) and (006) peaks can be distinguished at very high temperatures [152], therefore, confirming that the conversion of a rhenium oxide film in sulfur vapour is a viable method how to obtain crystalline ReS_2 thin films. The Bragg peak at 33 degrees is attributed to the diffraction at the SiO_2/Si(100) substrate, and no other phases were observed. XRD measurements indicate that a small amount of crystalline ReS_2 phase starts to appear even at 450°C, however, the conversion rate becomes more significant only at around 700°C. Furthermore, micro-Raman spectrum of the thin film reference sample (converted at 700°C) was measured (see *Fig. 5.19*). The most intense ReS_2 Raman bands at around 152 cm^{-1}, 213 cm^{-1} and 307 cm^{-1} can be observed, similarly to the *core-shell* NWs spectra.

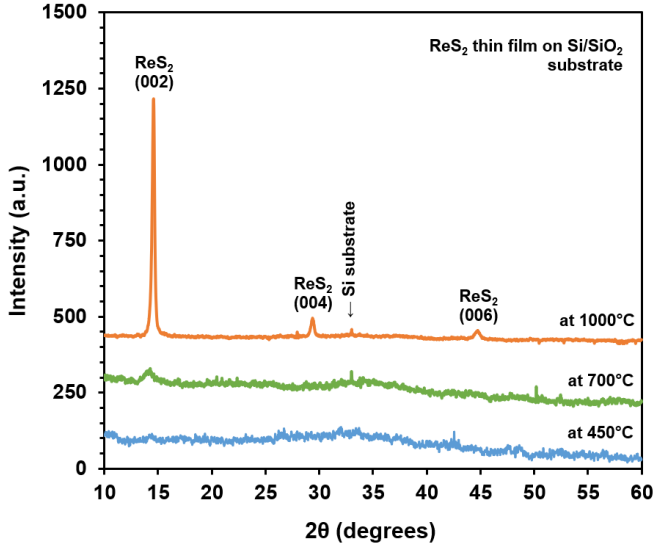

Figure 5.18. XRD patterns of ReS_2 thin films on Si(100)/SiO_2 substrates converted from magnetron-sputtered rhenium oxide at 450°C, 700°C and 1000°C.

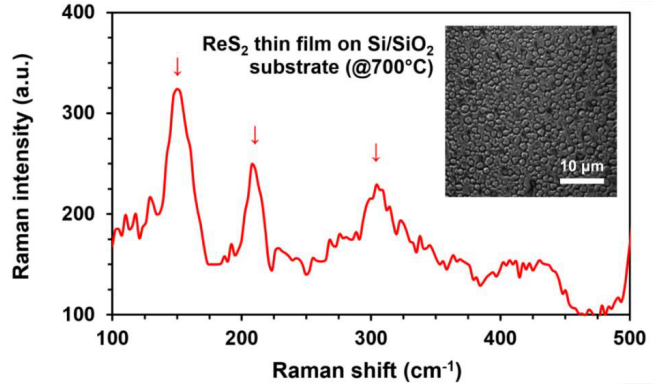

Figure 5.19. Micro-Raman spectrum of ReS_2 thin film on Si(100)/SiO_2 substrate converted from magnetron-sputtered rhenium oxide at 700°C. Arrows indicate the positions of the observed Raman active A_g phonon modes. The inset shows a confocal microscope image of the studied thin film.

5.3 Molybdenum disulfide MoS_2

MoS_2 might be the most popular and well-studied 2D TMD [9]. Bulk MoS_2 has a 1.2 eV indirect bandgap while its monolayer has a direct bandgap of 1.8 eV [17]. It has relatively good mobility (~700 $cm^2V^{-1}s^{-1}$), therefore, it has been widely studied for applications in electronics and optoelectronics. 2D monolayer MoS_2 has been obtained using quite a few different methods, most relevant to this work being CVD, conversion of MoO_3 and thermal

decomposition of $(NH_4)MoS_4$ [42]. In this work, first time synthesis of ZnO-MoS_2 *core-shell* NWs, where ZnS interlayer is formed between ZnO and MoS_2, was demonstrated [153]. The process involves immersion of pure ZnO NWs in ammonium heptamolybdate tetrahydrate solution followed by annealing in sulfur atmosphere at 700°C. More technical details are given in *Appendix A*.

5.3.1 ZnO-MoS_2 *core-shell* nanowires

SEM was used to tune the NW growth process and to observe the morphology change after MoS_2 shell growth. It is clearly visible in *Fig. 5.20(a,b)* that the smooth surface of ZnO NWs immersed in the ammonium heptamolybdate solution becomes significantly more rough and altered (see *Fig. 5.20(c,d)*) after annealing. The NW length is maintained after the heat treatment. Strong electrical charging was observed for the *core-shell* NWs, however was absent for pure ZnO NWs. This may indicate that electrical properties of ZnO NWs were strongly affected by a shell layer, making them less conductive. It is known that sulfur reacts with ZnO at temperatures above 400°C resulting in a formation of ZnS phase [154], which has the value of the bandgap (3.7 eV) larger than ZnO (3.4 eV).

TEM images of *core-shell* NWs annealed in sulfur atmosphere at 500°C and 700°C are shown in *Fig. 5.21*. Sample annealed at 500°C has a polycrystalline shell with some remaining amorphous phase. No MoS_2 shell was found around the NW, however, few crystallites appearing as parallel black lines (*Fig. 5.21(c)*) may be identified as MoS_2. The shell in the

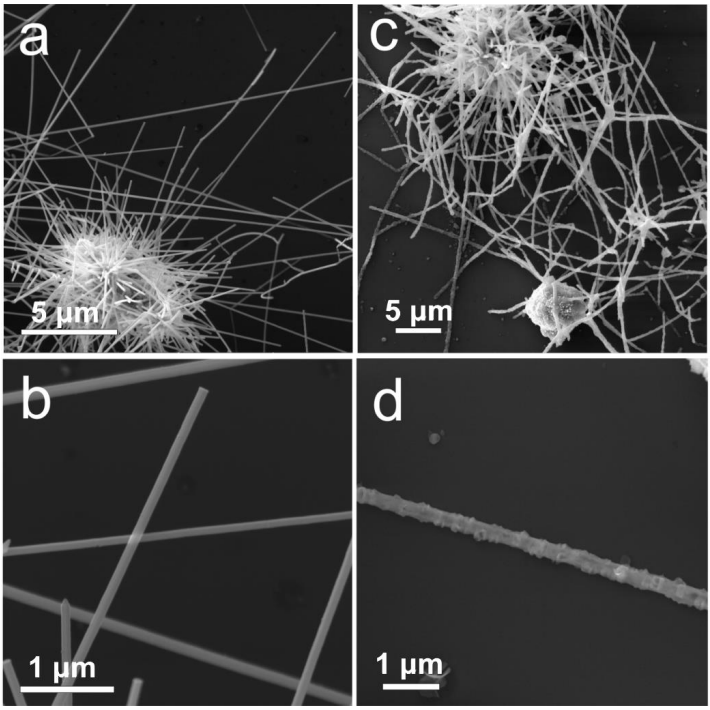

Figure 5.20. SEM images of (a,b) ZnO NWs, immersed in ammonium heptamolybdate solution and dried; (c,d) ZnO-MoS_2 *core-shell* NWs after annealing in sulfur atmosphere at 700°C.

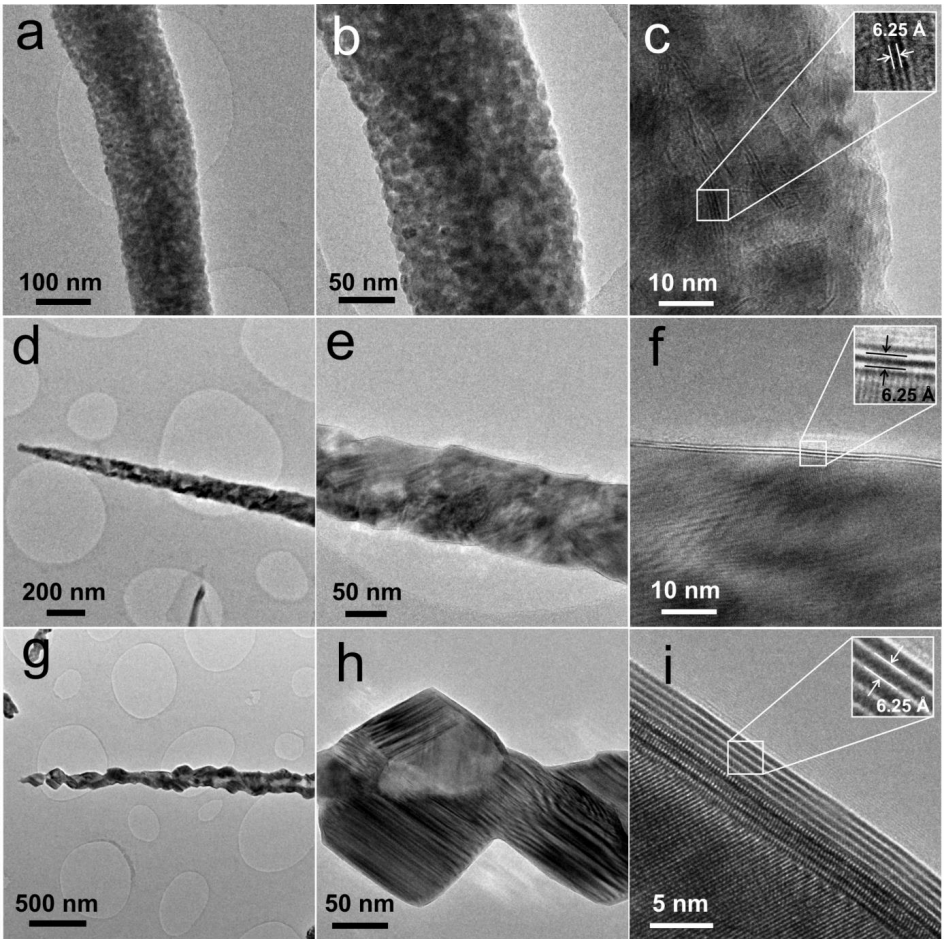

Figure 5.21. TEM images at different magnifications of ZnO-MoS_2 *core-shell* NWs, prepared at (a-c) 500°C and (d-i) 700°C. The insets show the measured atomic interlayer distances between MoS_2 layers.

sample annealed at 700°C is non-homogeneous and appears as a mosaic of dark and bright spots (*Fig. 5.21(d,e)*) or as microcrystals formed around the NW core (*Fig. 5.21(g,h)*). According to interplanar distance measurements, microcrystals on NW surface can be attributed to zincblende ZnS phase with the interplanar distance d=3.1-3.2 Å (ICDD-PDF #36-1450). It is known that ZnO reacts with sulfur and forms ZnS starting from 400°C. Due to the lattice mismatch and different crystal structure of ZnO core and ZnS shell, the upper layer cannot grow as a smooth single crystal layer on top of ZnO NW surface. Furthermore, NWs prepared at 700°C are coated by few layers of MoS_2, which appears as a number of parallel black lines (*Fig. 5.21(f,i)*). The number of MoS_2 layers varies in the range of 1-8 monolayers, which is probably related to nonhomogeneous coating by ammonium molybdate precursor. The measured distance between monolayers is about 6.25 Å, which corresponds well to 6.2-6.3 Å interlayer distance in MoS_2 (ICDD-PDF #37-1492).

SAED analysis of the *core-shell* NW (see *Fig. 5.22*) revealed the following phases: ZnO zincite (zone axis <0001>), ZnS zincblende (zone axis <001>), and MoS_2 molybdenite phases (zone axis <-2201> and <14-53>). Dominating (the most intensive) diffraction spots belong to the ZnO core, while less intensive to ZnS and MoS_2 phases. Symmetric orientation of MoS_2 reflexes relative to ZnO reflexes may indicate epitaxial growth of MoS_2.

Micro-Raman spectroscopy was used to confirm the formation of MoS_2 layers on the NWs. The in-plane E^1_{2g} mode at 384 cm^{-1} and the out-of-plane A_{1g} mode at 407 cm^{-1} were clearly resolved on the *core-shell* NW (see *Fig. 5.23*) that corresponds to typical MoS_2 Raman

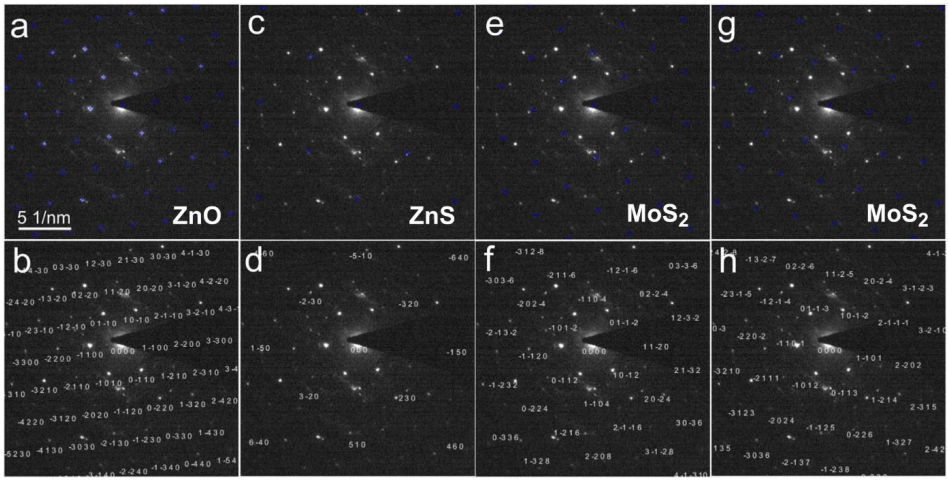

Figure 5.22. SAED analysis of ZnO-MoS_2 *core-shell* NWs. The presence of (a,b) ZnO zincite zone axis ⟨0001⟩, (c,d) ZnS zincblende zone axis ⟨001⟩, MoS_2 molybdenite phases of (e,f) zone axis ⟨−2201⟩ and (g, h) zone axis ⟨14–53⟩ were identified.

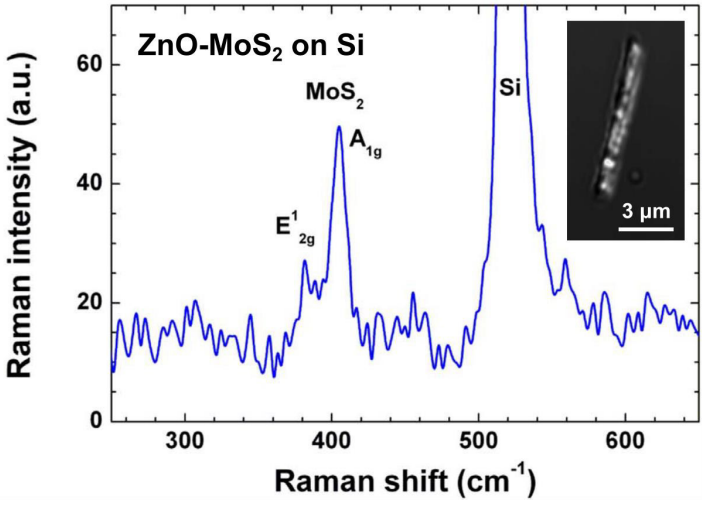

Figure 5.23. Micro-Raman spectra of ZnO-MoS_2 *core-shell* NW on Si(100)/SiO_2 substrate. The inset shows a confocal microscope image of the studied NW.

spectra [156], and also matches the 2D MoS_2 microcrystal reference sample. Note that the large peak at ~521 cm^{-1} is the first order of optical mode at k=0 of the underlying silicon substrate.

Alternatively, MoO_3 sacrificial layer was deposited on pure ZnO NWs by reactive DC magnetron sputtering, similar to ZnO-WS_2 *core-shell* NW preparation method discussed previously. After sulfurization of ZnO-MoO_3 NWs at 700°C, morphology of thus obtained *core-shell* NWs is rather similar to the ones produced by immersion in ammonium heptamolybdate solution (see SEM images in *Fig. 5.24(a,b)*). However, MoS_2 shell is usually significantly thicker due to the large amount of deposited MoO_3 precursor (it is difficult to deposit very thin layer of MoO_3 by magnetron sputtering), therefore, the immersion method of molybdenum precursor deposition is more preferable in this case compared to the magnetron sputtering. Nevertheless, TEM image (see *Fig. 5.24(c)*) shows that it is still a viable method how to obtain few-layer MoS_2 on NWs but with less uniformity.

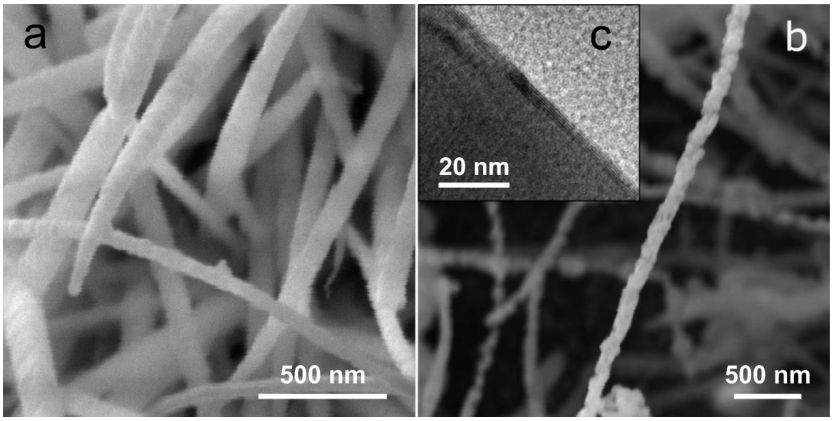

Figure 5.24. SEM images of (a) ZnO-MoO_3 *core-shell* NWs, where the shell has been deposited by magnetron sputtering, (b) ZnO-MoS_2 *core-shell* NWs after annealing in sulfur atmosphere at 700°C. (c) TEM image of the as-prepared *core-shell* NW.

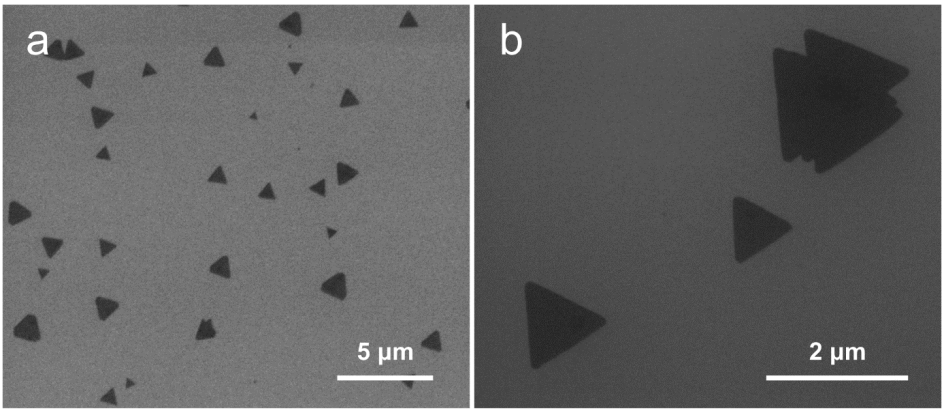

Figure 5.25. SEM images at different magnifications of 2D MoS_2 microcrystals on Si(100)/SiO_2 substrate.

5.3.2 MoS_2 reference sample

2D MoS_2 flake reference sample was synthesised via the CVD method, as described in *Appendix A*, to compare the Raman spectrum with the one of a ZnO-MoS_2 *core-shell* NW. The triangular 2D MoS_2 microcrystals (see SEM images in *Fig. 5.25*) exhibit the same Raman E^1_{2g} mode at 384 cm^{-1} and A_{1g} mode at 407 cm^{-1} (see *Fig. 5.26*) as the *core-shell* NWs, thus confirming the presence of few-layer MoS_2 on the NWs.

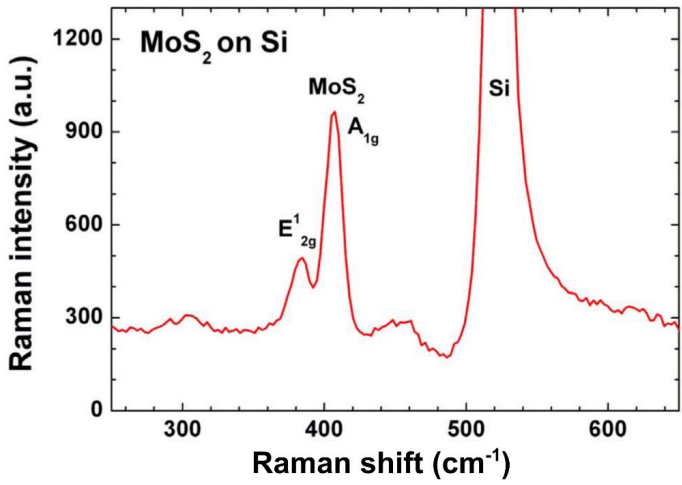

Figure 5.26. Micro-Raman spectra of 2D MoS_2 microcrystals on Si(100)/SiO_2 substrate.

5.4 Lead iodide PbI_2

PbI_2 is a layered vdW material with a similar structure and physical properties as TMDs, however, it is not a TMD but has iodine atoms instead of chalcogens. It is a semiconductor material with a direct 2.2–2.55 eV bandgap and can be used as a photodetector or as an X-ray and γ-ray detector material [157,158]. There are theoretical and experimental studies that show band structure shift from direct bandgap to indirect bandgap when the PbI_2 thickness is reduced from bulk to monolayer [26], as opposed to other more commonly studied vdW materials. Therefore, monolayer PbI_2 is not expected to be an efficient material for optoelectronics applications. Few-layer PbI_2 flakes can be synthesised in a liquid phase [159] or via CVD process [157,160]. In this work, a novel two-step growth process for uniform crystalline PbI_2 nanosheets via reactive magnetron deposition of a lead oxide film followed by subsequent iodination at 420°C to PbI_2 on a ZnO NW substrate was demonstrated, and as-grown hybrid nanostructures were compared with ones prepared via thermal evaporation method [161]. More technical details are given in *Appendix A*. Few-layer PbI_2 did not uniformly cover all surface of NWs, therefore, such heterostructures are not called *core-shell* NWs but PbI_2-decorated NWs instead.

5.4.1 PbI_2-decorated ZnO nanowires

SEM was used to image as-grown individual NWs and NW arrays and study their morphology. Pure ZnO NWs are typically 20–30 μm long with a diameter around 100 nm and exhibit a smooth surface. *Fig. 5.27(a,b)* shows ZnO NWs with a thermally deposited PbI_2 coating. No significant change in diameter is observed; however, a very fine increase in surface roughness is visible. NWs with a sputter-deposited lead oxide coating with a fine roughness are shown in *Fig. 5.27(c,d)*, where a considerable (up to 100 nm) increase in diameter can be seen. After annealing such NWs in iodine vapour at elevated temperatures, the surface roughness greatly increased; however the diameter is significantly reduced as a fraction of the coated material is sublimated after the transformation (see *Fig. 5.27(e,f)*). The final coating is not uniform over the entire length of NWs as some thicker particles and islands can be observed.

A deeper insight into the nanostructures' inner structure was obtained using TEM. *Fig. 5.28(a–c)* shows TEM images of ZnO-PbI_2 NWs obtained by the thermal evaporation method at different magnifications. The lower resolution images show noticeable contrast between the two NW sides (PbI_2 layers correspond to the darker region), indicating non-uniform coating deposition, which is expected from the thermal evaporation approach since it is a line-of-sight method. At a high resolution, the crystalline structure of the nanostructure is revealed. The layers of PbI_2 grown on the ZnO NW surface are distinguishable as parallel black lines. Typically, the thickness of the coating varies between 5–10 monolayers (each consisting of I-Pb-I atomic planes), with interlayer distance measured around 7 Å, which is in a good agreement with the lattice constant (a = 6.979 Å) of bulk hexagonal PbI_2 (ICDD-PDF #07-0235). Furthermore, the single-crystalline nature of the ZnO NWs is clearly visible; the

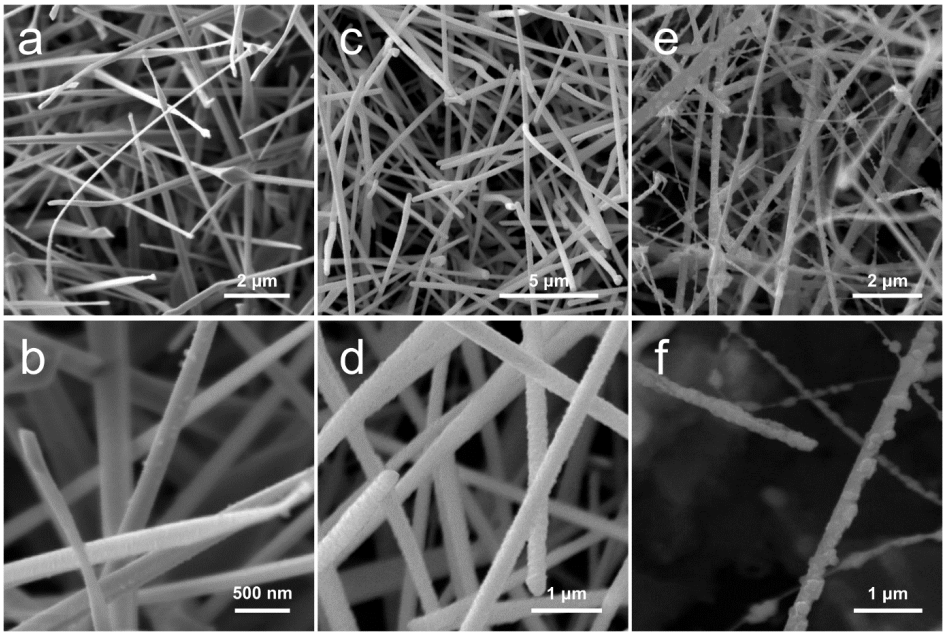

Figure 5.27. SEM images of images of (a,b) ZnO-PbI_2 NWs made by using the thermal evaporation approach; (c,d) ZnO NWs covered by lead oxide deposited by magnetron sputtering; (e,f) ZnO-PbI_2 NWs made by converting the lead oxide coating.

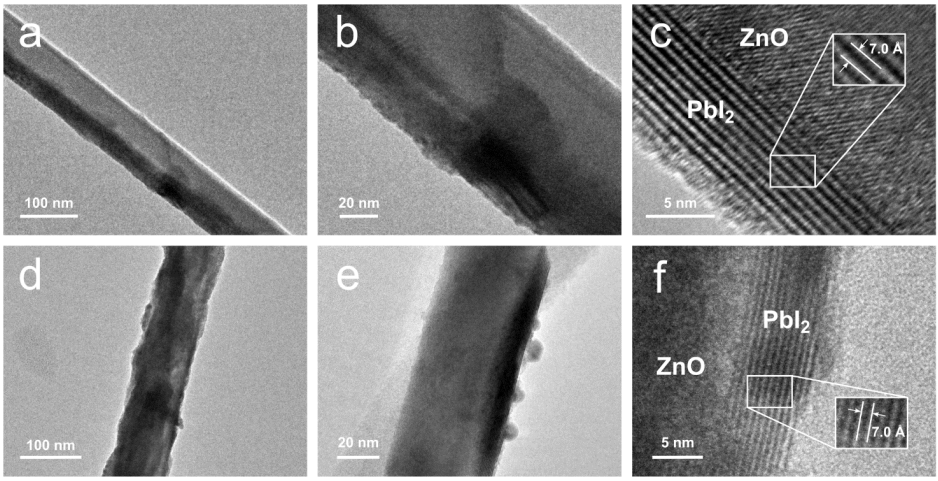

Figure 5.28. TEM images at different magnifications of (a-c) ZnO-PbI_2 NWs made by using the thermal evaporation approach, and (d-f) ZnO-PbI_2 NWs made by converting the magnetron-sputtered lead oxide coating. The insets show the measured atomic interlayer distances between PbI_2 layers.

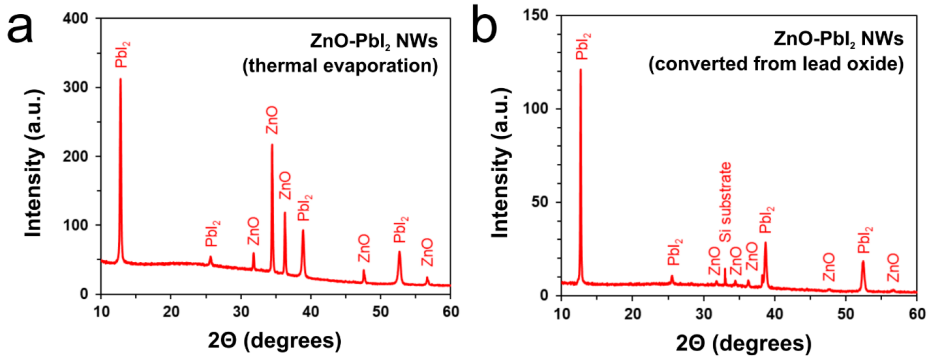

Figure 5.29. XRD patterns of (a) ZnO-PbI_2 NW arrays on Si(100)/SiO_2 substrate made by using the thermal evaporation approach; (b) ZnO-PbI_2 NW arrays on Si(100)/SiO_2 substrate made by converting the magnetron-sputtered lead oxide coating.

measured interplanar distance is 2.8 Å, corresponding to hexagonal ZnO wurtzite (ICDD-PDF #36-1451). The TEM images of the ZnO-PbI_2 nanostructures obtained by conversion of sputter-deposited lead oxide coating are shown in *Fig. 5.28(d–f)*. In this case, the PbI_2 coating is uniformly distributed over the entire ZnO NW surface; however, the surface roughness is significantly increased. The thickness of the coating typically varies between 5–15 monolayers, with some islands being even thicker. As in to the first approach, the measured interlayer distance is around 7 Å.

To complement TEM structural investigations and confirm the presence of phases, XRD measurements were performed on the as-prepared samples. *Fig. 5.29* shows XRD patterns of NW arrays prepared by the two approaches: thermal evaporation and converting the magnetron-

sputtered lead oxide coating, respectively. Both patterns indicate highly crystalline hexagonal ZnO wurtzite (ICDD-PDF #36-1451) and hexagonal PbI_2 (ICDD-PDF #07-0235) phases. No other phases were observed, confirming the high crystallinity of the as-prepared nanostructures, as did the TEM investigations. It is worth noting that the ratio between PbI_2 and ZnO peak intensity is not only related to the amount of PbI_2 on ZnO NWs but also the amount of PbI_2 crystallites on the Si/SiO_2 substrate. Therefore, spectra cannot be properly used to describe the phase composition ratio in the nanostructures. Furthermore, ZnO NW Bragg peak intensities vary between the samples - due to an inhomogeneous gold nanoparticle catalyst deposition from colloid on the silicon substrate; the density of as-grown ZnO nanowires arrays was also not homogeneous while the PbI_2 layer is relatively homogeneous over the substrate due to the precisely controllable deposition method. In *Fig. 5.29(b)*, the Bragg peak at 33° is attributed to diffraction in the Si(100) substrate (forbidden Si(200) reflection).

To study the optical properties, room temperature PL in the as-prepared samples was measured in a wavelength range from 400 to 650 nm, excited by a 266 nm laser. Generally, PbI_2 has a direct band-to-band transition at around 495 nm (~2.5 eV) [162]; however, a broad band peaked at 510–525 nm has been previously observed and attributed to recombination through defects, such as iodine and lead vacancies [157]. The PL spectrum of pure ZnO NWs exhibits a defect-related band at ~520 nm [147]. Therefore, the interpretation of the ZnO-PbI_2 nanostructure spectra might be ambiguous due to this ZnO and PbI_2 PL band overlapping, since higher ZnO PL intensities might lead to indistinguishable PbI_2 PL peaks or vice versa. *Fig. 5.30* depicts the measured PL spectra of pure ZnO NWs, the PbI_2 thin film reference sample, and the ZnO-PbI_2 nanostructures prepared via both approaches. It is worth noting that the PL intensity is depicted in arbitrary units and does not contain information about the relative intensities between the obtained spectra. The ZnO NW spectrum exhibits the typical defect band at 520 nm and the PbI_2 thin film sample (prepared by converting lead oxide film) shows two emission

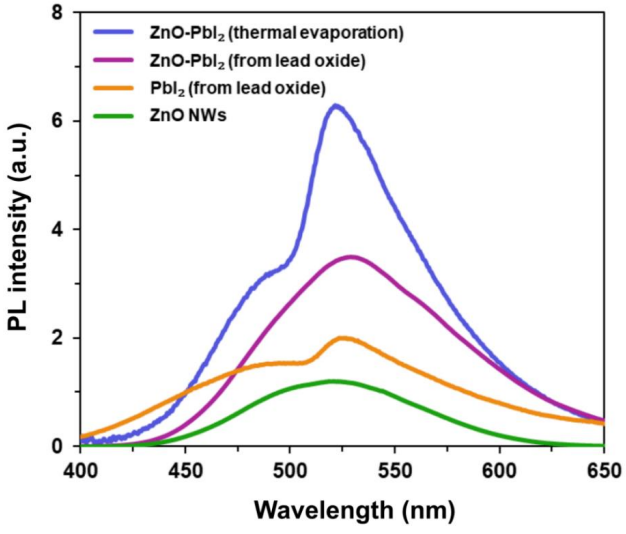

Figure 5.30. Room-temperature photoluminescence spectra at the excitation wavelength of 266 nm of the different as-prepared samples.

peaks: the direct band-to-band transition at around 495 nm and the defect-related band at around 530 nm. The ZnO-PbI_2 nanostructures (prepared by thermal evaporation approach) exhibit two peaks at 495 nm and 525 nm; however, the nanostructures prepared via lead oxide conversion exhibit only one band with a peak at 530 nm due to the higher intensity overlapping ZnO peak. One can see and interpret the difference between the PbI_2 peak ratio for samples prepared with different methods due to the defect-related peak maximum shift. For example, the defect/band-to-band peak intensity ratio for thermally evaporated PbI_2 is ~2, while for lead oxide converted PbI_2, it is ~1.33. Therefore, by also considering the ZnO peak contribution, one can qualitatively assume that lead oxide conversion via iodination leads to fewer defects in PbI_2 coatings than the thermal evaporation approach.

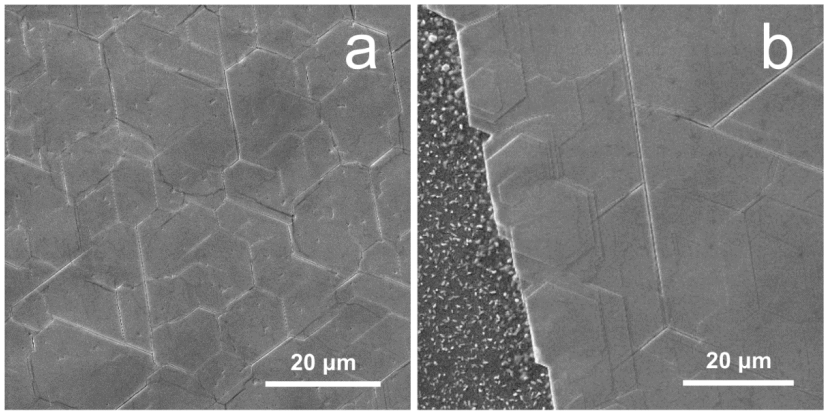

Figure 5.31. SEM images of PbI_2 thin film on Si(100)/SiO_2 substrate made by converting a lead oxide film.

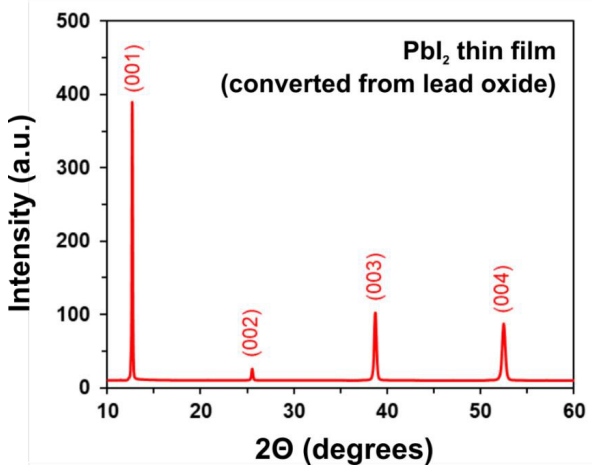

Figure 5.32. XRD pattern of PbI_2 thin film on Si(100)/SiO_2 substrate made by converting a lead oxide film.

5.4.2 PbI_2 reference sample

As a reference sample for comparison, a PbI_2 thin film on SiO_2/Si substrate was prepared using iodination of a sputter-deposited lead oxide coating. SEM images of the reference sample are shown in *Fig. 5.31*. The film exhibits hexagonal domains, presumably highly crystalline as PbI_2 typically crystallizes in a hexagonal structure. The XRD pattern of the reference sample confirms its highly crystalline structure (see *Fig. 5.32*), showing that the conversion of a lead oxide film in iodine vapour is a viable method how to obtain crystalline PbI_2 thin films. As discussed before, room-temperature PL spectrum of the reference sample was also measured (see *Fig. 5.30*).

5.5 Single nanowire photodetectors

To demonstrate the applicability of the developed NW heterostructures in optoelectronics, two-terminal single-NW photodetector devices were fabricated for the most perspective nanostructures. The selection was based on the structural and composition studies. The device fabrication and characterization procedures were previously described in *Chapters 4.5* and *4.6*. A typical as-fabricated device is shown in *Fig. 5.33*, where a single NW is placed between gold microelectrodes. At least five single-NW photodetectors for each material or synthesis method were fabricated so that consistent conclusions could be made.

To characterize such devices, dark state I_{ds}-V_{ds} curves, dark current, current enhancement ratio I_{on}/I_{off}, rise and decay photoresponse time, spectral responsivity R_λ and external quantum efficiency EQE were determined; devices were measured at 405, 532 and 660 nm wavelength light illumination and usually at 1V bias voltage. Stability and reversibility of on-off measurements was also evaluated. Rise and decay time of NW devices is defined as the required time for the photocurrent to increase or decrease to 90% or 10% of its maximum value, respectively. R_λ and EQE are used to evaluate photoconductive properties of a material - R_λ and EQE are respectively defined as $R_\lambda = \Delta I/(PS)$ and $EQE = hcR_\lambda/(e\lambda)$, where ΔI is the difference between the photocurrent I_{on} and the dark current I_{off}, P is the light power density, S is the effective illumination area (estimated as the NW length between contacts × NW diameter), h is Planck's constant, c is the speed of light, e is the electron charge and λ is the light wavelength. Large R_λ and EQE values correspond to high photodetector sensitivity.

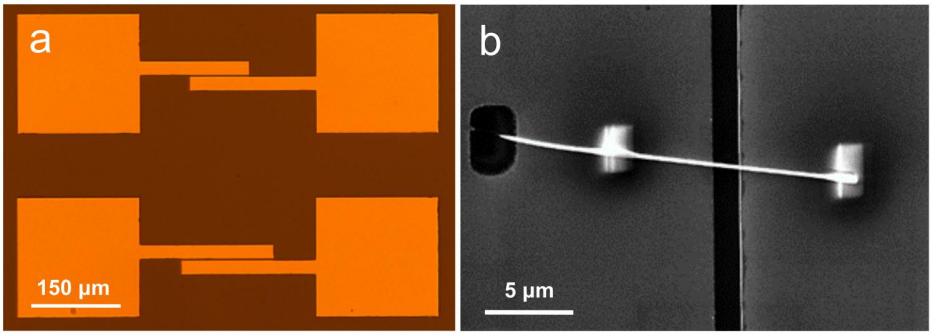

Figure 5.33. (a) Optical microscope image of gold microelectrodes on an oxidized silicon substrate; (b) SEM image of a typical as-prepared nanowire photoresistor.

5.5.1 PbS, In_2S_3, CdS and ZnSe nanowire photodetectors

Firstly, the method of single-NW device fabrication and characterization was developed and tested on pure metal chalcogenide NWs [163]. A study of such pure NW devices is necessary in order to better understand the photoelectric behaviour of more complicated *core-shell* systems afterwards. The synthesis details of the studied PbS, In_2S_3, CdS and ZnSe NWs can be found in *Appendix A*, and some characterization data in *Fig. B2* in *Appendix B*.

Fig. 5.34 shows the measured I_{ds}-V_{ds} curves of different as-prepared NW devices. Typically, nearly symmetrical characteristics were obtained for all investigated NW materials, therefore, indicating that ohmic contacts were formed between the electrodes and the NW. Features of non-linear quadratic ($I \sim V^2$) behaviour of the I-V curves may be interpreted as an effect of the space-charge limited current (SCLC), as other groups have previously shown in different material nanowires [164,165]. In addition, it is worth noting that as-fabricated devices exhibit high resistance, wherein, most probably a considerable part arises due to the contacts. Possible causes of such increased resistance include high resistance of deposited Pt contacts due to a carbon presence from the metal-organic precursor [166].

Next, as-prepared NW device electrical response to an illumination of a light at different wavelengths was investigated. On-off photoresponse measurements, which are based on photoinduced conductivity changes, for three different illumination wavelengths at V_{ds}=1V bias of as-prepared NW photodetector devices are depicted in *Fig. 5.35*. It can be seen that all four studied NW materials exhibit rapid (< 1 second, in most cases) increase and decrease of the current after the illumination is turned on or off, respectively, except in the case of the In_2S_3

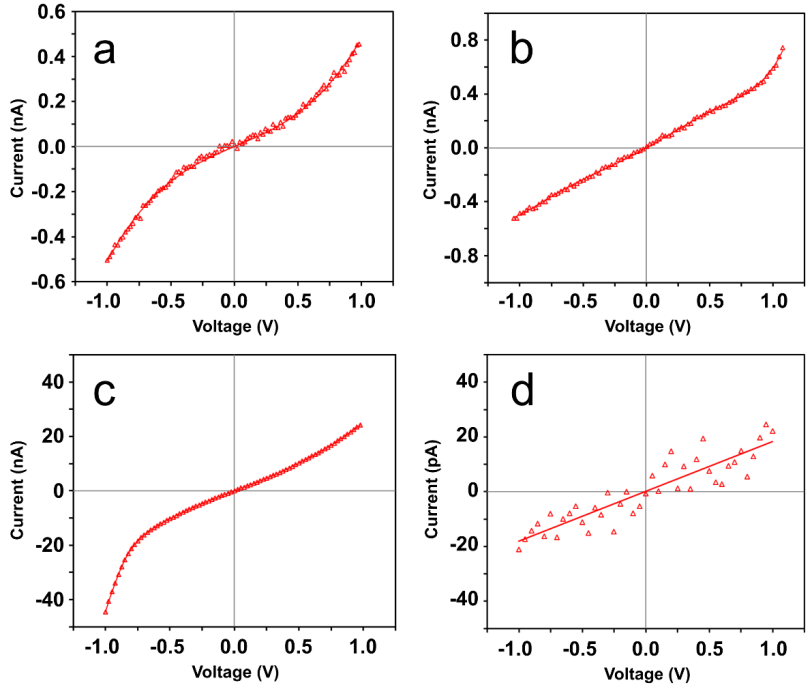

Figure 5.34. Dark-state I_{ds}-V_{ds} characteristics of (a) PbS, (b) In_2S_3, (c) CdS and (d) ZnSe NW photodetectors.

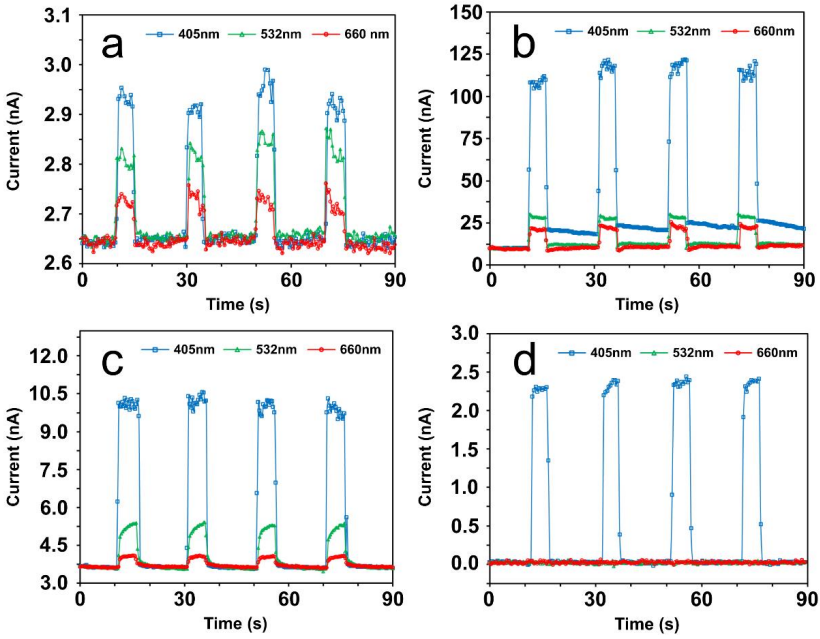

Figure 5.35. On-off photoresponse measurements of (a) PbS, (b) In_2S_3, (c) CdS and (d) ZnSe nanowire photodetectors at V_{ds} = 1 V bias voltage and 0.5 W/cm^2 light intensity of 405 nm, 532 nm and 660 nm wavelength light illumination.

NW current decay time for 405 nm illumination, which features a second, slower time component, most probably do to a presence of trapping centres.

Table 5.1 shows the comparison of current enhancement ratios (I_{on}/I_{off}) of the studied NW materials in the context of their respective bandgap, which determines their cut-off wavelengths. Firstly, it can be seen that PbS NWs exhibit weak (I_{on}/I_{off} close to 1) photoresponse to all three illumination wavelengths; however, linear ratio vs. wavelength dependence was observed. Secondly, In_2S_3 and CdS NWs exhibit strong photoresponse to 405 nm illumination, and significantly weaker one to 532 nm and 660 nm illumination. Finally, ZnSe NWs show very strong response to 405 nm light, and no photoresponse was observed while illuminating them with 532 nm and 660 nm wavelength light. Obtained I_{on}/I_{off} value tendencies, for the most part, are as was anticipated from the material bandgap values; however, relatively weaker photoresponse to 660 nm illumination was expected for either CdS or In_2S_3

Table 5.1. Comparison of the photoresponses of the studied single-nanowire photodetectors.

Materials	**E_g (eV)**	**I_{dark} at 1V (nA)**	**I_{on}/I_{off} ratio**		
			at 405 nm (3.06 eV)	**at 532 nm (2.33 eV)**	**at 660 nm (1.88 eV)**
PbS NW	0.41	2.65	1.11	1.07	1.03
In_2S_3 NW	2.1	9.95	11.3	2.8	2.1
CdS NW	2.4	3.65	2.7	1.4	1.1
ZnSe NW	2.7	0.02	115	1	1

NWs. Such above-cut-off-wavelength photosensitivity may be caused by defects, like impurity doping or surface states. *Table 5.2* contains the calculated R_λ and EQE values of the studied NW devices. The obtained data shows a relatively wide range of values for different NW materials, however, these values are comparable to other typical *state-of-art* 1D nanostructure photodetector [167], thus indicating the potential to use such materials in future applications.

Table 5.2. Responsivity R_λ and external quantum efficiency EQE values of the studied single-nanowire photodetectors at different illumination wavelengths.

Materials	Responsivity R_λ, A/W			EQE		
	at 405 nm	at 532 nm	at 660 nm	at 405 nm	at 532 nm	at 660 nm
PbS NW	0.06	0.04	0.02	18%	9%	3%
In_2S_3 NW	16.01	2.80	1.71	4903%	652%	321%
CdS NW	0.86	0.20	0.05	264%	47%	10%
ZnSe NW	0.20	0	0	62%	0	0

5.5.2 ZnO-WS_2 *core-shell* nanowire photodetectors

ZnO-WS_2 *core-shell* NW photoelectric properties were compared with the ones of pure ZnO NWs and few-layer WS_2 flakes. WS_2 flake photodetector preparation procedure is described in *Appendix A*. *Fig. 5.36(a-c)* shows measured typical current-voltage characteristics of photodetectors built using pure ZnO NWs, WS_2 flakes and ZnO-WS_2 *core-shell* NWs, respectively. The ZnO photodetector demonstrates a non-symmetric I_{ds}-V_{ds} curve and this is typical for Schottky barrier of ZnO NWs on gold contacts [168]. However, nearly symmetric characteristics were obtained for WS_2 flakes and ZnO-WS_2 NW devices.

On-off photoresponse measurements were performed at the bias voltage of 1V, laser wavelengths of 405, 532 and 660 nm and laser power of 0.5 W/cm^2. Typical photoresponse measurements of pure ZnO NW, WS_2 flake and ZnO-WS_2 *core-shell* NW devices are shown in *Fig. 5.36(d-f)*. Pure ZnO NWs respond only to the illumination of 405 nm wavelength and do not respond to wavelengths of 532 and 660 nm (*Fig. 5.36(d)*), while the photoresponse of WS_2 flakes is almost identical at wavelengths of 405, 532 and 660 nm (*Fig. 5.36(e)*). The photoresponse of ZnO-WS_2 *core-shell* NWs at 532 and 660 nm are similar, but the photoresponse is significantly stronger at 405 nm (*Fig. 5.36(f)*). Since pure ZnO NWs do not respond to green 532 nm (2.33 eV) and red 660 nm (1.88 eV) light because of their wide band gap (E_g=3.2–3.3 eV), the photoresponse of ZnO-WS_2 *core-shell* NWs to red and green light can be attributed to the WS_2 shell. For violet light (405 nm), both ZnO core and WS_2 shell contribute proportionally to the photoresponse of ZnO-WS_2 *core-shell* NWs.

Time-resolved photoresponse measurements are presented in *Fig. 5.36(g-i)*, and the corresponding data are given in *Table 5.3*. A slow response of pure ZnO NWs on the timescale of seconds is typical for this material [90,168]. In addition, the response time of WS_2 flakes depends on the material fabrication method and the number of WS_2 layers [169,170]. Perea-López et al. reported the response time of a few layer WS_2 photodetector as fast as 5.3 ms [169],

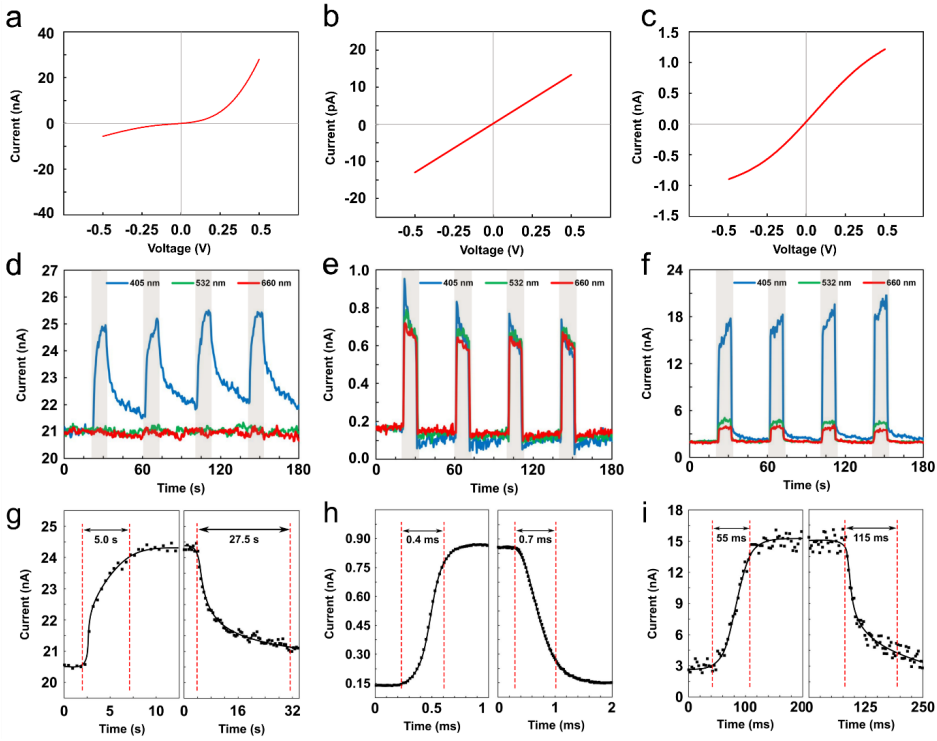

Figure 5.36. Dark-state I_{ds}-V_{ds} characteristics of (a) ZnO NW, (b) WS_2 flakes and (c) ZnO-WS_2 NW photodetectors. On-off photoresponse measurements of (d) ZnO NW, (e) WS_2 flakes and (f) ZnO-WS_2 NW photodetectors at V_{ds} = 1 V bias voltage and 0.5 W/cm^2 light intensity of 405 nm, 532 nm and 660 nm wavelength light illumination. Time-resolved photoresponse measurements of (g) ZnO NW, (h) WS_2 flakes and (i) ZnO-WS_2 NW photodetectors at V_{ds} = 1 V bias voltage and 0.5 W/cm^2 light intensity of 405 nm wavelength light illumination.

while Huo et al. reported the response time of a multilayer WS_2 photodetector to be faster than 20 ms [170]. The response time of the prepared ZnO-WS_2 *core-shell* NWs is significantly faster than that of ZnO-WS_2-based heterostructured thin film devices [171]. The calculated values of $R\lambda$ and *EQE* for the photodetectors are given in *Table 5.4*, and the obtained data are comparable

Table 5.3. Photoresponse (rise and decay) time of the studied photodetectors fabricated from pure ZnO NWs, WS_2 flakes and ZnO-WS_2 *core-shell* NWs.

λ, nm	ZnO NWs		WS_2 flakes		ZnO-WS_2 NWs	
	Rise, s	Decay, s	Rise, ms	Decay, ms	Rise, ms	Decay, ms
405	5	27.5	0.4	0.7	55	115
532	-	-	0.3	0.65	21	95
660	-	-	0.53	1.35	22	50

to other *state-of-the-art* ZnO nanowire- and WS_2 nanotube-based photodetectors. For example, Guo et al. demonstrated the high responsivity of a ZnO nanowire-based UV photodetector having 40 A/W; however, at 10 V bias the kinetics of the photodetector was measured in the range of seconds [168]. In contrast, Zhang et al. demonstrated a multiwall WS_2 nanotube-based photodetector with R_λ = 3.14 A/W (at 0.5 V bias) and *EQE* = 615% for 633 nm light [172].

The presence of WS_2 shell results in a modification of ZnO-WS_2 *core-shell* NW interface leading to a decrease of charge carrier trapping in ZnO NW. Comparing the positions of valence and conduction bands of ZnO and WS_2 shows that both electrons and holes should sink into the WS_2 shell [171] and serve as a charge carrier channel in ZnO-WS_2 heterostructure (*Fig. 5.37(a)*). This conclusion is supported by electronic density of states (DOS) calculated for the ZnO-WS_2 interface layer by means of density functional theory (DFT) [144,146]. The doping of the surface of NWs with sulfur is an initial stage of ZnO-WS_2 interface formation and it has a narrower band gap of 1.42 eV. The formation of an array of WS_2 bridges complete interface formation and makes its band gap even more narrow at 1.14 eV [144]. Therefore, according to DFT calculations the interface layer i-WS_2, bridging ZnO surface and WS_2 shell (see *Fig. 5.37(b)*), has even more narrow gap than WS_2 itself, leading to a formation of energy barrier able to prevent backward diffusion of charge carriers into ZnO NW.

Table 5.4. Responsivity R_λ and external quantum efficiency EQE values of the studied photodetectors fabricated from pure ZnO NWs, WS_2 flakes and ZnO-WS_2 *core-shell* NWs.

Parameters	λ, nm	ZnO NWs	WS_2 flakes	ZnO-WS_2 NWs
R_λ, A/W	405	1.50	5.03×10^{-4}	7.00
	532	-	4.84×10^{-4}	2.25
	660	-	4.58×10^{-4}	1.75
EQE, %	405	4.59	1.5×10^{-3}	21.4
	532	-	1.1×10^{-3}	5.2
	660	-	8.6×10^{-4}	3.3

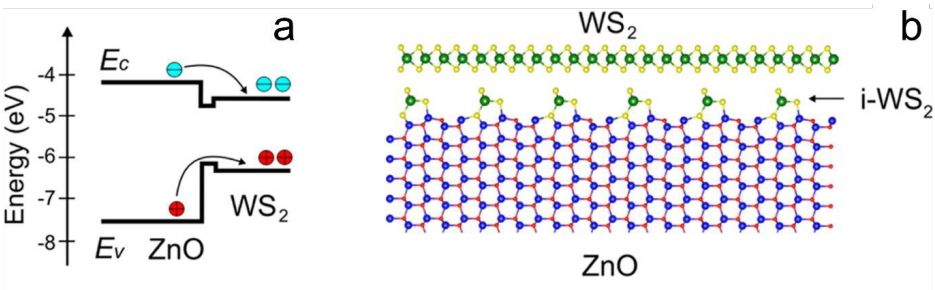

Figure 5.37. (a) A simplified band diagram of ZnO-WS_2 *core-shell* NW. (b) Atomic structure of ZnO-WS_2 interface.

5.5.3 PbI_2-decorated ZnO nanowire photodetectors

Photoelectric properties of PbI_2-decorated ZnO NWs prepared via reactive magnetron deposition of a lead oxide film followed by subsequent iodination to PbI_2 were investigated and compared to ones of hybrid nanostructures prepared via thermal evaporation method. *Fig. 5.38(a–c)* shows the characteristics of the two-terminal ZnO-PbI_2 single NW devices made using the thermal evaporation approach, while *Fig. 5.38(d–f)* shows the characteristics of the ZnO-PbI_2 single NW devices made by converting the magnetron-sputtered lead oxide coating. Both dark state current-voltage (I_{ds}-V_{ds}) characteristics of ZnO-PbI_2 NWs in *Fig. 5.38(a)* and *Fig. 5.38(d)* exhibit linear behaviour, indicating that ohmic contacts formed between the nanostructures and the electrodes, as is expected for PbI_2 on gold [173] and which is beneficial for efficient photogenerated carrier collection. In contrast, pure ZnO NWs typically form Schottky contact with gold electrodes (see the nonsymmetric I-V curve in *Fig. 5.36(a)*) [168].

The devices were illuminated with 405 nm wavelength light in a periodic fashion to study their photoresponse properties as shown in *Fig. 5.38(b)* and *Fig. 5.38(e)*. All the devices were also tested for 532 nm and 660 nm light illumination; however, no increase in current was observed due to the relatively wide bandgap of the studied materials. On-off measurements demonstrate a steady, rapid and repeatable increase and decrease of the current when the illumination is turned on or off, respectively; therefore, showing good stability and reversibility of the devices. ZnO-PbI_2 NWs exhibit low dark current (10–100 pA) which is necessary for high-performance photodetectors, while for pure ZnO NWs, it can be up to several tens of nA (see *Fig. 5.36(d)*). The current enhancement ratios (I_{on}/I_{off}) for the nanostructures prepared via both approaches were measured to be at around 10–20, in contrast to less than 2 for pure ZnO NWs.

Time-resolved photoresponse measurements were performed to evaluate the rise and decay time of the as-prepared ZnO-PbI_2 devices. As shown in *Fig. 5.38(c)* and *Fig. 5.38(f)*, the

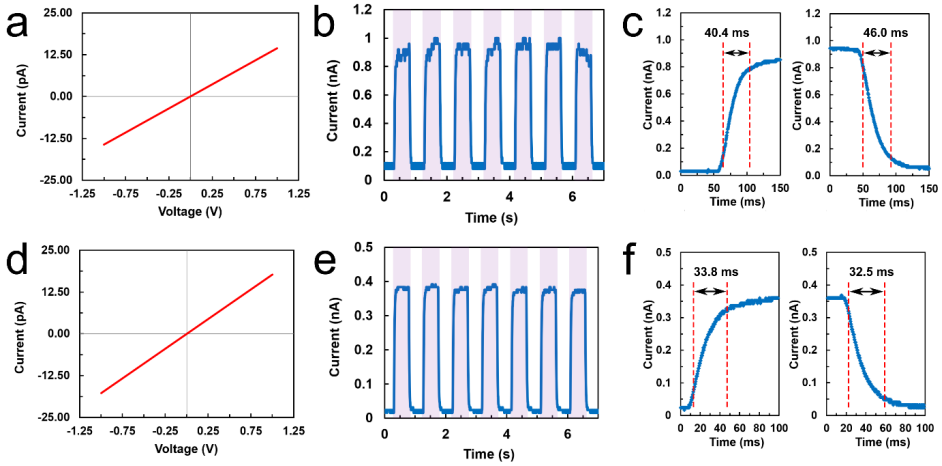

Figure 5.38. ZnO-PbI_2 single NW made by using the thermal evaporation approach (a) dark-state I_{ds}-V_{ds} characteristics, (b) on−off photoresponse, (c) time-resolved photoresponse measurements; and ZnO-PbI_2 single NW made by converting the lead oxide coating (d) dark-state I_{ds}-V_{ds} characteristics, (e) on−off photoresponse, (f) time-resolved photoresponse measurements at 1 V bias voltage and 0.5 W/cm^2 light intensity of 405 nm wavelength light.

obtained values are in the 30-50 ms range, which is almost two orders of magnitude faster than the pure ZnO NWs (see *Fig. 5.36(g)*) and comparable to typical NW or 2D PbI_2 photodetector response times [26,159,160,167]. The slow response of ZnO NWs is due to the influence of oxygen molecules on the surface states and their effect on photoresponse kinetics is widely discussed in the literature [174,175].

In this work, surface of ZnO NWs was passivated using a thin PbI_2 or WS_2 coating, and photodetectors of such heterostructures exhibit reduced dark current and photoresponse time, although it also decreases on-state current I_{on} in comparison to pure ZnO NWs. It is well known that adsorbed oxygen species influence electrical properties (electrical conductivity decreases with exposure to oxygen) of metal oxide nanostructures [90,176,177]. Consequently, band bending, induced by adsorbed oxygen molecules that capture free electrons, causes an efficient photogenerated electron-hole separation that leads to high gain in single-nanowire photodetectors. The presence of the PbI_2 layers in the nanostructures protects the ZnO surface from oxygen adsorption that might influence surface-related photoinduced processes and decrease the number of charge carrier trapping centres.

The thickness of PbI_2 on ZnO NWs, which were used in the as-fabricated photodetector devices, was typically 6–13 layers. No significant changes in the photodetector characteristics, such as spectral responsivity R_λ, response time or current enhancement ratios (I_{on}/I_{off}), were observed between the samples in this PbI_2 thickness range. It is worth noting, that there are theoretical and experimental studies that show a band structure shift from direct bandgap to indirect bandgap when the PbI_2 thickness is reduced from bulk to monolayer [26]; therefore, monolayer PbI_2 is not expected to be an efficient material for optoelectronics applications and few-layer PbI_2 should be used instead.

A responsivity as high as ~0.6 A/W (EQE ~180%) was calculated for the ZnO-PbI_2 single NW devices made using the thermal evaporation approach and ~0.3 A/W (EQE ~90%) for the ones made by converting the magnetron-sputtered lead oxide coating; however, it is not valid to compare the two different synthesis approaches based only on the responsivity values as the value range for all as-fabricated devices overlapped no matter which method was used. The obtained R_λ and EQE values are comparable to other typical *state-of-the-art* 1D nanostructure [167] and 2D PbI_2 [159,160,178] photodetectors.

6. CONCLUSIONS AND THESIS

In this work, development and characterization of various material nanowire and transition metal dichalcogenide *core-shell* heterostructures was demonstrated, including investigation of the nanostructure photoelectric properties.

The synthesis methods developed in this work are not limited to the demonstrated heterostructures and can be applied for other materials, if their compatibility is considered. Numerous other combinations of materials have also been investigated, and it was concluded that: 1) the sulfurization of the sacrificial shell material must occur at a lower temperature than that of the NW core recrystallization temperature; 2) to grow the layered material parallelly and uniformly around the NW, usually the symmetry and the material lattice parameters should be similar, otherwise the layered material grows out-of-plane or as islands, with specific exceptions. Therefore, if the criteria are met, the novel method is quite versatile - many layered materials might be grown with such method, if the right NW material is selected. Here, it has been demonstrated that high-quality layered materials can be grown around single crystal NWs parallel to the substrate NW surface plane.

In most of the cases, the shell thickness is not symmetrical on both sides of NWs. This is mainly due to different angular distribution of nanowires during magnetron deposition of the precursor material – nanowires oriented perpendicular to substrate plane are covered more homogeneously, while for nanowires oriented horizontally the upper side is covered with more material compared to the bottom side. For vertically oriented nanowires with length up to 10-20 μm, the coverage should be homogenous. Precursor deposition via the salt solution immersion method exhibits much more uniform shell thickness that does not depend on the NW orientation, in contrast to the magnetron deposition. With finely tuned process parameters, such as pre-deposited oxide thickness, NW length and orientation, temperature, sulfur vapour and carrier gas flow, precise control over the number of layers should be achievable with the proposed methods.

ZnO NWs were of particular interest in this work due to the pronounced change of their photoelectric properties after the surface modification. By fabricating two-terminal single-nanowire photodetectors from the NW heterostructures, it was shown that few layers of WS_2 or PbI_2 can significantly affect photoconductive properties of ZnO NWs. For example, ZnO-WS_2 *core-shell* NW two-terminal devices exhibit enhanced spectral responsivity in comparison to pure ZnO NWs, and light absorption in the WS_2 shell extends the active spectral range to the red part of the spectrum. Notably, ZnO NW surface passivation with layered vdW materials shell improves their photoresponse time for almost two orders of magnitude due to thus limited photo-induced processes related to adsorption/desorption of atmospheric oxygen species which typically slows down photoresponse in ZnO NWs. Therefore, fast operation of NW-based photodetectors might be achieved using such *core-shell* materials.

Two-terminal photodetectors based on the as-prepared *core-shell* NWs are comparable to other *state-of-the-art* 1D and 2D nanostructure photodetectors reported in literature. However, the combination of different materials in more complex hybrid NWs gives extra freedom to flexibly design their properties and add custom-made functionality. Such novel heterostructures could also be used for other applications in optoelectronics and in photo- or electrocatalytic hydrogen evolution reactions, which can be assumed from the favourable heterostructure band alignment.

Thesis

1. Few-layer WS_2 can be epitaxially grown on ZnO nanowires at 800°C by sulfurization of a WO_3 coating, pre-deposited on nanowires via reactive magnetron sputtering. The WS_2 shell enhances ZnO nanowire photosensitivity in the short wavelength range (spectral responsivity increases from 1.5 A/W to 7.0 A/W at 405 nm, dark current remains similar) and extends the spectral range to the red part of the spectrum. ZnO nanowire surface passivation with few-layer WS_2 improves photoresponse time for almost two orders of magnitude from several seconds to tens of miliseconds.
2. Few-layer PbI_2 was synthesised using a new method – iodination at 420°C of a PbO_x coating, pre-deposited via reactive magnetron sputtering. ZnO nanowire decoration with few-layer PbI_2 leads to significantly decreased dark current (from several nanoamperes to tens of picoamperes) at a cost of slightly reduced spectral responsivity from 1.5 A/W to 0.6 A/W at 405 nm. ZnO nanowire surface passivation with few-layer PbI_2 decreases photoresponse time by more than one order of magnitude from several seconds to tens of miliseconds.
3. Decomposition and sulfurization at 700°C of an ammonium heptamolybdate tetrahydrate coating, pre-deposited on ZnO nanowires via solution immersion, was found to be a viable method for ZnO-MoS_2 *core-shell* nanowire synthesis. Compared with similar two-step method of magnetron-sputtered MoO_3 coating conversion, the immersion method of molybdenum precursor deposition yields significantly thinner and more uniform few-layer MoS_2 shell compared to sputter-deposited MoO_3.
4. Preparation of novel GaN-ReS_2, ZnS-ReS_2 and ZnO-ReS_2 *core-shell* nanowire heterostructures was demonstrated using new few-layer ReS_2 synthesis method – sulfurization at 800°C of a ReO_x coating, pre-deposited via reactive magnetron sputtering. ZnO nanowire recrystallization and conversion to ZnS phase was observed at the temperature necessary for highly-crystalline ReS_2 growth. GaN and ZnS nanowires were found to be stable for the *core-shell* heterostructure synthesis, however, the ReS_2 shell crystalline quality was lower than that on the recrystallized ZnO substrate.

LIST OF PUBLICATIONS

Included in Dissertation:

I. **E. Butanovs,** S. Piskunov, A. Zolotarjovs, B. Polyakov. Growth and characterization of PbI2-decorated ZnO nanowires for photodetection applications. *J. Alloys Compd.* 825, 154095 (2020)

II. **E. Butanovs**, S. Vlassov, A. Kuzmin, S. Piskunov, J. Butikova, B. Polyakov. Fast-response single-nanowire photodetector based on ZnO/WS2 core/shell heterostructures. *ACS Appl. Mater. Interfaces*. 10, 13869-13876 (2018)

III. **E. Butanovs**, J. Butikova, A. Zolotarjovs, B. Polyakov. Towards metal chalcogenide nanowire-based colour-sensitive photodetectors. *Opt. Mater.* 75, 501–507 (2018)

IV. **E. Butanovs**, A. Kuzmin, J. Butikova, S. Vlassov, K. Smits, B. Polyakov. Synthesis and characterization of ZnO/ZnS/MoS2 core-shell nanowires. *J. Crys. Growth*. 459, 100-104 (2017)

V. B. Polyakov, K. Smits, A. Kuzmin, J. Zideluns, **E. Butanovs**, J. Butikova, S. Vlassov, S. Piskunov, Y. Zhukovskii. Unexpected epitaxial growth of a few WS2 layers on $\{1\bar{1}00\}$ facets of ZnO nanowires. *J. Phys. Chem. C.* 120, 21451-21459 (2016)

VI. **E. Butanovs**, A. Kuzmin, S. Piskunov, K. Smits, A. Kalinko, B. Polyakov. Synthesis and characterization of GaN/ReS2, ZnS/ReS2 and ZnO/ReS2 core/shell nanowire heterostructures. *Submitted manuscript*.

Other publications:

B. Polyakov, A. Kuzmin, S. Vlassov, **E. Butanovs**, J. Zideluns, J. Butikova, R. Kalendarev, M. Zubkins. Production and characterisation of heterostructured CuO/CuWO4 nanowires and thin films. *J. Crys. Growth,* 480, 78–84 (2017)

J. Butikova, B. Polyakov, L. Dimitrocenko, **E. Butanovs**, I. Tale. Laser scribing on HOPG for graphene stamp printing on silicon wafer. *Central European Journal of Physics*. 11, 580-583 (2013)

Author's contribution to publications

Paper I: Corresponding author, body of the article written; materials synthesis; SEM, XRD measurements; device fabrication and characterization.

Paper II: Parts of the article written; materials synthesis; device fabrication and characterization.

Paper III: Corresponding author, body of the article written; materials synthesis; SEM measurements; device fabrication and characterization.

Paper IV: Parts of the article written; materials synthesis.

Paper V: Materials synthesis.

Paper VI: Corresponding author, body of the article written; materials synthesis; SEM, XRD measurements.

PARTICIPATION IN SUMMER SCHOOLS AND CONFERENCES

Summer Schools:

1. “European School On Nanosciences & Nanotechnologies 2019 (ESONN-2019)”. Grenoble, France, August 25th – September 14th 2019.

2. Summer School “Optoelectronics on 2D materials”. Davos, Switzerland, August 20th – 25th 2018.

Conferences:

1. International conference “Functional materials and nanotechnologies 2018 (FM&NT-2018)”. Poster presentation: “ZnO/WS_2 nanowire core/shell heterostructures for light detection”. Riga, October 2018.

2. ISSP, University of Latvia 34th Scientific Conference. Oral presentation: “1D and 2D ReS_2-based nanostructure photodetectors”. Riga, February 2018

3. International conference “Functional materials and nanotechnologies 2017 (FM&NT-2017)”. Poster presentation: “Engineering of metal sulfide nanowire photoresistors”. Tartu, April 2017.

4. 13th International Young Scientist conference “Developments in Optics and Communications 2017”. Poster presentation: “Engineering of metal sulfide nanowire photoresistors”. Riga, April 2017.

5. ISSP, University of Latvia 33th Scientific Conference. Oral presentation: “Engineering of metal sulfide nanowire photodetectors”. Riga, February 2017.

6. Member in the local organizing committee and participation in “The Second European Workshop on Understanding and Controlling Nano and Mesoscale Friction”. Riga, July 2016.

7. 12th International Young Scientist conference “Developments in Optics and Communications 2016”. Poster presentation: “Photoluminescence in 2D transition metal dichalcogenide nanostructures”. Riga, March 2016.

8. ISSP, University of Latvia 32th Scientific Conference. Oral presentation: “2D transition metal dichalcogenide nanocrystals”. Riga, February 2016.

9. International symposium RCBJSF-2014-FMNT. Poster presentation: "HOPG patterning methods for graphene transferring onto the substrate". Riga, September 2014.

10. ISSP, University of Latvia 30th Scientific Conference. Oral presentation: “HOPG patterning methods for graphene stamp printing on silicon wafer”. Riga, February 2014.

11. ISSP, University of Latvia 29th Scientific Conference. Oral presentation: “Laser scribing on HOPG for graphene stamp printing on silicon wafer”. Riga, February 2013

REFERENCES

[1] Jeremy Ramsden. *Nanotechnology: An Introduction*. (Elsevier, 2016)

[2] Dasgupta, N. P. *et al.* 25th Anniversary Article: Semiconductor Nanowires - Synthesis, Characterization, and Applications. *Adv. Mater.* **26**, 2137–2184 (2014)

[3] Fan, Z. *et al.* Toward the Development of Printable Nanowire Electronics and Sensors. *Adv. Mater.* **21**, 3730–3743 (2009)

[4] Yang, P., Yan, R. & Fardy, M. Semiconductor Nanowire: What's Next? *Nano Lett.* **10**, 1529–1536 (2010)

[5] Sun, Y., Sun, B., He, J. & Wang, C. Compositional and structural engineering of inorganic nanowires toward advanced properties and applications. *InfoMat* **1**, 496–524 (2019)

[6] Lauhon, L. J., Gudiksen, M. S., Wang, D. & Lieber, C. M. Epitaxial core–shell and core–multishell nanowire heterostructures. *Nature* **420**, 57–61 (2002)

[7] Dong, Y., Tian, B., Kempa, T. J. & Lieber, C. M. Coaxial Group III−Nitride Nanowire Photovoltaics. *Nano Lett.* **9**, 2183–2187 (2009)

[8] Chhowalla, M. *et al.* The chemistry of two-dimensional layered transition metal dichalcogenide nanosheets. *Nat. Chem.* **5**, 263–275 (2013)

[9] Choi, W. *et al.* Recent development of two-dimensional transition metal dichalcogenides and their applications. *Mater. Today* **20**, 116–130 (2017)

[10] Walsh, L. A. & Hinkle, C. L. van der Waals epitaxy: 2D materials and topological insulators. *Appl. Mater. Today* **9**, 504–515 (2017)

[11] Duong, D. L., Yun, S. J. & Lee, Y. H. van der Waals Layered Materials: Opportunities and Challenges. *ACS Nano* **11**, 11803–11830 (2017)

[12] Novoselov, K. S. Electric Field Effect in Atomically Thin Carbon Films. *Science (80-.).* **306**, 666–669 (2004)

[13] Joensen, P., Frindt, R. F. & Morrison, S. R. Single-layer MoS2. *Mater. Res. Bull.* **21**, 457–461 (1986)

[14] Yang, D. & Frindt, R. F. Li-intercalation and exfoliation of WS2. *J. Phys. Chem. Solids* **57**, 1113–1116 (1996)

[15] Lu, X., Huang, H., Nemchuk, N. & Ruoff, R. S. Patterning of highly oriented pyrolytic graphite by oxygen plasma etching. *Appl. Phys. Lett.* **75**, 193–195 (1999)

[16] Geim, A. K. & Novoselov, K. S. The rise of graphene. *Nat. Mater.* **6**, 183–91 (2007)

[17] Mak, K. F., Lee, C., Hone, J., Shan, J. & Heinz, T. F. Atomically thin MoS2: A new direct-gap semiconductor. *Phys. Rev. Lett.* **105**, 2–5 (2010)

[18] Splendiani, A. *et al.* Emerging Photoluminescence in Monolayer MoS2. *Nano Lett.* **10**, 1271–1275 (2010)

[19] Gutiérrez, H. R. *et al.* Extraordinary Room-Temperature Photoluminescence in Triangular WS2 Monolayers. *Nano Lett.* **13**, 3447–3454 (2013)

[20] Rahman, M., Davey, K. & Qiao, S.-Z. Advent of 2D Rhenium Disulfide (ReS2): Fundamentals to Applications. *Adv. Funct. Mater.* **27**, 1606129 (2017)

[21] Rao, C. N. R., Ramakrishna Matte, H. S. S. & Maitra, U. Graphene analogues of inorganic layered materials. *Angew. Chemie - Int. Ed.* **52**, 13162–13185 (2013)

[22] Anasori, B., Lukatskaya, M. R. & Gogotsi, Y. 2D metal carbides and nitrides (MXenes) for energy storage. *Nat. Rev. Mater.* **2**, 16098 (2017)

[23] Mannix, A. J., Kiraly, B., Hersam, M. C. & Guisinger, N. P. Synthesis and chemistry of elemental 2D materials. *Nat. Rev. Chem.* **1**, 0014 (2017)

[24] Wang, Q. H., Kalantar-Zadeh, K., Kis, A., Coleman, J. N. & Strano, M. S. Electronics and optoelectronics of two-dimensional transition metal dichalcogenides. *Nat. Nanotechnol.* **7**, 699–712 (2012)

[25] Wilson, J. A. & Yoffe, A. D. The transition metal dichalcogenides discussion and interpretation of the observed optical, electrical and structural properties. *Adv. Phys.* **18**, 193–335 (1969)

[26] Zhong, M. *et al.* Large-scale 2D PbI2 monolayers: experimental realization and their indirect band-gap related properties. *Nanoscale* **9**, 3736–3741 (2017)

[27] Toulouse, A. S. *et al.* Frenkel-like Wannier-Mott excitons in few-layer PbI2. *Phys. Rev. B* **91**, 165308 (2015)

[28] Zhang, E. *et al.* ReS2-Based Field-Effect Transistors and Photodetectors. *Adv. Funct. Mater.* **25**, 4076–4082 (2015)

[29] Bertolazzi, S., Brivio, J. & Kis, A. Stretching and Breaking of Ultrathin MoS2. *ACS Nano* **5**, 9703–9709 (2011)

[30] Yi, F. *et al.* Wearable energy sources based on 2D materials. *Chem. Soc. Rev.* **47**, 3152–3188 (2018)

[31] Kelly, A. G. *et al.* All-printed thin-film transistors from networks of liquid-exfoliated nanosheets. *Science (80-.).* **356**, 69–73 (2017)

[32] Gupta, A., Sakthivel, T. & Seal, S. Recent development in 2D materials beyond graphene. *Prog. Mater. Sci.* **73**, 44–126 (2015)

[33] Marzik, J. V., Kershaw, R., Dwight, K. & Wold, A. Photoelectronic properties of ReS2 and ReSe2 single crystals. *J. Solid State Chem.* **51**, 170–175 (1984)

[34] Novoselov, K. S. *et al.* Two-dimensional atomic crystals. *Proc. Natl. Acad. Sci.* **102**, 10451–10453 (2005)

[35] Li, D., Windl, W. & Padture, N. P. Toward Site-Specific Stamping of Graphene. *Adv. Mater.* **21**, 1243–1246 (2009)

[36] Coleman, J. N. *et al.* Two-dimensional nanosheets produced by liquid exfoliation of layered materials. *Science (80-.).* **331**, 568–571 (2011)

[37] Backes, C. *et al.* Guidelines for Exfoliation, Characterization and Processing of Layered Materials Produced by Liquid Exfoliation. *Chem. Mater.* **29**, 243–255 (2017)

[38] Nicolosi, V., Chhowalla, M., Kanatzidis, M. G., Strano, M. S. & Coleman, J. N. Liquid Exfoliation of Layered Materials. *Science (80-.).* **340**, 1226419–1226419 (2013)

[39] Zhang, X., Lai, Z., Tan, C. & Zhang, H. Solution-Processed Two-Dimensional MoS2 Nanosheets: Preparation, Hybridization, and Applications. *Angew. Chemie Int. Ed.* **55**, 8816–8838 (2016)

[40] Jawaid, A. *et al.* Mechanism for Liquid Phase Exfoliation of MoS2. *Chem. Mater.* **28**, 337–348 (2016)

[41] Hu, G. *et al.* Functional inks and printing of two-dimensional materials. *Chem. Soc. Rev.* **47**, 3265–3300 (2018)

[42] Shi, Y., Li, H. & Li, L. J. Recent advances in controlled synthesis of two-dimensional

transition metal dichalcogenides via vapour deposition techniques. *Chem. Soc. Rev.* **44**, 2744–2756 (2015)

[43] Chen, P., Zhang, Z., Duan, X. & Duan, X. Chemical synthesis of two-dimensional atomic crystals, heterostructures and superlattices. *Chem. Soc. Rev.* **47**, 3129–3151 (2018)

[44] Cong, C. *et al.* Synthesis and Optical Properties of Large-Area Single-Crystalline 2D Semiconductor WS2 Monolayer from Chemical Vapor Deposition. *Adv. Opt. Mater.* **2**, 131–136 (2014)

[45] Van Der Zande, A. M. *et al.* Grains and grain boundaries in highly crystalline monolayer molybdenum disulphide. *Nat. Mater.* **12**, 554–561 (2013)

[46] Kang, K. *et al.* High-mobility three-atom-thick semiconducting films with wafer-scale homogeneity. *Nature* **520**, 656–660 (2015)

[47] Lin, Y.-C. *et al.* Wafer-scale MoS2 thin layers prepared by MoO3 sulfurization. *Nanoscale* **4**, 6637 (2012)

[48] Wu, C.-R. *et al.* Establishment of 2D Crystal Heterostructures by Sulfurization of Sequential Transition Metal Depositions: Preparation, Characterization, and Selective Growth. *Nano Lett.* **16**, 7093–7097 (2016)

[49] Bark, H. *et al.* Large-area niobium disulfide thin films as transparent electrodes for devices based on two-dimensional materials. *Nanoscale* **10**, 1056–1062 (2018)

[50] Liu, K. K. *et al.* Growth of large-area and highly crystalline MoS2 thin layers on insulating substrates. *Nano Lett.* **12**, 1538–1544 (2012)

[51] Novoselov, K. S., Mishchenko, A., Carvalho, A. & Castro Neto, A. H. 2D materials and van der Waals heterostructures. *Science (80-.).* **353**, aac9439 (2016)

[52] Castellanos-Gomez, A. *et al.* Deterministic transfer of two-dimensional materials by all-dry viscoelastic stamping. *2D Mater.* **1**, (2014)

[53] Frisenda, R., Molina-Mendoza, A. J., Mueller, T., Castellanos-Gomez, A. & van der Zant, H. S. J. Atomically thin p-n junctions based on two-dimensional materials. *Chem. Soc. Rev.* **47**, 3339–3358 (2018)

[54] Bakti Utama, M. I. *et al.* Recent developments and future directions in the growth of nanostructures by van der Waals epitaxy. *Nanoscale* **5**, 3570 (2013)

[55] Koma, A. Van der Waals epitaxy-a new epitaxial growth method for a highly lattice-mismatched system. *Thin Solid Films* **216**, 72–76 (1992)

[56] Zhang, C. *et al.* Interlayer couplings, Moiré patterns, and 2D electronic superlattices in MoS 2 /WSe 2 hetero-bilayers. *Sci. Adv.* **3**, e1601459 (2017)

[57] Tan, C. & Zhang, H. Epitaxial Growth of Hetero-Nanostructures Based on Ultrathin Two-Dimensional Nanosheets. *J. Am. Chem. Soc.* **137**, 12162–12174 (2015)

[58] Zhang, T. *et al.* Twinned growth behaviour of two-dimensional materials. *Nat. Commun.* **7**, 13911 (2016)

[59] Schulman, D. S., Arnold, A. J. & Das, S. Contact engineering for 2D materials and devices. *Chem. Soc. Rev.* **47**, 3037–3058 (2018)

[60] Farmanbar, M. & Brocks, G. Ohmic Contacts to 2D Semiconductors through van der Waals Bonding. *Adv. Electron. Mater.* **2**, 1500405 (2016)

[61] Kang, K. *et al.* Layer-by-layer assembly of two-dimensional materials into wafer-scale heterostructures. *Nature* **550**, 229–233 (2017)

[62] Wang, F. *et al.* Progress on Electronic and Optoelectronic Devices of 2D Layered

Semiconducting Materials. *Small* **13**, 1604298 (2017)

[63] Zhao, Y. *et al.* Doping, Contact and Interface Engineering of Two-Dimensional Layered Transition Metal Dichalcogenides Transistors. *Adv. Funct. Mater.* **27**, (2017)

[64] Xie, L. M. Two-dimensional transition metal dichalcogenide alloys: preparation, characterization and applications. *Nanoscale* **7**, 18392–18401 (2015)

[65] Schaibley, J. R. *et al.* Valleytronics in 2D materials. *Nat. Rev. Mater.* **1**, 1–15 (2016)

[66] Garcia, J. H., Vila, M., Cummings, A. W. & Roche, S. Spin transport in graphene/transition metal dichalcogenide heterostructures. *Chem. Soc. Rev.* **47**, 3359–3379 (2018)

[67] Schwierz, F., Pezoldt, J. & Granzner, R. Two-dimensional materials and their prospects in transistor electronics. *Nanoscale* **7**, 8261–8283 (2015)

[68] Novoselov, K. S. *et al.* A roadmap for graphene. *Nature* **490**, 192–200 (2012)

[69] Xie, C., Mak, C., Tao, X. & Yan, F. Photodetectors Based on Two-Dimensional Layered Materials Beyond Graphene. *Adv. Funct. Mater.* **27**, (2017)

[70] Yan, F. *et al.* Toward High-Performance Photodetectors Based on 2D Materials: Strategy on Methods. *Small Methods* **2**, 1700349 (2018)

[71] Li, C. *et al.* Engineering graphene and TMDs based van der Waals heterostructures for photovoltaic and photoelectrochemical solar energy conversion. *Chem. Soc. Rev.* **47**, 4981–5037 (2018)

[72] Withers, F. *et al.* Light-emitting diodes by band-structure engineering in van der Waals heterostructures. *Nat. Mater.* **14**, 301–6 (2015)

[73] Lien, D.-H. *et al.* Large-area and bright pulsed electroluminescence in monolayer semiconductors. *Nat. Commun.* **9**, 1229 (2018)

[74] Ponraj, J. S. *et al.* Photonics and optoelectronics of two-dimensional materials beyond graphene. *Nanotechnology* **27**, 462001 (2016)

[75] Yang, S., Jiang, C. & Wei, S. Gas sensing in 2D materials. *Appl. Phys. Rev.* **4**, 021304 (2017)

[76] Choi, S.-J. & Kim, I.-D. Recent Developments in 2D Nanomaterials for Chemiresistive-Type Gas Sensors. *Electron. Mater. Lett.* **14**, 221–260 (2018)

[77] Wen, W. *et al.* Recent advances in emerging 2D nanomaterials for biosensing and bioimaging applications. *Mater. Today* **21**, 164–177 (2018)

[78] Hu, Y. *et al.* Two-dimensional transition metal dichalcogenide nanomaterials for biosensing applications. *Mater. Chem. Front.* **1**, 24–36 (2017)

[79] Cui, C., Xue, F., Hu, W.-J. & Li, L.-J. Two-dimensional materials with piezoelectric and ferroelectric functionalities. *npj 2D Mater. Appl.* **2**, 18 (2018)

[80] Hinchet, R., Khan, U., Falconi, C. & Kim, S.-W. Piezoelectric properties in two-dimensional materials: Simulations and experiments. *Mater. Today* **21**, 611–630 (2018)

[81] Gong, C. *et al.* Electronic and Optoelectronic Applications Based on 2D Novel Anisotropic Transition Metal Dichalcogenides. *Adv. Sci.* **4**, 1700231 (2017)

[82] Di, J. *et al.* Ultrathin two-dimensional materials for photo- and electrocatalytic hydrogen evolution. *Mater. Today* **21**, 749–770 (2018)

[83] Wagner, R. S. & Ellis, W. C. Vapor-Liquid-Solid Mechanism Of Single Crystal Growth. *Appl. Phys. Lett.* **4**, 89–90 (1964)

[84] Yazawa, M., Koguchi, M., Muto, A. & Hiruma, K. Semiconductor nanowhiskers. *Adv. Mater.* **5**, 577–580 (1993)

[85] Trentler, T. J. *et al.* Solution-Liquid-Solid Growth of Crystalline III-V Semiconductors: An Analogy to Vapor-Liquid-Solid Growth. *Science (80-.).* **270**, 1791–1794 (1995)

[86] Sorger, V. J., Oulton, R. F., Ma, R.-M. & Zhang, X. Toward integrated plasmonic circuits. *MRS Bull.* **37**, 728–738 (2012)

[87] Sannicolo, T. *et al.* Metallic Nanowire-Based Transparent Electrodes for Next Generation Flexible Devices: a Review. *Small* **12**, 6052–6075 (2016)

[88] Long, Y.-Z., Yu, M., Sun, B., Gu, C.-Z. & Fan, Z. Recent advances in large-scale assembly of semiconducting inorganic nanowires and nanofibers for electronics, sensors and photovoltaics. *Chem. Soc. Rev.* **41**, 4560 (2012)

[89] Law, M., Goldberger, J. & Yang, P. Semiconductor Nanowires and Nanotubes. *Annu. Rev. Mater. Res.* **34**, 83–122 (2004)

[90] Soci, C. *et al.* ZnO Nanowire UV Photodetectors with High Internal Gain. *Nano Lett.* **7**, 1003–1009 (2007)

[91] Gogurla, N., Sinha, A. K., Santra, S., Manna, S. & Ray, S. K. Multifunctional Au-ZnO Plasmonic Nanostructures for Enhanced UV Photodetector and Room Temperature NO Sensing Devices. *Sci. Rep.* **4**, 6483 (2015)

[92] Thelander, C. *et al.* Nanowire-based one-dimensional electronics. *Mater. Today* **9**, 28–35 (2006)

[93] Lu, W., Xie, P. & Lieber, C. M. Nanowire Transistor Performance Limits and Applications. *IEEE Trans. Electron Devices* **55**, 2859–2876 (2008)

[94] Greytak, A. B., Lauhon, L. J., Gudiksen, M. S. & Lieber, C. M. Growth and transport properties of complementary germanium nanowire field-effect transistors. *Appl. Phys. Lett.* **84**, 4176–4178 (2004)

[95] Li, H. *et al.* One-dimensional CdS nanostructures: A promising candidate for optoelectronics. *Adv. Mater.* **25**, 3017–3037 (2013)

[96] Kim, W. & Chu, K. S. ZnO nanowire field-effect transistor as a UV photodetector; optimization for maximum sensitivity. *Phys. status solidi* **206**, 179–182 (2009)

[97] Lim, T., Lee, S., Meyyappan, M. & Ju, S. Control of semiconducting and metallic indium oxide nanowires. *ACS Nano* **5**, 3917–3922 (2011)

[98] Chen, D., Liu, Z., Liang, B., Wang, X. & Shen, G. Transparent metal oxide nanowire transistors. *Nanoscale* **4**, 3001 (2012)

[99] Li, Y., Qian, F., Xiang, J. & Lieber, C. M. Nanowire electronic and optoelectronic devices. *Mater. Today* **9**, 18–27 (2006)

[100] Han, N., Wang, F. & Ho, J. C. One-dimensional nanostructured materials for solar energy harvesting. *Nanomater. Energy* **1**, 4–17 (2012)

[101] Kempa, T. J., Day, R. W., Kim, S.-K., Park, H.-G. & Lieber, C. M. Semiconductor nanowires: a platform for exploring limits and concepts for nano-enabled solar cells. *Energy Environ. Sci.* **6**, 719 (2013)

[102] Deng, K. & Li, L. CdS Nanoscale Photodetectors. *Adv. Mater.* **26**, 2619–2635 (2014)

[103] Xie, X. & Shen, G. Single-crystalline In2S3 nanowire-based flexible visible-light photodetectors with an ultra-high photoresponse. *Nanoscale* **7**, 5046–5052 (2015)

[104] Soci, C. *et al.* Nanowire Photodetectors. *J. Nanosci. Nanotechnol.* **10**, 1430–1449 (2010)

[105] Yan, R., Gargas, D. & Yang, P. Nanowire photonics. *Nat. Photonics* **3**, 569–576 (2009)

[106] Eaton, S. W., Fu, A., Wong, A. B., Ning, C.-Z. & Yang, P. Semiconductor nanowire lasers. *Nat. Rev. Mater.* **1**, 16028 (2016)

[107] Barth, S., Hernandez-Ramirez, F., Holmes, J. D. & Romano-Rodriguez, A. Synthesis and applications of one-dimensional semiconductors. *Prog. Mater. Sci.* **55**, 563–627 (2010)

[108] Bermúdez-Ureña, E. *et al.* Plasmonic Waveguide-Integrated Nanowire Laser. *Nano Lett.* **17**, 747–754 (2017)

[109] Patolsky, F. & Lieber, C. M. Nanowire nanosensors. *Mater. Today* **8**, 20–28 (2005)

[110] Mai, L., Tian, X., Xu, X., Chang, L. & Xu, L. Nanowire Electrodes for Electrochemical Energy Storage Devices. *Chem. Rev.* **114**, 11828–11862 (2014)

[111] Pennelli, G. Review of nanostructured devices for thermoelectric applications. *Beilstein J. Nanotechnol.* **5**, 1268–1284 (2014)

[112] Espinosa, H. D., Bernal, R. A. & Minary-Jolandan, M. A Review of Mechanical and Electromechanical Properties of Piezoelectric Nanowires. *Adv. Mater.* **24**, 4656–4675 (2012)

[113] Yang, P. *et al.* Controlled Growth of ZnO Nanowires and Their Optical Properties. *Adv. Funct. Mater.* **12**, 323 (2002)

[114] Hannon, J. B., Kodambaka, S., Ross, F. M. & Tromp, R. M. The influence of the surface migration of gold on the growth of silicon nanowires. *Nature* **440**, 69–71 (2006)

[115] Wu, Y., Fan, R. & Yang, P. Block-by-Block Growth of Single-Crystalline Si/SiGe Superlattice Nanowires. *Nano Lett.* **2**, 83–86 (2002)

[116] Hayden, O., Greytak, A. B. & Bell, D. C. Core-shell nanowire light-emitting diodes. *Adv. Mater.* **17**, 701–704 (2005)

[117] Ra, Y.-H., Navamathavan, R., Yoo, H.-I. & Lee, C.-R. Single Nanowire Light-Emitting Diodes Using Uniaxial and Coaxial InGaN/GaN Multiple Quantum Wells Synthesized by Metalorganic Chemical Vapor Deposition. *Nano Lett.* **14**, 1537–1545 (2014)

[118] Adachi, M. M., Anantram, M. P. & Karim, K. S. Core-shell silicon nanowire solar cells. *Sci. Rep.* **3**, 1546 (2013)

[119] Czaban, J. A., Thompson, D. A. & LaPierre, R. R. GaAs Core−Shell Nanowires for Photovoltaic Applications. *Nano Lett.* **9**, 148–154 (2009)

[120] Wang, K. *et al.* Synthesis and photovoltaic effect of vertically aligned ZnO/ZnS core/shell nanowire arrays. *Appl. Phys. Lett.* **96**, 1–4 (2010)

[121] Wang, X. *et al.* High Gain Submicrometer Optical Amplifier at Near-Infrared Communication Band. *Phys. Rev. Lett.* **115**, 027403 (2015)

[122] Mieszawska, A. J., Jalilian, R., Sumanasekera, G. U. & Zamborini, F. P. The synthesis and fabrication of one-dimensional nanoscale heterojunctions. *Small* **3**, 722–756 (2007)

[123] Vlassov, S. *et al.* Shape Restoration Effect in Ag–SiO2 Core–Shell Nanowires. *Nano Lett.* **14**, 5201–5205 (2014)

[124] Liu, X. W., Hu, J. & Pan, B. C. The composition-dependent mechanical properties of Ge/Si core–shell nanowires. *Phys. E Low-dimensional Syst. Nanostructures* **40**, 3042–3048 (2008)

[125] Ma, J., Liu, Y., Hao, P., Wang, J. & Zhang, Y. Effect of different oxide thickness on the bending Young's modulus of SiO2@SiC nanowires. *Sci. Rep.* **6**, 18994 (2016)

[126] Dan, Y. *et al.* Dramatic reduction of surface recombination by in situ surface passivation of silicon nanowires. *Nano Lett.* **11**, 2527–2532 (2011)

[127] Han, S. *et al.* Transition Metal Oxide Core−Shell Nanowires: Generic Synthesis and Transport Studies. *Nano Lett.* **4**, 1241–1246 (2004)

[128] Fontcuberta i Morral, A. *et al.* Prismatic Quantum Heterostructures Synthesized on Molecular-Beam Epitaxy GaAs Nanowires. *Small* **4**, 899–903 (2008)

[129] Yu, H., Liu, C. M., Huang, X. Y. & Lei, M. Y. The microstructure and photoluminescence of ZnO–MoS2 core shell nano-materials. *Mater. Res. Express* **4**, 015024 (2017)

[130] Chen, F., Wang, T., Wang, L., Ji, X. & Zhang, Q. Improved light emission of MoS2 monolayers by constructing AlN/MoS2 core–shell nanowires. *J. Mater. Chem. C* **5**, 10225–10230 (2017)

[131] Seo, B., Jeong, H. Y., Hong, S. Y., Zak, A. & Joo, S. H. Impact of a conductive oxide core in tungsten sulfide-based nanostructures on the hydrogen evolution reaction. *Chem. Commun.* **51**, 8334–8337 (2015)

[132] Zhang, L., Liu, C., Wong, A. B., Resasco, J. & Yang, P. MoS2-wrapped silicon nanowires for photoelectrochemical water reduction. *Nano Res.* **8**, 281–287 (2014)

[133] Chen, Z. *et al.* Core–shell MoO3 –MoS2 Nanowires for Hydrogen Evolution: A Functional Design for Electrocatalytic Materials. *Nano Lett.* **11**, 4168–4175 (2011)

[134] Martin, P. M. *Handbook of Depositions Tecnologies for film and coating*. (2005)

[135] Jones, Anthony C.; Hitchman, M. L. *Chemical Vapour Deposition - Precursors, Processes and Applications*. (Royal Society of Chemistry, 2009)

[136] Goldstein, J. I. *et al. Scanning Electron Microscopy and X-ray Microanalysis*. (Springer, 2003)

[137] David B. Williams; C. Barry Carter. *Transmission Electron Microscopy: A Textbook for Materials Science*. (Springer, 2009)

[138] Klinger, M. More features, more tools, more CrysTBox. *J. Appl. Crystallogr.* **50**, 1226–1234 (2017)

[139] Abraham Clearfield; Joseph H. Reibenspies; Nattamai Bhuvanesh. *Principles and Applications of Powder Diffraction*. (Wiley, 2008)

[140] Kuzmany, H. *Solid-State Spectroscopy*. (Springer, 2009)

[141] Marc J. Madou. *Manufacturing Techniques for Microfabrication and Nanotechnology*. (Taylor & Francis, 2011)

[142] Peimyoo, N. *et al.* Nonblinking, intense two-dimensional light emitter: Monolayer WS2 Triangles. *ACS Nano* **7**, 10985–10994 (2013)

[143] Elías, A. L. *et al.* Controlled synthesis and transfer of large-area WS2 sheets: From single layer to few layers. *ACS Nano* **7**, 5235–5242 (2013)

[144] Polyakov, B. *et al.* Unexpected Epitaxial Growth of a Few WS2 Layers on $\{1\bar{1}00\}$ Facets of ZnO Nanowires. *J. Phys. Chem. C* **120**, 21451–21459 (2016)

[145] Krause, M., Mücklich, A., Zak, A., Seifert, G. & Gemming, S. High resolution TEM study of WS2 nanotubes. *Phys. Status Solidi Basic Res.* (2011) doi:10.1002/pssb.201100076

[146] Butanovs, E. *et al.* Fast-Response Single-Nanowire Photodetector Based on ZnO/WS2 Core/Shell Heterostructures. *ACS Appl. Mater. Interfaces* **10**, 13869–13876 (2018)

[147] Özgür, Ü. *et al.* A comprehensive review of ZnO materials and devices. *J. Appl. Phys.* **98**, 041301 (2005)

[148] Lin, Y.-C. *et al.* Single-Layer ReS2: Two-Dimensional Semiconductor with Tunable In-Plane Anisotropy. *ACS Nano* **9**, 11249–11257 (2015)

[149] He, X. *et al.* Chemical Vapor Deposition of High-Quality and Atomically Layered ReS2. *Small* **11**, 5423–5429 (2015)

[150] Qin, J.-K. *et al.* van der Waals epitaxy of large-area continuous ReS2 films on mica substrate. *RSC Adv.* **7**, 24188–24194 (2017)

[151] Urakami, N., Okuda, T. & Hashimoto, Y. Epitaxial growth of ReS2 (001) thin film via deposited-Re sulfurization. *Jpn. J. Appl. Phys.* **57**, 02CB07 (2018)

[152] Ho, C. ., Huang, Y. ., Liao, P. . & Tiong, K. . Crystal structure and band-edge transitions of ReS2−xSex layered compounds. *J. Phys. Chem. Solids* **60**, 1797–1804 (1999)

[153] Butanovs, E., Kuzmin, A., Butikova, J., Vlassov, S. & Polyakov, B. Synthesis and characterization of ZnO/ZnS/MoS2 core-shell nanowires. *J. Cryst. Growth* **459**, 100–104 (2017)

[154] Panda, S. K., Dev, A. & Chaudhuri, S. Fabrication and Luminescent Properties of c-Axis Oriented ZnO−ZnS Core−Shell and ZnS Nanorod Arrays by Sulfidation of Aligned ZnO Nanorod Arrays. *J. Phys. Chem. C* **111**, 5039–5043 (2007)

[155] Feng, Y. *et al.* Raman vibrational spectra of bulk to monolayer ReS2 with lower symmetry. *Phys. Rev. B* **92**, 054110 (2015)

[156] Tonndorf, P. *et al.* Photoluminescence emission and Raman response of monolayer MoS2, MoSe2, and WSe2. *Opt. Express* **21**, 4908 (2013)

[157] Zhang, J. *et al.* Layered ultrathin PbI2 single crystals for high sensitivity flexible photodetectors. *J. Mater. Chem. C* **3**, 4402–4406 (2015)

[158] Sun, H. *et al.* Laser-induced surface recrystallization of polycrystalline PbI2 thick films for X-ray detector application. *Appl. Surf. Sci.* **427**, 1146–1151 (2018)

[159] Zheng, W. *et al.* High-Crystalline 2D Layered PbI2 with Ultrasmooth Surface: Liquid-Phase Synthesis and Application of High-Speed Photon Detection. *Adv. Electron. Mater.* **2**, 1600291 (2016)

[160] Wang, Y., Gan, L., Chen, J., Yang, R. & Zhai, T. Achieving highly uniform two-dimensional PbI2 flakes for photodetectors via space confined physical vapor deposition. *Sci. Bull.* **62**, 1654–1662 (2017)

[161] Butanovs, E., Piskunov, S., Zolotarjovs, A. & Polyakov, B. Growth and characterization of PbI2-decorated ZnO nanowires for photodetection applications. *J. Alloys Compd.* **825**, 154095 (2020)

[162] Condeles, J. F., Ando, R. A. & Mulato, M. Optical and structural properties of PbI2 thin films. *J. Mater. Sci.* **43**, 525–529 (2008)

[163] Butanovs, E., Butikova, J., Zolotarjovs, A. & Polyakov, B. Towards metal chalcogenide nanowire-based colour-sensitive photodetectors. *Opt. Mater. (Amst).* **75**, 501–507 (2018)

[164] Talin, A. A., Léonard, F., Swartzentruber, B. S., Wang, X. & Hersee, S. D. Unusually Strong Space-Charge-Limited Current in Thin Wires. *Phys. Rev. Lett.* **101**, 076802 (2008)

[165] Katzenmeyer, A. M. *et al.* Observation of Space-Charge-Limited Transport in InAs

Nanowires. *IEEE Trans. Nanotechnol.* **10**, 92–95 (2011)

[166] Vilà, A. *et al.* Fabrication of metallic contacts to nanometre-sized materials using a focused ion beam (FIB). *Mater. Sci. Eng. C* **26**, 1063–1066 (2006)

[167] Zhai, T. *et al.* Recent Developments in One-Dimensional Inorganic Nanostructures for Photodetectors. *Adv. Funct. Mater.* **20**, 4233–4248 (2010)

[168] Lao, C. S. *et al.* ZnO Nanobelt/Nanowire Schottky Diodes Formed by Dielectrophoresis Alignment across Au Electrodes. *Nano Lett.* **6**, 263–266 (2006)

[169] Perea-López, N. *et al.* Photosensor Device Based on Few-Layered WS2 Films. *Adv. Funct. Mater.* **23**, 5511–5517 (2013)

[170] Huo, N. *et al.* Photoresponsive and Gas Sensing Field-Effect Transistors based on Multilayer WS2 Nanoflakes. *Sci. Rep.* **4**, 5209 (2015)

[171] Lan, C. *et al.* ZnO–WS2 heterostructures for enhanced ultra-violet photodetectors. *RSC Adv.* **6**, 67520–67524 (2016)

[172] Zhang, C. *et al.* High-performance photodetectors for visible and near-infrared lights based on individual WS2 nanotubes. *Appl. Phys. Lett.* **100**, 243101 (2012)

[173] Zhong, M. *et al.* Flexible photodetectors based on phase dependent PbI2 single crystals. *J. Mater. Chem. C* **4**, 6492–6499 (2016)

[174] Cheng, G. *et al.* ZnO nanowire Schottky barrier ultraviolet photodetector with high sensitivity and fast recovery speed. *Appl. Phys. Lett.* **99**, 203105 (2011)

[175] Mallampati, B., Nair, S. V., Ruda, H. E. & Philipose, U. Role of surface in high photoconductive gain measured in ZnO nanowire-based photodetector. *J. Nanoparticle Res.* **17**, 176 (2015)

[176] Wu, J.-M. & Kuo, C.-H. Ultraviolet photodetectors made from SnO2 nanowires. *Thin Solid Films* **517**, 3870–3873 (2009)

[177] Yamazoe, N., Fuchigami, J., Kishikawa, M. & Seiyama, T. Interactions of tin oxide surface with O2, H2O AND H2. *Surf. Sci.* **86**, 335–344 (1979)

[178] Zhang, J. *et al.* Low-Temperature Heteroepitaxy of 2D PbI 2 /Graphene for Large-Area Flexible Photodetectors. *Adv. Mater.* **30**, 1803194 (2018)

ACKNOWLEDGEMENTS

I would like to express my greatest gratitude to Dr. Boris Polyakov for supervising my bachelor, master and PhD thesis, for introducing me to the field of nanotechnologies, for teaching me philosophy of science and so many experimental techniques and tricks. Thank you for the long-term contribution to my scientific development!

I would like to thank all my colleagues from Thin Film laboratory and Laboratory of Semiconductor Optoelectronics for help and the given knowledge over the years. Special thanks to Dr. Alexei Kuzmin for Raman measurements, Aleksejs Zolotarjovs for photoluminescence measurements, Dr. Krišjānis Šmits for assistance with TEM and SAED measurements, Dr. Sergei Piskunov for DFT calculations, Dr. Edgars Nitišs and Dr. Roberts Rimša for teaching me lithography steps.

I would like to thank my family for the support throughout my studies. I owe great gratitude to my friends for the support, especially Arturs Bundulis for many great discussions we had, Agnese Čikule and Sindija Balode for actively motivating me to work harder and write my Dissertation.

I would like to acknowledge financial support from Latvian National Research Program IMIS2, Scientific Research Projects for Students and Young Researchers No. SJZ/2016/6, No. SJZ/2017/1 and No. SJZ/2018/7 realized at the Institute of Solid State Physics, University of Latvia, and Latvian Council of Science grants LZP FLPP No. lzp-2018/2-0353 and No. lzp-2018/2-0083.

APPENDIX A

Growth recipes of nanowires

GaN NWs: 3 g metallic Ga (*99.999%, Alfa Aeasar*) was loaded in a ceramic boat and placed in the centre of the quartz tube, Au/Si substrates were placed downstream in a lower temperature region. The reactor was heated to 920°C under a flow of carrier gas mixture Ar/H_2-35%, then gaseous NH_3 flow in 1:1 ratio to the carrier gas was introduced and maintained for 30 minutes for the gas-phase reaction and nanowire growth, followed by natural cooling to the room temperature under Ar/H_2 flow. As a result, 5 – 10 μm long GaN NWs were produced on the SiO_2/Si substrate.

ZnS NWs: 0.4 g ZnS powder (>97%, *Sigma Aldrich*) was thermally evaporated in a quartz tube at 950°C temperature for 30 minutes, followed by a natural cooling. The vapour was carried downstream to the Au/Si substrate by N_2 gas to grow 20 – 100 μm long ZnS NWs.

ZnO NWs: 1:1 mixture of ZnO and carbon powders was loaded in a ceramic boat in the centre of the quartz tube at 900°C, the vapour was transported downstream to the Au/Si substrate at a lower temperature region using N_2 as a carrier gas. The temperature during the growth was held constant for 90 minutes, followed by a natural cooling to the room temperature. As a result, 10 – 50 μm long ZnO NWs were obtained on the SiO_2/Si substrate.

PbS NWs: 0.25 g $PbCl_2$ powder (*98%, Sigma Aldrich*) was loaded in a ceramic boat and placed in the centre of the quartz tube at 650°C, Au/Si substrate was placed downstream in a lower temperature region. Excessive amount of sulfur powder (*enola SIA*) was placed upstream at 250°C to create sulphur-rich atmosphere, while N_2 was used as a carrier gas. The temperature was kept constant for 20 minutes, followed by natural cooling to room temperature.

In_2S_3 NWs: Mixture of 0.5 g In and 0.5 g $InCl_3$ (*98%, Sigma-Aldrich*) powders were used as a source material and sent to the centre of the quartz tube. Au/Si substrate and sulfur powder were placed downstream and upstream, respectively, as in the previous case. Ar/H_2 (5%) gas mixture was used as a vapour carrier. The furnace was heated to 800°C, temperature was held constant for 45 minutes and then was let to cool down naturally to room temperature.

CdS NWs: CdS powder (*98%, Alfa Aesar*) was thermally evaporated in a quartz tube at 950°C temperature for 30 minutes, followed by a natural cooling. The vapour was carried downstream to the Au/Si substrate by N_2 gas.

ZnSe NWs: 0.2 g home-made ZnSe powder was placed at the centre of the quartz tube and evaporated at 1000°C for 2.5 hours, using Ar/H_2 (5%) gas to carry vapour downstream to the Au/Si substrate at a lower temperature region, and then cooled down naturally to the room temperature.

Growth recipes of 2D TMDs flakes

Commercial WO_3, MoO_3 and sulfur were used as solid sources. Either 1 mg of WO_3 or MoO_3 powder was put into the quartz tube near the centre in the high-temperature zone, and 0,25g sulfur powder was loaded in a tube near the inlet of carrier gas in the low-temperature zone. SiO_2/Si substrate was placed downstream of precursors in the high-temperature zone. After the growth stage, the furnace was cooled down to the room temperature naturally. The gas flow rate was held constant throughout the procedure. Separate substrates were used to prepare each WS_2 and MoS_2 samples. The optimal growth parameters for the procedure of

synthesizing 2D MoS_2 microcrystals were found to be 22 minutes at 700°C in the high temperature zone, and 30 minutes at 800°C for synthesizing 2D WS_2 microcrystals.

Ultrasonication of WS_2 flakes

4 mg of WS_2 powder was dispersed in 1.5 ml deionized (DI) water and ultrasonicated for several hours until a uniform and stable suspension of few-layer WS_2 flakes was obtained. WS_2 flakes from a suspension were drop-casted onto as-fabricated gold electrodes as a reference for WS_2 photoelectric properties.

Growth recipes of *core-shell* nanowire heterostructures

ZnO-WS_2 and *GaN-WS_2 NWs*: As-grown ZnO and GaN NWs were coated with amorphous WO_3 layer using reactive DC magnetron sputtering of a metallic tungsten target in mixed Ar/O_2 atmosphere. The thickness of the coating on a flat substrate was 100 nm, however, varied from 10 to 50 nm on NWs. Afterwards, ZnO- and GaN-WO_3 NWs were annealed in a quartz tube reactor in a sulfur atmosphere at 800°C for 30 minutes to convert the oxide coating to WS_2, followed by annealing in N_2 atmosphere for 30 minutes to sublimate the remaining WO_3.

ReS_2 on ZnO, ZnS and GaN NWs: ReS_2 shell surrounding the pure NW core was produced by a two-step process. Firstly, amorphous nonstoichiometric ReO_x coating was deposited by reactive DC magnetron sputtering of a metallic rhenium (Re) target in mixed Ar/O_2 atmosphere (1 minute at 100W DC power) in *Sidrabe SAF25/50* multifunctional cluster tool. Secondly, to convert rhenium oxide to ReS_2, as-prepared ReO_x samples were annealed for 20 minutes in a quartz tube reactor in a sulfur-rich atmosphere, created by placing sulfur powder upstream of the sample at 250°C and using N_2 as a carrier gas. Different temperatures in the range of 450-800°C were used to study the degree of crystallinity of as-grown ReS_2.

ZnO-MoS_2 NWs: As-grown ZnO NWs were immersed in a solution of 125 mg ammonium heptamolybdate $(NH_4)_6Mo_7O_{24}\cdot 4H_2O$ in 20 ml DI H_2O and subsequently dried at room temperature. Afterwards, the samples were annealed in a quartz tube reactor in a sulfur atmosphere at 700°C for 30 minutes to decompose and convert the precursor to MoS_2. Additional sample was prepared at 500°C to compare the MoS_2 crystallinity at different conversion temperatures. Furthermore, another approach was investigated – amorphous MoO_3 coating was deposited on pure ZnO NWs via magnetron sputtering (similarly to WO_3), followed by annealing in sulfur atmosphere at 700°C for 30 minutes.

ZnO-PbI_2 NWs: few layers of PbI_2 were deposited on the as-grown ZnO NW arrays via two different approaches: (1) thermal evaporation of a PbI_2 powder and (2) sputter deposition of a lead oxide coating followed by iodination at elevated temperatures. Both evaporation and sputtering were carried out in *Sidrabe SAF25/50* multifunctional cluster tool. In the first method, a simple thermal evaporation process was carried out in a vacuum chamber while rotating the ZnO NW sample (60 mg PbI_2 powder was evaporated from an Al_2O_3 crucible). The second method consists of two steps. Firstly, a lead oxide PbO_x coating was obtained by reactive DC magnetron sputtering of a metallic lead target in mixed Ar/O_2 atmosphere ($20\cdot 10^{-3}$ torr, 20 sccm Ar and 10 sccm O_2 gas flows, 5 minutes of sputtering at 100 W DC power). Secondly, as-prepared ZnO-PbO_x samples were annealed in a quartz tube in an iodine atmosphere at 420°C for 15 minutes using Ar/H_2 5% mixture as a carrier gas to convert lead oxide to lead iodide. An

iodine-rich atmosphere was obtained by placing 0.25 g iodine powder upstream of the sample at 120°C. The optimal annealing temperature was found to be 420°C, and the lead oxide conversion to PbI_2 starts around 350°C. One must optimize between a high coating crystallinity and the sublimation rate of the converted PbI_2 film, which increases rapidly above 400°C.

Photolithography process

Spin coating: MegaPosit SPR-700 positive-tone photoresist spin-coated for 40 seconds at 3500 rpm to obtain 1 μm thick coating.
Soft-bake: 60 seconds at 100°C on a hotplate.
Exposure: 140 mW at 80% intensity.
Hard-bake (post-exposure bake): 60 seconds at 120°C on a hotplate.
Development: MF-701 developer for 60 seconds in a single spray puddle at room temperature.
Metallization: Thermal evaporation to obtain 5/50 nm of Cr/Au film.
Lift-off: 24h in acetone.

APPENDIX B

Characterization of as-grown pure nanowires

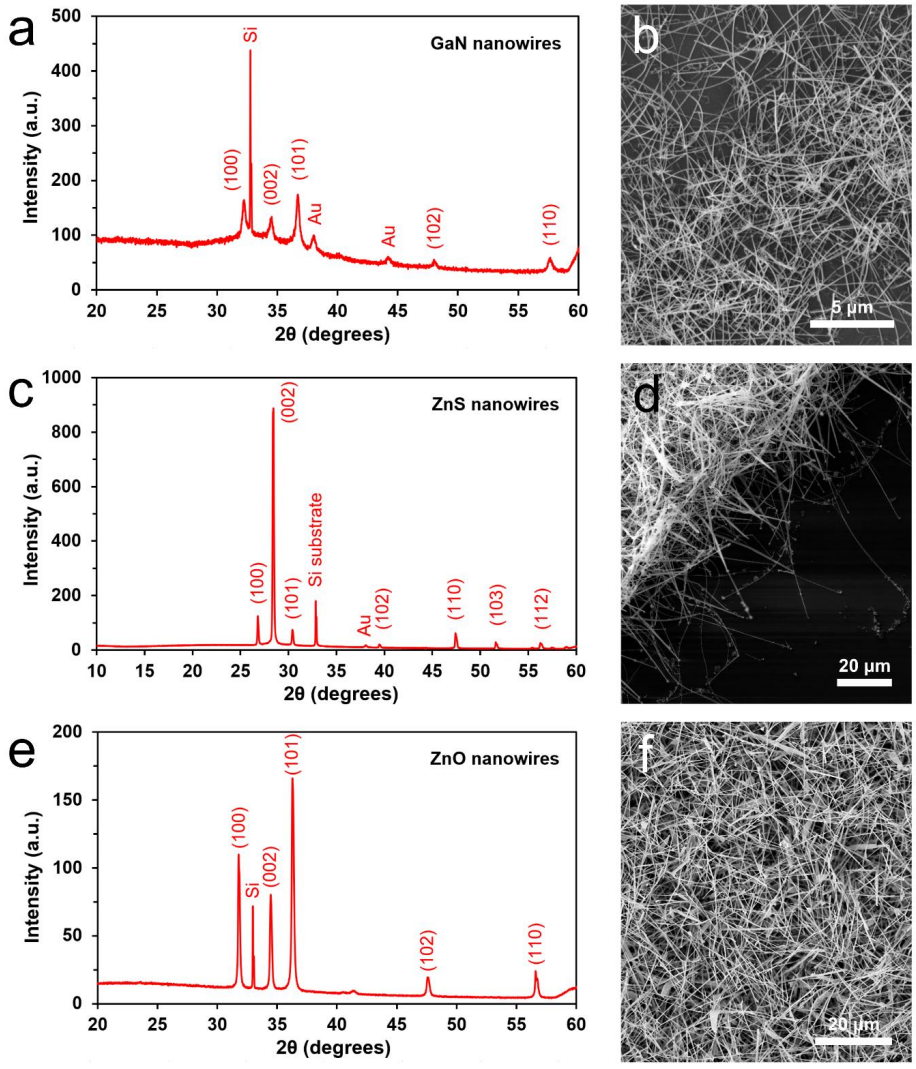

Figure B1. XRD patterns and SEM images of as-grown pure (a,b) GaN, (c,d) ZnS and (e,f) ZnO NW arrays on Si(100)/SiO_2 substrates.

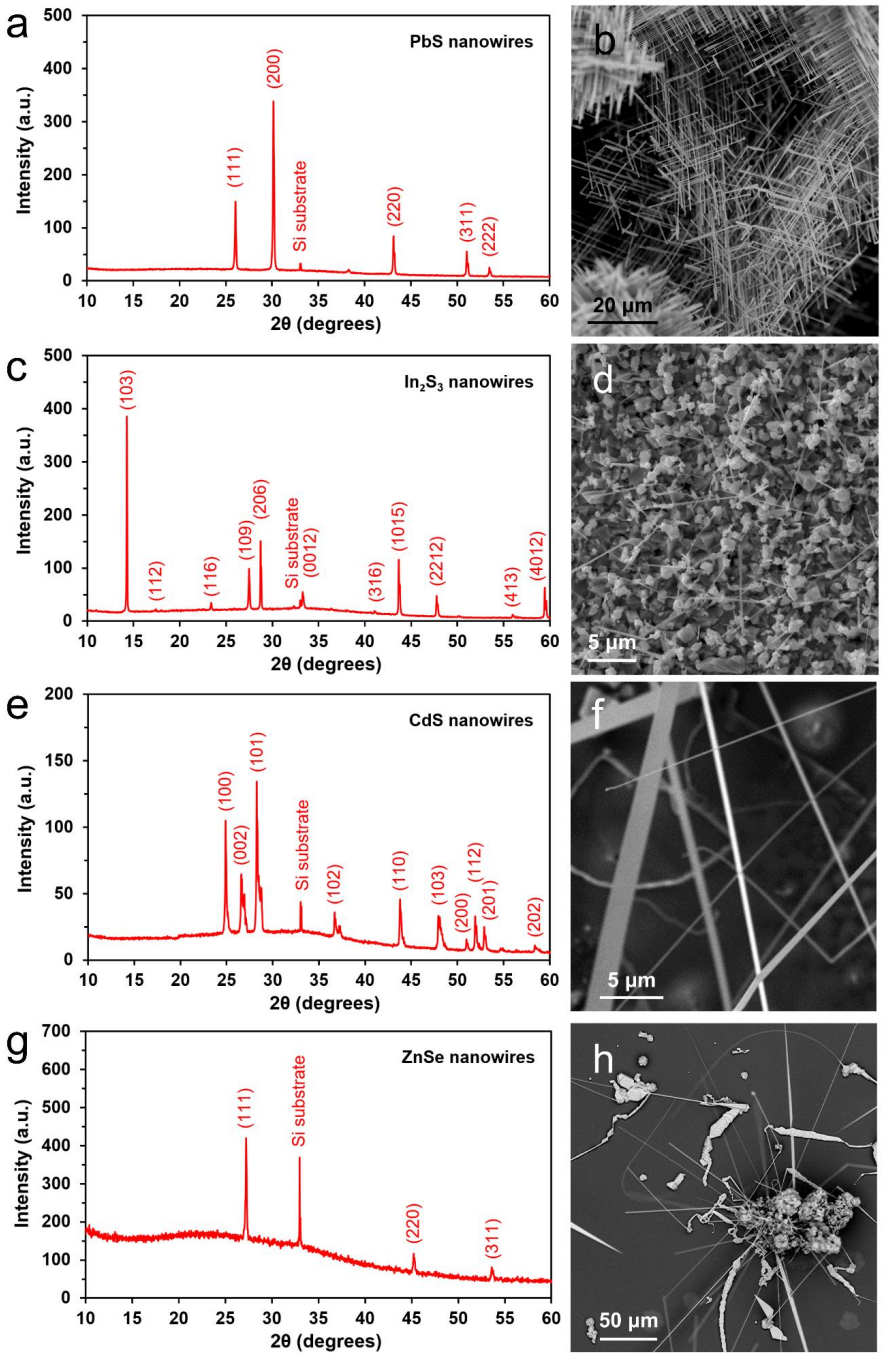

Figure B2. XRD patterns and SEM images of as-grown pure (a,b) PbS, (c,d) In_2S_3, (e,f) CdS and (g,h) ZnSe NW arrays on Si(100)/SiO_2 substrates.

Paper I

Journal of Alloys and Compounds 825 (2020) 154095

Contents lists available at ScienceDirect

Journal of Alloys and Compounds

journal homepage: http://www.elsevier.com/locate/jalcom

Growth and characterization of PbI_2-decorated ZnO nanowires for photodetection applications

Edgars Butanovs *, Sergei Piskunov , Aleksejs Zolotarjovs , Boris Polyakov

Institute of Solid State Physics, University of Latvia, Kengaraga Street 8, Riga, LV-1063, Latvia

ARTICLE INFO

Article history:
Received 1 October 2019
Received in revised form
23 January 2020
Accepted 27 January 2020
Available online xxx

Keywords:
PbI_2
Layered materials
Nanowire
Photodetector
Electron microscopy
Electronic structure calculations

ABSTRACT

In this study, we demonstrated for the first time the growth of ZnO nanowires (NWs) decorated with highly crystalline few-layer PbI_2 and fabricated two-terminal single-nanowire photodetector devices to investigate the photoelectric properties of the hybrid nanostructures. We developed a novel two-step growth process for uniform crystalline PbI_2 nanosheets via reactive magnetron deposition of a lead oxide film followed by subsequent iodination to PbI_2 on a ZnO NW substrate, and we compared as-grown hybrid nanostructures with ones prepared via thermal evaporation method. ZnO−PbI_2 NWs were characterized by scanning and transmission electron microscopy, X-ray diffraction analysis and photoluminescence measurements. By fabricating two-terminal single-nanowire photodetectors of the as-grown ZnO−PbI_2 nanostructures, we showed that they exhibit reduced dark current and decreased photoresponse time in comparison to pure ZnO NWs and have responsivity up to 0.6 A/W. *Ab initio* calculations of the electronic structure of both PbI_2 nanosheets and ZnO NWs have been performed, and show potential for photoelectrocatalytic hydrogen production. The obtained results show the benefits of combining layered van der Waals materials with semiconducting NWs to create novel nanostructures with enhanced properties for applications in optoelectronics or X-ray detectors.

1. Introduction

The surface plays an exceptionally important role in determining nanomaterial physical and chemical properties. The impact of surface modification on nanoscale material properties has been intensively explored for the last few decades [1–3]. Nanowires (NWs) are one-dimensional (1D) nanomaterials that exhibit promising properties beneficial for integration in functional devices, such as photodetectors, nanolasers, LEDs, etc. [4,5], and modification of their surface can significantly improve their electrical, optical and mechanical characteristics [3,4,6]. Modification or decoration of a NW surface has no restrictions of material lattice mismatch and its caused stress at the interface, unlike the conventional thin film growth [5,7,8], therefore, opening new possibilities to engineer novel hybrid nanostructures with desired properties, such as photon detection capability in a broad spectral range [9]. Currently, most research in this field is focused on developing precisely controllable nanostructure fabrication methods and tuning nanostructure properties for specific applications [6,7,9].

Zinc oxide (ZnO) is one of the most commonly studied NW materials due to its simple synthesis and wide field of applications, such as ultraviolet photodetectors [10,11] and piezoelectric nanogenerators [12], as well as the potential to be a scintillator material for X-ray detectors [13–15]. ZnO is an *n*-type semiconductor with a direct bandgap around 3.2–3.4 eV and it has a high exciton binding energy (60 meV), which allows room temperature excitonic emission [16]. ZnO NWs have frequently been used as template material for nanomaterial synthesis [17,18]. Furthermore, in several studies, it has been demonstrated that passivating the surface of ZnO nanostructures or decorating the NWs with specifically selected materials enhances light and gas detecting properties [19–24].

Lead (II) iodide (PbI_2) is a photoconductor material with 2.2–2.55 eV bandgap [25] and is typically employed in fabricating perovskite solar cells and photodetectors [26–30], and as an X-ray and γ-ray detector material [31–34]. PbI_2 has a layered structure in which the covalently bonded I–Pb–I repeating layers are bound by weak van der Waals (vdW) interaction [35]. Recently, it has gained more attention due to the extensive research on various 2D vdW materials, such as graphene and transition metal dichalcogenides

* Corresponding author.
E-mail address: edgarsb@cfi.lu.lv (E. Butanovs).

https://doi.org/10.1016/j.jallcom.2020.154095
0925-8388/

[36,37]. There are theoretical and experimental studies that show band structure shift from direct bandgap to indirect bandgap when the PbI_2 thickness is reduced from bulk to monolayer [35,38], as opposed to well-studied vdW materials, MoS_2, for example [39]. Therefore, monolayer PbI_2 is not expected to be an efficient material for optoelectronics applications. In the last few years, there have been several studies that demonstrate the growth of few-layer PbI_2 crystals and investigate their promising photodetection properties both on rigid and flexible substrates [25,35,40–42]. The growth of 1D PbI_2 NWs for high-sensitivity photodetector applications has also been reported [43]. Zhang et al. proposed low-temperature heteroepitaxial growth of PbI_2 thin film on submeter-sized graphene/polyethylene terephthalate (PET) substrate and showed its applicability in light detection [44]. However, there are challenges remaining in obtaining highly-crystalline and uniform large-area PbI_2 films.

Alternatively, NWs can be used as a template for growth and easier manipulation of layered vdW materials, such as WS_2 and MoS_2, while maintaining the high crystallinity of the materials used and even enhancing their properties [20,45–47]. Large-scale printing of NWs at specified locations on flexible substrates via roll-to-roll transfer has been demonstrated [48], therefore enabling the advancement of all-printed layered material- and NW-based electronic and optoelectronic devices in the future. Furthermore, some research has been done on the development of high-resolution NW-arrays for X-ray imaging [49,50]. There are also few reports on using single-nanowire devices for X-ray detection and beam shape characterization [51–53]. Consequently, using ZnO and PbI_2 materials in 1D hybrid nanostructures could potentially lead to next-generation high-resolution direct-conversion digital X-ray detector devices with advanced properties.

In this work, we demonstrate two different approaches to synthesise novel 1D ZnO–PbI_2 nanostructures. Highly crystalline few-layer PbI_2 was grown on ZnO NWs by: (1) direct thermal evaporation of PbI_2 powder, and (2) the conversion of a sputter-deposited lead oxide coating in iodine vapour at an elevated temperature. Two-terminal single-nanowire photodetectors were fabricated to show their enhanced photoelectric properties compared to pure ZnO NWs. The results show the potential of combining layered vdW materials with semiconducting nanowires to create novel nanostructures with advanced properties for potential photodetection applications. From our *ab initio* modelling, nanosized ZnO–PbI_2 heterostructures might be used for efficient photocatalytic hydrogen production from water.

2. Experimental details

2.1. Nanostructure synthesis and characterization

ZnO NWs were synthesised on oxidized silicon wafers SiO_2/Si(100) (*Semiconductor Wafer, Inc.*) via atmospheric pressure chemical vapour transport in an open-end horizontal quartz tube reactor using spherical Au nanoparticles (*Smart materials*, water suspension, 100 nm diameter) as a catalyst for the vapour-liquid-solid mechanism [54]. In short, 0.5 g of a 1:1 mixture of ZnO and carbon powders was loaded in a ceramic boat in the centre of the quartz tube at 900 °C. The vapour was transported downstream to the Au/Si substrate at a lower temperature region using N_2 as a carrier gas. The temperature was held constant for 90 min, followed by natural cooling to the room temperature. See Fig. S1 for the scanning electron microscope (SEM) images and X-ray diffraction (XRD) pattern of the as-grown ZnO NWs.

In the next step, a few layers of PbI_2 were deposited on the as-grown ZnO NW arrays via two different approaches: (1) thermal evaporation of a PbI_2 powder and (2) sputter deposition of a lead oxide coating followed by iodination at elevated temperatures. Both evaporation and sputtering were carried out in a *Sidrabe SAF25/50* multifunctional cluster tool. In the first method, a simple thermal evaporation process was carried out in a vacuum chamber at 10^{-5} torr while rotating the ZnO NW sample (60 mg PbI_2 powder was evaporated from an Al_2O_3 crucible). The second method consists of two steps. First, a lead oxide PbO_x coating (consisting of different phases, including PbO and PbO_2 as shown by the XRD data in Fig. S2) was obtained by reactive DC magnetron sputtering of a metallic lead target in a mixed Ar/O_2 atmosphere ($20 \cdot 10^{-3}$ torr, 20 sccm Ar and 10 sccm O_2 gas flows, 5 min of sputtering at 100 W DC power). Second, as-prepared ZnO-PbO_x samples were annealed in a quartz tube in an iodine atmosphere for 15 min using an Ar/H_2 5% mixture as the carrier gas to convert lead oxide to lead iodide. An iodine-rich atmosphere was obtained by placing 0.25 g iodine powder upstream of the sample at 120 °C. The optimal annealing temperature was found to be 420 °C, and the lead oxide conversion to PbI_2 starts around 350 °C. One must optimize between a high coating crystallinity and the sublimation rate of the converted PbI_2 film, which increases rapidly above 400 °C. As a reference sample for comparison, a PbI_2 thin film on SiO_2/Si substrate was prepared using the second approach.

The as-prepared nanostructure morphology was characterized using SEM-FIB (Lyra, Tescan), while the crystalline structure of the PbI_2 coating and ZnO NW was using a transmission electron microscope (TEM, Tecnai GF20, FEI) operated at a 200 kV accelerating voltage. The phase composition of the samples was studied using XRD (θ-θ Bragg–Brentano powder diffractometer PANalytical X'Pert Pro) with monochromatic Cu Kα irradiation and the spectra were analysed using PDXL2 software. Room-temperature photoluminescence (PL, Hamamatsu R92P PMT) spectra with a 266 nm excitation wavelength (fourth harmonic of CryLas Nd:YAG laser, 0.3 μJ power, 1 ns pulse duration, 5 kHz repetition rate) were measured to investigate the as-prepared nanostructure optical properties.

2.2. Single nanowire two-terminal photodetector device fabrication

To fabricate two-terminal single-nanowire photodetectors, first, gold microelectrodes with a 2 μm gap width were prepared on an oxidized silicon wafer by a conventional photolithography technique (see Fig. S3). The microelectrode array pattern was obtained using direct-write laser lithography (μPG101, Heidelberg Instruments) on Megaposit SPR700 photoresist (*Rohm and Haas Electronic Materials*), 5/45 nm Cr/Au film was deposited via thermal evaporation method followed by a lift-off procedure. Second, NWs were transferred onto the electrode array by mechanically pressing it to the substrate with the as-grown nanostructures, followed by welding selected single NWs to the corresponding underlying gold microelectrodes using electron-beam-assisted platinum deposition inside SEM-FIB to ensure the electric contact and fixed position. At least ten single-nanowire photodetectors (more than five for each synthesis method) were fabricated so consistent conclusions could be made.

2.3. Device measurements

Current–voltage (I–V) characteristics and photoresponse of the fabricated single-NW photodetector devices were measured with a two-contact microprobe station connected to a low-noise current preamplifier (SR570, Stanford Research Systems) and oscilloscope (TDS2004B, Tektronix). A 405 nm wavelength semiconductor diode laser (CNI Laser) with 1 W/cm^2 power was the illumination source for the photoresponse measurements. An optical beam shutter (Thorlabs SH05) was used for time-resolved measurements. All the

measurements were performed at room temperature and in air.

2.4. Computational details

Total energy first-principle calculations for [0001]-oriented mono- (ML), bi- (2 ML) and three-layered (3 ML) PbI_2 nanosheets, and 24-layer thick [1−100] oriented slabs, to mimic the surface of ZnO nanowires, were performed using the HSE06 hybrid exchange-correlational functional [55] within the density functional theory (DFT), as implemented in the computer code CRYSTAL17 [56]. Localized Gaussian type functions (GTFs) in the form of atom-centred basis sets (BSs) for expansion of periodic crystalline orbitals for Zn and O were taken in the form of full electron Triple-Zeta Valence BS with polarization functions [56], while effective-core pseudopotential BS were taken for Pb and I [56]. The reliability of the chosen theoretical method were proven by calculations of bandgap energy (δ) for bulk phase ZnO and PbI_2 crystals (see Fig. S5). The calculated bandgaps for all materials under study are in good agreement with those experimentally observed. To provide a balanced summation in both direct and reciprocal lattices, reciprocal space integration was performed by sampling the Brillouin zone (BZ) with a $6 \times 6 \times 1$ Pack-Monkhorst mesh [57], which results in a total of 20 k-points evenly distributed over the BZs. For every fixed crystalline geometry calculation, the convergency was reached only when the total energy differed by less than 10^{-7} a.u. in two successive cycles of the self-consistent field (SCF) procedure [56]. Full geometry optimization was performed for all nanostructures considered in this study.

3. Results and discussion

3.1. Morphology, structure and photoluminescence measurements

SEM was used to image as-grown individual NWs and NW arrays and study their morphology. Pure ZnO NWs are typically 20−30 μm long with a diameter around 100 nm and exhibit a smooth surface (see Figs. S1(a and b)). Fig. 1(a and b) shows ZnO NWs with a thermally deposited PbI_2 coating. No significant change in diameter is observed; however, a very fine increase in surface roughness is visible. NWs with a sputter-deposited lead oxide coating with a fine roughness are shown in Fig. 1(c and d), where a considerable (up to 100 nm) increase in diameter can be seen. After annealing such NWs in iodine vapour at elevated temperatures, the surface roughness greatly increased; however the diameter is significantly reduced as a fraction of the coated material is sublimated after the transformation (see Fig. 1(e and f)). The final coating is not uniform over the entire length of NWs as some thicker particles and islands can be observed. SEM images of the reference sample, PbI_2 thin film converted from sputter-deposited lead oxide, are shown in Fig. 1(g and h). The film exhibits hexagonal domains, presumably highly crystalline as PbI_2 typically crystallizes in a hexagonal structure.

A deeper insight into the nanostructures' inner structure was obtained using TEM. Fig. 2(a−*c)* shows TEM images of ZnO−PbI_2 NWs obtained by the thermal evaporation method at different magnifications. The lower resolution images show noticeable contrast between the two NW sides (PbI_2 layers correspond to the darker region), indicating non-uniform coating deposition, which is expected from the thermal evaporation approach since it is a line-of-sight method. At a high resolution, the crystalline structure of the nanostructure is revealed. The layers of PbI_2 grown on the ZnO NW surface are distinguishable as parallel black lines. Typically, the thickness of the coating varies between 5 and 10 monolayers (each consisting of I−Pb−I atomic planes), with interlayer distance measured around 7 Å, which is in a good agreement with the lattice constant (a = 6.979 Å) of bulk hexagonal PbI_2 (ICDD-PDF #07−0235). Furthermore, the single-crystalline nature of the ZnO NWs is clearly visible; the measured interplanar distance is 2.8 Å, corresponding to hexagonal ZnO wurtzite (ICDD-PDF #36−1451), as confirmed by the XRD pattern (see Fig. S1(c)). The TEM images of the ZnO−PbI_2 nanostructures obtained by conversion of sputter-deposited lead oxide coating are shown in Fig. 2(d−*f)*. In this case, the PbI_2 coating is uniformly distributed over the entire ZnO NW surface; however, the surface roughness is significantly increased. The thickness of the coating typically varies between 5 and 15 monolayers, with some islands being even thicker. As in to the first approach, the measured interlayer distance is around 7 Å.

To complement TEM structural investigations and confirm the presence of phases, XRD measurements were performed on the as-prepared samples. Fig. 3(a and b) show XRD patterns of NW arrays prepared by the two approaches: thermal evaporation and converting the magnetron-sputtered lead oxide coating, respectively.

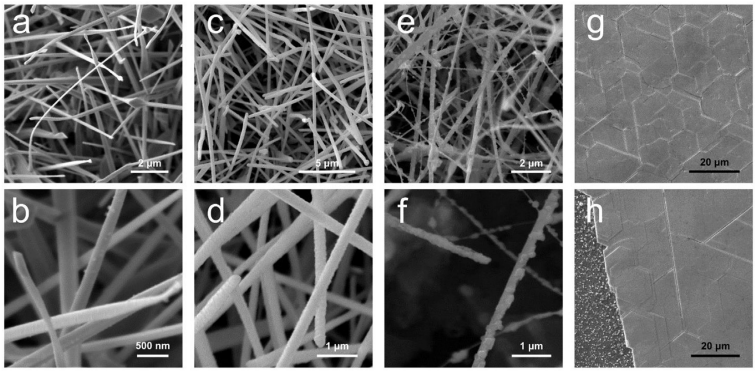

Fig. 1. Scanning electron microscope images of (a,b) ZnO−PbI_2 NWs made using the thermal evaporation approach; (c,d) ZnO NWs covered by lead oxide deposited by magnetron sputtering; (e,f) ZnO−PbI_2 NWs made by converting the lead oxide coating; (g,h) PbI_2 thin film made by converting a lead oxide film.

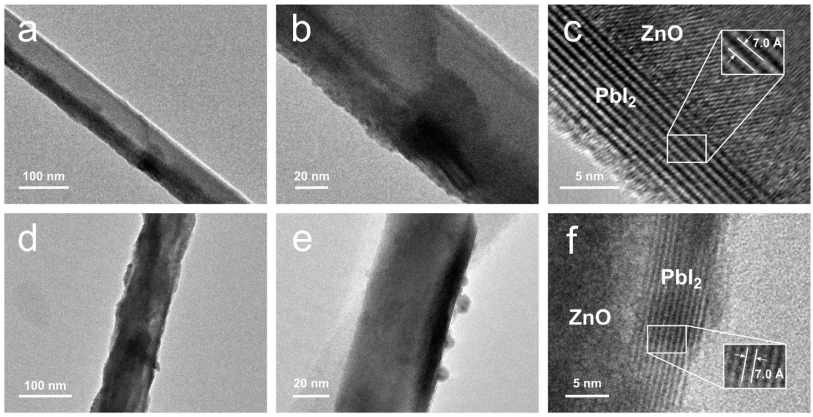

Fig. 2. Transmission electron microscope images at different magnifications of (a,b,c) ZnO–PbI_2 NWs made using the thermal evaporation approach, and (d,e,f) ZnO–PbI_2 NWs made by converting the magnetron-sputtered lead oxide coating. The insets show measured atomic interlayer distances between PbI_2 layers.

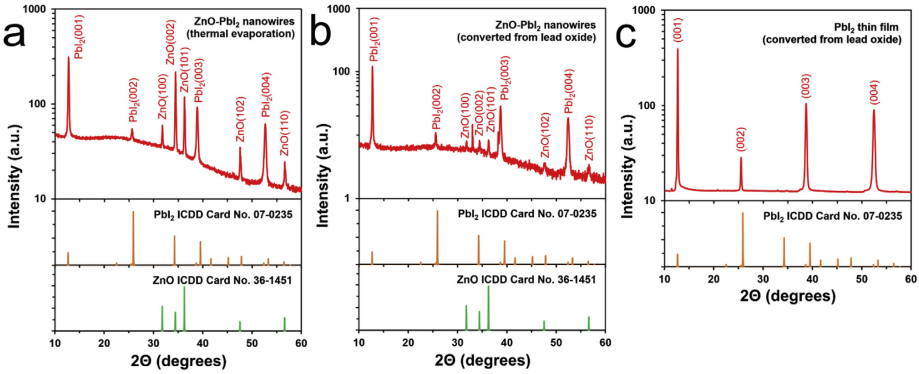

Fig. 3. X-ray diffraction patterns of (a) ZnO–PbI_2 NW arrays on Si/SiO_2 substrate made using the thermal evaporation approach; (b) ZnO–PbI_2 NW arrays on Si/SiO_2 substrate made by converting the magnetron-sputtered lead oxide coating; (c) PbI_2 thin film made by converting a lead oxide film.

Both patterns indicate highly crystalline hexagonal ZnO wurtzite (ICDD-PDF #36–1451) and hexagonal PbI_2 (ICDD-PDF #07–0235) phases. No other phases were observed, confirming the high crystallinity of the as-prepared nanostructures, as did the TEM investigations. It is worth noting that the ratio between PbI_2 and ZnO peak intensity is not only related to the amount of PbI_2 on ZnO NWs but also the amount of PbI_2 crystallites on the Si/SiO_2 substrate. Therefore, spectra cannot be properly used to describe the phase composition ratio in the nanostructures. Furthermore, ZnO NW Bragg peak intensities vary between the samples - due to an inhomogeneous gold nanoparticle catalyst deposition from colloid on the silicon substrate; the density of as-grown ZnO nanowires arrays was also not homogeneous while the PbI_2 layer is relatively homogeneous over the substrate due to the precisely controllable deposition method. In Fig. 3(b), the Bragg peak at 33° is attributed to diffraction in the Si(100) substrate (forbidden Si(200) reflection). The XRD pattern of pure ZnO NWs is given in Fig. S1(c). The XRD pattern of the PbI_2 thin film reference sample shows its highly crystalline structure (see Fig. 3(c)), confirming that the conversion of a lead oxide film in iodine vapour is a viable method how to obtain crystalline PbI_2 thin films.

To study the optical properties, room temperature PL in the as-prepared samples was measured in a wavelength range from 400 to 650 nm, excited by a 266 nm laser. Generally, PbI_2 has a direct band-to-band transition at around 495 nm (~2.5 eV) [58]; however, a broad band peaked at 510–525 nm has been previously observed and attributed to recombination through defects, such as iodine and lead vacancies [25]. The PL spectrum of pure ZnO NWs exhibits a defect-related band at ~520 nm [16]. Therefore, the interpretation of the ZnO–PbI_2 nanostructure spectra might be ambiguous due to this ZnO and PbI_2 PL band overlapping, since higher ZnO PL intensities might lead to indistinguishable PbI_2 PL peaks or vice versa.

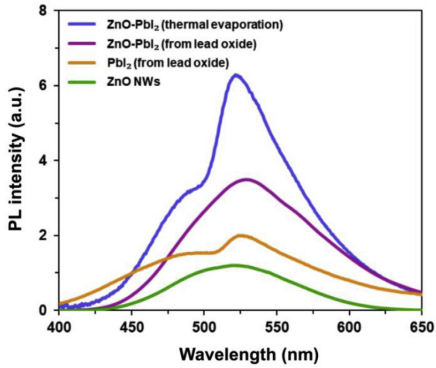

Fig. 4. Room temperature photoluminescence (PL) spectra at 266 nm excitation wavelength for the different as-prepared samples. The PL intensity is depicted in arbitrary units and does not contain information about relative intensities between the measured spectra.

Fig. 4 depicts our measured PL spectra of pure ZnO NWs, the PbI_2 thin film reference sample, and the ZnO–PbI_2 nanostructures prepared via both approaches. It is worth noting that the PL intensity is depicted in arbitrary units and does not contain information about the relative intensities between the obtained spectra. The ZnO NW spectrum exhibits the typical defect band at 520 nm and the PbI_2 thin film sample (prepared by converting lead oxide film) shows two emission peaks: the direct band-to-band transition at around 495 nm and the defect-related band at around 530 nm. The ZnO–PbI_2 nanostructures (prepared by thermal evaporation approach) exhibit two peaks at 495 nm and 525 nm; however, the nanostructures prepared via lead oxide conversion exhibit only one band with a peak at 530 nm due to the higher intensity overlapping ZnO peak. One can see and interpret the difference between the PbI_2 peak ratio for samples prepared with different methods due to the defect-related peak maximum shift. For example, the defect/band-to-band peak intensity ratio for thermally evaporated PbI_2 is ~2, while for lead oxide converted PbI_2, it is ~1.33 Therefore, by also considering the ZnO peak contribution, one can qualitatively assume that lead oxide conversion via iodination leads to fewer defects in PbI_2 coatings than the thermal evaporation approach.

3.2. Device photoresponse measurements

Two-terminal single-nanowire photodetectors were fabricated from the nanostructures prepared via both approaches, and pure ZnO NWs. Fig. 5(a–*c*) shows the characteristics of the ZnO–PbI_2 single NW devices made using the thermal evaporation approach, while Fig. 5(d–*f*) shows the characteristics of the ZnO–PbI_2 single NW devices made by converting the magnetron-sputtered lead oxide coating (more than five single-nanowire photodetectors for each synthesis method were fabricated so that consistent conclusions could be made). The inset contains an SEM image of a typical as-prepared NW device. Both dark state current-voltage (I–V) characteristics of ZnO–PbI_2 NWs in Fig. 5(a) and (d) exhibit linear behaviour, indicating that ohmic contacts formed between the nanostructures and the electrodes, as is expected for PbI_2 on gold [40,59] and which is beneficial for efficient photogenerated carrier collection. In contrast, pure ZnO NWs typically form Schottky contact with gold electrodes (see the nonsymmetric I–V curve in Fig. S4(a)) [60]. The devices were illuminated with 405 nm wavelength light in a periodic fashion to study their photoresponse properties as shown in Fig. 5(b) and (e). All the devices were also tested for 532 nm and 660 nm light

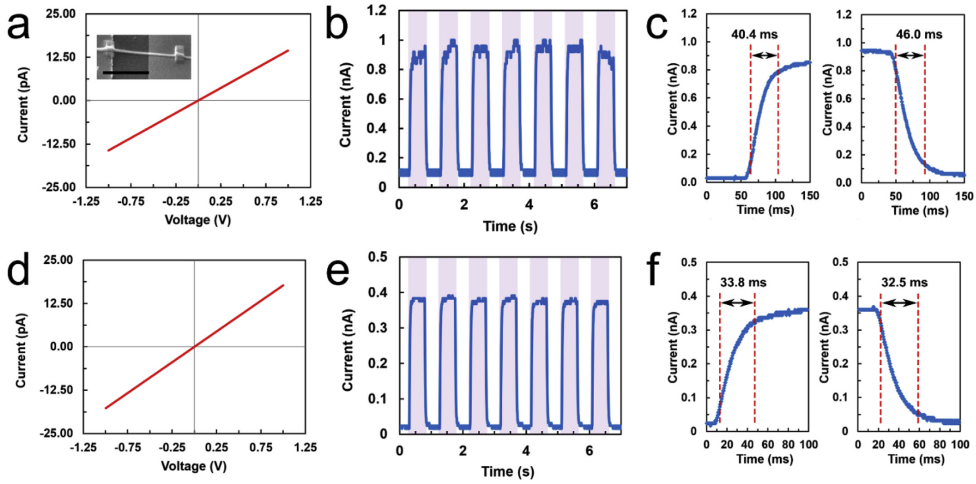

Fig. 5. ZnO–PbI_2 single NW made using the thermal evaporation approach (a) dark state I–V characteristics, (b) on–off photoresponse, (c) time-resolved photoresponse measurements; and ZnO–PbI_2 single NW made by converting the lead oxide coating (d) dark state I–V characteristics, (e) on–off photoresponse, (f) time-resolved photoresponse measurements at 1 V bias voltage and 1 W/cm^2 light intensity with 405 nm wavelength light. The inset shows an SEM image of a typical single-nanowire two-terminal photodetector. The scale bar corresponds to 2 μm.

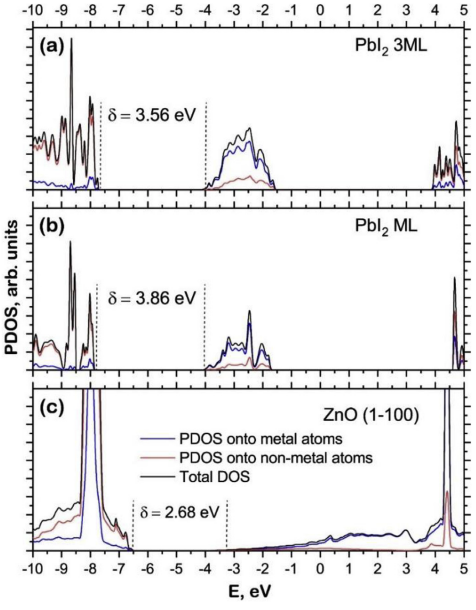

Fig. 6. Total and projected densities of states (PDOS) calculated for (a) 3-monolayer thick PbI_2 nanosheet, (b) monolayer thick PbI_2 nanosheet, and (c) ZnO (1–100) slab. The 24-layer thick slab of ZnO substrate is symmetrically terminated to mimic the surface of the nanowires. PDOS projected onto all orbitals of corresponding metal or non-metal atoms. The energy scale is shown with respect to the vacuum level.

illumination; however, no increase in current was observed due to the relatively wide bandgap of the studied materials. On-off measurements demonstrate a steady, rapid and repeatable increase and decrease of the current when the illumination is turned on or off, respectively; therefore, showing good stability and reversibility of the devices. ZnO–PbI_2 NWs exhibit low dark current (10–100 pA) which is necessary for high-performance photodetectors, while for pure ZnO NWs, it can be up to several tens of nA (see Fig. S4(b)). The current enhancement ratios (I_{on}/I_{off}) for the nanostructures prepared via both approaches were measured to be at around 10–20, in contrast to less than 2 for pure ZnO NWs. Time-resolved photoresponse measurements were performed to evaluate the rise and decay time of the as-prepared ZnO–PbI_2 devices, defined as the required time for the photocurrent to increase or decrease to 90% or 10% of its maximum value, respectively. As shown in Fig. 5(c) and (f), the obtained values are in the 30–50 ms range, which is almost two orders of magnitude faster than the pure ZnO NWs (see Fig. S4(c)) and comparable to typical NW or 2D PbI_2 photodetector response times [35,41,42,59,61]. The slow response of ZnO NWs is due to the influence of oxygen molecules on the surface states and their effect on photoresponse kinetics is widely discussed in the literature [62,63]. Here and in our previous work [20], we passivated the surface of ZnO NWs using a thin PbI_2 or WS_2 coating, respectively, and photodetectors of such heterostructures exhibit reduced dark current and photoresponse time, although it also decreased on-state current I_{on} in comparison to pure ZnO NWs. It is well known that adsorbed oxygen species influence electrical properties (electrical conductivity decreases with exposure to oxygen) of metal oxide nanostructures [11,64–66]. Consequently, band bending, induced by adsorbed oxygen molecules that capture free electrons, causes an efficient photogenerated electron-hole separation that leads to high gain in single-nanowire photodetectors. The presence of the PbI_2 layers in our nanostructures protects the ZnO surface from oxygen adsorption that might influence surface-related photoinduced processes and decrease the number of charge carrier trapping centres.

The thickness of PbI_2 on ZnO NWs, which were used in the as-fabricated photodetector devices, was typically 6–13 layers. No significant changes in the photodetector characteristics, such as spectral responsivity R_λ, response time or current enhancement ratios (I_{on}/I_{off}), were observed between the samples in this PbI_2 thickness range. It is worth noting, that there are theoretical and experimental studies that show a band structure shift from direct bandgap to indirect bandgap when the PbI_2 thickness is reduced from bulk to monolayer [35,38]; therefore, monolayer PbI_2 is not expected to be an efficient material for optoelectronics applications and few-layer PbI_2 should be used instead.

Spectral responsivity (R_λ) and external quantum efficiency (EQE) are used to evaluate photoconductive properties of a material. R_λ and EQE are respectively defined as $R_\lambda = \Delta I/(PS)$ and $EQE = hcR_\lambda/(e\lambda)$ [40], where ΔI is the difference between the photocurrent I_{on} and the dark current I_{off}, P is the light power density, S is the effective illumination area (estimated as the electrode gap width × NW diameter), h is Planck's constant, c is the speed of light, e is the electron charge and λ is the light wavelength. Large R_λ and EQE values correspond to high photodetector sensitivity. A responsivity as high as ~0.6 A/W (EQE ~180%) was calculated for the ZnO–PbI_2 single NW devices made using the thermal evaporation approach and ~0.3 A/W (EQE ~90%) for the ones made by converting the magnetron-sputtered lead oxide coating; however, it is not valid to compare the two different synthesis approaches based only on the responsivity values as the value range for all as-fabricated devices overlapped no matter which method was used. The obtained R_λ and EQE values are comparable to other typical state-of-the-art 1D nanostructure [61] and 2D PbI_2 [41,42,44,59] photodetectors.

3.3. Electronic structure calculations

Fig. 6 compares the total and projected densities of states (PDOS) calculated for [0001]-oriented monolayered (ML) and three-layered (3 ML) PbI_2 nanosheets, Fig. 6(a) and (b), respectively, and the PDOS calculated for slab models of [1–100] oriented ZnO NW (Fig. 6(c)). The PDOS calculated for bi-layered (2 ML) PbI_2 nanosheet is not presented in Fig. 6 since its electronic structure does not practically differ from that calculated for 3 ML PbI_2. For all PbI_2 nanosheets under study, the upper part of the valence band (VB) is predominantly formed by the iodine (5*p*) orbitals with significant contributions from lead (6*s*) orbitals. The bottom of the conduction band (CB) of PbI_2 nanosheets is formed mainly from Pb (6*p*) states. In the case of ZnO (1–100) surfaces, the VB top is formed by oxygen 2*p* states, while 3*d* orbitals of Zn mainly form the CB bottom. The band edge positions of ML and 3 ML PbI_2 differ from those of bulk (Fig. S5(a)). The bottom of the CB is shifted down, closer to the hydrogen evolution potential of −4.44 eV. The position of the top of the VB calculated for (1–100) ZnO NW surfaces is located near −5.67 eV oxygen reduction potential, which allows us to conclude that the hybrid ZnO–PbI_2 NWs can be considered as promising potential materials for efficient solar-driven photo (electro)catalytic water splitting.

4. Conclusions

In this paper, we demonstrated for the first time the growth of ZnO NWs decorated with highly crystalline few-layer PbI_2 and fabricated two-terminal single-nanowire photodetector devices to investigate the photoelectric properties of the hybrid ZnO−PbI_2 nanostructures. We developed a novel two-step growth process for uniform crystalline PbI_2 nanosheets via reactive magnetron deposition of a lead oxide film followed by subsequent iodination in iodine vapour to PbI_2 at 420 °C on a ZnO NW substrate, and we compared as-grown hybrid nanostructures with ones prepared via thermal evaporation method. As-prepared two-terminal single-nanowire ZnO−PbI_2 photodetectors are comparable to state-of-the-art 1D nanostructure and 2D PbI_2 photodetectors and exhibit enhanced optoelectronic characteristics, such as reduced dark current and significantly decreased photoresponse time compared to pure ZnO NWs, and have responsivity up to 0.6 A/W. We found that the preparation method does not significantly affect the photoelectric properties of the nanostructures; however, PbI_2 obtained by thermal evaporation benefits from a smoother coating and, presumably, less optical defect states, but lacks the uniform coverage of PbI_2 converted from lead oxide coating. First principle DFT calculations on few-layer PbI_2 nanosheets, thin slabs to mimic the surface of ZnO NWs, and bulk phase ZnO and PbI_2 crystals, were performed to obtain the electronic structure of the materials under study. The results show the potential of combining layered vdW materials with semiconducting nanowires to create novel nanostructures with enhanced properties for applications in optoelectronics or X-ray detectors. Our *ab initio* modelling also shows that nanosized ZnO−PbI_2 heterostructures might be used for efficient photocatalytic and electrocatalytic hydrogen production from water.

Declaration of competing interest

There are no conflicts of interest to declare.

CRediT authorship contribution statement

Edgars Butanovs: Methodology, Validation, Investigation, Visualization, Writing - original draft. **Sergei Piskunov:** Methodology, Formal analysis, Visualization. **Aleksejs Zolotarjovs:** Investigation. **Boris Polyakov:** Conceptualization, Supervision, Investigation, Writing - review & editing.

Acknowledgements

Financial support provided by Scientific Research Project for Students and Young Researchers Nr. SJZ/2017/1 realized at the Institute of Solid State Physics, University of Latvia is greatly acknowledged. The authors are grateful to Liga Bikse for XRD measurements.

Appendix A. Supplementary data

Supplementary data to this article can be found online at https://doi.org/10.1016/j.jallcom.2020.154095.

References

[1] J. Wen, et al., Photocatalysis fundamentals and surface modification of TiO2 nanomaterials, Chin. J. Catal. 36 (2015) 2049−2070.
[2] Y. Guo, K. Xu, C. Wu, J. Zhao, Y. Xie, Surface chemical-modification for engineering the intrinsic physical properties of inorganic two-dimensional nanomaterials, Chem. Soc. Rev. 44 (2015) 637−646.
[3] A. Pescaglini, D. Iacopino, Metal nanoparticle−semiconductor nanowire hybrid nanostructures for plasmon-enhanced optoelectronics and sensing, J. Mater. Chem. C 3 (2015) 11785−11800.
[4] R. Yan, D. Gargas, P. Yang, Nanowire photonics, Nat. Photon. 3 (2009) 569−576.
[5] Y. Li, F. Qian, J. Xiang, C.M. Lieber, Nanowire electronic and optoelectronic devices, Mater. Today 9 (2006) 18−27.
[6] L.J. Lauhon, M.S. Gudiksen, D. Wang, C.M. Lieber, Epitaxial core−shell and core−multishell nanowire heterostructures, Nature 420 (2002) 57−61.
[7] Y. Dong, B. Tian, T.J. Kempa, C.M. Lieber, Coaxial group III−Nitride nanowire photovoltaics, Nano Lett. 9 (2009) 2183−2187.
[8] T.J. Kempa, R.W. Day, S.-K. Kim, H.-G. Park, C.M. Lieber, Semiconductor nanowires: a platform for exploring limits and concepts for nano-enabled solar cells, Energy Environ. Sci. 6 (2013) 719.
[9] W. Tian, D. Liu, F. Cao, L. Li, Hybrid nanostructures for photodetectors, Adv. Opt. Mater. 5 (2017) 1600468.
[10] Y. Zhang, M.K. Ram, E.K. Stefanakos, D.Y. Goswami, Synthesis, characterization, and applications of ZnO nanowires, J. Nanomater. 1−22 (2012), 2012.
[11] C. Soci, et al., ZnO nanowire UV photodetectors with high internal gain, Nano Lett. 7 (2007) 1003−1009.
[12] Z.L. Wang, Piezoelectric nanogenerators based on zinc oxide nanowire arrays, Science 312 (2006) 242−246.
[13] M.J.F. Empizo, et al., Photoluminescence properties of a single ZnO microstructure for potential scintillator applications, Opt. Mater. (Amst). 38 (2014) 256−260.
[14] P.J. Simpson, R. Tjossem, A.W. Hunt, K.G. Lynn, V. Munné, Superfast timing performance from ZnO scintillators, Nucl. Instrum. Methods Phys. Res. Sect. A Accel. Spectrom. Detect. Assoc. Equip. 505 (2003) 82−84.
[15] P.A. Rodnyi, I.V. Khodyuk, Optical and luminescence properties of zinc oxide (Review), Optic Spectrosc. 111 (2011) 776−785.
[16] Ü. Özgür, et al., A comprehensive review of ZnO materials and devices, J. Appl. Phys. 98 (2005), 041301.
[17] Z.L. Wang, ZnO nanowire and nanobelt platform for nanotechnology, Mater. Sci. Eng. R Rep. 64 (2009) 33−71.
[18] H. Liu, Z. Feng, J. Wang, J. Diao, D. Su, Synthesis of hollow carbon nanostructures using a ZnO template method, N. Carbon Mater. 31 (2016) 87−91.
[19] K. Liu, M. Sakurai, M. Liao, M. Aono, Giant improvement of the performance of ZnO nanowire photodetectors by Au nanoparticles, J. Phys. Chem. C 114 (2010) 19835−19839.
[20] E. Butanovs, et al., Fast-response single-nanowire photodetector based on ZnO/WS2 core/shell heterostructures, ACS Appl. Mater. Interfaces 10 (2018) 13869−13876.
[21] A. Pescaglini, et al., Hot-electron injection in Au nanorod−ZnO nanowire hybrid device for near-infrared photodetection, Nano Lett. 14 (2014) 6202−6209.
[22] O. Lupan, V. Postica, T. Pauporté, M. Hoppe, R. Adelung, UV nanophotodetectors: a case study of individual Au-modified ZnO nanowires, Sensor Actuator Phys. 296 (2019) 400−408.
[23] J. Gröttrup, et al., UV detection properties of hybrid ZnO tetrapod 3-D networks, Vacuum 146 (2017) 492−500.
[24] H.-M. Kim, J.-H. Park, S.-K. Lee, Fiber optic sensor based on ZnO nanowires decorated by Au nanoparticles for improved plasmonic biosensor, Sci. Rep. 9 (2019) 15605.
[25] J. Zhang, et al., Layered ultrathin PbI2 single crystals for high sensitivity flexible photodetectors, J. Mater. Chem. C 3 (2015) 4402−4406.
[26] Y. Fu, et al., Metal halide perovskite nanostructures for optoelectronic applications and the study of physical properties, Nat. Rev. Mater. 4 (2019) 169−188.
[27] H.L. Zhu, et al., Achieving high-quality Sn−Pb perovskite films on complementary metal-oxide-semiconductor-compatible metal/silicon substrates for efficient imaging array, ACS Nano 13 (2019) 11800−11808.
[28] H.L. Zhu, et al., Low-bandgap methylammonium-rubidium cation Sn-rich perovskites for efficient ultraviolet-visible-near infrared photodetectors, Adv. Funct. Mater. 28 (2018) 1706068.
[29] H.L. Zhu, et al., Room-temperature solution-processed NiOx:PbI2 nanocomposite structures for realizing high-performance perovskite photodetectors, ACS Nano 10 (2016) 6808−6815.
[30] F. Ye, et al., High-quality cuboid CH3NH3PbI3 single crystals for high performance X-ray and photon detectors, Adv. Funct. Mater. 29 (2019) 1806984.
[31] K. Shah, et al., Lead iodide X-ray detection systems, Nucl. Instrum. Methods Phys. Res. Sect. A Accel. Spectrom. Detect. Assoc. Equip. 380 (1996) 266−270.
[32] J.F. Condeles, et al., Fabrication and characterization of thin films of PbI2 for medical imaging, J. Non-Cryst. Solids 338−340 (2004) 81−85.
[33] X.H. Zhu, Z.R. Wei, Y.R. Jin, A.P. Xiang, Growth and characterization of a PbI2 single crystal used for gamma ray detectors, Cryst. Res. Technol. 42 (2007) 456−459.
[34] H. Sun, et al., Laser-induced surface recrystallization of polycrystalline PbI2 thick films for X-ray detector application, Appl. Surf. Sci. 427 (2018) 1146−1151.
[35] M. Zhong, et al., Large-scale 2D PbI2 monolayers: experimental realization and their indirect band-gap related properties, Nanoscale 9 (2017) 3736−3741.
[36] D.L. Duong, S.J. Yun, Y.H. Lee, van der Waals layered materials: opportunities and challenges, ACS Nano 11 (2017) 11803−11830.
[37] W. Choi, et al., Recent development of two-dimensional transition metal dichalcogenides and their applications, Mater. Today 20 (2017) 116−130.

[38] A.S. Toulouse, et al., Frenkel-like Wannier-Mott excitons in few-layer PbI2, Phys. Rev. B 91 (2015) 165308.
[39] A. Splendiani, et al., Emerging photoluminescence in monolayer MoS2, Nano Lett. 10 (2010) 1271–1275.
[40] M. Zhong, et al., Flexible photodetectors based on phase dependent PbI2 single crystals, J. Mater. Chem. C 4 (2016) 6492–6499.
[41] W. Zheng, et al., High-crystalline 2D layered PbI2 with ultrasmooth surface: liquid-phase synthesis and application of high-speed photon detection, Adv. Electron. Mater. 2 (2016) 1600291.
[42] Y. Wang, L. Gan, J. Chen, R. Yang, T. Zhai, Achieving highly uniform two-dimensional PbI2 flakes for photodetectors via space confined physical vapor deposition, Sci. Bull. 62 (2017) 1654–1662.
[43] J. Liu, et al., Synthesis of PbI2 nanowires for high sensitivity photodetectors, RSC Adv. 6 (2016) 59445–59449.
[44] J. Zhang, et al., Low-temperature heteroepitaxy of 2D PbI 2/graphene for large-area flexible photodetectors, Adv. Mater. 30 (2018) 1803194.
[45] B. Polyakov, et al., Unexpected epitaxial growth of a few WS2 layers on {1100} facets of ZnO nanowires, J. Phys. Chem. C 120 (2016) 21451–21459.
[46] E. Butanovs, A. Kuzmin, J. Butikova, S. Vlassov, B. Polyakov, Synthesis and characterization of ZnO/ZnS/MoS2 core-shell nanowires, J. Cryst. Growth 459 (2017) 100–104.
[47] F. Chen, T. Wang, L. Wang, X. Ji, Q. Zhang, Improved light emission of MoS2 monolayers by constructing AlN/MoS2 core–shell nanowires, J. Mater. Chem. C 5 (2017) 10225–10230.
[48] Z. Fan, et al., Toward the development of printable nanowire electronics and sensors, Adv. Mater. 21 (2009) 3730–3743.
[49] M. Kobayashi, et al., Development of vertically aligned ZnO-nanowires scintillators for high spatial resolution x-ray imaging, Appl. Phys. Lett. 106 (2015), 081909.
[50] A. Taheri, S. Saramad, S. Setayeshi, ZnO nanowires in polycarbonate membrane as a high resolution X-ray detector (a Geant4 simulation), Nucl. Instrum. Methods Phys. Res. Sect. A Accel. Spectrom. Detect. Assoc. Equip. 716 (2013) 15–22.
[51] J. Wallentin, et al., Hard X-ray detection using a single 100 nm diameter nanowire, Nano Lett. 14 (2014) 7071–7076.
[52] J. Wallentin, M. Osterhoff, T. Salditt, In operando X-ray nanodiffraction reveals electrically induced bending and lattice contraction in a single nanowire device, Adv. Mater. 28 (2016) 1788–1792.
[53] A. Johannes, et al., In operando X-ray imaging of nanoscale devices: composition, valence, and internal electrical fields, Sci. Adv. 3 (2017) eaao4044.
[54] P. Yang, et al., Controlled growth of ZnO nanowires and their optical properties, Adv. Funct. Mater. 12 (2002) 323.
[55] J. Heyd, G.E. Scuseria, M. Ernzerhof, Hybrid functionals based on a screened Coulomb potential, J. Chem. Phys. 118 (2003) 8207–8215.
[56] R. Dovesi, et al., Quantum-mechanical condensed matter simulations with CRYSTAL, Wiley Interdiscipl. Rev. Comput. Mol. Sci. 8 (2018), e1360.
[57] H.J. Monkhorst, J.D. Pack, Special points for Brillouin-zone integrations, Phys. Rev. B 13 (1976) 5188–5192.
[58] J.F. Condeles, R.A. Ando, M. Mulato, Optical and structural properties of PbI2 thin films, J. Mater. Sci. 43 (2008) 525–529.
[59] C. Lan, et al., Large-scale synthesis of freestanding layer-structured PbI2 and MAPbI3 nanosheets for high-performance photodetection, Adv. Mater. 29 (2017) 1702759.
[60] C.S. Lao, et al., ZnO nanobelt/nanowire Schottky diodes formed by dielectrophoresis alignment across Au electrodes, Nano Lett. 6 (2006) 263–266.
[61] T. Zhai, et al., Recent developments in one-dimensional inorganic nanostructures for photodetectors, Adv. Funct. Mater. 20 (2010) 4233–4248.
[62] G. Cheng, et al., ZnO nanowire Schottky barrier ultraviolet photodetector with high sensitivity and fast recovery speed, Appl. Phys. Lett. 99 (2011) 203105.
[63] B. Mallampati, S.V. Nair, H.E. Ruda, U. Philipose, Role of surface in high photoconductive gain measured in ZnO nanowire-based photodetector, J. Nanoparticle Res. 17 (2015) 176.
[64] J.-M. Wu, C.-H. Kuo, Ultraviolet photodetectors made from SnO2 nanowires, Thin Solid Films 517 (2009) 3870–3873.
[65] N. Yamazoe, J. Fuchigami, M. Kishikawa, T. Seiyama, Interactions of tin oxide surface with O2, H2O AND H2, Surf. Sci. 86 (1979) 335–344.
[66] S.C. Chang, Oxygen chemisorption on tin oxide: correlation between electrical conductivity and epr measurements, J. Vac. Sci. Technol. 17 (1979) 366–369.

Paper II

ACS APPLIED MATERIALS & INTERFACES

Research Article

Cite This: ACS Appl. Mater. Interfaces 2018, 10, 13869−13876

www.acsami.org

Fast-Response Single-Nanowire Photodetector Based on ZnO/WS_2 Core/Shell Heterostructures

Edgars Butanovs,[†] Sergei Vlassov,[‡] Alexei Kuzmin,[†] Sergei Piskunov,[†] Jelena Butikova,[†] and Boris Polyakov*[,†]

[†]Institute of Solid State Physics, University of Latvia, Kengaraga Street 8, LV-1063 Riga, Latvia

[‡]Institute of Physics, University of Tartu, W. Ostwaldi 1, 50411 Tartu, Estonia

Supporting Information

ABSTRACT: The surface plays an exceptionally important role in nanoscale materials, exerting a strong influence on their properties. Consequently, even a very thin coating can greatly improve the optoelectronic properties of nanostructures by modifying the light absorption and spatial distribution of charge carriers. To use these advantages, 1D/1D heterostructures of ZnO/WS_2 core/shell nanowires with a-few-layers-thick WS_2 shell were fabricated. These heterostructures were thoroughly characterized by scanning and transmission electron microscopy, X-ray diffraction, and Raman spectroscopy. Then, a single-nanowire photoresistive device was assembled by mechanically positioning ZnO/WS_2 core/shell nanowires onto gold electrodes inside a scanning electron microscope. The results show that a few layers of WS_2 significantly enhance the photosensitivity in the short wavelength range and drastically (almost 2 orders of magnitude) improve the photoresponse time of pure ZnO nanowires. The fast response time of ZnO/WS_2 core/shell nanowire was explained by electrons and holes sinking from ZnO nanowire into WS_2 shell, which serves as a charge carrier channel in the ZnO/WS_2 heterostructure. First-principles calculations suggest that the interface layer i-WS_2, bridging ZnO nanowire surface and WS_2 shell, might play a role of energy barrier, preventing the backward diffusion of charge carriers into ZnO nanowire.

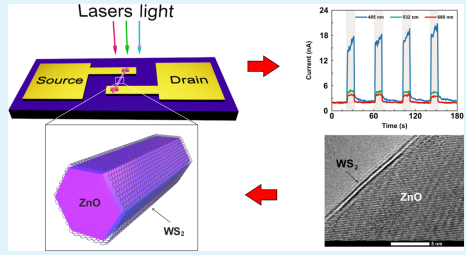

KEYWORDS: *core/shell nanowires, 1D/1D heterostructures, van der Waals epitaxy, transitional metal chalcogenides, photodetectors*

INTRODUCTION

Nanostructured photodetectors operating from ultraviolet (UV) to terahertz frequencies have attracted much attention during the last few decades due to their appealing performance for various applications.[1] Such nanodevices made of quantum dots, nanowires (NWs), nanobelts, nanotubes, or nanolayers demonstrate high integration density and sensitivity, fast response, and multifunctionality.[2−5] Current developments in the field are concentrated on precisely controlling the manufacturing of nanostructured materials, modifying their properties, and developing methods for mass production.[6]

Photodetectors based on one-dimensional (1D) nanostructured materials have become one of the most attractive photoelectronic devices that can be implemented using individual or assemblies of nanostructures.[4,7] A fabrication of hybrid nanostructures composed of two or more components opens new possibilities to control their properties, in particular, in photodetection capability in a broad spectral range from UV to infrared.[7] Depending on the dimensionality of the constituting components, hybrid nanostructures can be classified into six types,[7] and the 1D/1D nanostructured photodetectors constitute the subject of the present study. Furthermore, they can be realized as core/shell, branched or axial heterojunctions.

Radially heterostructured core/shell nanowires (NWs) are intriguing and prospective types of nanomaterials, and these NWs have been intensively explored recently.[8−10] The surface of NWs plays an important role because the surface is often the origin of structural and electronic defects. Properly chosen shell material can protect the core and significantly improve its electrical, mechanical, and optical properties.[9,11,12] Therefore, the engineering of core/shell heterostructures is a versatile tool for creating a novel advanced nanostructures with desired properties.

ZnO NWs are among the most popular nanomaterials with a wide range of applications in nanoelectronics, sensorics, and nanophotonics, including the use of ZnO NWs as piezoelectric nanogenerators and ultraviolet (UV) photodetectors.[13,14] At ambient conditions, the most stable phase of ZnO has n-type conductivity and is hexagonal wurtzite-type with a direct band

Received: February 7, 2018
Accepted: April 5, 2018
Published: April 5, 2018

DOI: 10.1021/acsami.8b02241
ACS Appl. Mater. Interfaces 2018, 10, 13869−13876

gap of about 3.2−3.3 eV.[15] Cubic zinc blend and rock-salt ZnO phases can be also obtained at specific conditions.[15] ZnO NW UV photodetectors demonstrate excellent performance and sensitivity; however, their time response is relatively slow, being in the range of seconds.[16−18] There are several reasons for slow photoresponse of ZnO NW photodetectors, namely, surface charge traps and surface states related to adsorbed oxygen molecules.[19] An obvious method to make photodetector faster is to etch and passivate NW surface layer, as it was demonstrated by Mallampati et al.[20] Cheng et al. used the electric field of Shottky barrier to increase both speed and gain of ZnO NW photodetector.[19] In a number of works, significant improvement in ZnO NW photodetectors responsivity and speed was achieved by Au nanoparticles decoration.[21,22]

Another promising class of nanomaterials consists of layered two-dimensional (2D) transition metal dichalcogenides (TMDs), and they have recently attracted much attention.[23,24] For example, several state-of-the-art 1D and 2D WS_2 and MoS_2-based high-sensitivity UV and vis photodetectors was demonstrated.[6,24,26] In addition, a-few-layers-thick TMDs show a transition from indirect to direct band gap behavior. For example, bulk WS_2 is an n-type semiconductor having an indirect band gap $\Delta\varepsilon_{ig}$ = 1.3−1.4 eV, whereas a monolayer has a direct optical band gap $\Delta\varepsilon_{dg}$ = 1.7−1.9 eV and a strong optical absorption, being able to absorb 5−10% of the incident light.[27−29] Furthermore, epitaxial growth of WS_2 and MoS_2 is possible on sapphire wafers because the (0001) plane of c-sapphire is hexagonally arranged, matching the crystal lattice of the two sulfides.[30] Recently, the authors have demonstrated that both WS_2 and MoS_2 can be epitaxially grown around ZnO NWs, producing ZnO/WS_2 and ZnO/MoS_2 core/shell nanostructures.[31,32]

Hybrid or composite TMDs materials have recently attracted significant attention.[24] The use of 2D ZnO/WS_2 heterostructures for enhanced UV photodetectors was demonstrated by Lan et al.[33] The heterostructured device was produced by transferring chemical vapor deposition grown WS_2 monolayer onto the surface of polycrystalline ZnO film deposited by direct current (dc) magnetron sputtering on glass substrate, and, finally, the aluminum electrodes were fabricated by thermal evaporation through a shadow mask.[33] An enhancement by 16 times (in vacuum) of UV light photodetection by ZnO/WS_2 heterostructure was observed relatively to pure ZnO film. However, the photoresponse time was still measured in the range of seconds.[33]

This study demonstrates a significantly enhanced photodetection by ZnO NWs coated with a few WS_2 monolayers (ZnO/WS_2 core/shell NWs) and a drastic (almost 2 orders of magnitude) improvement in the photoresponse time compared to that of pure ZnO NWs. Our results show a potential of combining layered 2D TMDs materials with semiconducting NWs to create new core/shell heterostructures with advanced optoelectronic properties.

EXPERIMENTAL SECTION

Synthesis. The synthesis of ZnO/WS_2 core/shell NWs was described in the authors' previous article.[31] In brief, amorphous a-WO_3 shell was deposited over ZnO NWs by reactive dc magnetron sputtering of a metallic tungsten target in mixed Ar/O_2 atmosphere. Then, ZnO/a-WO_3 NW samples were annealed in a quartz tube in a sulfur atmosphere during 0.5 h at 800 °C to convert amorphous tungsten trioxide into tungsten sulfide (WS_2). This process was followed by heating for 0.5 h in an inert atmosphere to sublimate excess material.

Sample Characterization. The phase composition of ZnO/WS_2 NWs was studied by X-ray diffraction (XRD) at room temperature (20 °C) using a θ−θ Bragg−Brentano powder diffractometer PANalytical X'Pert Pro MPD equipped with copper anode X-ray tube (Model PW3373, Cu Kα radiation). Micro-Raman spectroscopy measurements were performed using a confocal microscope with spectrometer Nanofinders-S (SOLAR TII). A diode pumped solid-state Nd:YAG laser (λ = 532 nm, max continuous wave power P = 150 mW) was used as an excitation source. The Raman spectra were recorded using the monochromator with a 520 mm focal length equipped with 600 grooves/mm diffraction grating and the edge filter to eliminate the elastic component. A Peltier-cooled back-thinned CCD camera (ProScan HS-101H) was employed as a detector of Raman spectra. All of the measurements were performed in backscattering geometry at room temperature (20 °C) through a Nikon CF Plan Apo 100× (NA = 0.95) optical objective. Furthermore, the morphology of NWs was observed by a scanning electron microscope (SEM) (Tescan Lyra XM), and the inner structure of ZnO and ZnO/WS_2 NWs was characterized using a transmission electron microscope (TEM) (Tecnai GF20, FEI) operated at the accelerating voltage of 180 kV.

Fabrication of Photodetectors. To fabricate single-nanowire photodetectors, gold microelectrodes with the gap width of 2 μm were first obtained on an oxidized silicon wafer by the conventional photolithography technique (as shown in Figure 1). Briefly, the

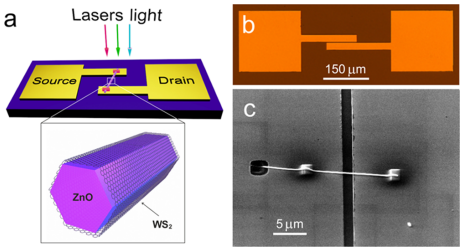

Figure 1. Schematics of ZnO/WS_2 core/shell nanowire-based photodetector (a). Optical microscope image of gold microelectrodes on the oxidized silicon substrate (b). SEM image of a typical nanowire photoresistor (c).

microelectrode pattern was obtained using a direct write laser lithography (μPG 101, Heidelberg Instruments) on SU-8 2003 photoresist (MicroChem), and 5/45 nm Cr/Au film was deposited via thermal evaporation method, followed by a liftoff procedure.

Next, single NW photoresistors were fabricated using in situ nanomanipulations inside SEM-FIB Tescan Lyra XM. The as-grown ZnO and ZnO/WS_2 NWs were mechanically transferred from the Si substrate to the as-prepared gold microelectrodes by welding a single NW to the tungsten (W) nanomanipulator probe using an electron-beam-assisted platinum (Pt) deposition. Finally, the NW was aligned and placed on top of the microelectrodes, following its cutting off from the W probe with gallium (Ga) ion beam and welding to the electrodes using Pt deposition to ensure the electric contact and fixed position. A SEM image of a typical as-prepared photoresistor is shown in Figure 1c, where the narrow dark strip is the gap between the electrodes, two small rectangles on the NW are the deposited Pt contacts, and the trench is visible where the NW was cut by the ion beam.

For comparison, WS_2 water suspension was prepared using an ultrasound exfoliation of WS_2 powder (Sigma-Aldrich). A small amount (36 mg) of WS_2 powder in 6 mL of pure deionized water was ultrasonically processed at 100 W for 3 h. After 1 day, water suspension of WS_2 was centrifuged and resuspended in 1 mL tube. A droplet of WS_2 suspension was cast on gold electrodes and heated at 150 °C during 5 min.

DOI: 10.1021/acsami.8b02241
ACS Appl. Mater. Interfaces 2018, 10, 13869−13876

Device Measurements. Current−voltage (I−V) characteristics and photoresponse of the fabricated single-NW photodetectors were measured with a two-contact microprobe station connected to a Model 6485 Keithley Picoammeter, a Model 2000 Keithley multimeter, and a voltage source (33220A Waveform Generator, Agilent). Semiconductor diode lasers with the wavelengths of 405, 532, and 660 nm and the power of 0.5 W/cm^2 were used as illumination sources for the photoresponse measurements. Optical beam shutter Thorlabs SH05 was employed for time-resolved measurements, and all of the measurements were performed at room temperature in air.

Computational Details. In this study, hybrid density functional theory (DFT) calculations have been performed using the CRYSTAL computer code,[34] and the code utilizes localized Gaussian type functions (GTFs) in the form of a basis set (BS) centered on atomic nuclei to expand the crystalline orbitals as linear combinations of atomic orbitals. Fully relaxed ZnO/WS_2 2D interfaces were calculated by means of hybrid exchange correlation functional PBE0 according to the derivations by Perdew et al. and Adamo and Barone.[35,36] For oxygen atoms, the all-valence BSs of atomic GTFs (constructed using pure s- and hybrid sp-AOs) in the form of 8s-411sp were used, and for zinc atoms, the all-valence BS in the form 8s-64111sp-41d were used. In addition, the BS adopted for sulfur atoms had the form of ECP-1111s-1111p-11d,[37] whereas for tungsten atoms, the BS that had the form of ECP-11sp-31d56 was used, where ECP represents the effective core pseudopotentials employed to accelerate computation. To provide a balanced summation in both direct and reciprocal lattices, the reciprocal space integration was performed by sampling the interface Brillouin zone (BZ) with the 12 × 12 × 1 Monkhorst−Pack mesh[38] that gives in total 16 k-points evenly distributed at the BZ. The calculations were considered as converged only when the total energy differs by less than 10^{-9} au in two successive cycles of the self-consistent field procedure.

RESULTS AND DISCUSSION

The phase composition of as-prepared ZnO/WS_2 core/shell NWs on the silicon substrate was studied by X-ray diffraction using the Rietveld method and implemented in the PROFEX code.[39] The result of the Rietveld refinement is shown in Figure 2a. Four crystalline phases corresponding to the Si substrate, ZnO NWs, WS_2 shell, and ZnS were detected. Although the amount of ZnS on the substrate was high enough to be detected in the XRD measurements, only a sub-monolayer was present inside the ZnO/WS_2 core/shell nanowires.[31]

For room-temperature micro-Raman measurements, the NWs were transferred onto a clean silicon substrate. The Raman spectrum and confocal image (see the inset) of typical individual ZnO/WS_2 core/shell NW are shown in Figure 2b. Two main bands at 354 and 419 cm^{-1} were detected and attributed to the WS_2 phase. In contrast, no Raman signal from the ZnO NW core was observed because of its very weak intensity when excited at 532 nm. The Raman spectrum of bulk WS_2 measured in a backscattering geometry includes the first-order modes at the center of the Brillouin zone [in-plane $^1E_{2g}(\Gamma) \approx 355$ cm^{-1} and out-of-plane $A_{1g}(\Gamma) \approx 420$ cm^{-1}], a zone-edge longitudinal acoustic mode LA(M) ≈ 350 cm^{-1}, and several multiphonon combinations of these modes.[40−42] When the thickness of WS_2 was reduced to a monolayer, the resonant Raman scattering occurs under 532 nm excitation, enhancing the second-order effects significantly, and the spectrum became very rich in the region of LA(M)−$^1E_{2g}(\Gamma)$ modes.[41,43] In this case, the intensity of the strongest second-order Raman peak, 2LA(M) mode at 354 cm^{-1} (Figure 2b), became dominant, and it overlaps strongly with the first-order $^1E_{2g}(\Gamma)$ mode. Thus, the intensity ratio between 354 and 419 cm^{-1} bands in the Raman spectrum of the ZnO/WS_2 core/shell NW implies the thickness of the WS_2 shell to be on the order of a monolayer.

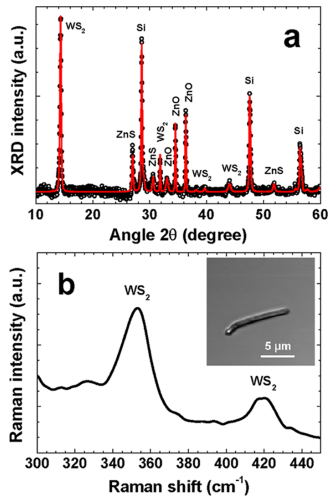

Figure 2. Rietveld refinement (solid line) of the X-ray diffraction pattern (open circles) of the ZnO/WS_2 sample (a). Raman spectrum of the ZnO/WS_2 core/shell nanowire (inset: confocal microscope image of the nanowire) (b).

The TEM images of pure ZnO NW, ZnO/WS_2 core/shell NW after annealing for 0.5 h in a sulfur atmosphere and after additional annealing in inert atmosphere are shown in Figure 3. Pure ZnO NWs have a smooth surface and a single-crystalline structure (Figure 3b). After annealing in a sulfur atmosphere, many WS_2 layers and protruding WS_2 microplates can be seen on the surface of the NW (Figure 3c,d). However, after annealing in an inert atmosphere, only a few layers of WS_2 remain in agreement with the results of Raman spectroscopy (Figure 2b): the layers appear as black lines parallel to the ZnO NW surface (Figure 3e,f). A more detailed description of the TEM investigation of ZnO/WS_2 core/shell NWs and related theoretical models have been published by the authors previously.[31]

Figure 4 shows the measured current−voltage characteristics of photodetectors built using pure ZnO and ZnO/WS_2 core/shell NWs, as well as pure WS_2 flakes. At least five photodetectors of each material were fabricated and measured. The ZnO photoresistor demonstrates a nonsymmetric current−voltage $I(V)$ curve (Figure 4a), and this is typical for the Schottky barrier of ZnO NWs on gold contacts.[44] At the same time, a nearly symmetric response was obtained for WS_2 flakes and ZnO/WS_2 devices (Figure 4b,c).

On−off photoresponse measurements were performed at the bias voltage of 1 V, laser wavelengths of 405, 532, and 660 nm, and laser power of 0.5 W/cm^2. The typical photoresponse measurements of pure ZnO and ZnO/WS_2 core/shell NWs and WS_2 flakes-based devices are shown in Figure 5. Pure ZnO NWs respond only to the illumination at a wavelength of 405 nm and do not respond to the wavelengths of 532 and 660 nm (Figure 5a). In addition, the photoresponse of WS_2 flakes is almost identical at the wavelengths of 405, 532, and 660 nm (Figure 5b). In particular, the photoresponses of ZnO/WS_2 core/shell NWs are similar at 532 and 660 nm but significantly

DOI: 10.1021/acsami.8b02241
ACS Appl. Mater. Interfaces 2018, 10, 13869−13876

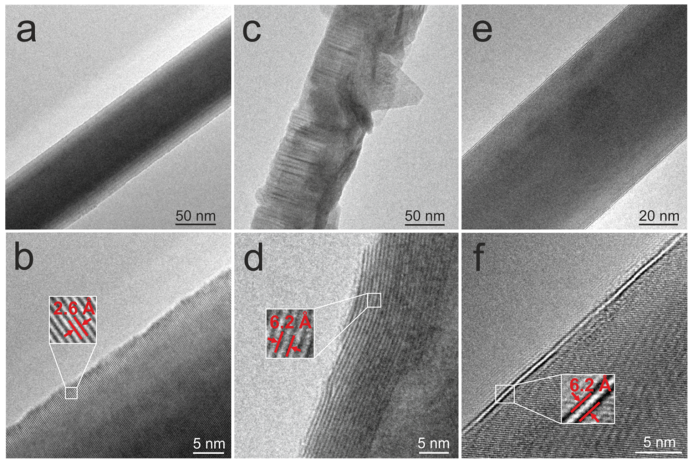

Figure 3. TEM images of pure ZnO nanowire (a, b), ZnO/WS_2 nanowire annealed in sulfur atmosphere (c, d), and ZnO/WS_2 nanowire additionally annealed in an inert atmosphere (e, f).

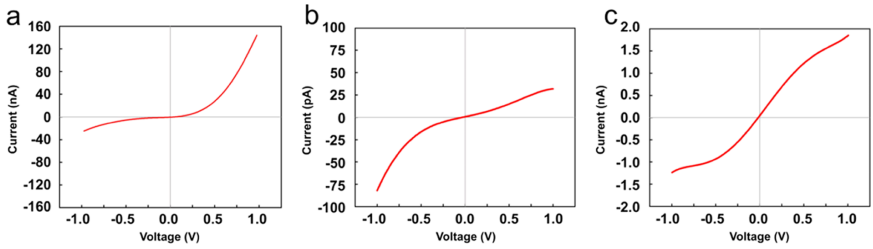

Figure 4. *I*–*V* characteristics of pure ZnO NW (a) and WS_2 flakes drop-casted on electrodes (b) and annealed ZnO/WS_2 NW (c).

stronger at 405 nm (Figure 5c). Because pure ZnO NWs do not respond to green 532 nm (2.33 eV) and red 660 nm (1.88 eV) light owing to their wide band gap (E_g = 3.2–3.3 eV), the photoresponse of ZnO/WS_2 core/shell NWs to red and green light is caused by the WS_2 shell. For violet light (405 nm), both ZnO core and WS_2 shell contribute proportionally to the photoresponse of ZnO/WS_2 core/shell NWs.

Time-resolved photoresponse measurements are presented in Figure 5d–f, and the corresponding data are given in Table 1. A slow response of pure ZnO NWs on the timescale of seconds is typical for this material.[16−18] The photoresponse time of WS_2 flake devices is significantly faster than that of ZnO-based devices: it depends on the material fabrication method and the number of WS_2 layers.[45,46] Perea-López et al. reported the response time of a few-layer WS_2 photodetector to be as fast as 5.3 ms,[45] whereas Huo et al. reported the response time of a multilayer WS_2 photodetector to be faster than 20 ms.[46] The time response of the proposed 1D ZnO/WS_2 core/shell NWs is significantly faster than that of 2D ZnO/WS_2-based heterostructured thin-film devices.[33] We believe that the faster response time of 1D ZnO/WS_2 NWs in comparison to 2D heterostructures can be explained by a good quality of ZnO–WS_2 interface (perfect match and close contact between WS_2 and ZnO), which allows a fast transfer of photogenerated charge carriers from ZnO to WS_2. The quality of the interface is achieved by the direct growth of WS_2 layer on the ZnO nanowire surface.

The influence of oxygen molecules on the surface states of ZnO NW and their effect on photoresponse kinetics were widely discussed in the literature.[19,20] The presence of WS_2 shell protects the ZnO surface from oxygen adsorption and might influence surface-related photoinduced processes. Moreover, WS_2 shell might passivate ZnO surface leading to a decrease in charge carrier trapping centers in ZnO NW and be responsible for faster photodetector kinetics. A comparison of the positions of valence and conduction bands of ZnO and WS_2 shows that both electrons and holes should sink into the WS_2 shell[31] and serve as a charge carrier channel in ZnO/WS_2 heterostructure (Figure 6). This conclusion is supported by the electronic density of states (DOSs) calculated for the ZnO/WS_2 interface layer by means of the density functional theory (Figure 6c–e). The DOS calculated for pristine n-type ZnO ($(\bar{1}100)$ surface of the bare ZnO NW yields a band gap of 3.36 eV (Figure 6c), in good agreement with the experimental observation (3.3 eV[15]). The doping of the surface of NWs with sulfur is the initial stage of ZnO/WS_2 interface formation.[31]

DOI: 10.1021/acsami.8b02241
ACS Appl. Mater. Interfaces 2018, 10, 13869–13876

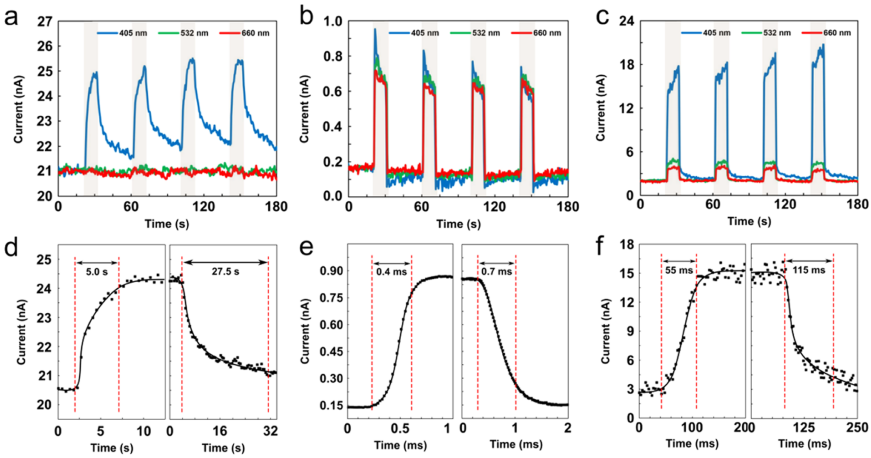

Figure 5. On−off photoresponse measurements of ZnO nanowire (a), WS_2 flakes (b), and ZnO/WS_2 nanowire (c) photoresistors at 1 V bias voltage and light illumination using 0.5 W/cm^2 light intensity of 405, 532, and 660 nm wavelengths. Time-resolved photoresponse measurements of ZnO nanowire (d), WS_2 flakes (e), and ZnO/WS_2 nanowire (f) photoresistors at 1 V bias voltage and light illumination using 0.5 W/cm^2 intensity of at 405, 532, and 660 nm wavelengths.

Table 1. Photoresponse (Rise and Decay) Time of Photodetectors Fabricated from Pure ZnO and ZnO/WS_2 Core/Shell NWs as well as WS_2 Flakes

	ZnO NWs		WS_2 flakes		ZnO/WS_2 NWs	
wavelength (nm)	rise (s)	decay (s)	rise (ms)	decay (ms)	rise (ms)	decay (ms)
405	5	27.5	0.4	0.7	55	115
532			0.3	0.65	21	95
660			0.53	1.35	22	50

The surface of NWs doped with sulfur has a narrower band gap of 1.42 eV due to the presence of occupied in-gap sulfur levels located at 1−2 eV above the top of the valence band of pristine ZnO ($\bar{1}100$), as shown in Figure 6d. The formation of a net of WS_2 bridges as precursors for complete interface formation[31] makes the band gap even more narrow at 1.14 eV (Figure 6e) due to the presence of a sharp peak containing an admixture of W and S states at the top of the valence band. Therefore, according to the DFT calculations, the interface layer i-WS_2, bridging the ZnO surface and WS_2 shell, has an even more narrow gap than WS_2 itself, leading to the formation of energy barrier that is able to prevent the backward diffusion of charge carriers into ZnO NW.

To evaluate the parameters of photoconducting materials, spectral responsivity R_λ and external quantum efficiency (EQE) were calculated according to the following formulas:[6,25,26] $R_\lambda = I_\lambda/P_\lambda S$, where I_λ represents the photocurrent, P_λ represents the light intensity, and S represents the effective illuminated area; and EQE = $hcR_\lambda/e\lambda$, where h represents Planck's constant, c represents the velocity of light, e represents the charge of electron, and λ represents the wavelength. In addition, a higher R_λ and EQE corresponds to a higher light sensitivity of a material. The calculated values of R_λ and EQE for our photodetectors are given in Table 2, and the obtained data are comparable to other state-of-the-art ZnO nanowire- and WS_2 nanotube-based photodetectors. For example, Guo et al. demonstrated the high responsivity of a ZnO nanowire-based UV photodetector having 40 A/W; however, at 10 V, the kinetics of the photodetector was measured in the range of seconds.[17] In contrast, Zhang et al. demonstrated a multiwall WS_2 nanotube-based photodetector with R_λ = 3.14 A/W (at 0.5 V) and EQE = 615% for 633 nm light.[26]

Finally, ZnO/WS_2 core/shell NWs with a few WS_2 layers thickness are considered as a WS_2 nanotube wrapped around a ZnO NW core. However, such WS_2 nanotubes with the same diameter collapse without an inner ZnO core because the ZnO core can be etched away in template-assisted synthesis methods.[47,48] Therefore, 1D/1D ZnO/WS_2 core/shell NWs were considered as a convenient object (where ZnO may be a sacrificial template if necessary[49] to manipulate a few-layers-thick 2D materials (WS_2, MoS_2, and others)), and similar materials can be useful in nanoelectronic and optoelectronic devices.

CONCLUSIONS

In summary, an effective photodetector based on ZnO/WS_2 core/shell nanowire (with a few layers of WS_2) is demonstrated in this work. The photodetector responds to illumination at the wavelengths of 660 nm (R_λ = 1.75), 532 nm (R_λ = 2.25), and 405 nm (R_λ = 7). The ZnO/WS_2 core/shell nanowire-based device shows a clear advantage over pure ZnO nanowire-based photodetector in terms of both higher responsivity (4.6-fold) and faster operation (90-fold) for 405 nm illumination. The photodetector band diagram was supported by the first-principles calculations, suggesting that the interface layer i-WS_2, bridging ZnO nanowire surface, and WS_2 shell, might play an important role in preventing backward diffusion of charge carriers into the ZnO nanowire, whereas WS_2 shell serves as a charge carrier channel in the ZnO/WS_2 heterostructure. The obtained results clearly show the potential of combining

DOI: 10.1021/acsami.8b02241
ACS Appl. Mater. Interfaces 2018, 10, 13869−13876

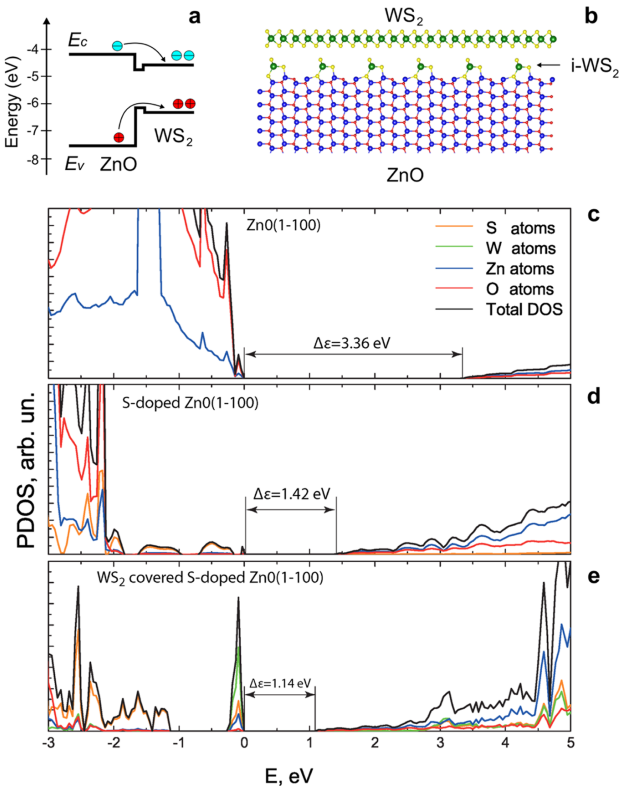

Figure 6. Simplified band diagram of the ZnO/WS_2 core−shell NW (a). Atomic structure of ZnO/WS_2 interface (b). Total and projected densities of states (DOSs) of (c) n-type ZnO ($\bar{1}$100) substrate, (d) S-doped ZnO ($\bar{1}$100) substrate, and (e) WS_2 covered S-doped ZnO ($\bar{1}$100) substrate as calculated by means of density functional theory. Zero energy corresponds to the top of the valence band.

Table 2. Characteristic Parameters of Photodetectors Fabricated from Pure ZnO and ZnO/WS_2 Core/Shell NWs as well as WS_2 Flakes

parameter	wavelength (nm)	ZnO NWs	WS_2 flakes	ZnO/WS_2 core/shell NWs
responsivity or R_λ (A/W)	405	1.50	5.03×10^{-4}	7.00
	532		4.84×10^{-4}	2.25
	660		4.58×10^{-4}	1.75
EQE (%)	405	4.59	1.5×10^{-3}	21.4
	532		1.1×10^{-3}	5.2
	660		8.6×10^{-4}	3.3

layeread 2D TMDs materials with semiconducting nanowires to create novel core/shell heterostructures with advanced optoelectronic properties.

■ ASSOCIATED CONTENT

Supporting Information

The Supporting Information is available free of charge on the ACS Publications website at DOI: 10.1021/acsami.8b02241.

On−off photoresponse graphs for selected ZnO/WS_2- and ZnO-based photodetector devices (PDF)

■ AUTHOR INFORMATION

Corresponding Author

*E-mail: boris@cfi.lu.lv.

ORCID

Boris Polyakov: 0000-0002-6626-1065

Author Contributions

The manuscript was written through contributions of all the authors. All the authors have given approval to the final version of the manuscript.

Notes

The authors declare no competing financial interest.

■ ACKNOWLEDGMENTS

This work was supported by the Latvian National Research Program IMIS2 and ISSP project for Students and Young Researchers Nr. SJZ/2016/6. S.P. is grateful to the ERA.Net RUS Plus WATERSPLIT project no. 237 for the financial

support. S.V. is grateful for partial support by the Estonian Science Foundation grant PUT1689.

ABBREVIATIONS

1D, one-dimensional; 2D, two-dimensional; NW, nanowire; TMD, transitional metal dichalcogenide; CVD, chemical vapor deposition; SEM, scanning electron microscope; TEM, transmission electron microscope; XRD, X-ray diffraction; DFT, density functional theory; EQE, external quantum efficiency

REFERENCES

(1) Chen, H.; Liu, H.; Zhang, Z.; Hu, K.; Fang, X. Nanostructured photodetectors: from ultraviolet to terahertz. *Adv. Mater.* **2016**, *28*, 403−433.
(2) Sang, L.; Liao, M.; Sumiya, M. A comprehensive review of semiconductor ultraviolet photodetectors: from thin film to one-dimensional nanostructures. *Sensors* **2013**, *13*, 10482−10518.
(3) Koppens, F. H. L.; Mueller, T.; Avouris, P.; Ferrari, A. C.; Vitiello, M. S.; Polini, M. Photodetectors based on graphene, other two-dimensional materials and hybrid systems. *Nat. Nanotechnol.* **2014**, *9*, 780.
(4) Chen, H.; Liu, K.; Hu, L.; Al-Ghamdi, A. A.; Fang, X. New concept ultraviolet photodetectors. *Mater. Today* **2015**, *18*, 493−502.
(5) Dhanabalan, S. C.; Ponraj, J. S.; Zhang, H.; Bao, Q. Present perspectives of broadband photodetectors based on nanobelts, nanoribbons, nanosheets and the emerging 2D materials. *Nanoscale* **2016**, *8*, 6410−6434.
(6) Xie, C.; Mak, C.; Tao, X.; Yan, F. Photodetectors based on two-dimensional layered materials beyond graphene. *Adv. Funct. Mater.* **2017**, *27*, No. 1603886.
(7) Tian, W.; Liu, D.; Cao, F.; Li, L. Hybrid nanostructures for photodetectors. *Adv. Opt. Mater.* **2017**, *5*, No. 1600468.
(8) Li, Y.; Qian, F.; Xiang, J.; Lieber, C. M. Nanowire electronic and optoelectronic devices. *Mater. Today* **2006**, *9*, 18−27.
(9) Yan, R.; Gargas, D.; Yang, P. Nanowire photonics. *Nat. Photonics* **2009**, *3*, 569.
(10) Kempa, T. J.; Day, R. W.; Kim, S.-K.; Park, H.-G.; Lieber, C. M. Semiconductor nanowires: a platform for exploring limits and concepts for nano-enabled solar cells. *Energy Environ. Sci.* **2013**, *6*, 719−733.
(11) Lauhon, L. J.; Gudiksen, M. S.; Wang, D.; Lieber, C. M. Epitaxial Core−shell and core−multishell nanowire heterostructures. *Nature* **2002**, *420*, 57.
(12) Vlassov, S.; Polyakov, B.; Dorogin, L. M.; Vahtrus, M.; Mets, M.; Antsov, M.; Saar, R.; Romanov, A. E.; Lõhmus, A.; Lõhmus, R. Shape restoration effect in Ag−SiO_2 core−shell nanowires. *Nano Lett.* **2014**, *14*, 5201−5205.
(13) Zhang, Y.; Ram, M. K.; Stefanakos, E. K.; Goswami, D. Y. Synthesis, Characterization, and applications of ZnO nanowires. *J. Nanomater.* **2012**, *2012*, 1−22.
(14) Wang, Z. L. ZnO nanowire and nanobelt platform for nanotechnology. *Mater. Sci. Eng., R* **2009**, *64*, 33−71.
(15) Özgür, Ü.; Alivov, Y. I.; Liu, C.; Teke, A.; Reshchikov, M. A.; Doğan, S.; Avrutin, V.; Cho, S.-J.; Morkoç, H. A Comprehensive review of ZnO materials and devices. *J. Appl. Phys.* **2005**, *98*, No. 041301.
(16) Soci, C.; Zhang, A.; Xiang, B.; Dayeh, S. A.; Aplin, D. P. R.; Park, J.; Bao, X. Y.; Lo, Y. H.; Wang, D. ZnO nanowire UV photodetectors with high internal gain. *Nano Lett.* **2007**, *7*, 1003−1009.
(17) Guo, L.; Zhang, H.; Zhao, D.; Li, B.; Zhang, Z.; Jiang, M.; Shen, D. High responsivity ZnO nanowires based UV detector fabricated by the dielectrophoresis method. *Sens. Actuators, B* **2012**, *166−167*, 12−16.
(18) Ates, E. S.; Kucukyildiz, S.; Unalan, H. E. Zinc oxide nanowire photodetectors with single-walled carbon nanotube thin-film electrodes. *ACS Appl. Mater. Interfaces* **2012**, *4*, 5142−5146.
(19) Cheng, G.; Wu, X.; Liu, B.; Li, B.; Zhang, X.; Du, Z. ZnO nanowire Schottky barrier ultraviolet photodetector with high sensitivity and fast recovery speed. *Appl. Phys. Lett.* **2011**, *99*, No. 203105.
(20) Mallampati, B.; Nair, S. V.; Ruda, H. E.; Philipose, U. Role of surface in high photoconductive gain measured in ZnO nanowire-based photodetector. *J. Nanopart. Res.* **2015**, *17*, 176.
(21) Ghimire, R. R.; Nath, R.; Neogy, R. K.; Raychaudhuri, A. K. Ligand-free attachment of plasmonic Au nanoparticles on ZnO nanowire to make a high-performance broadband photodetector using a laser-based method. *Nanotechnology* **2017**, *28*, No. 295703.
(22) Liu, K.; Sakurai, M.; Liao, M.; Aono, M. Giant improvement of the performance of ZnO nanowire photodetectors by Au nanoparticles. *J. Phys. Chem. C* **2010**, *114*, 19835−19839.
(23) Choi, W.; Choudhary, N.; Han, G. H.; Park, J.; Akinwande, D.; Lee, Y. H. Recent development of two-dimensional transition metal dichalcogenides and their applications. *Mater. Today* **2017**, *20*, 116−130.
(24) Duan, X.; Wang, C.; Pan, A.; Yu, R.; Duan, X. Two-dimensional transition metal dichalcogenides as atomically thin semiconductors: opportunities and challenges. *Chem. Soc. Rev.* **2015**, *44*, 8859−8876.
(25) Zeng, L.; Tao, L.; Tang, C.; Zhou, B.; Long, H.; Chai, Y.; Lau, S. P.; Tsang, Y. H. High-responsivity UV-Vis photodetector based on transferable WS_2 film deposited by magnetron sputtering. *Sci. Rep.* **2016**, *6*, No. 20343.
(26) Zhang, C.; Wang, S.; Yang, L.; Liu, Y.; Xu, T.; Ning, Z.; Zak, A.; Zhang, Z.; Tenne, R.; Chen, Q. High-performance photodetectors for visible and near-infrared lights based on individual WS_2 nanotubes. *Appl. Phys. Lett.* **2012**, *100*, No. 243101.
(27) Kam, K. K.; Parkinson, B. A. Detailed photocurrent spectroscopy of the semiconducting Group VIB transition metal dichalcogenides. *J. Phys. Chem.* **1982**, *86*, 463−467.
(28) Kuc, A.; Zibouche, N.; Heine, T. influence of quantum confinement on the electronic structure of the transition metal sulfide TS_2. *Phys. Rev. B* **2011**, *83*, No. 245213.
(29) Braga, D.; Gutiérrez Lezama, I.; Berger, H.; Morpurgo, A. F. Quantitative determination of the band gap of WS_2 with ambipolar ionic liquid-gated transistors. *Nano Lett.* **2012**, *12*, 5218−5223.
(30) Xu, Z.-Q.; Zhang, Y.; Lin, S.; Zheng, C.; Zhong, Y. L.; Xia, X.; Li, Z.; Sophia, P. J.; Fuhrer, M. S.; Cheng, Y.-B.; Bao, Q. Synthesis and transfer of large-area monolayer WS_2 crystals: moving toward the recyclable use of sapphire substrates. *ACS Nano* **2015**, *9*, 6178−6187.
(31) Polyakov, B.; Kuzmin, A.; Smits, K.; Zideluns, J.; Butanovs, E.; Butikova, J.; Vlassov, S.; Piskunov, S.; Zhukovskii, Y. F. Unexpected epitaxial growth of a few WS_2 layers on {1−100} facets of ZnO nanowires. *J. Phys. Chem. C* **2016**, 21451.
(32) Butanovs, E.; Kuzmin, A.; Butikova, J.; Vlassov, S.; Polyakov, B. Synthesis and characterization of ZnO/ZnS/MoS_2 core-shell nanowires. *J. Cryst. Growth* **2017**, *459*, 100−104.
(33) Lan, C.; Li, C.; Wang, S.; Yin, Y.; Guo, H.; Liu, N.; Liu, Y. ZnO−WS_2 heterostructures for enhanced ultra-violet photodetectors. *RSC Adv.* **2016**, *6*, 67520−67524.
(34) Dovesi, R.; Saunders, V. R.; Roetti, C.; Orlando, R.; Zicovich-Wilson, C. M.; Pascale, F.; Civalleri, B.; Doll, K.; Causà, N. M. H.; Bush, I. J.; D'Arco, P.; M. Llunell, M.; Noël, Y. *CRYSTAL14 User's Manual*; University of Torino: Torino, 2014.
(35) Perdew, J. P.; Ernzerhof, M.; Burke, K. Rationale for mixing exact exchange with density functional approximations. *J. Chem. Phys.* **1996**, *105*, 9982−9985.
(36) Adamo, C.; Barone, V. Toward reliable density functional methods without adjustable parameters: the PBE0 model. *J. Chem. Phys.* **1999**, *110*, 6158−6170.
(37) Bandura, A. V.; Evarestov, R. A. Structure and stability of SnS2-based single- and multi-wall nanotubes. *Surf. Sci.* **2015**, *641*, 6−15.
(38) Monkhorst, H. J.; Pack, J. D. Special points for Brillouin-zone integrations. *Phys. Rev. B* **1976**, *13*, 5188−5192.
(39) Doebelin, N.; Kleeberg, R. Profex: A graphical user interface for the Rietveld refinement program BGMN. *J. Appl. Crystallogr.* **2015**, *48*, 1573−1580.

DOI: 10.1021/acsami.8b02241
ACS Appl. Mater. Interfaces 2018, 10, 13869−13876

(40) Sourisseau, C.; Cruege, F.; Fouassier, M.; Alba, M. Second-order Raman effects, inelastic neutron scattering and lattice dynamics in 2H-WS_2. *Chem. Phys.* **1991**, *150*, 281−293.
(41) Berkdemir, A.; Gutiérrez, H. R.; Botello-Méndez, A. R.; Perea-López, N.; Elías, A. L.; Chia, C.-I.; Wang, B.; Crespi, V. H.; López-Urías, F.; Charlier, J.-C.; Terrones, H.; Terrones, M. Identification of individual and few layers of WS_2 using Raman spectroscopy. *Sci. Rep.* **2013**, *3*, No. 1755.
(42) Liang, L.; Meunier, V. First-principles Raman spectra of MoS_2, WS_2 and their heterostructures. *Nanoscale* **2014**, *6*, 5394−5401.
(43) Mitioglu, A. A.; Plochocka, P.; Deligeorgis, G.; Anghel, S.; Kulyuk, L.; Maude, D. K. Second-order resonant Raman scattering in single-layer tungsten disulfide WS_2. *Phys. Rev. B* **2014**, *89*, No. 245442.
(44) Lao, C. S.; Liu, J.; Gao, P.; Zhang, L.; Davidovic, D.; Tummala, R.; Wang, Z. L. ZnO nanobelt/nanowire Schottky diodes formed by dielectrophoresis alignment across au electrodes. *Nano Lett.* **2006**, *6*, 263−266.
(45) Perea-López, N.; Elías, A. L.; Berkdemir, A.; Castro-Beltran, A.; Gutiérrez, H. R.; Feng, S.; Lv, R.; Hayashi, T.; López-Urías, F.; Ghosh, S.; et al. Photosensor device based on few-layered WS_2 films. *Adv. Funct. Mater.* **2013**, *23*, 5511−5517.
(46) Huo, N.; Yang, S.; Wei, Z.; Li, S.-S.; Xia, J.-B.; Li, J. Photoresponsive and gas sensing field-effect transistors based on multilayer WS_2 nanoflakes. *Sci. Rep.* **2014**, *4*, No. 5209.
(47) Carreon, M. L.; Thapa, A. K.; Jasinski, J. B.; Sunkara, M. K. The capacity and durability of amorphous silicon nanotube thin film anode for lithium ion battery applications. *ECS Electrochem. Lett.* **2015**, *4*, A124−A128.
(48) Liu, J.; Li, Y.; Fan, H.; Zhu, Z.; Jiang, J.; Ding, R.; Hu, Y.; Huang, X. Iron oxide-based nanotube arrays derived from sacrificial template-accelerated hydrolysis: large-area design and reversible lithium storage. *Chem. Mater.* **2010**, *22*, 212−217.
(49) Yan, C.; Liu, J.; Liu, F.; Wu, J.; Gao, K.; Xue, D. Tube formation in nanoscale materials. *Nanoscale Res. Lett.* **2008**, *3*, 473−480.

DOI: 10.1021/acsami.8b02241
ACS Appl. Mater. Interfaces 2018, 10, 13869−13876

Paper III

Optical Materials 75 (2018) 501–507

Contents lists available at ScienceDirect

Optical Materials

journal homepage: www.elsevier.com/locate/optmat

Towards metal chalcogenide nanowire-based colour-sensitive photodetectors

Edgars Butanovs*, Jelena Butikova, Aleksejs Zolotarjovs, Boris Polyakov

Institute of Solid State Physics, University of Latvia, Kengaraga Street 8, Riga, LV-1063, Latvia

ARTICLE INFO

Article history:
Received 21 August 2017
Received in revised form
20 October 2017
Accepted 6 November 2017

Keywords:
PbS
In_2S_3
CdS
ZnSe
Nanowire
Photodetector

ABSTRACT

In recent years, nanowires have been shown to exhibit high photosensitivities, and, therefore are of interest in a variety of optoelectronic applications, for example, colour-sensitive photodetectors. In this study, we fabricated two-terminal PbS, In_2S_3, CdS and ZnSe single-nanowire photoresistor devices and tested applicability of these materials under the same conditions for colour-sensitive (405 nm, 532 nm and 660 nm) light detection. Nanowires were grown via atmospheric pressure chemical vapour transport method, their structure and morphology were characterized by scanning and transmission electron microscopy (SEM and TEM), X-ray diffraction (XRD), and optical properties were investigated with photoluminescence (PL) measurements. Single-nanowire photoresistors were fabricated via *in situ* nanomanipulations inside SEM, using focused ion beam (FIB) cutting and electron-beam-assisted platinum welding; their current-voltage characteristics and photoresponse values were measured. Applicability of the tested nanowire materials for colour-sensitive light detection is discussed.

1. Introduction

Colour-sensitive photodetectors are desirable for a large variety of applications, for instance, in optical communications, digital imaging and environmental monitoring [1–4]. In recent years, nanowires (NWs) have been demonstrated to be superior to their bulk counterparts as photodetector materials mainly due to their higher sensitivities, which arise from the NW high surface area/volume ratio resulting in high density of surface states that act as trap sites for photogenerated holes, therefore increasing electron lifetime and enhancing the photocurrent [5,6]. Semiconducting chalcogenide materials with direct bandgap and large absorption coefficients, such as PbS, In_2S_3, CdS, ZnSe, are great candidates for next-generation NW-based light detectors due to their excellent photodetection properties [6–9]. Typical photodetectors can detect only a specific spectral band, therefore are not suitable for multi-colour detection with spectral selectivity. There are two general approaches of making colour-sensitive detectors: using broad-spectrum materials and wavelength-selective filters, or combining several materials with different bandgaps, including material doping and composition tuning. Using broad-spectrum photodetector materials combined with absorptive colour filters is a possibility; however, it involves additional fabrication steps and, to obtain highest efficiency, one would prefer light to be converted to photocurrent rather than reflected or absorbed in the filter layer. Research has been done on compositionally tuneable NWs and doping of NWs for wavelength-selective light detection [10,11], but there is a difficulty to extend the optical band outside the visible light range. Furthermore, it has been demonstrated that colour imaging is possible by varying the radius of silicon NWs to control spectral sensitivities [12]. However, a versatile strategy to obtain spectral selectivity is to select arbitrary photosensitive material NWs with different bandgaps, and incorporate them in a composite thin film or on an insulating substrate. Liu et al. demonstrated a method of incorporating photosensitive CdS, CdSeS and CdSe NWs into an amorphous indium zinc oxide thin film to obtain a transparent thin-film-transistor array, showing that such concept could be possibly used to fabricate multi-colour photodetectors [13]. Sang et al. utilized CdS, SnO_2, ZnO and Ga_2O_3 one-dimensional nanostructures to demonstrate colour-sensitive photodetection by simultaneously integrating them into an insulating substrate with a two-terminal device structure [14]. In such a way, the cut-off wavelengths of the selected semiconductor NW materials, defined by the bandgap, will determine the spectral selectivity. This approach benefits from substantial freedom to choose NW materials with desirable spectral band and high

* Corresponding author.
E-mail address: edgarsb@cfi.lu.lv (E. Butanovs).

https://doi.org/10.1016/j.optmat.2017.11.010
0925-3467/

photoresponse. Furthermore, large-scale printing of NWs at defined locations on flexible substrates via roll-to-roll transfer has been demonstrated [15], thus enabling the development of NW based all-printed electronic and optoelectronic devices at low cost and with high performance.

In this work, we synthesised PbS, In_2S_3, CdS and ZnSe NWs and fabricated single-nanowire two-terminal photoresistor devices to test the applicability of these materials for colour-sensitive (red, green and blue light) photodetector applications, if they would be simultaneously incorporated on the same substrate. It is important to note that all these devices were prepared using the same method and tested under the same conditions. The measured NW photodetector properties were compared and analysed.

2. Experimental details

2.1. Nanowire synthesis and characterization

The following material NWs were synthesised via atmospheric pressure chemical vapour transport method in a horizontal quartz tube reactor by adjusting previously reported growth parameters: PbS [16], In_2S_3 [17], CdS [18], and ZnSe [19]. In all the cases, the NWs were grown on oxidized silicon wafers Si(110)/SiO_2 (*Semiconductor Wafer, Inc.*) coated with spherical Au nanoparticles used as a catalyst (*Smart materials*, water suspension, 50 nm diameter).

PbS NWs: 0.25 g $PbCl_2$ powder (*98%, Sigma Aldrich*) was loaded in a ceramic boat and placed in the centre of the quartz tube at 650 °C, Au/Si substrate was placed downstream in a lower temperature region. Excessive amount of sulphur powder (*enola SIA*) was placed upstream at 250 °C to create sulphur-rich atmosphere, while N_2 was used as a carrier gas. The temperature was kept constant for 20 min, followed by natural cooling to room temperature.

In_2S_3 NWs: Mixture of 0.5 g In and 0.5 g $InCl_3$ (*98%, Sigma-Aldrich*) powders were used as a source material and sent to the centre of the quartz tube. Au/Si substrate and sulphur powder were placed downstream and upstream, respectively, as in the previous case. Ar/H_2 (5%) gas mixture was used as a vapour carrier. The furnace was heated to 800 °C, temperature was held constant for

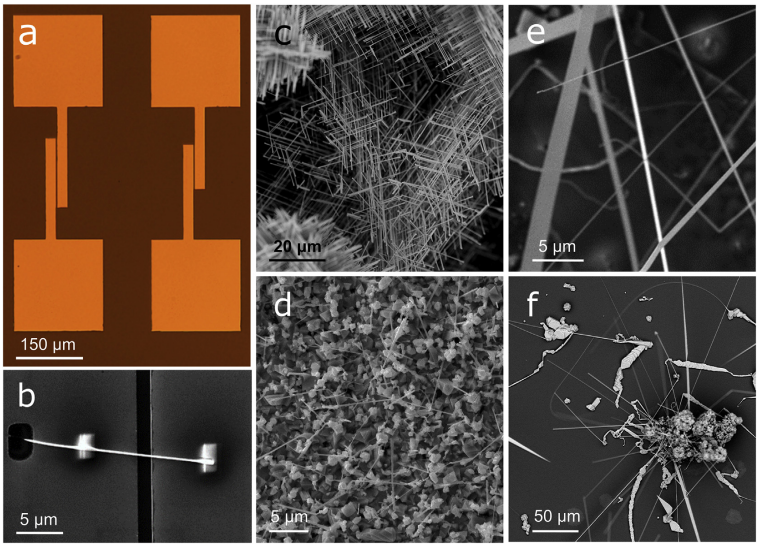

Fig. 1. (a) Optical microscope image of gold microelectrodes on the oxidized silicon substrate; SEM images of (b) a typical as-prepared nanowire photoresistor; as-grown (c) PbS, (d) In_2S_3, (e) CdS and (f) ZnSe nanowires.

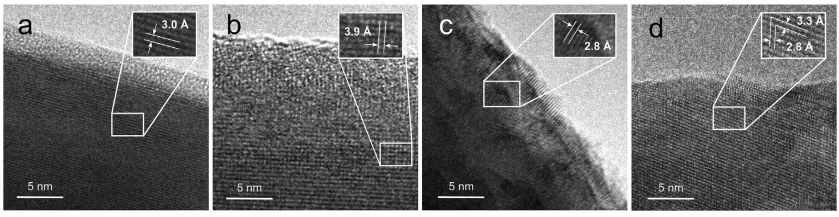

Fig. 2. TEM images of (a) PbS, (b) In_2S_3, (c) CdS and (d) ZnSe nanowires. Insets show measured atomic interlayer distances.

45 min and then was let to cool down naturally to room temperature.

CdS NWs: CdS powder (*98%, Alfa Aesar*) was thermally evaporated in a quartz tube at 950 °C temperature for 30 min, followed by a natural cooling. The vapour was carried downstream to the Au/Si substrate by N_2 gas.

ZnSe NWs: 0.2 g home-made ZnSe powder was placed at the centre of the quartz tube and evaporated at 1000 °C for 2.5 h, using Ar/H_2 (5%) gas to carry vapour downstream to the Au/Si substrate at a lower temperature region, and then cooled down naturally to the room temperature.

As-prepared NW morphology was characterized by scanning electron microscopy (SEM, Lyra, Tescan), whereas the inner crystalline structure was revealed by transmission electron microscopy (TEM, Tecnai GF20, FEI) using the operating voltage of 200 kV. X-ray diffraction (XRD, PANalytical, X'Pert Pro Powder) was carried out by monochromatic Cu Kα irradiation to confirm the material and the phase of a NW. Room-temperature photoluminescence (PL, Hamamatsu R92P PMT) spectra with the excitation wavelength of 266 nm (fourth harmonic of Nd:YAG laser) for all NWs and infrared (IR) absorption spectrum (Bruker Equinox 55 FT-IR Spectrometer) for PbS NWs were measured to investigate their optical properties.

2.2. Single nanowire photoresistor fabrication

Firstly, gold microelectrodes with the gap width of 2 μm were prepared on an oxidized silicon wafer by conventional photolithography technique (see Fig. 1(a)). Briefly, microelectrode pattern was obtained using direct write laser lithography (μPG 101, Heidelberg Instruments) on SU-8 2003 photoresist (MicroChem), 5/45 nm Cr/Au film was deposited via thermal evaporation method, followed by a *lift-off* procedure.

Secondly, single NW photoresistors were fabricated using *in situ* nanomanipulations inside SEM-FIB. As-grown NWs were mechanically transferred from the Si substrate to the as-prepared gold microelectrodes by welding a single NW to the tungsten (W) nanomanipulator probe using electron-beam-assisted platinum (Pt) deposition. After aligning and placing it on top of the microelectrodes, NW was cut off from the W probe with gallium (Ga) ion beam and welded to the electrodes with Pt deposition to ensure the electric contact and fixed position. SEM image of a typical as-prepared photoresistor is displayed in Fig. 1(b), where the narrow dark strip is the gap between the electrodes, two small rectangles on the NW are the deposited Pt contacts, and the trench appeared due to the cutting NW by ion beam milling.

2.3. Device measurements

Current-voltage (I_{ds}-V_{ds}) characteristics and photoresponse of the fabricated two-terminal devices were measured at zero gate voltage ($V_g = 0$ V) with a two-contact micro probe station connected with Model 6485 Keithley Picoammeter, Model 2000 Keithley Multimeter and a voltage source (33220A Waveform Generator, Agilent). 405 nm, 532 nm and 660 nm wavelength semiconductor diode lasers with light intensity of 2 W/cm^2 were used as an illumination source for the photoresponse measurements. All measurements were carried out in air and at room temperature.

3. Results and discussion

3.1. Morphology, structure and PL measurements

SEM was used to image as-grown NW arrays (see Fig. 1(c–f)) and to determine the size of individual NWs. The length varied from 20 to 30 μm for PbS and In_2S_3 NWs to several hundred micrometres for CdS and ZnSe NWs. The diameter of NWs was in the range of 50–300 nm. The Au catalyst nanoparticles were observed on the top end of In_2S_3, CdS and ZnSe NWs, which indicates Vapour-Liquid-Solid (VLS) growth, as was expected [20–22]; however, that was not the case for PbS NWs: these NWs exhibited growth in hierarchical, orthogonally branched clusters, as reported previously [23]. It is worth noting that nanobelts were also observed on as-prepared CdS and ZnSe samples, along with the NWs, though only NWs were used to fabricate photoresistor

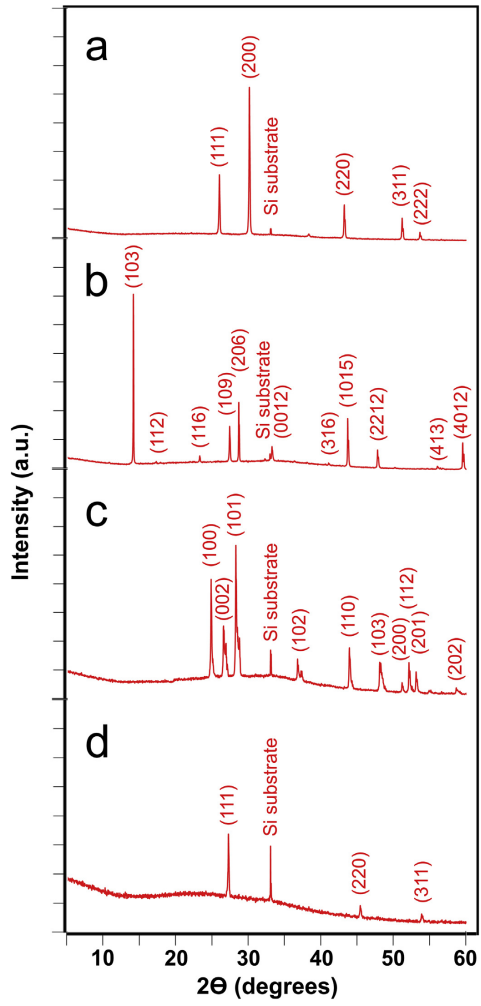

Fig. 3. XRD spectra of (a) PbS, (b) In_2S_3, (c) CdS and (d) ZnSe nanowire arrays on a silicon substrate.

devices.

TEM investigations revealed inner crystalline structure of the NWs. Fig. 2(a) shows highly crystalline nature of a PbS NW. Resolved atomic planes are separated by a distance of 3.0 Å, which corresponds to (200) planar spacing of a cubic (rock-salt) PbS crystal (a = 5.94 Å [24]). Similarly, an In_2S_3 NW exhibited high crystallinity, as can be seen in Fig. 2(b). Interplanar spacing was measured to be 3.9 Å, which is in a good agreement with the lattice constant of tetragonal β-In_2S_3 (a = 7.8 Å [25]). Polycrystalline shell was observed around the CdS NW, which is visible in Fig. 2(c). According to interplanar distance measurements, such crystallites have cubic (zinc blende) structure with planar spacing of 2.7–2.8 Å, which corresponds to the lattice constant value a = 5.45 Å [26]. As can be seen in Fig. 2(d), the distances between adjacent ZnSe lattice planes was measured to be 3.3 Å and 2.8 Å, which corresponds to cubic (zinc blende) structure (a = 5.6 Å [27]).

Fig. 3 depicts the XRD patterns of the as-grown NW arrays, which verifies their material and phase. The diffraction peaks in PbS NW XRD pattern were indexed to a cubic PbS crystal [24], In_2S_3 NW pattern to a tetragonal β-In_2S_3 crystal [25], CdS NW pattern to a hexagonal wurtzite structure [28], and ZnSe XRD pattern was indexed to cubic (zinc blende) ZnSe crystal structure [27]. The peak at 33° is attributed to the diffraction in the Si substrate.

PL properties of the as-grown NWs were studied at the room temperature in the wavelength range from 380 nm to 580 nm, excited by 266 nm laser. Measured spectra are shown in Fig. 4. The bandgap of PbS NWs is around 0.4 eV and the optical absorption starts at 3100 nm, therefore luminescence band with maximum at 425 nm (see Fig. 4(a)) corresponds to higher energy band transitions [29,30]. Similar luminescence was measured on PbS nanocubes and thin films in other works by Cao et al. [31] and Tohidi et al. [32]. The inset of Fig. 4(a) depicts measured optical absorption spectrum of PbS NWs, thus confirming that the absorption starts around 3 μm wavelength light. Fig. 4(b, c, d) shows measured luminescence bands of In_2S_3, CdS and ZnSe, respectively. Their according maxima are 505 nm, 510 nm and 460 nm, that corresponds to bandgap values of 2.45 eV, 2.43 eV and 2.7 eV, in agreement with previous reports [6,19,20].

3.2. Device photoresponse measurements

Fig. 5 shows measured I_{ds}-V_{ds} curves of different as-prepared two-terminal NW devices. At least four photoresistors of each material were fabricated, so consistent conclusions could be made. Typically, nearly symmetrical characteristics were measured for all investigated NW materials, therefore indicating that ohmic contacts were formed between the electrodes and the NW. Features of non-linear quadratic ($I \sim V^2$) behaviour of the I-V curves may be interpreted as an effect of the space-charge limited current (SCLC), as other groups have previously shown in different material nanowires [33,34]. In addition, it is worth noting that as-fabricated devices exhibit high resistance, wherein, most probably, a considerable part arises due to a high contact resistance since performed NW characterization indicated highly crystalline structure. Possible causes of such increased resistance include high resistance of deposited Pt contacts due to a carbon presence from the metal-organic precursor [35].

Next, as-prepared NW device electrical response to an illumination of a light at different wavelengths was investigated. On-off photoresponse measurements, which are based on photoinduced conductivity changes, for three different illumination wavelengths at V_{ds} = 1 V bias of as-prepared NW photoresistor devices are

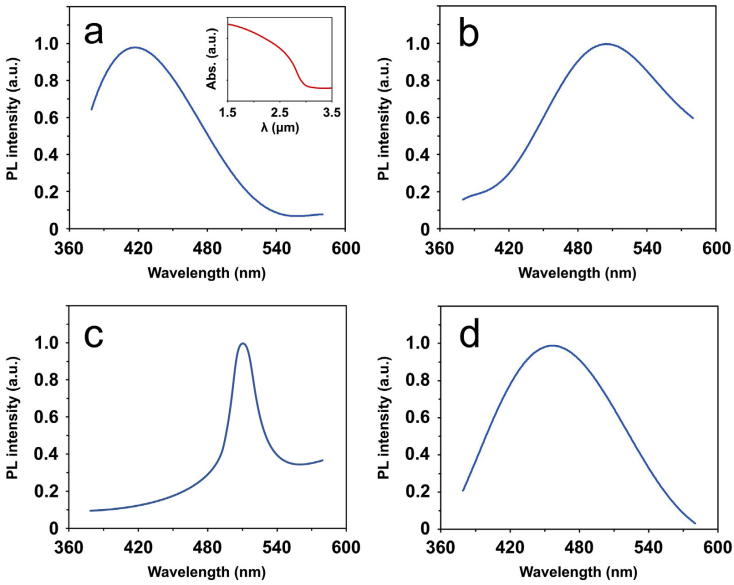

Fig. 4. Room-temperature PL spectra at the excitation wavelength of 266 nm of (a) PbS, (b) In_2S_3, (c) CdS and (d) ZnSe nanowire arrays on a silicon substrate. The inset shows the optical absorption in PbS NWs in 1.5–3.5 μm wavelength range.

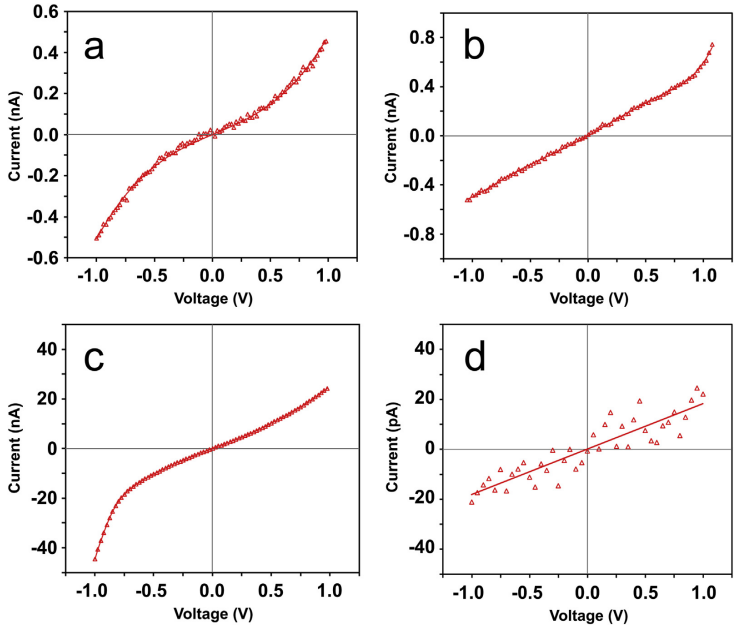

Fig. 5. Output (I_{ds}-V_{ds}) characteristics at $V_g = 0$ V of (a) PbS, (b) In_2S_3, (c) CdS and (d) ZnSe nanowire photoresistors.

depicted in Fig. 6. It can be seen that all four studied NW materials exhibit rapid (<1 s, in most cases) increase and decrease of the current after the illumination is turned on or off, respectively, except in the case of the In_2S_3 NW current decay time for 405 nm illumination, which features a second, slower time component, most probably do to a presence of trapping centres.

Table 1 shows the comparison of current enhancement ratios (I_{on}/I_{off}) of the studied NW materials in the context of their respective bandgap, which determines their cut-off wavelengths. Firstly, it can be seen that PbS NWs exhibit weak (I_{on}/I_{off} close to 1) photoresponse to all three illumination wavelengths; however, linear ratio vs. wavelength dependence was observed. Secondly, In_2S_3 and CdS NWs exhibit strong photoresponse to 405 nm illumination, and significantly weaker one to 532 nm and 660 nm illumination. Finally, ZnSe NWs show very strong response to 405 nm light, and no photoresponse was observed while illuminating them with 532 nm and 660 nm wavelength light. Obtained I_{on}/I_{off} value tendencies, for the most part, are as was anticipated from the material bandgap values; however, relatively weaker photoresponse to 660 nm illumination was expected for either CdS or In_2S_3 NWs.

Two important parameters for evaluating the quality of photoconductors are the current responsivity (R_λ) and the external quantum efficiency (EQE). R_λ and EQE are defined, respectively, as $R_\lambda = \Delta I/(PS)$ and $EQE = hcR_\lambda/(e\lambda)$ [36], where ΔI is the difference between the photocurrent I_{on} and the dark current I_{off}, P is the light power density, S is the effective illumination area (estimated as the electrode gap width × NW diameter), h is Planck's constant, c is the speed of light, e is the electron charge, and λ is the light wavelength. Large R_λ and EQE values correspond to a high photodetector sensitivity. Table 2 contains the calculated R_λ and EQE values of the studied NW devices. The obtained data shows a relatively wide range of values for different NW materials, however these values are comparable to other typical state-of-art 1D nanostructure photodetectors [37], thus indicating the potential to use such materials in future applications.

In principle, there are two approaches for determining the colour (red (660 nm), green (532 nm) or blue (405 nm)) of the incident light with such NW photoresistors, if they would be simultaneously incorporated on the same substrate as one optoelectronic device: by the wavelength cut-off due to the bandgap (signal or no signal) and by comparison of I_{on}/I_{off} values of at least two different materials. In the perfect case, red, green and blue colours could be recognized by selecting three different materials with cut-off wavelengths in three different regions of the optical spectrum: one material that responds only to the blue light ($405\text{ nm} < \lambda_{cut\text{-}off} < 532\text{ nm}$), one that responds to the blue and green light ($532\text{ nm} < \lambda_{cut\text{-}off} < 660\text{ nm}$), and one that responds to all three ($\lambda_{cut\text{-}off} > 660$ nm); and by illuminating them simultaneously with the same light and comparing all photoresponse signals. However, in our case, only ZnSe measurement solely determined the incident (blue) light due to its cut-off wavelength. Other studied materials exhibited substantial decrease in photoresponse in respect of the increasing wavelength, but still significant response was measured for the light with the longest wavelength, presumably due to some defect states, such as NW surface, or impurity doping. Thus, in such instance, one can only distinguish red and green or blue and green light of the same intensity by comparing absolute I_{on}/I_{off} values of, for example, PbS and CdS. Comparison could be made through logic operations of the

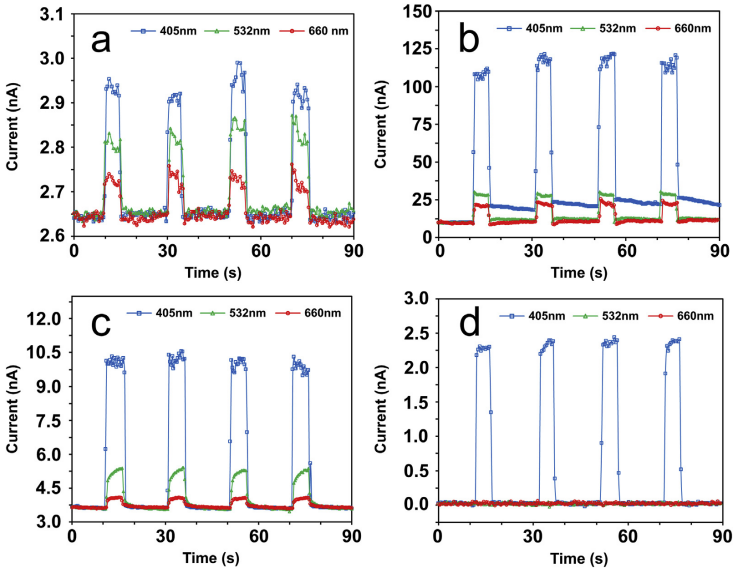

Fig. 6. On-off photoresponse measurements of (a) PbS, (b) In_2S_3, (c) CdS and (d) ZnSe nanowire photoresistors at V_{ds} = 1 V bias voltage and 2 W/cm^2 light intensity of 405 nm, 532 nm and 660 nm wavelength light illumination. The diameters of PbS, In_2S_3, CdS and ZnSe NWs are 120, 160, 180 and 280 nm, respectively.

Table 1
Comparison of the photoresponses of the studied nanowire-based photoresistors.

Materials	E_g (eV)	I_{dark} at 1 V (nA)	I_{on}/I_{off} ratio		
			at 405 nm (3.06 eV)	at 532 nm (2.33 eV)	at 660 nm (1.88 eV)
PbS NW	0.41	2.65	1.11	1.07	1.03
In_2S_3 NW	2.1	9.95	11.3	2.8	2.1
CdS NW	2.4	3.65	2.7	1.4	1.1
ZnSe NW	2.7	0.02	115	1	1

Table 2
Responsivity R_λ and external quantum efficiency EQE values of the studied nanowire-based photoresistors at different illumination wavelengths.

Materials	R_λ, A/W			EQE		
	at 405 nm	at 532 nm	at 660 nm	at 405 nm	at 532 nm	at 660 nm
PbS NW	0.06	0.04	0.02	18%	9%	3%
In_2S_3 NW	16.01	2.80	1.71	4903%	652%	321%
CdS NW	0.86	0.20	0.05	264%	47%	10%
ZnSe NW	0.20	0	0	62%	0	0

specific NW current signals, which arise from distinct photoresponse values of NWs [38,39]. However, this above-cut-off-wavelength photoresponse might be considerably reduced by surface passivation, therefore simplifying the principle of colour distinction. That could be done by producing a shell layer around the core material that eliminates its surface trap states, and could even lead to an enhanced photosensitivity [40–42]. In general, choosing different photosensitive NWs for desired spectral range, depending on the application, is possible yet not always sufficient – defects, such as NW surface, or impurity doping can result in above-cut-off-wavelength photosensitivity.

4. Conclusions

PbS, In_2S_3, CdS and ZnSe NWs were synthesised via atmospheric pressure chemical vapour transport method. Samples were characterized by SEM, TEM methods, XRD technique, which revealed their highly crystalline structure, and PL measurements to investigate their optical properties. Two-terminal photoresistor devices were fabricated from as-grown NWs using *in situ* nanomanipulations and electron-beam-assisted Pt deposition inside SEM-FIB; their current-voltage and photoresponse measurements were performed under the same conditions. Two approaches for

determining the colour (red, green or blue) with as-prepared NW photoresistors were discussed. While determination via the cut-off wavelength due to the bandgap would be the best approach in this case, considerable above-cut-off-wavelength photosensitivity was observed; therefore, a method for reducing this undesired photoresponse is necessary to be implemented.

Acknowledgements

Financial support provided by Scientific Research Project for Students and Young Researchers Nr. SJZ/2016/6 realized at the Institute of Solid State Physics, University of Latvia is greatly acknowledged. Authors are grateful to Reinis Ignatans for XRD measurements.

References

[1] E.H. Steenbergen, M.J. DiNezza, W.H.G. Dettlaff, S.H. Lim, Y.-H. Zhang, Optically-addressed two-terminal multicolor photodetector, Appl. Phys. Lett. 97 (2010) 161111, https://doi.org/10.1063/1.3505137.
[2] G. Konstantatos, E.H. Sargent, Nanostructured materials for photon detection, Nat. Nanotechnol. 5 (2010) 391–400, https://doi.org/10.1038/nnano.2010.78.
[3] Y. Liu, R. Cheng, L. Liao, H. Zhou, J. Bai, G. Liu, L. Liu, Y. Huang, X. Duan, Plasmon resonance enhanced multicolour photodetection by graphene, Nat. Commun. 2 (2011) 579, https://doi.org/10.1038/ncomms1589.
[4] E. Laux, C. Genet, T. Skauli, T.W. Ebbesen, Plasmonic photon sorters for spectral and polarimetric imaging, Nat. Photonics 2 (2008) 161–164, https://doi.org/10.1038/nphoton.2008.1.
[5] C. Soci, A. Zhang, B. Xiang, S.A. Dayeh, D.P.R. Aplin, J. Park, X.Y. Bao, Y.H. Lo, D. Wang, ZnO nanowire UV photodetectors with high internal gain, Nano Lett. 7 (2007) 1003–1009, https://doi.org/10.1021/nl070111x.
[6] K. Deng, L. Li, CdS nanoscale photodetectors, Adv. Mater. 26 (2014) 2619–2635, https://doi.org/10.1002/adma.201304621.
[7] R. Graham, C. Miller, E. Oh, D. Yu, Electric field dependent photocurrent decay length in single lead sulfide nanowire field effect transistors, Nano Lett. 11 (2011) 717–722, https://doi.org/10.1021/nl1038456.
[8] X. Xie, G. Shen, Single-crystalline In2S3 nanowire-based flexible visible-light photodetectors with an ultra-high photoresponse, Nanoscale 7 (2015) 5046–5052, https://doi.org/10.1039/C5NR00410A.
[9] C.H. Hsiao, S.J. Chang, S.B. Wang, S.P. Chang, T.C. Li, W.J. Lin, C.H. Ko, T.M. Kuan, B.R. Huang, ZnSe nanowire photodetector prepared on oxidized silicon substrate by molecular-beam epitaxy, J. Electrochem. Soc. 156 (2009), https://doi.org/10.1149/1.3077580. J73.
[10] T. Takahashi, P. Nichols, K. Takei, A.C. Ford, A. Jamshidi, M.C. Wu, C.Z. Ning, A. Javey, Contact printing of compositionally graded CdSxSe1-x nanowire parallel arrays for tunable photodetectors, Nanotechnology 23 (2012) 45201, https://doi.org/10.1088/0957-4484/23/4/045201.
[11] H. Dedong, L. Ying-Kai, D. Yu, Multicolor photodetector of a single Er3+-Doped CdS nanoribbon, Nanoscale Res. Lett. 10 (2015) 285, https://doi.org/10.1186/s11671-015-0975-3.
[12] H. Park, Y. Dan, K. Seo, Y.J. Yu, P.K. Duane, M. Wober, K.B. Crozier, Filter-free image sensor pixels comprising silicon nanowires with selective color absorption, Nano Lett. 14 (2014) 1804–1809, https://doi.org/10.1021/nl404379w.
[13] X. Liu, L. Jiang, X. Zou, X. Xiao, S. Guo, C. Jiang, X. Liu, Z. Fan, W. Hu, X. Chen, W. Lu, W. Hu, L. Liao, Scalable integration of indium zinc oxide/photosensitive-nanowire composite thin-film transistors for transparent multicolor photodetectors array, Adv. Mater. 26 (2014) 2919–2924, https://doi.org/10.1002/adma.201305073.
[14] L. Sang, J. Hu, R. Zou, Y. Koide, M. Liao, Arbitrary multicolor photodetection by hetero-integrated semiconductor nanostructures, Sci. Rep. 3 (2013) 2368, https://doi.org/10.1038/srep02368.
[15] Z. Fan, J.C. Ho, T. Takahashi, R. Yerushalmi, K. Takei, A.C. Ford, Y.-L. Chueh, A. Javey, Toward the development of printable nanowire electronics and sensors, Adv. Mater. 21 (2009) 3730–3743, https://doi.org/10.1002/adma.200900860.
[16] S.Y. Jang, Y.M. Song, H.S. Kim, Y.J. Cho, Y.S. Seo, G.B. Jung, C. Lee, J. Park, M. Jung, J. Kim, B. Kim, J.-G. Kim, Y.-J. Kim, Three synthetic routes to single-crystalline PbS nanowires with controlled growth direction and their electrical transport properties, ACS Nano 4 (2010) 2391–2401, https://doi.org/10.1021/nn100163k.
[17] M. Zervos, P. Papageorgiou, A. Othonos, High yield–low temperature growth of indium sulphide nanowires via chemical vapor deposition, J. Cryst. Growth 312 (2010) 656–661, https://doi.org/10.1016/j.jcrysgro.2009.12.023.
[18] Y. Wang, G. Meng, L. Zhang, C. Liang, J. Zhang, Catalytic growth of large-scale single-crystal CdS nanowires by physical evaporation and their photoluminescence, Chem. Mater. 14 (2002) 1773–1777, https://doi.org/10.1021/cm0115564.
[19] U. Philipose, P. Sun, T. Xu, H.E. Ruda, L. Yang, K.L. Kavanagh, Structure and photoluminescence of ZnSe nanostructures fabricated by vapor phase growth, J. Appl. Phys. 101 (2007) 14326, https://doi.org/10.1063/1.2424400.
[20] A. Datta, G. Sinha, S.K. Panda, A. Patra, Growth, optical, and electrical properties of In2S3 zigzag nanowires, Cryst. Growth Des. 9 (2009) 427–431, https://doi.org/10.1021/cg800663t.
[21] L. Dong, J. Jiao, M. Coulter, L. Love, Catalytic growth of CdS nanobelts and nanowires on tungsten substrates, Chem. Phys. Lett. 376 (2003) 653–658, https://doi.org/10.1016/S0009-2614(03)01059-5.
[22] S. Kar, S. Biswas, S. Chaudhuri, Catalytic growth and photoluminescence properties of ZnS nanowires, Nanotechnology 16 (2005) 737–740, https://doi.org/10.1088/0957-4484/16/6/018.
[23] Y.K. Albert Lau, D.J. Chernak, M.J. Bierman, S. Jin, Epitaxial growth of hierarchical PbS nanowires, J. Mater. Chem. 19 (2009) 934, https://doi.org/10.1039/b818187j.
[24] JCPDS Card No. 78–1058, (n.d.).
[25] JCPDS Card No. 25–0390, (n.d.).
[26] JCPDS Card No. 21–829, (n.d.).
[27] JCPDS Card No. 37–1463, (n.d.).
[28] JCPDS Card No. 41–1049, (n.d.).
[29] N.S. Dantas, A.F. da Silva, C. Persson, Electronic band-edge properties of rock salt PbY and SnY (Y= S, Se, and Te), Opt. Mater. (Amst) 30 (2008) 1451–1460, https://doi.org/10.1016/j.optmat.2007.09.001.
[30] A.D. Andreev, A.A. Lipovskii, Anisotropy-induced optical transitions in PbSe and PbS spherical quantum dots, Phys. Rev. B 59 (1999) 15402–15404, https://doi.org/10.1103/PhysRevB.59.15402.
[31] H. Cao, G. Wang, S. Zhang, X. Zhang, Growth and photoluminescence properties of PbS nanocubes, Nanotechnology 17 (2006) 3280–3287, https://doi.org/10.1088/0957-4484/17/13/034.
[32] T. Tohidi, K. Jamshidi-Ghaleh, Optical and structural properties of nanocrystalline PbS thin film grown by CBD on Si(1 0 0) substrate, Philos. Mag. 94 (2014) 3368–3381, https://doi.org/10.1080/14786435.2014.959579.
[33] A.A. Talin, F. Léonard, B.S. Swartzentruber, X. Wang, S.D. Hersee, Unusually strong space-charge-limited current in thin wires, Phys. Rev. Lett. 101 (2008) 76802, https://doi.org/10.1103/PhysRevLett.101.076802.
[34] A.M. Katzenmeyer, F. Leonard, A.A. Talin, M.E. Toimil-Molares, J.G. Cederberg, J.Y. Huang, J.L. Lensch-Falk, Observation of space-charge-limited transport in InAs nanowires, IEEE Trans. Nanotechnol. 10 (2011) 92–95, https://doi.org/10.1109/TNANO.2010.2062198.
[35] A. Vilà, F. Hernández-Ramirez, J. Rodríguez, O. Casals, A. Romano-Rodríguez, J.R. Morante, M. Abid, Fabrication of metallic contacts to nanometre-sized materials using a focused ion beam (FIB), Mater. Sci. Eng. C 26 (2006) 1063–1066, https://doi.org/10.1016/j.msec.2005.09.092.
[36] Y. Ye, L. Dai, X. Wen, P. Wu, R. Pen, G. Qin, High-performance single CdS nanobelt metal-semiconductor field-effect transistor-based photodetectors, ACS Appl. Mater. Interfaces 2 (2010) 2724–2727, https://doi.org/10.1021/am100661x.
[37] T. Zhai, L. Li, X. Wang, X. Fang, Y. Bando, D. Golberg, Recent developments in one-dimensional inorganic nanostructures for photodetectors, Adv. Funct. Mater. 20 (2010) 4233–4248, https://doi.org/10.1002/adfm.201001259.
[38] Y.-Q. Bie, Z.-M. Liao, H.-Z. Zhang, G.-R. Li, Y. Ye, Y.-B. Zhou, J. Xu, Z.-X. Qin, L. Dai, D.-P. Yu, Self-powered, ultrafast, visible-blind UV detection and optical logical operation based on ZnO/GaN nanoscale p-n junctions, Adv. Mater. 23 (2011) 649–653, https://doi.org/10.1002/adma.201003156.
[39] Z. Fan, J.C. Ho, Z.A. Jacobson, H. Razavi, A. Javey, Large-scale, heterogeneous integration of nanowire arrays for image sensor circuitry, Proc. Natl. Acad. Sci. 105 (2008) 11066–11070, https://doi.org/10.1073/pnas.0801994105.
[40] L. Qin, C. Shing, S. Sawyer, P.S. Dutta, Enhanced ultraviolet sensitivity of zinc oxide nanoparticle photoconductors by surface passivation, Opt. Mater. (Amst) 33 (2011) 359–362, https://doi.org/10.1016/j.optmat.2010.09.020.
[41] K. Moazzami, T.E. Murphy, J.D. Phillips, M.C.-K. Cheung, A.N. Cartwright, Sub-bandgap photoconductivity in ZnO epilayers and extraction of trap density spectra, Semicond. Sci. Technol. 21 (2006) 717–723, https://doi.org/10.1088/0268-1242/21/6/001.
[42] Y. Dan, K. Seo, K. Takei, J.H. Meza, A. Javey, K.B. Crozier, Dramatic reduction of surface recombination by in situ surface passivation of silicon nanowires, Nano Lett. 11 (2011) 2527–2532, https://doi.org/10.1021/nl201179n.

Paper IV

Journal of Crystal Growth 459 (2017) 100–104

Contents lists available at ScienceDirect

Journal of Crystal Growth

journal homepage: www.elsevier.com/locate/jcrysgro

Synthesis and characterization of ZnO/ZnS/MoS_2 core-shell nanowires

Edgars Butanovs[a], Alexei Kuzmin[a], Jelena Butikova[a], Sergei Vlassov[b], Boris Polyakov[a,*]

[a] Institute of Solid State Physics, University of Latvia, Kengaraga street 8, LV-1063 Riga, Latvia
[b] Institute of Physics, University of Tartu, Ravila 14c, 50412 Tartu, Estonia

ARTICLE INFO

Communicated by K. Nakajima

Keywords:
A1 Characterization
A1 Crystal morphology
A1 Nanostructures
B1 Oxides
B1 Sulfides
B1 Zinc compounds

ABSTRACT

Hybrid nanostructures composed of layered materials have recently attracted a lot of attention due to their promising electronic and catalytic properties. In this study, we describe a novel synthesis strategy of ZnO/ZnS/MoS_2 core-shell nanowire growth using a three-step route. First, ZnO nanowire array was grown on a silicon wafer. Second, the sample was immersed in ammonium molybdate solution and dried. At the third step, the sample was annealed in a sulfur atmosphere at 700 °C. Two solid state chemical reactions occur simultaneously during the annealing and result in a formation of ZnS and MoS_2 phases. Produced ZnO/ZnS/MoS_2 core-shell nanowires were characterized by scanning and transmission electron microscopy, whereas their chemical composition was confirmed by selected area electron diffraction and micro-Raman spectroscopy.

1. Introduction

Recent advances in research of layered materials, as for example, graphene, have stimulated studies of two-dimensional (2D) transition metal dichalcogenides (TMDs) with unique properties that do not exist in their bulk counterparts [1,2]. TMDs, such as MS_2 (M=W, Mo), are indirect bandgap semiconductors in bulk form, however, when scaled down to monolayers, a direct energy bandgap emerges due to quantum confinement effects [2,3]. WS_2 and MoS_2 monolayers are widely studied due to their unique optical [4,5] and electronic [6] properties and potential applications in electronics and optoelectronics [7,8].

MoS_2 probably is the most explored TMD. It can be synthesized in a form of powder, polycrystalline film, 2D nanosheets and nanotubes [9]. MoS_2 is an n-type semiconductor having the indirect and direct band gaps of E_{ig}=1.2 eV and E_{dg}=1.8 eV, respectively. MoS_2 is also chemically inert, thermally stable and not toxic [10].

Zinc oxide (ZnO) nanowires (NWs), that have been in focus of scientific community for decades, are still gaining increased attention due to the simplicity of synthesis and a number of beneficial properties. Among other applications, ZnO NWs can be used as a template for the synthesis of heterostructured nanomaterials [11]. Zinc oxide has two main phases: hexagonal wurtzite and cubic zincblende. Wurtzite is the most common and most stable structure, while zincblende form grows on substrates with cubic lattice structure. Bulk ZnO is known to be a direct band gap (3.2–3.3 eV) n-type semiconductor [12].

It is known that the use of core-shell materials with the shell having higher band gap leads to an enhancement of optical properties. Band gap of zinc sulfide (ZnS) for both zincblende (3.7 eV) and wurtzite (3.9 eV) forms is wider than that of ZnO at room temperature [13]. Therefore, ZnS is frequently used to improve luminescent properties of ZnO [14]. There are many methods to produce ZnS shell around ZnO core [15], and one of them is direct sulfidation process as it was demonstrated in [16].

Recently, several groups reported on wet chemical synthesis of ZnO-MoS_2 hybrid heterostructures [17–19]. In these studies, superior photocatalytic properties of ZnO-MoS_2 hybrid heterostructures were demonstrated, in particular for photocatalytic hydrogen evolution reaction and photodegradation of methylene blue and other organic dyes. Also direct coupling between ZnO nanorods and MoS_2 monolayers was used in [20] to enhance Raman and photoluminescence emission.

In this study we report for the first time on the synthesis of ZnO/ZnS/MoS_2 core-shell NWs by immersion of ZnO NWs in the solution of ammonium molybdate followed by annealing in the sulfur atmosphere. Such ZnO/ZnS/MoS_2 core-shell nanostructures could potentially be applied for photocatalytic hydrogen evolution reaction and in dye-sensitized-like solar cells.

2. Experimental details

ZnO/ZnS/MoS_2 core-shell nanowires were produced by a three-step route: 1) synthesis of ZnO NWs on a silicon wafer, 2) immersion of the ZnO NW sample in ammonium molybdate solution, 3) annealing of the sample in sulfur atmosphere.

ZnO NWs were grown by a chemical vapour transport method using spherical Au nanoparticles as a catalyst (*Smart materials*, water

* Corresponding author.
E-mail address: boris.polyakov@cfi.lu.lv (B. Polyakov).

http://dx.doi.org/10.1016/j.jcrysgro.2016.11.106
Received 12 August 2016; Received in revised form 19 October 2016; Accepted 25 November 2016
Available online 26 November 2016

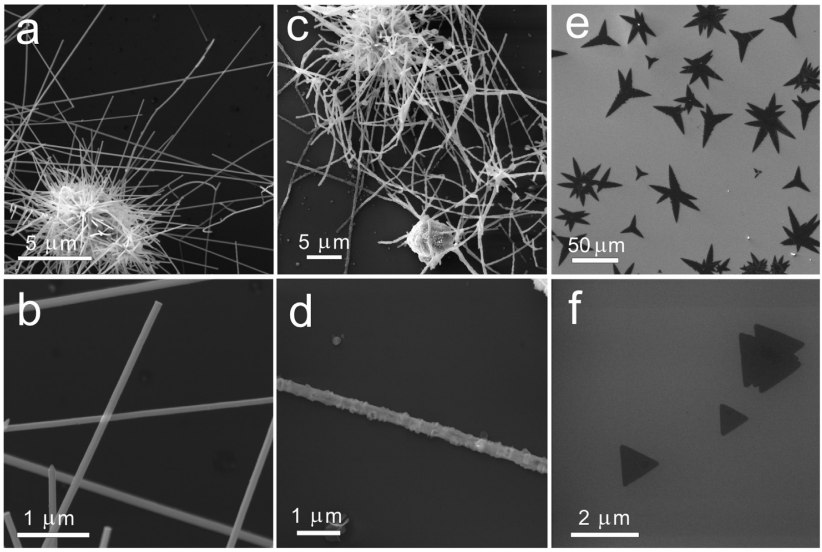

Fig. 1. SEM images of ZnO NWs, immersed in ammonium heptamolybdate solution and dried (a, b); core-shell ZnO/ZnS/MoS_2 NWs after annealing in sulfur atmosphere at 700 °C (c, d); 2D MoS_2 nanosheets grown on a silicon wafer at 700 °C (e,f).

suspension, 50 nm in diameter) [10]. A 1:4 mixture of ZnO and graphite powders was heated to 900 °C in a quartz tube for 30 min in a stream of the carrier gas N_2. Nanowires were synthesized on an oxidized silicon wafers Si(100)/SiO_2 (*Semiconductor Wafer, Inc.)*. At the next step, the samples were immersed into the solution of 0.125 g ammonium heptamolybdate $(NH_4)_6Mo_7O_{24}{\cdot}4H_2O$ in 20 ml H_2O and subsequently dried at room temperature. It is known that ammonium heptamolybdate decomposes at 350–400 °C with a formation of MoO_3 [21]. Therefore, finally, the samples were annealed in a quartz tube in the sulfur atmosphere during 0.5 h at 700 °C to convert the molybdenum precursor (MoO_3) into MoS_2. Additional sample was prepared by annealing in the sulfur atmosphere during 0.5 h at 500 °C to compare quality of MoS_2 shell at lower synthesis temperatures [22].

Morphology of pure ZnO and core-shell NWs on a silicon substrate was characterized by scanning electron microscopy (SEM, Lyra, Tescan). The inner crystalline structure of core-shell NWs was revealed using transmission electron microscopy (TEM, Tecnai GF20, FEI) operated at the accelerating voltage of 200 kV. The diffraction pattern was processed by CrysTBox software [23]. Confocal imaging and micro-Raman measurements were performed with confocal microscope with spectrometer Nanofinder-S (SOLAR TII). A diode pumped solid-state (DPSS) Nd: YAG laser (532 nm, max continuous wave (cw) power P_{ex}=150 mW) was used as the excitation source. A Peltier-cooled back-thinned CCD camera (ProScan HS-101H) was used for detection of Raman spectra. All measurements were performed in a back-scattering geometry through a Nikon CF Plan Apo 100×(NA=0.95) optical objective.

2D MoS_2 nanosheets used as the reference sample were grown using a similar chemical vapour transport process in a quartz tube with a temperature gradient. Powders of MoO_3 (1 mg) and sulfur (0.25 g) were employed as solid sources: MoO_3 was heated to 700 °C and sulfur to 300 °C. Silicon substrate was placed downstream of precursors in the high-temperature zone (700 °C). At the end of the growth process, the furnace was let to cool down to the room temperature naturally. The gas flow rate was held constant throughout the procedure. The optimal growth parameters for the synthesis procedure of MoS_2 nanosheets were found to be 20 min at 700 °C in the high-temperature zone.

Freshly grown MoS_2 nanosheets were studied by Eclipse L150 (Nikon) optical microscope; for higher resolution and contrast images SEM (Tescan, Vega II) was used. The thickness of prepared nanostructures was determined by atomic force microscope (AFM, CP-II, Veeco) in the tapping mode using PPP-NCHR probes with force constant 42 N/m and tip radius of curvature < 10 nm (Nanosensors).

3. Results and discussion

SEM was used to control the growth of pure ZnO NWs and the change of their morphology after subsequent annealing in the sulfur atmosphere. It is clearly visible that the smooth surface of ZnO NWs, immersed in the ammonium heptamolybdate solution, (Fig. 1(a,b)) becomes significantly more rough and altered (Fig. 1(c,d)) after annealing.

Strong electrical charging was observed for the core-shell NWs, however was absent for pure ZnO NWs sample and sample immersed in the ammonium heptamolybdate solution. This may indicate that electrical properties of ZnO NWs were strongly affected by a shell layer, making them less conductive. It is known that sulfur reacts with ZnO at temperatures above 400 °C resulting in a formation of ZnS phase [16], which has the value of the bang gap (3.7 eV) larger than ZnO (3.4 eV) [13]. Alternatively, MoS_2 shell may be responsible for electrical charging.

SEM images of 2D MoS_2 nanosheets with triangular and star shapes grown on Si(100)/SiO_2 wafer at 700 °C are shown in Fig. 1(e,f). These MoS_2 nanosheets were prepared as a reference sample for Raman spectroscopy.

TEM images of core-shell NWs annealed in sulfur atmosphere at 500 °C and 700 °C are shown in Fig. 2. Sample annealed at 500 °C has polycrystalline shell structure of zincblende ZnS, with remaining amorphous phase (Supplementary materials, Fig. S1). No MoS_2 shell

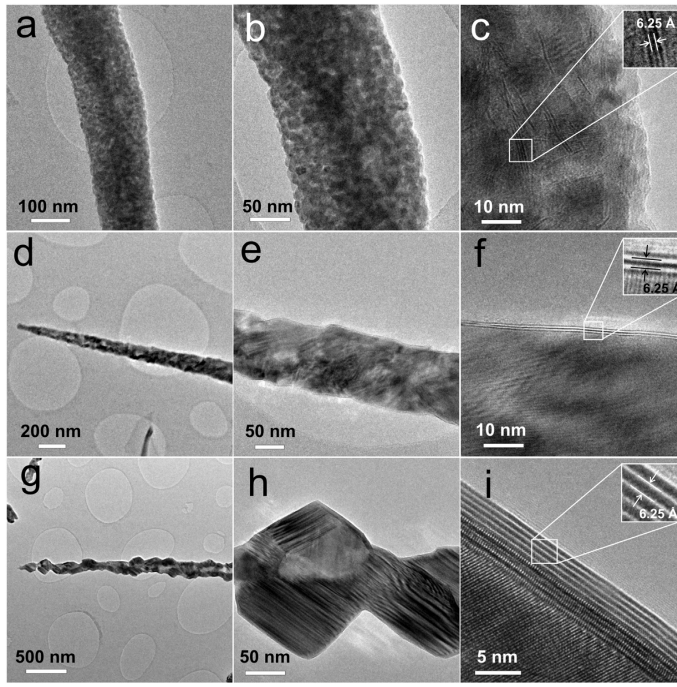

Fig. 2. TEM images of core-shell NWs annealed in sulfur atmosphere at 500 °C (a–c) and 700 °C (d–i). Layers of MoS_2 are visible as black lines on top of the NWs surface (f, i).

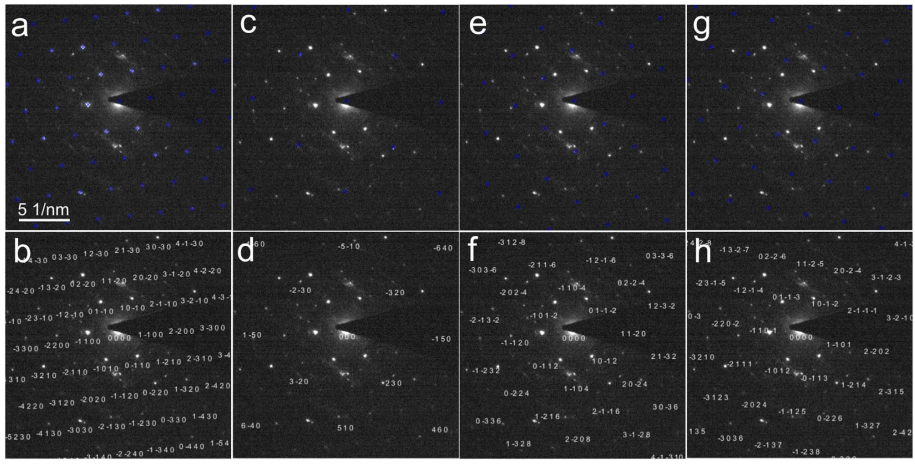

Fig. 3. SAED analysis of core-shell NWs annealed in sulfur atmosphere at 700 °C. The presence of ZnO zincite zone axis ⟨0001⟩ (a, b), ZnS zincblende zone axis ⟨001⟩ (c, d), and MoS_2 molybdenite phases of zone axis ⟨−2201⟩ (e, f) and zone axis ⟨14–53⟩ (g, h) were identified.

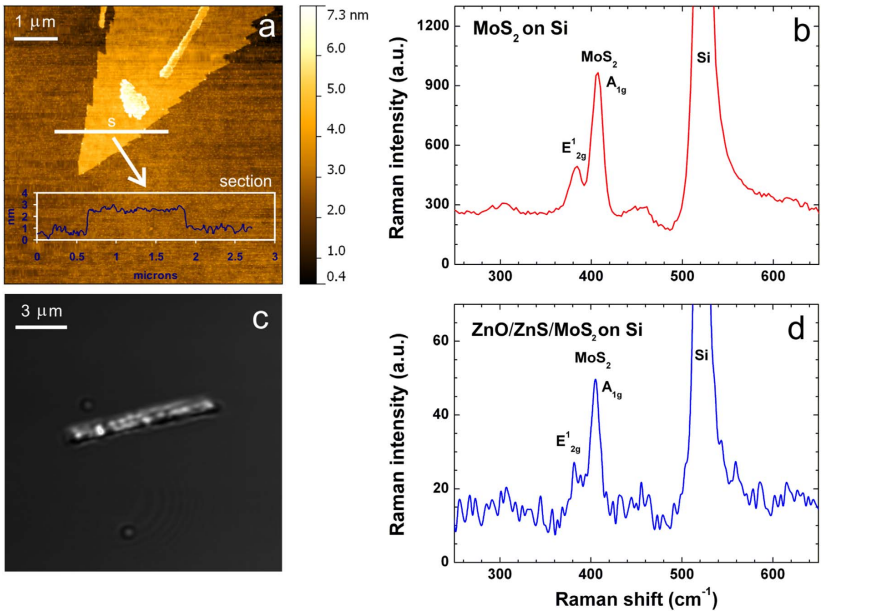

Fig. 4. AFM image (a) and micro-Raman spectrum (b) of 2D MoS_2 nanosheet on a silicon substrate. Confocal microscope image of ZnO/ZnS/MoS_2 NW on a silicon substrate (c) and the corresponding micro-Raman spectrum (d).

was found around the NW, however few crystallites appearing as parallel black lines (Fig. 2(c)) may be identified as MoS_2.

It is easy to see that the shell is non-homogeneous and appears as a mosaic of dark and bright spots (Fig. 2(d,e)) or as microcrystals formed around the NW core (Fig. 2(g,h)) for the sample annealed at 700 °C. Analysis of selected area electron diffraction (SAED) image of a core-shell NW (Fig. 3) reveals the following phases: ZnO zincite (zone axis ⟨0001⟩), ZnS zincblende (zone axis ⟨001⟩), and MoS_2 molybdenite phases (zone axis ⟨−2201⟩ and ⟨14−53⟩). Dominating (most intensive) diffraction spots belong to the ZnO core, while less intensive to ZnS and MoS_2 phases. Symmetric orientation of MoS_2 reflexes relative to ZnO reflexes may indicate epitaxial growth of MoS_2.

According to interplanar distance measurements and SAED analysis data, microcrystals on NW surface can be attributed to zincblende ZnS phase with the interplanar distance d=3.1–3.2 Å [16,24]. Due to the lattice mismatch and different crystal structure of ZnO core and ZnS shell, the upper layer cannot grow as a smooth single crystal layer on top of ZnO NW surface.

We found that samples prepared at 700 °C are coated by a thin layer of MoS_2, which appears as a number of parallel black lines (MoS_2 monolayers) in Fig. 2(f, i). The number of MoS_2 layers varies in the range of 1–8 monolayers, which is probably related to nonhomogeneous coating by ammonium molybdate precursor. The measured distance between monolayers is about 6.25 Å, which corresponds well to 6.2–6.3 Å interlayer distance in MoS_2 nanostructures [18,25].

Alternatively, MoO_3 layer can be deposited on ZnO NWs by DC magnetron sputtering of Mo target in argon-oxygen atmosphere [26]. After sulfidation of ZnO-MoO_3 NWs at 700 °C, morphology of thus obtained core-shell NWs is rather similar to the ones produced by immersion in ammonium heptamolybdate solution (Supplementary materials, Fig. S2). However, MoS_2 shell is usually significantly thicker due to the large amount of deposited MoO_3 precursor (it is difficult to deposit very thin layer of MoO_3 by magnetron sputtering), therefore we can conclude that the immersion method of molybdenum precursor deposition is more preferable in such case compared to the magnetron sputtering.

In our previous work [27], no formation of detectable ZnS layer was observed after the synthesis of ZnO/WS_2 core-shell NWs at 800 °C, and ZnO core remained unaltered and single crystalline after the growth of WS_2 shell (Supplementary materials, Fig. S3). Worth noting that WS_2 growth starts on ZnO surface at the ZnO-WO_3 interface. Probably, WO_3 layer deposited by magnetron sputtering is able to protect ZnO core from sulfidation and/or WO_3 reaction with sulfur is more favourable than ZnO reaction with sulfur.

The phase composition of individual nano-objects such as NWs and 2D nanosheets can be probed by micro-Raman spectroscopy. The results for two samples, a NW and a 2D MoS_2 nanosheet, are reported in Fig. 4. Note that the thickness of the 2D MoS_2 reference nanosheet, measured by AFM, is about 2.6 nm that corresponds to approximately 4 monolayers [28].

The obtained Raman spectrum of the core-shell NW (Fig. 4(d)) is similar to that of the 2D MoS_2 nanosheet (Fig. 4(b)), which confirms the formation of MoS_2 layer on the NWs. The in-plane E^1_{2g} mode at 384 cm^{-1} and the out-of-plane A_{1g} mode at 407 cm^{-1} were clearly resolved on the 2D MoS_2 nanosheet (Fig. 4(b)). The same modes E^1_{2g} at 384 cm^{-1} and A_{1g} at 407 cm^{-1} were observed on the core-shell NW (Fig. 4(c,d)) [29,30]. Note that the large peak at ~521 cm^{-1} is the first order of optical mode at k=0 of the underlying silicon substrate [31]. No Raman bands due to ZnO [32] and ZnS [33] phases were observed because of their weak Raman activity.

4. Conclusions

In this study we demonstrated a simple process for the production

of core-shell ZnO/ZnS/MoS_2 nanowires. A few-layer MoS_2 shell was grown on ZnO NW core by immersing ZnO NWs in ammonium molybdate solution, followed by annealing in a sulfur atmosphere at 700 °C. Two solid state chemical reactions occur during the annealing and result in a formation of ZnS and MoS_2 layers. The annealing at lower temperature (500 °C) is not sufficient for a formation of continuous MoS_2 shell. Morphology and internal structure of the synthesized ZnO/ZnS/MoS_2 core-shell NWs were investigated by SEM and TEM, respectively. The formation of zincblende ZnS interlayer and MoS_2 shell was confirmed by SAED analysis and micro-Raman spectroscopy, respectively.

Acknowledgements

The present research was supported by the Latvian National Research Program IMIS2. Authors are grateful for Dr. Robert Kalendarev and Martins Zubkins for assistance in magnetron sputtering, Dr. Krisjanis Smits for TEM measurements, Dr. Roberts Zabels for AFM measurements and Reinis Ignatans for XRD measurements.

Appendix A. Supplementary material

Supplementary data associated with this article can be found in the online version at http://dx.doi.org/10.1016/j.jcrysgro.2016.11.106.

References

[1] P. Hajiyev, C.X. Cong, C.Y. Qiu, T. Yu, Contrast and Raman spectroscopy study of single-and few-layered charge density wave material: 2H-Tase$_2$, Sci. Rep. 3 (2013) 2593.
[2] A. Splendiani, L. Sun, Y. Zhang, T. Li, J. Kim, C.Y. Chim, F. Wang, Emerging photoluminescence in monolayer MoS_2, Nano Lett. 10 (4) (2010) 1271–1275.
[3] G.L. Frey, R. Tenne, M.J. Matthews, M.S. Dresselhaus, G. Dresselhaus, Optical properties of MS_2 (M=Mo, W) inorganic fullerene-like and nanotube material optical absorption and resonance Raman measurements, J. Mater. Res. 13 (1998) 2412–2417.
[4] C. Ballif, M. Regula, P.E. Schmid, M. Remškar, R. Sanjinés, F. Lévy, Preparation and characterization of highly oriented, photoconducting WS_2 thin films, Appl. Phys. A-Mater. 62 (1996) 543.
[5] K.F. Mak, C. Lee, J. Hone, J. Shan, T.F. Heinz, Atomically thin MoS_2: a new direct-gap semiconductor, Phys. Rev. Lett. 105 (2010) 136805.
[6] G. Eda, H. Yamaguchi, D. Voiry, T. Fujita, M. Chen, M. Chhowalla, Single-layer MoS_2 transistors, Nano Lett. 11 (2011) 5111.
[7] G. Eda, S.A. Maier, Two-dimensional crystals: managing light for optoelectronics, ACS Nano 7 (2013) 5660–5665.
[8] D. Xiao, G.B. Liu, W.X. Feng, X.D. Xu, W. Yao, Coupled spin and valley physics in monolayers of MoS_2 and other group-VI dichalcogenides, Phys. Rev. Lett. 108 (2012) 196802.
[9] I. Song, C. Park, H.C. Choi, Synthesis and properties of molybdenum disulphide: from bulk to atomic layers, RSC Adv. 5 (2015) 7495–7514.
[10] N. Wang, F. Wei, Y. Qi, H. Li, X. Lu, G. Zhao, Q. Xu, Synthesis of strongly fluorescent molybdenum disulfide nanosheets for cell-targeted labelling, ACS Appl. Mater. Interfaces 6 (22) (2014) 19888–19894.
[11] H.-Y. Liu, Z.-B. Feng, J. Wang, J.-Y. Diao, D.-S. Su, Synthesis of hollow carbon nanostructures using a ZnO template method, New Carbon Mater. 31 (1) (2016) 87–91.
[12] U. Ozgur, Y.I. Alivov, C. Liu, A. Teke, M.A. Reshchikov, S. Doğanc, V. Avrutin, S.-J. Cho, H. Morkoc, A comprehensive review of ZnO materials and devices, J. Appl. Phys. 98 (2005) 041301.
[13] Safa Kasap, Peter Capper (Eds.), Handbook of Electronic and Photonic materials, Springer US, 2007. 2 (Chapter 16).
[14] Y. Ding, X.D. Wang, Z.L. Wang, Phase controlled synthesis of ZnS nanobelts: zinc blende vs wurtzite, Chem. Phys. Lett. 398 (2004) 32–36.
[15] J. Li, D. Zhao, X. Meng, Z. Zhang, J. Zhang, D. Shen, Y. Lu, X. Fan, Enhanced ultraviolet emission from ZnS-coated ZnO nanowires fabricated by self-assembling method, J. Phys. Chem. B 110 (2006) 14685–14687.
[16] S.K. Panda, A. Dev, S. Chaudhuri, Fabrication and luminescent properties of c-Axis oriented ZnO-ZnS core-shell and ZnS nanorod arrays by sulfidation of aligned ZnO nanorod arrays, J. Phys. Chem. C 111 (2007) 5039–5043.
[17] Y.-J. Yuan, F. Wang, B. Hu, H.-W. Lu, Z.-T. Yu, Z.-G. Zou, Significant enhancement in photocatalytic hydrogen evolution from water by MoS_2 nanosheet-coated ZnO heterostructure photocatalyst, Dalton Trans. 44 (2015) 10997–11003.
[18] Y.-H. Tan, K. Yu, J.-Z. Li, H. Fu, Z.-Q. Zhu, MoS_2@ZnO nano-heterojunctions with enhanced photocatalysis and field emission properties, J. Appl. Phys. 116 (2014) 064305.
[19] Y. Liu, S. Xie, H. Li, X. Wang, A highly efficient sunlight driven ZnO nanosheet photocatalyst: synergetic effect of P-doping and MoS_2 atomic layer loading, ChemCatChem 6 (2014) 2522–2526.
[20] K. Zhang, Y. Zhang, T. Zhang, W. Dong, T. Wei, Y. Sun, X. Chen, G. Shen, N. Dai, Vertically coupling ZnO nanorods on MoS_2 monolayers with enhanced Raman and photoluminescence emission, Nano Res. 8 (3) (2015) 743–750.
[21] X.W. Lou, H.C. Zeng, Hydrothermal synthesis of r-MoO_3 nanorods via acidification of ammonium heptamolybdate tetrahydrate, Chem. Mater. 14 (2002) 4781–4789.
[22] L. Zhang, C. Liu, A.B. Wong, J. Resasco, P. Yang, MoS2-wrapped silicon nanowires for photoelectrochemical water reduction, Nano Res. 8 (2015) 281–287.
[23] M. Klinger, A. Jäger, Crystallographic tool box (CrysTBox): automated tools for transmission electron microscopists and crystallographers, J. Appl. Crystallogr. 48 (2015) 2012–2018.
[24] D. Jiang, L. Cao, W. Liu, G. Su, H. Qu, Y. Sun, B. Dong, Synthesis and luminescence properties of Core/Shell ZnS: mn/zno nanoparticles, Nanoscale Res. Lett. 4 (2009) 78–83.
[25] R. Francis, L. Deepak, A. Mayoral, A.J. Steveson, S. Mejia-Rosales, D.A. Blomd, M. Jose-Yacaman, Insights into the capping and structure of MoS_2 nanotubes as revealed by aberration-corrected STEM R, Nanoscale 2 (2010) 2286–2293.
[26] J. Purans, A. Kuzmin, P. Parent, C. Laffon, X-ray absorbtion study of the electronic structure of tungsten and molybdenum oxides on the O K-edge, Electrochim. Acta 46 (2001) 1973–1976.
[27] B. Polyakov, A. Kuzmin, K. Smits, J. Zideluns, E. Butanovs, J. Butikova, S. Vlassov, S. Piskunov, Yuri F. Zhukovskiiy, Unexpected epitaxial growth of Few WS_2 layers on {1-100} facets of ZnO nanowires, J. Phys. Chem. C 120 (2016) 21451–21459.
[28] Y.-H. Lee, X.-Q. Zhang, W. Zhang, M.-T. Chang, C.-T. Lin, K.-D. Chang, Y.-C. Yu, J.T.-W. Wang, C.-S. Chang, L.-J. Li, T.-W. Lin, Synthesis of large-area MoS_2 atomic layers with chemical vapor deposition, Adv. Mater. 24 (2012) 2320–2325.
[29] A.L. Elias, N. Perea-Lopez, A. Castro-Beltran, A. Berkdemir, S. Feng, M. Terrones, Controlled synthesis and transfer of large-area WS_2 sheets: from single layer to few layers, ACS Nano 7 (6) (2013) 5235–5242.
[30] P. Tonndorf, R. Schmidt, P. Bottger, X. Zhang, Photoluminescence emission and Raman response of monolayer MoS_2, $MoSe_2$ and WSe_2, Opt. Express 21 (4) (2013) 4908–4916.
[31] J.H. Parker, D.W. Feldman, M. Ashkin, Raman scattering by silicon and germanium, Phys. Rev. 155 (1967) 712–714.
[32] K.A. Alim, V.A. Fonoberov, M. Shamsa, A.A. Balandina, Micro-Raman investigation of optical phonons in ZnO nanocrystals, J. Appl. Phys. 97 (2005) 124313.
[33] Y.C. Cheng, C.Q. Jin, F. Gao, X.L. Wu, W. Zhong, S.H. Li, P.K. Chu, Raman scattering study of zinc blende and wurtzite ZnS, J. Appl. Phys. 106 (2009) 123505.

Paper V

THE JOURNAL OF PHYSICAL CHEMISTRY C

Article

pubs.acs.org/JPCC

Unexpected Epitaxial Growth of a Few WS_2 Layers on {1$\bar{1}$00} Facets of ZnO Nanowires

Boris Polyakov,*[,†] Alexei Kuzmin,*[,†] Krisjanis Smits,[†] Janis Zideluns,[†] Edgars Butanovs,[†] Jelena Butikova,[†] Sergei Vlassov,[‡] Sergei Piskunov,[†] and Yuri F. Zhukovskii[†]

[†]Institute of Solid State Physics, University of Latvia, Kengaraga Street 8, LV-1063 Riga, Latvia

[‡]Institute of Physics, University of Tartu, Ravila 14c, 50412 Tartu, Estonia

Supporting Information

ABSTRACT: Core−shell nanowires are an interesting and perspective class of radially heterostructured nanomaterials where epitaxial growth of the shell can be realized even at noticeable core−shell lattice mismatch. In this study epitaxial hexagonally shaped shell consisting of WS_2 nanolayers was grown on {1$\bar{1}$00} facets of prismatic wurtzite-structured [0001]-oriented ZnO nanowires for the first time. A synthesis was performed by annealing in a sulfur atmosphere of ZnO/WO_3 core−shell structures, produced by reactive dc magnetron sputtering of an amorphous a-WO_3 layer on top of ZnO nanowire array. The morphology and phase composition of synthesized ZnO/WS_2 core−shell nanowires were confirmed by scanning and transmission electron microscopy (SEM and TEM), micro-Raman, and photoluminescence spectroscopy. Epitaxial growth of WS_2(0001) layer(s) on {1$\bar{1}$00} facets of ZnO nanowire is unexpected due to incompatibility of their symmetry and structure parameters. To relax the interfacial incoherence, we propose a model of ZnO/WS_2 interface containing WS_2 bridging groups inside and use first-principles simulations to support its feasibility.

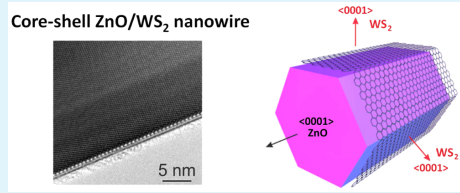

1. INTRODUCTION

Core−shell and multishell nanowires (NWs) are modern types of axially and radially heterostructured nanomaterials intensively explored during the last decades.[1−3] The core−shell approach has several important advantages as compared to conventional two-dimensional (2D) material production technologies: it allows one, for example, to combine materials with lattice mismatch and even to initiate epitaxial growth of shell material on the core template.[1,3,4] As a result, it is possible to significantly improve electrical, mechanical, and optical properties of NWs by proper combination of core and shell materials.[2,5,6] It is worth to mention heterojunction NWs, where p−n junction between core and shell materials turns a core−shell NW into a functional device like a photodetector, LED, nanolaser, etc.[1,2,4,7−9] Therefore, the engineering of core−shell heterostructures opens a new route for creation of novel nanomaterials with advanced properties.

Zinc oxide (ZnO) is among the most thoroughly explored NW materials due to simplicity of its synthesis and a number of beneficial properties.[10] Bulk ZnO is known to be a direct band gap (3.3−3.4 eV) n-type semiconductor.[11] It can be relatively easily grown in a form of NWs[12,13] also at atmospheric pressure.[14] ZnO is known to be a piezoelectric and piezoresistive material; moreover, a piezoelectric nanogenerator prototype, based on zinc oxide NW arrays, was demonstrated several years ago.[15] ZnO NWs are also frequently used as a template for nanomaterials synthesis.[10] Various ZnO/MeS core−shell heterostructures (Me = Pb, Cd, and Zn) were reported to be used for photovoltaic devices,[16] solar cells,[17] water splitting for hydrogen production,[18,19] high-temperature sensors,[19] and photodetectors.[20,21]

Layered transition metal dichalcogenides such as WS_2 and MoS_2 have attracted recently increasing attention.[22] WS_2 can be produced as thin films, 2D crystals, and nanotubes as well as a component of heterostructures.[23−28] WS_2 is an n-type semiconductor having an indirect band gap $\Delta\varepsilon_{ig}$ = 1.3−1.4 eV,[29−31] a direct optical band gap $\Delta\varepsilon_{dg}$ = 1.7−1.9 eV, and strong optical absorption (a = 5 × 10^4 cm^{-1} at 2 eV). Engineering of WS_2 band gap is possible by controlling its thickness from bulk to single layer.[32]

WS_2 is an extremely chemically inert (up to 1000 °C) and nontoxic substance[33] that makes it useful for biomedical applications.[34] It is widely used as a lubricant additive[35] and is studied for applications in lithium-ion batteries[36] and field-effect transistors.[37] Moreover, it can be utilized for solar cells or water splitting due to a good correspondence of its band gap to the solar spectrum.[33,38,39] Enhanced efficiency of H_2O splitting for hydrogen production by WS_2 was recently demonstrated for heterostructures.[38,40,41] Tahir et al. produced hierarchical WS_2−ZnO nanocomposites for electronic and photonic applications.[40] Seo et al. synthesized WO_3−WS_2 heterostructures by

Received: June 17, 2016
Revised: August 11, 2016
Published: August 26, 2016

DOI: 10.1021/acs.jpcc.6b06139
J. Phys. Chem. C 2016, 120, 21451−21459

partial sulfurization of WO_3 NWs for hydrogen electrocatalysis.[41]

Finally, the use of 2D ZnO−WS_2 heterostructures in significantly enhanced ultraviolet (UV) photodetectors was demonstrated recently in ref 42. The heterostructure was produced using a chemical vapor deposition grown monolayer WS_2 stacked onto the surface of ZnO 100 nm thin film deposited by magnetron sputtering on glass substrate.[42] In this case, the electron−hole pairs are photogenerated in ZnO nanothin film, whereas monolayer WS_2 functions as a charge transport layer.[42]

In this study, we report for the first time on the epitaxial growth of WS_2 nanolayers on ZnO nanowires. Direct epitaxial growth of WS_2(0001) on the $\{1\bar{1}00\}$ facet of ZnO nanowire is unexpected due to incompatibility of their symmetry and structure parameters. To relax the interfacial incoherence we propose a bridge-based model of ZnO/WS_2 interface and use first-principles simulations to estimate its feasibility.

2. METHODS AND MATERIALS

2.1. Synthesis of ZnO/WS_2 Core−Shell Nanowires. ZnO/WS_2 core−shell NWs were produced in three steps: (1) ZnO NWs growth on a SiO_2/Si(100) wafer; (2) amorphous a-WO_3 layer deposition onto ZnO NWs; (3) ZnO/WO_3 NWs annealing in sulfur atmosphere.

ZnO NWs were grown by a vapor transport method [also known as atmospheric pressure chemical vapor deposition (APCVD) method] using Au nanoparticles (BBI international, water suspension, 60 nm in diameter) as catalyst via VLS (vapor−liquid−solid growth mechanism).[16] NWs were synthesized on thermally oxidized silicon substrates [SiO_2/Si(100) wafer, Semiconductor Wafer, Inc.] by heating a 1:4 mixture of ZnO and graphite powder to 800−900 °C in an open-end quartz tube for 0.5 h. After synthesis samples were studied by scanning electron microscopy (SEM) to confirm successful growth of ZnO NWs.

Next, ZnO NW samples were coated by a layer of amorphous a-WO_3, having a 100 nm thickness on a flat substrate, using reactive dc magnetron sputtering of metallic tungsten target in mixed Ar/O_2 atmosphere. The thickness of the a-WO_3 layer on the surface of ZnO/WO_3 NW array on a SiO_2/Si(100) substrate was found to be 10−50 nm as estimated by SEM and transmission electron microscopy (TEM) (see Figure S1 in Supporting Information).

Finally, ZnO/a-WO_3 NW samples were annealed in a quartz tube in a sulfur atmosphere during 0.5 h at 800 °C to convert amorphous tungsten trioxide into tungsten sulfide, followed by heating for 0.5 h in inert atmosphere to sublimate some remaining amount of WO_3. It is important to note that the growth of the WS_2 sublayer takes place at the interface between ZnO core and WO_3 shell.

2.2. Morphological Characterization. The morphology of ZnO/WS_2 core−shell NWs was characterized by a high-resolution SEM focussed ion beam (FIB) electron microscope (Lyra, Tescan). The inner structure of core−shell NWs was revealed using a TEM (Tecnai GF20, FEI) operated at the accelerating voltage of 180 kV.

2.3. Photoluminescence and Micro-Raman Measurements. The photoluminescence (PL) measurements were performed at 9 and 300 K using the fourth harmonic (266 nm, or 4.66 eV) of a Nd:YAG laser FQSS266 (CryLas GmbH) as an excitation source. The photoluminescence spectra were recorded using the Andor Shamrock B-303i spectrograph equipped with a CCD camera (Andor DU-401A-BV).

Micro-Raman and PL spectromicroscopy measurements were performed using a confocal microscope with spectrometer Nanofinder-S (SOLAR TII).[43] A diode-pumped solid-state (DPSS) Nd:YAG laser [λ = 532 nm, max continuous wave (cw) power P_{ex} = 150 mW] was used as the excitation source. A Peltier-cooled back-thinned CCD camera (ProScan HS-101H) was used for detection of Raman and PL spectra. The Hamamatsu R928 photomultiplier tube was employed in confocal-spectral imaging experiments. All measurements were performed in backscattering geometry at room temperature (20 °C) through a Nikon CF Plan Apo 100× (NA = 0.95) optical objective.

3. THEORETICAL SECTION

3.1. Motivation of 2D Simulations on ZnO/WS_2 Core−Shell Nanowires. Regular hexagonal prismatic shape of wurtzite-structured NWs, e.g., ZnO NWs synthesized in our experiment,[44] can be formed if the NW axes are oriented along [0001] crystallographic directions being hollow-centered. Otherwise their symmetry is reduced while stability is lowered.[45] (The symmetry of hexagonally structured [0001]-oriented ZnO NWs can be described by $P6_3mc$ rod group.) Stability of these NWs can be achieved while they are terminated by lateral facets possessing the smallest surface energy among any wurtzite faces. This requirement is fulfilled for the family of six identical $(1\bar{1}00)$, $(\bar{1}100)$, $(10\bar{1}0)$, $(\bar{1}010)$, $(01\bar{1}0)$, and $(0\bar{1}10)$ ZnO facets (Figure 1).[46] Alternative $\{11\bar{2}0\}$ faceting of [0001]-oriented ZnO NW is energetically less favorable.

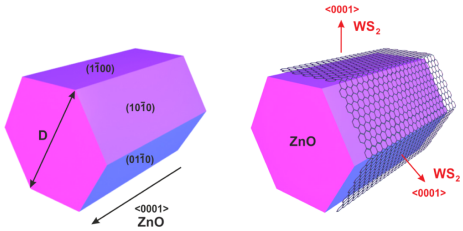

Figure 1. Axonometric view of ZnO [0001]-oriented nanowire and its lateral facets (left panel), as well as ZnO/WS_2 core−shell nanowire (right panel).

Large enough diameters (>50 nm) of ZnO NWs synthesized using the CVD method allowed us to assume that the key role in epitaxial WS_2 layer adhesion to nanowire is played by a family of $\{1\bar{1}00\}$ plane facets but not by tiny areas around ZnO nanowire ribs. This is why the 2D ZnO$(1\bar{1}00)$/WS_2 interface was initially selected for comparison with the experimental data for ZnO/WS_2 core−shell NWs. Note that core−shell NWs per se cannot be simulated when using the first-principle theory due to a complexity of their morphology and low symmetry. Therefore, we considered a slab model.

A 20-layer ZnO$(1\bar{1}00)$ slab model was chosen for simulations of zinc oxide substrate (thickness of which corresponds to [0001]-oriented NW possessing diameter of 3.5 nm) and its coverage by WS_2 nanolayers from both sides. Atomistic models used for simulation of hydrogen molecule

DOI: 10.1021/acs.jpcc.6b06139
J. Phys. Chem. C 2016, 120, 21451−21459

reactivity toward ZnO($1\bar{1}00$) substrate have been constructed by us recently.[47]

To simulate 2D ZnO/WS_2 core−shell interface, we have established qualitative compatibility between the structures of adsorbent and adsorbate when comparing their bulk morphologies (Figure 2 and Table 1). Note that unit cell of

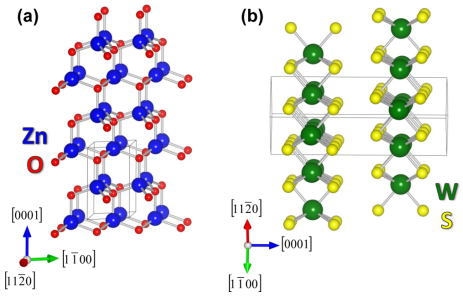

Figure 2. Structural parameters of ZnO (a) and WS_2 (b) lattices (small red, medium yellow, medium blue, and large green balls correspond to O, S, Zn, and W atoms, respectively). Light four-faceted prisms correspond to unit cells of ZnO (a) and WS_2 (b) crystals, respectively.

Table 1. Comparison of Lattice Parameters and Band Gaps for Bulk WS_2 and ZnO[a]

	WS_2		ZnO	
	exptl	theory	exptl	theory
a_0 (Å)	3.15	3.13	3.25	3.26
c_0 (Å)	12.32	12.31	5.21	5.21
$\Delta\varepsilon_{gap}$ (eV)	1.3−1.4	2.51	3.3−3.4	3.52

[a]Experimental values are taken from refs 29−31 and 48 for WS_2 and from refs 11, 49, and 50. for ZnO, respectively.

tungsten disulfide contains fragments of two inversely oriented WS_2 layers (Figure 2b). Both structures are described by hexagonal space symmetry groups $P6_3mc$ (Figure 2a) and $P6_3/mmc$ (Figure 2b), respectively.

Comparison between the structural parameters of a_0, and c_0 for ZnO and WS_2 bulk (Figure 2 and Table 1) obtained in calculations and measured experimentally shows their close proximity. This fact enhances the possibility to form a quasi-coherent interface since each $c_0^{WS_2} > 2c_0^{ZnO}$ (resulting in slight bend of WS_2 unit cell contacting to ZnO unit cell), while $a_0^{ZnO} \approx a_0^{WS_2}$. We have considered both n- and p-type terminations of ZnO($1\bar{1}00$) slab (Figures S2 and S3 and Table S1 in Supporting Information) although morphology of the former corresponds to a more smooth NW facet observed experimentally.[44] According to conditions of ZnO synthesis described before, we have also constructed slab model of n-type S-doped ZnO($1\bar{1}00$) substrate where all outer O atoms are substituted by S atoms (Figure S4 and Table S1 in Supporting Information). Other details of models used for ZnO/WS_2 interface are given below and in Supporting Information.

3.2. Computational Details. In this study, relaxed 3D models of ZnO and WS_2 lattices (Figure 2) as well as ZnO($1\bar{1}00$)/WS_2 2D interfaces were calculated using the periodic hybrid density functional theory (DFT)/Hartree−Fock (HF) LCAO method. The method utilizes localized Gaussian-type functions (GTFs) in the form of basis set (BS) centered on atomic nuclei for expansion of crystalline orbitals as linear combinations of atomic orbitals, implemented in CRYSTAL14 computer code[51] using the hybrid exchange-correlation functional PBE0.[52,53] For oxygen atoms we used the all-valence BSs of atomic GTFs (constructed using pure s- and hybrid sp-AOs) in the form of 8*s*-411*sp*, while for zinc atoms we used the all-valence BS in the form 8*s*-64111*sp*-41*d* as suggested previously.[54] BS for sulfur atoms was adopted in the form of ECP-1111*s*-1111*p*-11*d*,[55] while for tungsten atoms the ECP-11*sp*-31*d*[56] BS was used, where ECP is the effective core pseudopotentials employed for acceleration of calculations.

To provide a balanced summation in both direct and reciprocal lattices, the reciprocal space integration was performed by sampling the NW Brillouin zone (BZ) with the 12 × 12 × 1 Monkhorst−Pack mesh[57] that gives in total 16 *k*-points evenly distributed at the BZ. Calculations are considered as converged only when the total energy differs by less than 10^{-10} au in two successive cycles of the self-consistent field (SCF) procedure. All the calculations were performed with the total geometry optimization keeping initial symmetry fixed. The optimized geometries of both species were found in a qualitative agreement with those experimentally observed (Table 1). Analogous correlation was observed for electronic properties: the band gap value calculated for bulk ZnO was estimated to be overestimated 3.52 eV versus 3.3−3.4 eV in the experiment,[11,49,50] while for bulk WS_2 the band gap value was found to be 2.31 eV versus 1.3−1.4 eV in the experiment.[29−31] The difference between calculated and experimental values of the band gap for WS_2 is attributed to the incompleteness of the basis set for tungsten used in our hybrid LCAO calculations of its disulfide.

4. RESULTS AND DISCUSSION

4.1. Experimental Data. TEM images of ZnO/WS_2 core−shell NWs are shown in Figure 3. A gold nanoparticle, located at the end of ZnO NW (Figure 3a), is typical for the most of NWs due to gold-catalyzed VLS growth mechanism. A few layers of WS_2 grown at the ZnO NW surface are well visible as parallel black lines. Their thickness varies in the range of 1−5 monolayers (each of them contains three S−W−S atomic planes). Measured interlayer distance is about 6.0−6.7 Å, which is close to the 6.2−6.4 Å interlayer distance in WS_2 nanostructures.[41,58] It also corresponds to the interlayer distance in WS_2 bulk along the [0001] axis (Figure 2b and Table 1). At high magnification the single-crystalline structure of ZnO NWs is well visible (Figure 3b−d). Measured interplanar distance in core ZnO NWs is equal to 2.8 Å that corresponds to the interval between ($1\bar{1}00$) planes of hexagonal ZnO wurtzite.[59] Selected area electron diffraction (SAED) pattern of ZnO/WS_2 NW is shown in the inset in Figure 3c: its analysis by CrysTBox software[60] gives an evidence of the epitaxial growth WS_2 on top of ZnO core (see Figure S5 in Supporting Information). No other phases (as, for example, ZnS) are observed.

Raman spectroscopy was used to support the formation of WS_2 layers on ZnO NWs. Raman spectra of thin WS_2 nanoplates and ZnO/WS_2 individual NWs, recorded at room temperature, are shown in Figure 4, parts a and b. The Raman spectra of bulk WS_2 and their thickness dependence were interpreted in earlier works.[61−64] Two strongest optical phonon modes[26,65,66] $E^1_{2g}(\Gamma)$ and $A_{1g}(\Gamma)$ were, respectively, detected at

DOI: 10.1021/acs.jpcc.6b06139
J. Phys. Chem. C 2016, 120, 21451−21459

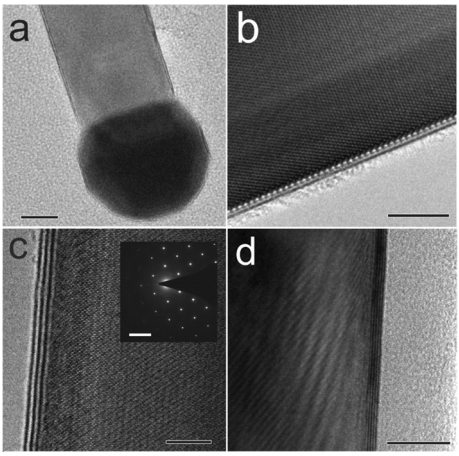

Figure 3. TEM images of ZnO/WS_2 core−shell nanowires at small (a) and high magnifications (b−d). The gold nanoparticle at the end of the nanowire is well visible in panel a. Layers of WS_2 are visible as black lines at the ZnO NW surface. The inset in panel c shows the SAED pattern. Scale bars are 20 nm in panel a, 5 nm in panels b−d, and 5 nm^{-1} in panel c, inset.

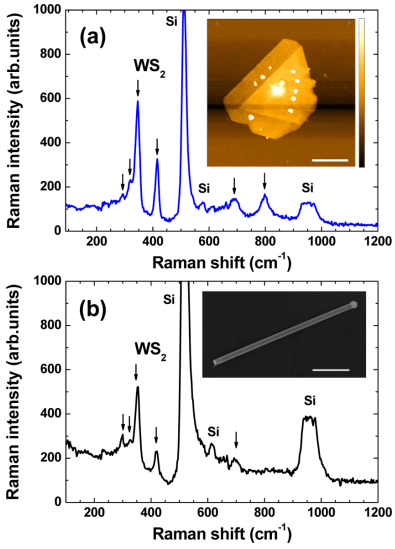

Figure 4. (a) Micro-Raman spectrum of WS_2 nanoplate on silicon substrate. Atomic force microscopy (AFM) image of WS_2 nanoplate is shown in the inset (scale bar is 1 μm, and color bar is 52 nm). (b) Micro-Raman spectrum of single ZnO/WS_2 NW on silicon substrate. SEM image of the NW is shown in the inset (scale bar is 500 nm). Raman bands of WS_2 phase are indicated by arrows in both images.

347 and 416 cm^{-1} in WS_2 nanoplates on silicon wafer and at 354 and 419 cm^{-1} in ZnO/WS_2 core−shell NW. These values are close to those of bulk WS_2 (355.5 and 420.5 cm^{-1}, respectively).[26] Several weak Raman bands of WS_2 phase were also observed and are indicated by arrows in Figure 4.[26,65,66] The large peak at 521 cm^{-1} and its satellite at 959 cm^{-1} are the first and second orders of optical mode at k = 0 of the underlying silicon substrate.[67]

Photoluminescence (PL) spectra of pure WS_2, ZnO, and ZnO/WS_2 NW samples measured at room temperature are shown in Figure 5. WS_2 is expected to transfer from an indirect

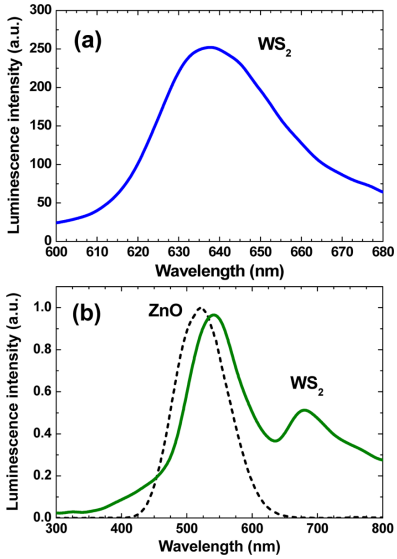

Figure 5. Room-temperature photoluminescence spectra of (a) WS_2 islands on a SiO_2/Si(100) wafer and (b) intact ZnO NWs (dashed curve) and ZnO/WS_2 core−shell NWs (solid curve).

band gap semiconductor in a multilayer form to a direct band gap semiconductor in a few-layer form (ref 26). The broad PL band at 640 nm (Figure 5a) recorded from WS_2 plates by confocal optical microscope corresponds to direct optical band gap of 1.9 eV.[26,68] The PL spectrum of intact ZnO NWs is shown in Figure 5b and has a defect-related band at ∼520 nm.[11] The PL spectrum of the ZnO/WS_2 NW array is more complicated and contains emission bands due to ZnO and WS_2 phases (Figure 5b). The emission band at ∼540 nm can be attributed to a ZnO core, while PL emission at 680 nm is associated with the WS_2 shell. It is important to note that the ZnO-related band is shifted to longer wavelength compared to intact ZnO NWs. The origin of such shift can be due to electron density redistribution, influence of additional defects, or a formation of ZnS submonolayer. Red shift of the WS_2-related PL may be caused by influence of the underlying ZnO substrate.[68]

4.2. Atomistic Prototypes of ZnO/WS_2 Interface to Model Core−Shell Nanowire. As mentioned in previous section, the interlayer distance in external nanolayers attributed

DOI: 10.1021/acs.jpcc.6b06139
J. Phys. Chem. C 2016, 120, 21451−21459

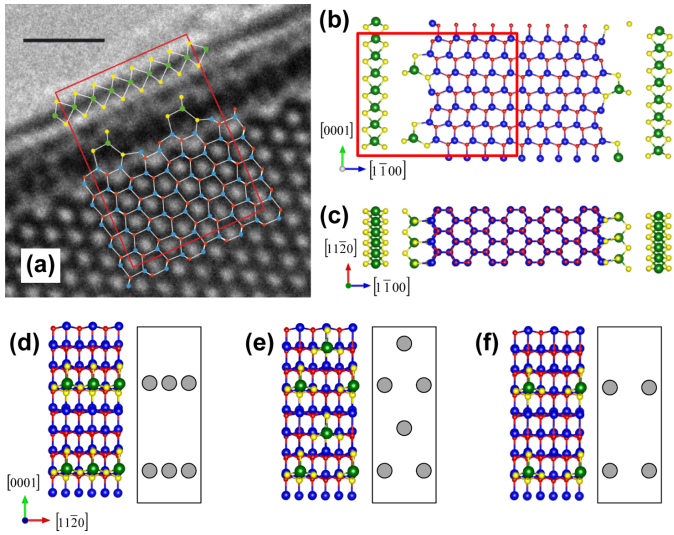

Figure 6. (a) Imposition of optimized atomistic model of ZnO(1$\bar{1}$00)/striped 0.5 ML WS_2(1$\bar{1}$00)/WS_2(0001) interface on top of the TEM image of ZnO/WS_2 core−shell NW (scale bar is 1 nm) and sections of the same interface across (b) (11$\bar{2}$0) and (c) (0001) planes. Three different atomistic models and pictograms of the WS_2 bridging groups atop of the ZnO(1$\bar{1}$00) surface: (d) striped 0.5 ML, (e) net 0.5 ML, and (f) net 0.25 ML. Gray circles show schematic views of the positions for the WS_2 bridging groups. Atom size and color are the same as in Figure 2. The indexing of axes corresponds to ZnO NW.

to the WS_2(0001) shell structure is about 6.0−6.7 Å (Figures 3, parts c and d, and 7a−c) which is qualitatively close to the interlayer distances of 6.2−6.4 Å in 2D WS_2 nanostructures (Figure 2b).[41,58] According to TEM observations, the outer WS_2 nanolayers are found to be [0001]-oriented. On the other hand, since ZnO(1$\bar{1}$00) slab and WS_2(0001) nanolayer are not spatially and symmetrically compatible (Figure 6a−c), we can insert between them additional 0.5WS_2 striped (Figure 6d), 0.5WS_2 net (Figure 6e), or 0.25WS_2 net (Figure 6f) (1$\bar{1}$00)-submonolayer, which provides structural relaxation in the two pairs of interfaces, S-doped ZnO(1$\bar{1}$00)/*s*WS_2(1$\bar{1}$00) (Figure 6 and Figures S6−S8 in Supporting Information) and *s*WS_2(1$\bar{1}$00)/WS_2(0001) (Figure 7), which are considered separately. Here *s* denotes the type of inserted submonolayer. This allowed us to preserve periodicity along the ZnO substrate during the structural relaxation of initial geometry. In principle, the intermediate *s*WS_2(1$\bar{1}$00) layer may have a different structure. For example, three possible arrangements of WS_2 groups are shown in Figure 6d−f: these bridging WS_2 groups can form infinite stripes as in Figure 6d, each second WS_2 group in the stripe can be absent as in Figure 6f, which corresponds to regular (net) 0.25 ML, or displaced along the NW direction as in Figure 6e describing regular (net) 0.5 ML. Configurations of WS_2(1$\bar{1}$00) submonolayers denoted in Figure 6d−f as adsorbate on ZnO substrate were also recalculated on WS_2(0001) monolayer as shown in Figure 7a−c. The last two models are likely more favorable for a compensation of structural relaxation in the interface, whereas the model shown in Figure 6d remains strained enough along the [1$\bar{1}$00]-oriented WS_2 stripes (Table 2).

Detailed description of n-type S-doped ZnO(1$\bar{1}$00)/*s*WS_2(1$\bar{1}$00) interfaces is given in the next section (Table 2) and in Supporting Information (Figures S6−S8). For comparison, overstrained ZnO(1$\bar{1}$00)/WS_2(1$\bar{1}$00) interfaces, both n- and p-types, are considered in Supporting Information (Figures S9 and S10).

Configurations of *s*WS_2(1$\bar{1}$00) submonolayers denoted in Figure 6d−f as adsorbate on ZnO substrate have been also recalculated upon WS_2(0001) monolayer as shown in Figure 7a−c. The former can be considered as models of a pad between WS_2(0001) layer and ZnO(1$\bar{1}$00) core nanowire, which are not spatially and symmetrically compatible. The *x*,*y* coordinates of W atoms in submonolayers have been frozen when optimizing *s*WS_2(1$\bar{1}$00)/WS_2(0001) interfaces.

4.3. Results of First-Principles Simulations. To estimate the interfacial binding energy for 0.25−1 ML WS_2 adsorbate on pure and S-doped ZnO(1$\bar{1}$00) substrates (see Figures S6−S10, Table 2 and Tables S1 and S2) we have applied the following expression

$$E_{\text{bind}} = 0.5[E_{\text{ZnO/2WS}_2} - (2E_{\text{WS}_2} + E_{\text{ZnO}})] \quad (1)$$

where $E_{\text{ZnO/2WS}_2}$, E_{WS_2}, and E_{ZnO} are the calculated total energies (per unit cell) of the optimized structures for pure or S-doped ZnO slab covered from both sides by WS_2 nanolayers as well as WS_2 nanolayer and pure or S-doped ZnO slab, respectively.

Binding energies per supercell in *s*WS_2(1$\bar{1}$00)/WS_2(0001) interfaces (Figure 7 and Table 3) are estimated according to

$$E_{\text{bind}} = E_{s\text{WS}_2(1\bar{1}00)/\text{WS}_2(0001)} - (E_{s\text{WS}_2(1\bar{1}00)} + E_{\text{WS}_2(0001)}) \quad (2)$$

DOI: 10.1021/acs.jpcc.6b06139
J. Phys. Chem. C 2016, 120, 21451−21459

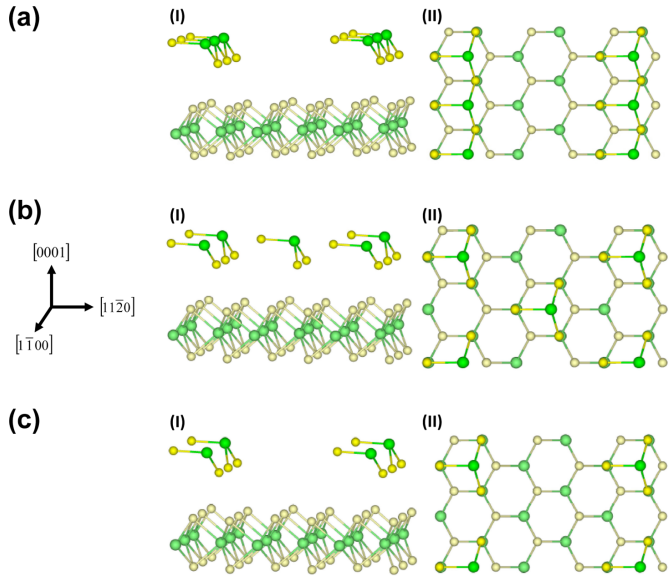

Figure 7. Three different arrangements of the sWS$_2$(1$\bar{1}$00) submonolayer atop WS$_2$(0001) layer: (a) striped s = 0.5 ML, (b) net s = 0.5 ML, and (c) net s = 0.25 ML. They correspond to the images of the same submonolayers atop ZnO(1$\bar{1}$00) substrate in Figure 6d–f. Aside (I) and atop (II) views of 3 × 3 supercells for the sWS$_2$(1$\bar{1}$00)/WS$_2$(0001) interface correspond to n-type morphology of the sWS$_2$/ZnO interface (Figures S6 and S7). Bright green and bright yellow balls correspond to W and S atoms of the (1$\bar{1}$00) submonolayer, while light green and light yellow balls correspond to tungsten and sulfur atoms of the (0001) monolayer.

Table 2. Energy and Geometry Parameters of Optimized ZnO(1$\bar{1}$00)/sWS$_2$ Interface Models (Figures S6–S8)[a]

		interlayer distances in substrate (Å)			
models of interface	E_{bind} (eV)	$h_{interlayer(outer)}$	$h_{interlayer(internal)}$	interfacial distance (Å)	band gap $\Delta\varepsilon_g$ (eV)
striped 0.5 ML	1.59	2.81	2.81	2.16	[b]
net 0.5 ML	2.21	2.78	2.79	2.15	1.16
net 0.25 ML	2.42	2.73	2.81	2.08	1.61

[a]The total and partial densities of electronic states are shown in Figure S11. [b]Conducting states.

Table 3. Energy and Geometry Parameters of Optimized WS$_2$ Interface Models WS$_2$(0001)/WS$_2$(0001) (Figure 2b) and sWS$_2$(1$\bar{1}$00)/WS$_2$(0001)[a]

		interlayer distances in WS$_2$ (Å)			
models of interface	E_{bind} (eV)	$h_{W-S\ external}$	$h_{W-S\ internal}$	interfacial distance (Å)	band gap $\Delta\varepsilon_g$ (eV)
WS$_2$(0001)/WS$_2$(0001)	0.04	1.56	3.11	6.15	2.70
striped 0.5WS$_2$(1$\bar{1}$00)/WS$_2$(0001)	0.08	1.54	3.09	5.95	1.61
net 0.5WS$_2$(1$\bar{1}$00)/WS$_2$(0001)	0.41	1.47	3.09	5.91	2.47
net 0.25WS$_2$(1$\bar{1}$00)/WS$_2$(0001)	0.58	1.44	3.10	5.82	2.51

[a]The total and partial densities of electronic states are shown in Figure S12.

where $E_{sWS_2(1\bar{1}00)/WS_2(0001)}$, $E_{sWS_2(1\bar{1}00)}$, and $E_{WS_2(0001)}$ are the calculated total energies (per unit cell) of the optimized structures of interface and both its constituents, respectively.

As compared to the initial interface configurations determined by the morphology of ZnO substrate, the optimized structures of ZnO(1$\bar{1}$00)/sWS$_2$ do not changed drastically (Tables 2 and S2), except for noticeable increase of $h_{interlayer(outer)}$ compared to the corresponding distance in the outer and internal layers of zinc oxide slabs (Table S1). On the other hand, this interlayer (1$\bar{1}$00) distance is well-correlated with the experimental value (2.8 Å) found by TEM (Figure 3).

Comparison of results obtained for three ZnO(1$\bar{1}$00)/sWS$_2$ interface configurations (Table 2 and Figures S6–S8) clearly shows lower stability of their striped configuration shown in Figure 6d as compared to both net configurations (Figure 6, parts e and f). Thus, the former is hardly to be realized. When

DOI: 10.1021/acs.jpcc.6b06139
J. Phys. Chem. C 2016, 120, 21451–21459

decreasing the concentration of WS_2 bridging groups their strain as well as interfacial distance to substrate also decrease.

Analogously with energy parameters for $ZnO(1\bar{1}00)/sWS_2$ interface configurations, the results were also obtained for $sWS_2(1\bar{1}00)/WS_2(0001)$ interfaces. Table 3 provides information on the binding energy E_{bind} between the two layers [for $WS_2(0001)/WS_2(0001)$ and three types of $sWS_2(1\bar{1}00)/WS_2(0001)$ interfaces], the band gap $\Delta\varepsilon_g$ and geometry parameters (interlayer and interfacial distances). Note that the low value of the binding energy for $WS_2(0001)/WS_2(0001)$ interface agrees well with that obtained by plane wave calculations.[69] The results reported in Table 3 indicate lower stability of the striped configuration shown in Figure 7a as compared to both net configurations (Figure 7, parts b and c). When decreasing the concentration of WS_2 bridging groups their strain as well as interfacial distance to (0001) substrate also decrease. Thus, considering models for both constituents of $ZnO(1\bar{1}00)/sWS_2(1\bar{1}00)/WS_2(0001)$ interface observed experimentally we can suppose that they are more stable and less strained for net 0.25 and 0.5 ML configurations.

5. CONCLUSIONS

An epitaxial shell consisting of a WS_2 nanolayer was grown on ZnO NW core for the first time using the specific procedure. An amorphous layer of WO_3 was deposited on ZnO NW array and converted into WS_2 in a sulfur atmosphere at 800 °C. Typical thickness of the WS_2 shell was found to be 1−5 monolayers. The formation of the WS_2 phase was confirmed by TEM studies as well as by Raman scattering and optical spectroscopy. Atomic arrangement of WS_2 layer on the $ZnO(1\bar{1}00)$ facets in different possible configurations as well as various structural and electronic properties of ZnO/WS_2 interface were clarified using large-scale first-principles calculations. We have constructed models of $ZnO(1\bar{1}00)/sWS_2(1\bar{1}00)$ interfaces, both pure and S-doped, as well as a justified model of $WS_2(0001)/sWS_2(1\bar{1}00)$ interface where $sWS_2(1\bar{1}00)$ submonolayer bridging structures serve as pads between experimentally observed $WS_2(0001)$ shell nanolayers and $ZnO(1\bar{1}00)$ substrate. Intermediate interfacial WS_2-containing and $\{1\bar{1}00\}$-oriented submonolayers are more stable when their quasimolecular groups are separated by at least next-neighboring distances which reduce essentially the strain of $WS_2(0001)$ shells. We have found qualitative agreement in estimate of interplanar interface distance when comparing experimental and theoretical results and provided an explanation for strong adhesion of WS_2 nanolayer to ZnO substrate.

■ ASSOCIATED CONTENT

Supporting Information

The Supporting Information is available free of charge on the ACS Publications website at DOI: 10.1021/acs.jpcc.6b06139.

Characterization of ZnO/WO_3 core−shell nanowires by TEM, results of selected area electron diffraction for ZnO/WS_2 core−shell nanowire, theoretical atomistic models of $ZnO(1\bar{1}00)$ substrates with various morphologies, sWS_2/S-covered $ZnO(1\bar{1}00)$ core−shell interfaces and the model of WS_2 monolayer coverage of pristine $ZnO(1\bar{1}00)$ substrate as well as the electronic density of states for $ZnO(1\bar{1}00)$ and $WS_2(0001)$ substrates and $ZnO(1\bar{1}00)/sWS_2$ or $sWS_2(1\bar{1}00)/WS_2(0001)$ interfaces (PDF)

■ AUTHOR INFORMATION

Corresponding Authors

*E-mail: boris.polyakov@cfi.lu.lv. Phone: +371-67187511. Fax: +371-67132778.

*E-mail: a.kuzmin@cfi.lu.lv. Phone: +371-67251691. Fax: +371-67132778.

Notes

The authors declare no competing financial interest.

■ ACKNOWLEDGMENTS

The present research was supported by the Latvian National Research Program IMIS2. S.P. and Y.F.Z. are grateful to the ERA.Net RUS Plus WATERSPLIT project no. 237 for the financial support. S.V. acknowledges the support of the project IUT2-25.

■ REFERENCES

(1) Li, Y.; Qian, F.; Xiang, J.; Lieber, C. M. Nanowire electronic and optoelectronic devices. *Mater. Today* **2006**, *9*, 18−27.

(2) Yan, R.; Gargas, D.; Yang, P. Nanowire photonics. *Nat. Photonics* **2009**, *3*, 569−576.

(3) Kempa, T. J.; Day, R. W.; Kim, S.-K.; Park, H.-G.; Lieber, C. M. Semiconductor nanowires: a platform for exploring limits and concepts for nano-enabled solar cells. *Energy Environ. Sci.* **2013**, *6*, 719−733.

(4) Dong, Y.; Tian, B.; Kempa, T. J.; Lieber, C. M. Coaxial group III - nitride nanowire photovoltaics. *Nano Lett.* **2009**, *9*, 2183−2187.

(5) Lauhon, L. J.; Gudiksen, M. S.; Wang, D.; Lieber, C. M. Epitaxial core-shell and core-multishell nanowire heterostructures. *Nature* **2002**, *420*, 57−61.

(6) Vlassov, S.; Polyakov, B.; Dorogin, L. M.; Vahtrus, M.; Mets, M.; Antsov, M.; Saar, R.; Romanov, A. E.; Lõhmus, A.; Lõhmus, R. Shape restoration effect in Ag-SiO_2 core-shell nanowires. *Nano Lett.* **2014**, *14*, 5201−5205.

(7) Qian, F.; Li, Y.; Gradecak, S.; Park, H.; Dong, Y.; Ding, Y.; Wang, Z. L.; Lieber, C. M. Multi-quantum-well nanowire heterostructures for wavelength-controlled lasers. *Nat. Mater.* **2008**, *7*, 701−706.

(8) Zhai, T.; Fang, X.; Liao, M.; Xu, X.; Zeng, H.; Yoshio, B.; Golberg, D. A comprehensive review of one-dimensional metal-oxide nanostructure photodetectors. *Sensors* **2009**, *9*, 6504−6529.

(9) Tian, W.; Lu, H.; Li, L. Nanoscale ultraviolet photodetectors based on onedimensional metal oxide nanostructures. *Nano Res.* **2015**, *8*, 382−405.

(10) Wang, Z. L. ZnO nanowire and nanobelt platform for nanotechnology. *Mater. Sci. Eng., R* **2009**, *64*, 33−71.

(11) Özgür, U.; Alivov, Y. I.; Liu, C.; Teke, A.; Reshchikov, M. A.; Doğan, S.; Avrutin, V.; Cho, S.-J.; Morkoç, H. A comprehensive review of ZnO materials and devices. *J. Appl. Phys.* **2005**, *98*, 041301.

(12) Lee, W.; Jeong, M.-C.; Myoung, J.-M. Catalyst-free growth of ZnO nanowires by metal-organic chemical vapour deposition (MOCVD) and thermal evaporation. *Acta Mater.* **2004**, *52*, 3949−3957.

(13) Chang, C.-W.; Wu, H.-T.; Huang, S.-H.; Chen, C.-K.; Un, I.-W.; Yen, T.-J. Single-crystalline heterostructure of ZnO nanowire arrays on large Ag microplates and its photocatalytic activity. *Acta Mater.* **2013**, *61*, 6993−6999.

(14) Huang, M. H.; Wu, Y.; Feick, H.; Tran, N.; Weber, E.; Yang, P. Catalytic growth of zinc oxide nanowires by vapor transport. *Adv. Mater.* **2001**, *13*, 113−116.

(15) Wang, Z. L.; Song, J. Piezoelectric nanogenerators based on zinc oxide nanowire arrays. *Science* **2006**, *312*, 242−246.

(16) Zhu, Y. F.; Zhou, G. H.; Ding, H. Y.; Liu, A. H.; Lin, Y. B.; Dong, Y. W. Synthesis and characterization of highly-ordered ZnO/PbS core/shell heterostructures. *Superlattices Microstruct.* **2011**, *50*, 549−556.

(17) Guerguerian, G.; Elhordoy, F.; Pereyra, C. J.; Marotti, R. E.; Martin, F.; Leinen, D.; Ramos-Barrado, J. R.; Dalchiele, E. A. ZnO

nanorod/CdS nanocrystal core/shell-type heterostructures for solar cell applications. *Nanotechnology* **2011**, *22*, 505401.
(18) Wang, X.; Liu, G.; Lu, G. Q.; Cheng, H. M. Stable photocatalytic hydrogen evolution from water over ZnO-CdS core-shell nanorods. *Int. J. Hydrogen Energy* **2010**, *35*, 8199−8205.
(19) Fang, X.; Zhai, T.; Gautam, U. K.; Li, L.; Wu, L.; Bando, Y.; Golberg, D. ZnS nanostructures: From synthesis to applications. *Prog. Mater. Sci.* **2011**, *56*, 175−287.
(20) Hu, L.; Yan, J.; Liao, M.; Xiang, H.; Gong, X.; Zhang, L.; Fang, X. An optimized ultraviolet - a light photodetector with wide-range photoresponse based on ZnS/ZnO biaxial nanobelt. *Adv. Mater.* **2012**, *24*, 2305−2309.
(21) Zhang, F.; Ding, Y.; Zhang, Y.; Zhang, X.; Wang, Z. L. Piezo-phototronic effect enhanced visible and ultraviolet photodetection using a ZnO-CdS core-shell micro/nanowire. *ACS Nano* **2012**, *6*, 9229−9236.
(22) Duan, X.; Wang, C.; Pan, A.; Yu, R.; Duan, X. Two-dimensional transition metal dichalcogenides as atomically thin semiconductors: opportunities and challenges. *Chem. Soc. Rev.* **2015**, *44*, 8859−8876.
(23) Tenne, R. Inorganic nanotubes and fullerene-like nanoparticles. *Nat. Nanotechnol.* **2006**, *1*, 103−111.
(24) Scharf, T.; Prasad, S.; Dugger, M.; Kotula, P.; Goeke, R.; Grubbs, R. Growth, structure, and tribological behavior of atomic layer-deposited tungsten disulphide solid lubricant coatings with applications to MEMS. *Acta Mater.* **2006**, *54*, 4731−4743.
(25) Morrish, R.; Haak, T.; Wolden, C. A. Low temperature synthesis of n-type WS_2 thin films via H_2S plasma sulfurization of WO_3. *Chem. Mater.* **2014**, *26*, 3986−3992.
(26) Gutierrez, H. R.; Perea-Lopez, N.; Elias, A. L.; Berkdemir, A.; Wang, B.; Lv, R.; Lopez-Urias, F.; Crespi, V. H.; Terrones, H.; Terrones, M. Extraordinary room-temperature photoluminescence in WS_2 triangular monolayers. *Nano Lett.* **2013**, *13*, 3447−3454.
(27) Gong, Y.; Lin, J.; Wang, X.; Shi, G.; Lei, S.; Lin, Z.; Zou, X.; Ye, G.; Vajtai, R.; Yakobson, B. I.; et al. Vertical and in-plane heterostructures from WS_2/MoS_2 monolayers. *Nat. Mater.* **2014**, *13*, 1135−1142.
(28) Sheng, Y.; Xu, W.; Wang, X.; He, Z.; Rong, Y.; Warner, J. H. Mixed multilayered vertical heterostructures utilizing strained monolayer WS_2. *Nanoscale* **2016**, *8*, 2639−2647.
(29) Kam, K. K.; Parkinson, B. A. Detailed photocurrent spectroscopy of the semiconducting group VIB transition metal dichalcogenides. *J. Phys. Chem.* **1982**, *86*, 463−467.
(30) Kuc, A.; Zibouche, N.; Heine, T. Influence of quantum confinement on the electronic structure of the transition metal sulfide TS_2. *Phys. Rev. B: Condens. Matter Mater. Phys.* **2011**, *83*, 245213.
(31) Braga, D.; Gutiérrez Lezama, I.; Berger, H.; Morpurgo, A. F. Quantitative determination of the band gap of WS_2 with ambipolar ionic liquid-gated transistors. *Nano Lett.* **2012**, *12*, 5218−5223.
(32) Long, H.; Tao, L.; Tang, C. Y.; Zhou, B.; Zhao, Y.; Zeng, L.; Yu, S. F.; Lau, S. P.; Chai, Y.; Tsang, Y. H. Tuning nonlinear optical absorption properties of WS_2 nanosheets. *Nanoscale* **2015**, *7*, 17771−17777.
(33) Jager-Waldau, A.; Lux-Steiner, M. C.; Bucher, E. WS_2 thin films: a new candidate for solar cells. *Preprint 23th IEEE Photovoltaic Specialist Conf.* **1993**, 1−6.
(34) Yong, Y.; Zhou, L.; Gu, Z.; Yan, L.; Tian, G.; Zheng, X.; Liu, X.; Zhang, X.; Shi, J.; Cong, W.; et al. WS_2 nanosheet as a new photosensitizer carrier for combined photodynamic and photothermal therapy of cancer cells. *Nanoscale* **2014**, *6*, 10394−10403.
(35) Ratoi, M.; Niste, V. B.; Walker, J.; Zekonyte, J. Mechanism of action of WS_2 lubricant nanoadditives in high-pressure contacts. *Tribol. Lett.* **2013**, *52*, 81−91.
(36) Rui, X.; Tan, H.; Yan, Q. Nanostructured metal sulfides for energy storage. *Nanoscale* **2014**, *6*, 9889−9924.
(37) Iqbal, M. W.; Iqbal, M. Z.; Khan, M. F.; Shehzad, M. A.; Seo, Y.; Eom, J. Deep-ultraviolet-light-driven reversible doping of WS_2 field-effect transistors. *Nanoscale* **2015**, *7*, 747−757.
(38) Yan, Y.; Xia, B.; Li, N.; Xu, Z.; Fisher, A.; Wang, X. Vertically oriented MoS_2 and WS_2 nanosheets directly grown on carbon cloth as efficient and stable -dimensional hydrogen-evolving cathodes. *J. Mater. Chem. A* **2015**, *3*, 131−135.
(39) Sang, Y.; Zhao, Z.; Zhao, M.; Hao, P.; Leng, Y.; Liu, H. From UV to near-infrared, WS_2 nanosheet: A novel photocatalyst for full solar light spectrum photodegradation. *Adv. Mater.* **2015**, *27*, 363−369.
(40) Tahir, M. N.; Yella, A.; Therese, H. A.; Mugnaioli, E.; Panthofer, M.; Khan, H. U.; Knoll, W.; Kolb, U.; Tremel, W. Synthesis of hierarchically grown ZnO@NT-WS_2 nanocomposites. *Chem. Mater.* **2009**, *21*, 5382−5387.
(41) Seo, B.; Jeong, H. Y.; Hong, S. Y.; Zak, A.; Joo, S. H. Impact of a conductive oxide core in tungsten sulfide-based nanostructures on the hydrogen evolution reaction. *Chem. Commun.* **2015**, *51*, 8334−8337.
(42) Lan, C.; Li, C.; Wang, S.; Yin, Y.; Guo, H.; Liu, N.; Liu, Y. ZnO-WS_2 heterostructures for enhanced ultra-violet photodetectors. *RSC Adv.* **2016**, *6*, 67520−67524.
(43) Kuzmin, A.; Kalendarev, R.; Kursitis, A.; Purans, J. Confocal spectromicroscopy of amorphous and nanocrystalline tungsten oxide films. *J. Non-Cryst. Solids* **2007**, *353*, 1840−1843.
(44) Polyakov, B.; Dorogin, L.; Lohmus, A.; Romanov, A.; Lohmus, R. In situ measurement of the kinetic friction of ZnO nanowires inside a scanning electron microscope. *Appl. Surf. Sci.* **2012**, *258*, 3227−3231.
(45) Evarestov, R. A. *Theoretical Modeling of Inorganic Nanostructures. Symmetry and ab-initio Calculations of Nanolayers, Nanotubes and Nanowires*; Springer-Verlag: Berlin-Heidelberg, Germany, 2015.
(46) Zhukovskii, Y. F.; Piskunov, S.; Lisovski, O.; Spohr, E.; Evarestov, R. A. Quantum chemical simulations of doped ZnO nanowires for photocatalytic hydrogen generation. *Phys. Status Solidi B* **2016**, DOI: 10.1002/pssb.201600452.
(47) Usseinov, A. B.; Kotomin, E. A.; Akilbekov, A. T.; Zhukovskii, Y. F.; Purans, J. Hydrogen induced metallization of ZnO($1\bar{1}00$) surface: Ab initio study. *Thin Solid Films* **2014**, *553*, 38−42.
(48) Schutte, W.; De Boer, J. L.; Jellinek, F. Crystal structures of tungsten disulfide and diselenide. *J. Solid State Chem.* **1987**, *70*, 207−209.
(49) Abrahams, S. C.; Bernstein, J. L. Remeasurement of the structure of hexagonal ZnO. *Acta Crystallogr., Sect. B: Struct. Crystallogr. Cryst. Chem.* **1969**, *25*, 1233−1236.
(50) Karzel, H.; Potzel, W.; Köfferlein, M.; Schiessl, W.; Steiner, M.; Hiller, U.; Kalvius, G. M.; Mitchell, D. W.; Das, T. P.; Blaha, P.; et al. Lattice dynamics and hyperfine interactions in ZnO and ZnSe at high external pressures. *Phys. Rev. B: Condens. Matter Mater. Phys.* **1996**, *53*, 11425−11438.
(51) Dovesi, R.; Saunders, V. R.; Roetti, C.; Orlando, R.; Zicovich-Wilson, C. M.; Pascale, F.; Civalleri, B.; Doll, K.; Harrison, N. M.; Bush, I. J.; D'Arco, P.; et al. *CRYSTAL14 User's Manual*; University of Torino: Torino, Italy, 2014.
(52) Perdew, J. P.; Ernzerhof, M.; Burke, K. Rationale for mixing exact exchange with density functional approximations. *J. Chem. Phys.* **1996**, *105*, 9982−9985.
(53) Adamo, C.; Barone, V. Toward reliable density functional methods without adjustable parameters: The PBE0 model. *J. Chem. Phys.* **1999**, *110*, 6158−6170.
(54) Gryaznov, D.; Blokhin, E.; Sorokine, A.; Kotomin, E.; Evarestov, R.; Bussmann-Holder, A.; Maier, J. A comparative ab initio thermodynamic study of oxygen vacancies in ZnO and $SrTiO_3$: Emphasis on phonon contribution. *J. Phys. Chem. C* **2013**, *117*, 13776−13784.
(55) Bandura, A. V.; Evarestov, R. A. Structure and stability of SnS_2-based single- and multi-wall nanotubes. *Surf. Sci.* **2015**, *641*, 6−15.
(56) Corà, F.; Patel, A.; Harrison, N. M.; Dovesi, R.; Catlow, C. R. A. An ab initio Hartree-Fock study of the cubic and tetragonal phases of bulk tungsten trioxide. *J. Am. Chem. Soc.* **1996**, *118*, 12174−12182.
(57) Monkhorst, H. J.; Pack, J. D. Special points for Brillouin-zone integrations. *Phys. Rev. B* **1976**, *13*, 5188−5192.
(58) Krause, M.; Mucklich, A.; Zak, A.; Seifert, G.; Gemming, S. High resolution TEM study of WS_2 nanotubes. *Phys. Status Solidi B* **2011**, *248*, 2716−2719.

DOI: 10.1021/acs.jpcc.6b06139
J. Phys. Chem. C 2016, 120, 21451−21459

(59) Wang, W.; Wang, L.; Liu, L.; He, C.; Tan, J.; Liang, Y. Morphology-controlled synthesis and growth mechanism of ZnO nanostructures via the NaCl nonaqueous ionic liquid route. *CrystEngComm* **2012**, *14*, 4997−5004.
(60) Klinger, M.; Jäger, A. Crystallographic Tool Box (CrysTBox): automated tools for transmission electron microscopists and crystallographers. *J. Appl. Crystallogr.* **2015**, *48*, 2012−2018.
(61) Sourisseau, C.; Cruege, F.; Fouassier, M.; Alba, M. Second-order Raman effects, inelastic neutron scattering and lattice dynamics in 2H-WS_2. *Chem. Phys.* **1991**, *150*, 281−293.
(62) Berkdemir, A.; Gutierrez, H. R.; Botello-Mendez, A. R.; Perea-Lopez, N.; Elias, A. L.; Chia, C.-I.; Wang, B.; Crespi, V. H.; Lopez-Urias, F.; Charlier, J.-C.; et al. Identification of individual and few layers of WS_2 using Raman Spectroscopy. *Sci. Rep.* **2013**, *3*, 1755.
(63) Mitioglu, A. A.; Plochocka, P.; Deligeorgis, G.; Anghel, S.; Kulyuk, L.; Maude, D. K. Second-order resonant Raman scattering in single-layer tungsten disulfide WS_2. *Phys. Rev. B: Condens. Matter Mater. Phys.* **2014**, *89*, 245442.
(64) Liang, L.; Meunier, V. First-principles Raman spectra of MoS_2, WS_2 and their heterostructures. *Nanoscale* **2014**, *6*, 5394−5401.
(65) Molina-Sanchez, A.; Wirtz, L. Phonons in single-layer and few-layer MoS_2 and WS_2. *Phys. Rev. B: Condens. Matter Mater. Phys.* **2011**, *84*, 155413.
(66) Peimyoo, N.; Shang, J.; Yang, W.; Wang, Y.; Cong, C.; Yu, T. Thermal conductivity determination of suspended mono- and bilayer WS_2 by Raman spectroscopy. *Nano Res.* **2015**, *8*, 1210−1221.
(67) Parker, J. H.; Feldman, D. W.; Ashkin, M. Raman scattering by silicon and germanium. *Phys. Rev.* **1967**, *155*, 712−714.
(68) Xu, Z. Q.; Zhang, Y.; Lin, S.; Zheng, C.; Zhong, Y. L.; Xia, X.; Li, Z.; Sophia, P. J.; Fuhrer, M. S.; Cheng, Y. B.; et al. Synthesis and transfer of large-area monolayer WS_2 crystals: Moving toward the recyclable use of sapphire substrates. *ACS Nano* **2015**, *9*, 6178−6187.
(69) He, J.; Hummer, K.; Franchini, C. Stacking effects on the electronic and optical properties of bilayer transition metal dichalcogenides MoS_2, $MoSe_2$, WS_2, and WSe_2. *Phys. Rev. B: Condens. Matter Mater. Phys.* **2014**, *89*, 075409.

DOI: 10.1021/acs.jpcc.6b06139
J. Phys. Chem. C 2016, 120, 21451−21459